Probing high-velocity outflows in active galactic nuclei and their relationship to the inner disc environment with X-ray observations

by

Adam G. Gonzalez

A Thesis Submitted to Saint Mary's University, Halifax, Nova Scotia
in Partial Fulfillment of the Requirements for the Degree of PhD in Astronomy
(Department of Astronomy and Physics)

August 2021, Halifax, Nova Scotia

Approved: _____
Dr. Luigi Gallo
Supervisor

Approved: _____
Dr. Ivana Damjanov
Examiner

Approved: _____
Dr. Philip Bennett
Examiner

Approved: _____
Dr. Filippo D'Ammando
External Examiner

Date: 10 August 2021.

Acknowledgements

On 13 March 2020, one day after my 27th birthday, the global COVID-19 pandemic shut-down Saint Mary's University for what was originally scheduled to be only two weeks. Since then, I have been to campus exactly once, to reboot my lonely computer. Though the pandemic remains ongoing at the time of writing, things are improving rapidly due to high vaccine uptake in Nova Scotia. I would like to acknowledge all of the lives lost and forever changed by COVID-19, as well as the tireless efforts of front-line and health care workers who have kept things running and progressing as smoothly as possible.

Of course, I am eternally grateful for the outstanding guidance and support provided by Dr. Luigi Gallo, who has always kept me on track. As you have found out, I like to tinker with and explore things, which works well when I'm pointed in the right direction, but can easily find me distracted by the smallest of details for extended periods of time. Without your guidance and support, I would not have successfully completed any of this to the degree that it is presented here. I would like to thank my family for always being supportive and encouraging me on my long academic road. At long last, you are finally able to stop telling people that I am a student. I would also like to thank my fellow graduate students for all of the friendship and support over the years. Finally, without the love and support of my wonderful partner, Hannah, and our three pets, Willow, Finnegan, and Xena, this would have surely been a much more difficult and lonely endeavour.

I acknowledge and am grateful for the support of the Natural Sciences and Engineering Research Council of Canada through the Canada Graduate Scholarships Doctoral program.

Contents

List of Figures

List of Tables

Abstract

Probing high-velocity outflows in active galactic nuclei and their relationship to the inner disc environment with X-ray observations

by Adam G. Gonzalez

High-velocity outflows in active galactic nuclei usually manifest as either a collimated jet or diffuse wind. These outflows carry a significant amount of energy from the central environment surrounding the supermassive black hole into the host galaxy, potentially altering the course of star formation therein. Our current understanding of how these outflows relate to the central engine, however, remains incomplete. We do not know why some active galactic nuclei exhibit jets, why some have winds, how either outflow responds to changes in the conditions of the X-ray emitting region, and if the ones that have no outflows are intrinsically different systems. In Chapters 2 and 3, I present case studies of two radio-loud active galaxies with jets, III Zw 2 and IRAS 17020+4544, in an effort to explore the postulated disc-jet connection in such systems using X-ray observations. Spectral and variability properties in each source suggest that an outflowing X-ray source may act as the jet base. In a future work, this interpretation will be explored using a sample of both radio-loud and radio-quiet sources to test its validity. A sample of 20 active galaxies that have been previously reported as exhibiting ultra-fast winds in their X-ray spectra is used to probe what underlying driving mechanisms may produce such outflows, as well as how the outflow properties relate to the conditions of the central engine. We find that wind properties are closely linked to a variety of source parameters, such as accretion rate and disc inclination angle. The properties of six extreme accretors may suggest non-standard accretion disc scenarios for which no wind is necessary, highlighting the need to explore alternative models. Future X-ray missions with enhanced spectral resolution will enable more accurate determinations on the energetics and locations of these extreme winds, which are ill-constrained with current data.

10 August 2021

Chapter 1

Introduction

1.1 A brief history

Black holes (BHs) are among the most extreme natural phenomena in the Universe, being objects of immense mass yet incredible compactness, resulting in the production of a gravitational potential that even light is incapable of escaping. Their introduction to science came via the solutions to the Einstein field equations of general relativity derived by Schwarzschild (1916) and Droste (1917), both of whom described the existence of a mathematical singularity at what is now called the Schwarzschild radius, $r_{\rm S} = 2GM_{\rm BH}/c^2$, where $M_{\rm BH}$ is the mass of a non-rotating BH, within which no information can be retrieved. Einstein (1939), however, was famously unconvinced of such solutions and their implications, doubting the physical plausibility of the existence of such objects, stating "that matter cannot be concentrated arbitrarily ... due to the fact that otherwise the constituting particles would reach the velocity of light." A century later, the first ever image[1] of a black hole was published (Event Horizon Telescope Collaboration et al. 2019), a magnificent keystone result in a field that has developed tremendously since the inception of these bizarre astrophysical objects.

[1]The black hole *itself* is, by definition, not observable; its shadow, however, is.

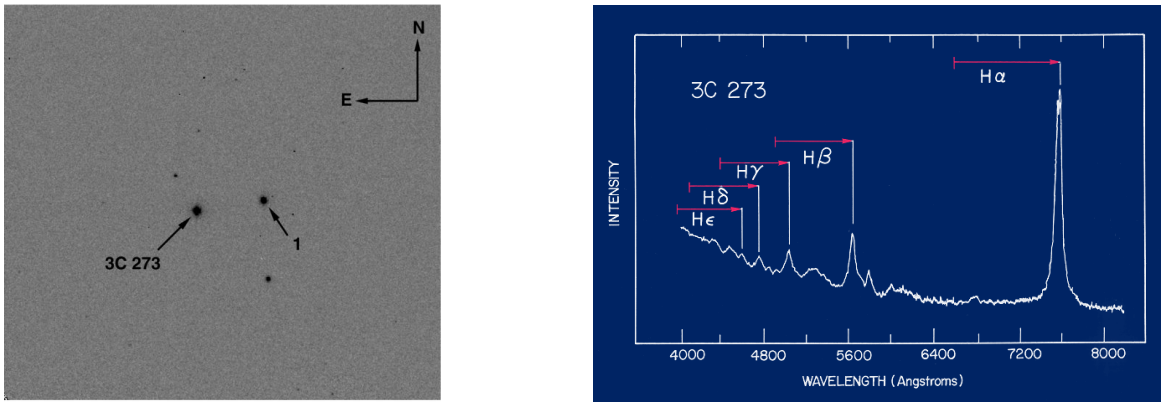

Figure 1.1: *Left panel*: Optical image of 3C 273 from the SMARTS catalogue. Object 1 is a star in the field-of-view. Figure credit: Bonning et al. (2012). *Right panel*: Optical spectrum of 3C 273. Red arrows denote wavelength shift of the observed lines, at $\lambda_{\rm obs}$, from their intrinsic rest-frame wavelengths, at $\lambda_{\rm em}$, denoted by the left vertical endpoint on each arrow. The observed line wavelengths may be computed using the redshift of 3C 273 ($z = 0.158$) as $\lambda_{\rm obs} = (1 + z)\lambda_{\rm em}$. Figure credit: Mihos, C. (2018).

Moving from theoretical to physical origins, when an exceptionally massive star with $M_\star \gtrsim 20 - 25\ M_\odot$ (Nomoto et al. 2004), where $M_\odot = 1.988 \times 10^{30}$ kg is the mass of the Sun, runs out of fuel in its core, the internal pressure of the star is no longer sufficient to counteract its own gravity. As the stellar core collapses, a hypernova is produced, emitting a shock-wave that ejects the outer layers of the progenitor, spewing the various chemical elements that were formed in the now dead star out into the cosmos. The collapsed stellar core now exists as a BH with $M_{\rm BH} \sim 5 - 10\ M_\odot$, referred to as a stellar mass BH. These BHs are most often observed as the compact constituent in binary systems, accompanied by some stellar companion. Indeed, the very first black hole candidate ever discovered, Cygnus X-1, exists in such a binary system (e.g. Orosz et al. 2011, for an unambiguous confirmation of its candidacy as a BH).

On the other end of the mass scale, and the focus of the present work, exist supermassive

BHs (SMBHs), with $M_{\rm BH} \sim 10^6 - 10^9\ M_\odot$. Seyfert (1943) noted that several nearby spiral galaxies possessed nuclei far more luminous than in other spiral galaxies, as well as significantly broadened optical emission lines. The existence of SMBHs was inferred in such systems two decades later, when Oke (1963) and Schmidt (1963)[2] observed the optical spectrum of 3C 273, which possessed highly redshifted broad emission lines ($z = 0.158$) indicating that the source existed a significant distance from Earth (see Figure 1.1). These properties led to the conclusion of an extremely luminous yet, at the time, unknown class of astrophysical object as the only viable source of emission. One year later, both Salpeter (1964) and Zel'dovich (1964) independently showed that the accretion of matter onto a compact object of radius $r \sim 10^{-7}$ pc with $M \sim 10^6\ M_\odot$ could explain the observed source properties of 3C 273. Thus, SMBHs were revealed to astronomy for the first time, after which numerous systems hosting actively accreting SMBHs were identified, with Lynden-Bell & Rees (1971) notably suggesting that even our own Milky Way harboured one of these peculiar objects, albeit in an inactive/dormant state. Now, we believe that there exists a SMBH at the centre of every single massive galaxy in the Universe (e.g. Ferrarese & Merritt 2000; Gebhardt et al. 2000).

Galaxies like 3C 273, however, only represent $\sim 10\%$ of all observed galaxies, being distinguished by the fact that the SMBHs within this small portion of the galactic population are actively accreting material, hence their classification as active galactic nuclei (AGNs). In AGNs, we observe the most luminous continuous sources of broad band emission in the Universe, with the brightest sources exhibiting $L \gtrsim 10^{12} L_\odot$, where $L_\odot = 3.828 \times 10^{33}$ erg s^{-1}

[2]It was here that the term "quasi-stellar" object, or quasar, was first used to describe these objects.

is the solar luminosity. They possess relatively flat spectral energy distributions (SEDs) from radio to γ-ray wavelengths, indicating a variety of physical processes at work. In fact, the production of this extreme luminosity can be linked directly to the central SMBH and its extreme environment, the so-called AGN central engine, which represents $\ll 1\%$ the total volume of the host galaxy, yet can outshine it many times over.

1.2 The AGN central engine

While the central SMBH is the reason for all of the extreme phenomena manifested in AGNs, by definition it does not communicate any direct observational information to us. Instead, we rely on the characteristic emission produced by the various physical structures in the vicinity of the SMBH that enable analyses of their variability and/or spectral properties which thereby inform us of their nature.

All AGNs are commonly defined by the accretion process, which itself usually manifests as an accretion disc orbiting around the central SMBH (see Figure 1.2) that extends to $r_{\rm AD} \sim 1000\ r_g$, where $r_g = GM_{\rm BH}/c^2$. The first full characterisation of AGN accretion discs was provided by Shakura & Sunyaev (1973), where it was proposed that they can be well represented as geometrically thin, optically thick structures whose characteristic emission spectrum is approximately that of a multi-temperature black body. The effective temperature, $T_{\rm e}$, of this black body-like disc emission spectrum scales as $T_{\rm e} \propto M_{\rm BH}^{-1/4}$, which for AGNs finds that this component peaks at $kT_{\rm e} \sim 10$ eV or $\lambda_{\rm e} \sim 125$ nm for a SMBH with $M_{\rm BH} = 10^8\ M_\odot$. Unfortunately, this waveband is heavily attenuated due to

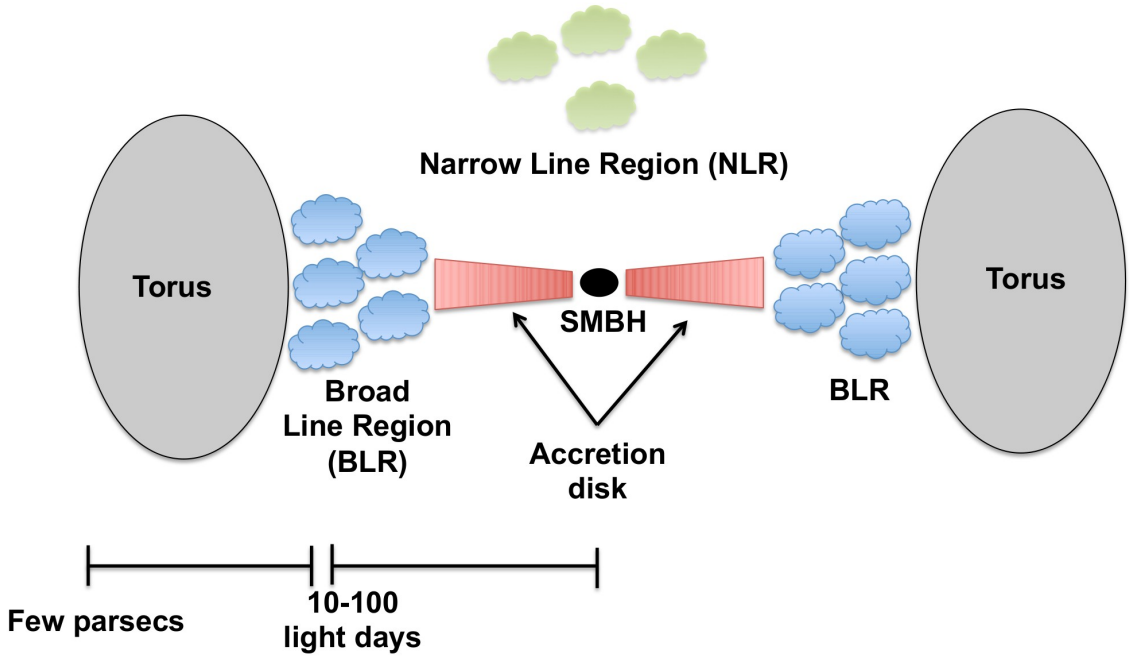

Figure 1.2: Schematic representation of the various components in the central engine of AGNs. Note that structures are not drawn to scale. Figure credit: Ricci, C. (2013).

extinction in the interstellar medium (ISM), making it essentially unobservable in AGNs[3]. Perhaps the most crucial aspect of any accretion disc theory, however, is the proposed mechanism through which matter from large distances with large gravitational potential energy is somehow brought down to the SMBH event horizon, requiring the dissipation of an immense amount of angular momentum. The α-disc theory of Shakura & Sunyaev (1973) proposed a kinematic disc viscosity ν as a plausible mechanism through which angular momentum may be transferred, such that $\nu = \alpha c_{\rm s} H$, where $c_{\rm s}$ is the sound speed, H is the disc scale height, and $\alpha \in [0, 1]$ is a free parameter[4]. In a rotating disc, orbits with large

[3]For stellar mass BHs accretion disc emission peaks in the X-ray band, where a multi-temperature black body describes their observed spectra well in the disc-dominated soft state.

[4]Although α is a free parameter in this model, most derived disc properties depend only weakly on it.

radii have lower angular velocity but higher angular momentum, while orbits with small radii have higher angular velocity but lower angular momentum comparatively; therefore, significant differential rotation exists between concentric annuli in the disc. By invoking the proposed viscosity ν, friction between differentially rotating annuli results in the conversion of angular momentum into thermal radiation, thereby producing the UV-peaked multi-temperature black body emission spectrum of the disc as well as allowing material from large distances to slowly decay in orbit toward the innermost stable circular orbit (ISCO). Balbus & Hawley (1991) alternatively proposed a model in which a magnetized accretion disc, even weakly so, exhibits magnetorotational instability (MRI) such that material on interior orbits experiences a drag force by material on exterior orbits via the magnetic field. This dragging reduces the angular momentum of the interior material resulting in a reduction of its orbital radius, eventually allowing for the accretion of this material onto the SMBH.

The X-ray emitting region, contained within $r_{\rm X} \sim 10 - 20\ r_g$ of the ISCO, is comprised of material in the disc that is subjected to the most extreme conditions anywhere in the Universe. At present, it is thought that free electrons liberated from the ionised material in the accretion disc become concentrated into an optically thin plasma with $T \sim 10^9$ K forming some geometry (e.g. compact, radially extended, vertically extended; see Section 1.4 for more details) near the SMBH via the reconnection of disc magnetic field lines (Galeev et al. 1979; Haardt & Maraschi 1991; Merloni & Fabian 2001). UV seed photons from the disc passing through this so-called corona will then become inverse-Compton scattered to X-ray energies, as relativistic electrons impart some fraction of their energy to incoming photons via inelastic scattering. For both thermal (i.e. energies following a Maxwell-Boltzmann

distribution) and non-thermal (i.e. energies following a power law distribution) populations of electrons this inverse-Compton scattering process produces a characteristic X-ray power law spectrum $F(E) \propto E^{-\alpha}$, where $\Gamma = \alpha + 1$ and in AGNs $\Gamma \sim 1.8 - 2$ (e.g. Dadina 2008; Beckmann et al. 2009). The precise structure of the corona, however, remains difficult to characterize with present-day observatories. A simple, and often adequate, assumption made is that it exists as an isotropically emitting point-like structure some height above the black hole. Some fraction of the coronal X-rays will illuminate the innermost region of the accretion disc, with some sources exhibiting an enhanced effect due to light-bending near the SMBH (Miniutti & Fabian 2004), resulting in the absorption and re-emission of these X-rays forming a so-called disc reflection spectrum (Fabian et al. 1989). The reflection spectrum can reveal a wealth of information about the inner disc environment in AGNs, through both variability and spectral analyses (see Section 1.4 for more details).

On larger scales exists the broad-line region (BLR) at distances of $r_{\rm BLR} \sim 10,000\ r_g$ from the central SMBH (see Figure 1.2). The BLR receives its descriptive name from the observed broad (i.e. full-width half-maximum, FWHM, $\sim 1000 - 10\ 000$ km s^{-1}) permitted optical emission lines (e.g. Hβ) it produces, with line broadening attributed to orbital motion of dense (i.e. $n_e \gtrsim 10^9$ cm^{-3}) emitting matter photoionised by the interior UV and X-ray radiation (see, e.g., Peterson et al. 2004 for details). Models for the exact structure for this region, however, remain incomplete. One description of the BLR is that of an ensemble of numerous (i.e. $N \gtrsim 10^6$) discrete "clouds" of photoionised material co-rotating with the accretion disc (e.g. Peterson 2006). Another model postulates that the BLR may instead be a continuous disc-wind that is raised off of the accretion disc, suggesting its origin as an

outflow (e.g Espey 1997; Leighly 2000; Vestergaard et al. 2000). Regardless of the exact description, the measured widths of BLR emission lines provide some of the most precise $M_{\rm BH}$ estimates to date via reverberation mapping techniques. By measuring the time delay between coherent continuum and line flux variations τ, the mass of the central SMBH may then be estimated using the virial theorem as $M_{\rm BH} = f c\tau v_{\rm K}^2/G$, where f is of order unity that encodes the unknown geometry of the BLR and $v_{\rm K}$ is the Keplerian orbital velocity inferred from the line FWHM (Peterson et al. 2004). The results of reverberation mapping campaigns of large samples of AGNs reveal $M_{\rm BH} \sim 10^6 - 10^9\ M_\odot$ (see Bentz & Katz 2015 for a collection of results).

Encompassing the entirety of the aforementioned structures is the dusty torus (see Figure 1.2), on scales of $r_{\rm T} \gg 1,000,000\ r_g$, or $r_{\rm T} \sim 1$ pc. With a Compton thick column density (i.e. $N_{\rm H} > 10^{24}$ cm^{-2}) and low ionisation state (i.e. neutral), the torus is a source of significant obscuration / absorption for AGNs in which our line of sight intersects it (see Ramos Almeida & Ricci 2017 for a review). Its absorption and scattering of the central ionising continuum produces a characteristic emission spectrum peaked at infrared wavelengths. As with the BLR, the exact structure of the torus is debated, with some models hypothesizing a patchy geometry of discrete clouds and others suggesting it too may be part of a outflowing wind structure (e.g. Elitzur 2006).

On galactic scales exists the narrow-line region (NLR) at distances of $r_{\rm NLR} \sim 100$ pc from the central SMBH (see Figure 1.2). In the NLR the production of narrow (i.e. FWHMs $\sim 500 - 1000$ km s^{-1}) forbidden emission lines (e.g. [O III]) indicate the low-density (i.e. $n_e \sim 10^3$ cm^{-3}) nature of this most extended structure that is still pho-

toionised by the extreme processes of the central $\sim 10 - 20\ r_g$ (e.g. Storchi-Bergmann et al. 2010). Blueshifted emission lines from the NLR indicated mild outflow velocities (e.g. $v_{\rm out} \sim 100 - 1000$ km s^{-1}). Furthermore, analysis of NLR and BLR line ratios (e.g. [O III] /Hβ) reveals that a combination of both collisional ionisation and photoionisation sources are required to appropriately describe the NLR, which some have interpreted as evidence of shock front propagation through the NLR, posssibly due to jet activity (e.g. Wang et al. 2009).

1.3 Classification

The central engine described above is *the* defining component of all AGNs. Observationally, however, a number of AGN classifications exist based on the apparently very different properties measured in these systems (e.g. luminosity, line widths, line ratios, level of obscuration, SED components, etc.). The most used distinction between AGNs is made by assessing the level of radio loudness, often defined by the ratio of fluxes at 5 GHz and in the optical B-band as $R_{\rm L} = f_{\rm 5GHz}/f_B$ (Kellermann et al. 1989). Historically, a division between radio-loud ($R_{\rm L} > 10$; RL) and radio-quiet ($R_{\rm L} < 10$; RQ) has been used to distinguish AGNs.

1.3.1 Radio-loud

On the largest scales of up to $\sim$ 1 Mpc a sub-population of $\sim$ 10% of observed AGNs (e.g. Kellermann & Pauliny-Toth 1966; Shapiro & Weinreb 1966) display enhanced radio emission when compared to the bulk population, distinguishing themselves as RL-AGNs. It

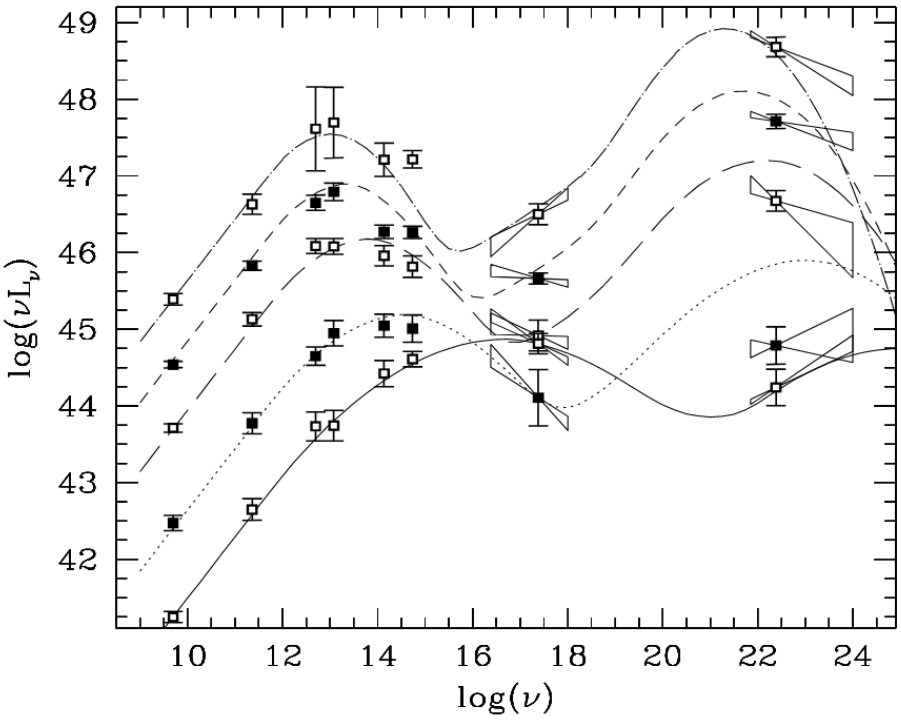

Figure 1.3: Example mean blazar SEDs (data points), with no BL Lac or FSRQ classification separation, in five bins of $L_{5\mathrm{GHz}}$ from radio to γ-ray frequencies with analytic approximations (curves) overlaid. More luminous radio sources exhibit more dominant γ-ray peaks. Less luminous radio sources exhibit peaks shifted to higher frequencies. The similarity in SEDs spanning ~ 5 orders of magnitude in $L_{5\mathrm{GHz}}$ irrespective of blazar classification suggests a continuous spectral sequence in blazars rather than distinct classes of objects. Figure credit: Fossati et al. (1998).

is in these AGNs that the most rapid and powerful outflows in the Universe are observed (i.e. jets; see Section 1.5.1 for more details). Although all RL-AGNs exhibit enhanced radio emission, a variety of sub-classifications exist based on their different observed properties.

Blazars are the most extreme of the RL-AGNs, being divided into flat-spectrum radio quasars (FSRQs) and BL Lac objects[5]. Both types of objects comprise the population of the most luminous AGNs, with SEDs typically dominated by a double-peaked non-thermal

[5]The BL Lac classification gets its name from the prototype AGN of the class, BL Lacertae.

power law component (see Figure 1.3). The SED shape has been inferred as due to relativistic beaming of a powerful radio jet that is aligned closely with our line-of-sight viewing angle to the AGN (Urry & Padovani 1995). In general, BL Lacs are of lower luminosity than FSRQs by a factor of ~ 10 (e.g. Sambruna et al. 1996) and sometimes display increased X-ray variability relative to FSRQs, though all blazars exhibit significant variability across all wavelengths.

RL-AGNs observed on line-of-sight viewing angles that do not closely align with the radio jet are more generally referred to as radio galaxies (RGs). Broad-line radio galaxies (BLRGs) exhibit both broad and narrow optical emission lines, originating from the BLR and NLR of the AGN, respectively, while narrow-line radio galaxies (NLRGs) comparatively lack broad optical emission lines. BLRGs and NLRGs that exhibit strong optical continuum emission, attributed to bright accretion discs, are referred to as Type I and Type II QSOs, respectively. Finally, radio morphology has been used to classify RGs as either Fanaroff-Riley I (FR-I; Fanaroff & Riley 1974), displaying low-power and weakly collimated jets, and FR-II AGNs, displaying high-power and highly collimated jets. See Hardcastle & Croston (2020) for a recent and extensive review on RL-AGN multi-wavelength properties.

1.3.2 Radio-quiet

The vast majority of AGNs exhibit far less intense radio emission (i.e. by several orders of magnitude), hence being defined as RQ-AGNs. Sources classified as Seyfert 1s typically exhibit both broad and narrow emission lines (see Figure 1.4, top), indicating significant contributions from the BLR and NLR, respectively, as well as strong inner disc reflection

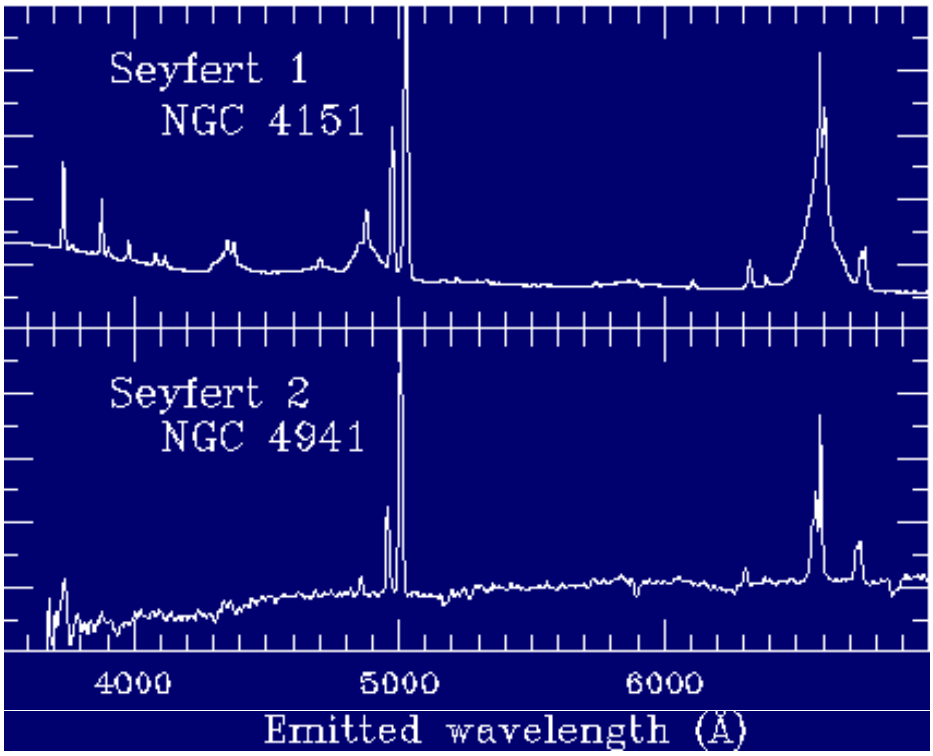

Figure 1.4: Example optical spectra of Seyfert 1 and Seyfert 2 AGNs, with y-axis in arbitrary units of flux. Broad and narrow lines are evident in the Seyfert 1 spectrum, while the Seyfert 2 displays only narrow lines. Figure credit: Keel, B. (2002).

spectra. Seyfert 2s, however, typically only exhibit narrow optical emission lines and notably lack broad lines altogether (see Figure 1.4, bottom), with the reflection spectrum usually dominated by an inferred distant, neutral origin (i.e. the torus). It seems, then, that a straightforward correspondence can be made between RL- and RQ-AGNs: FSRQs and Seyfert 1s possess contributions from all components of the central engine, while FR-type sources and Seyfert 2s may be interpreted as having an apparently absent inner disc and BLR such that only the torus and NLR are directly observed.

Among the RQ-AGNs, narrow-line Seyfert 1s (NLS1s) present themselves as those ex-

hibiting some of the most extreme source properties. They were originally distinguished from other Seyfert 1s as those with Hβ FWHMs of $\lesssim 2000$ km s^{-1} (Goodrich 1989), leading to the conclusion that they possess less massive SMBHs of $M_{\rm BH} \sim 10^6 - 10^7$ $M_\odot$, and exhibiting strong Fe II but weak [O III] emission lines (Osterbrock & Pogge 1985). Since then, however, they have been found to exhibit steeper than average X-ray continua (i.e. $\Gamma \gtrsim 2.2$), enhanced disc reflection spectra, and rapid, large amplitude variability (e.g. Boller et al. 1996; Brandt et al. 1997; Komossa et al. 2017; Gallo 2018). Interpretations as to the underlying cause of their extremity when compared to 'normal' Seyfert 1s suggest that NLS1s have extreme accretion rates close to or in excess of the Eddington limit[6] (e.g. Boroson & Green 1992).

1.3.3 Unified Model

The various distinctions highlighted above make it unclear as to whether the described differences between RL- and RQ-AGNs (and sub-classes therein) are due to *bona fide* physical differences in each class of AGN or if there exists a more straightforward explanation assuming a common underlying physical scenario.

Antonucci (1993) proposed a unified AGN model in which only two intrinsically different populations of AGNs exist: RL and RQ sources, with all sub-classes encompassed by them explained by changes in our viewing angle θ toward the central engine (see Figure 1.5). In this model, Type I AGNs are defined as having low inclination angles to the central engine

[6]The Eddington limit in AGNs is defined as $L_{\rm Edd} = 4\pi G M_{\rm BH} m_{\rm p} c/\sigma_{\rm T}$ where $m_{\rm p}$ is the proton mass and $\sigma_{\rm T}$ is the Thomson scattering cross-section, derived assuming spherically symmetric accretion. When $L = L_{\rm Edd}$ pressure from radiative processes (i.e. radiation pressure) is equivalent to the gravitational pull from the SMBH.

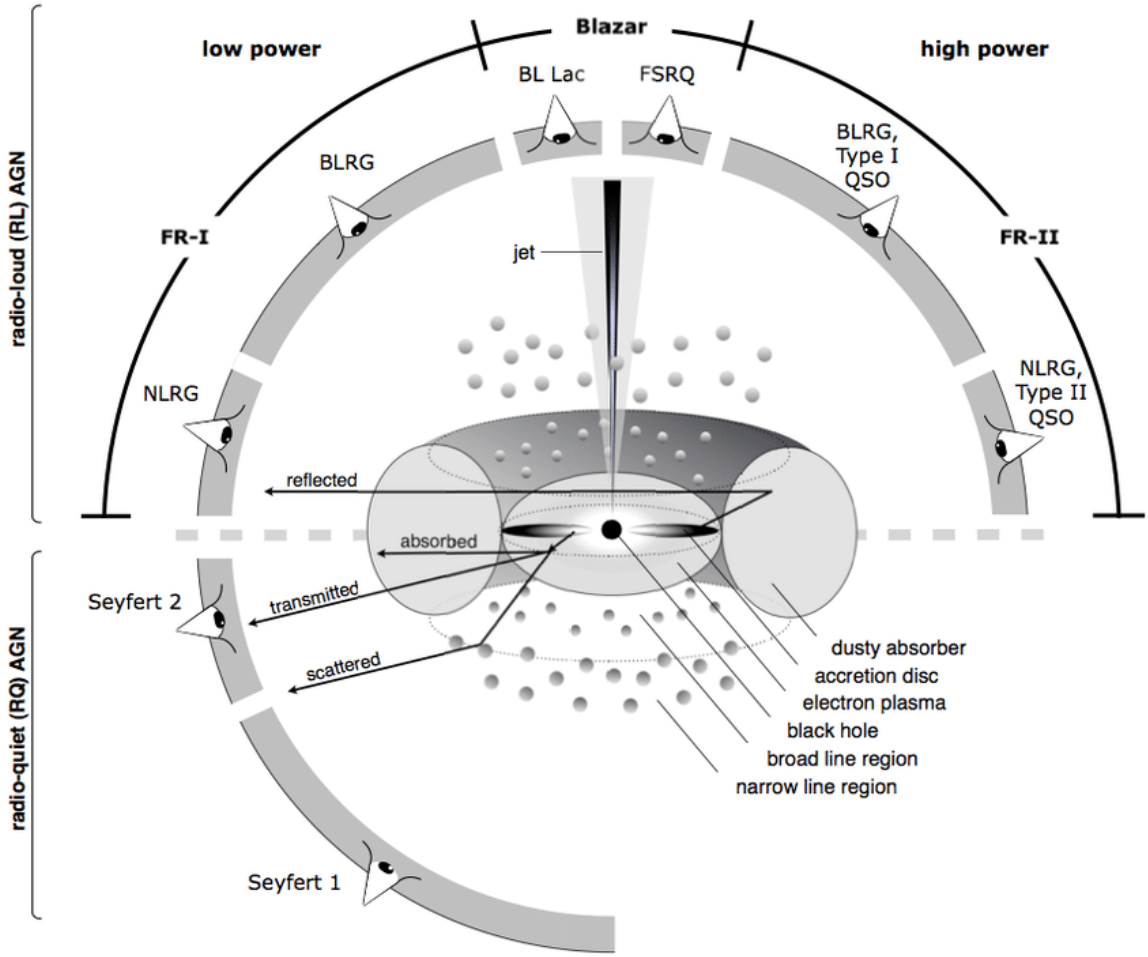

Figure 1.5: Schematic representation of the various unified models proposed for AGNs. Figure credit: Beckmann & Shrader (2012).

(i.e. $\theta \lesssim 60°$, face-on) while Type II AGNs are simply Type I AGNs viewed at larger inclination angles (i.e. $\theta \gtrsim 60°$, edge-on). The key component in determining the observed properties of any particular AGN, according to the assumptions of this model, is the torus. In Type I AGNs, our line of sight to the innermost region is unimpeded by the torus, and thus the inner disc and BLR contributions to the SED are readily measured. In Type II AGNs, however, the torus effectively blocks the inner disc and BLR, therefore allowing only

observations of the NLR and scattered emission from the torus to be made.

Urry & Padovani (1995) later proposed that viewing angle could also explain the observed properties in RL-AGNs, with blazars being the RL Type I counterparts and the FR-type AGNs being the RL Type II counterparts (see Figure 1.5). In this model, blazars are those AGNs in which the jet is closely aligned to our line of sight viewing angle of the central engine, thus we observe jet dominated SEDs and enhanced luminosities due to relativistic beaming in the jet (e.g. Blandford & Königl 1979). Then, as θ increases, the beaming effect is reduced and the jet component dominates the spectrum less intensely, thus revealing the BLR, as observed in some FSRQs. For high θ, the torus again impedes our view of the inner disc and BLR, and therefore we measure only the narrow emission lines, as in the FR-type sources. Indeed, in FR-type RL-AGNs symmetric double-sided jets are frequently observed, while in blazars only one side of the jet is observable, often exhibiting super-luminal motion. These effects are all expected based on the described observing angles of relativistic jets for each source type.

Providing observational support to the unification of AGNs based on viewing angle are the results of X-ray polarimetry studies on Seyfert 2 AGNs (e.g. Antonucci 1984; Miller & Goodrich 1990). Such studies have found evidence of broad emission lines in polarized light, thus revealing the hidden BLR in some Seyfert 2s behind the obscuring torus.

It is important to note that this unification model makes no attempt to explain the observed RL-RQ dichotomy, only addressing why the RL/RQ sub-classes *appear* different from one another. The classification of AGNs into discrete categories around $R_{\rm L} = 10$ is indeed rather arbitrary, with a more natural explanation being one that would address radio-

loudness as a continuous parameter based on some physical mechanism(s). Wilson & Colbert (1995) suggested that galaxy mergers may play a key role in producing RL-AGNs, which has been corroborated observationally (e.g. Ramos Almeida et al. 2012; Chiaberge et al. 2015) by findings of RL-AGNs displaying significantly higher merger fractions (i.e. $\gtrsim 80\%$) than RQ-AGNs (i.e. $\lesssim 40\%$). Importantly, AGN classification as RQ does not indicate radio *silence*, though in many RQ-AGNs the observed radio luminosity is consistent with a star formation origin in the host galaxy (see, e.g., Condon 1992 for a review), and thus is not attributable to AGN/SMBH activity. In those systems, dying massive stars (signifying very recent star formation, as they are short-lived) produce supernovae that accelerate relativistic electrons and ionise regions of H II gas, then end result of which is synchrotron as well as free-free radiation (i.e. Bremsstrahlung) at radio wavelengths.

1.4 X-ray properties of AGNs

It is perhaps in the X-ray band that the central engine of AGNs can be most closely examined, and it is therefore the focus of the work presented here. Through variability and spectral analyses (often a complementary use of both) of the X-ray emission (i.e. $0.1 - 100$ keV) in AGNs, we have been able to learn much about the inner disc region. The dominant X-ray emission source in the majority of AGNs is the X-ray corona, producing a characteristic power law emission spectrum with $\Gamma \sim 2$. Many AGNs, however, cannot be fit with a single power law component, also displaying significant excess emission at $E \lesssim 2$ keV, known as

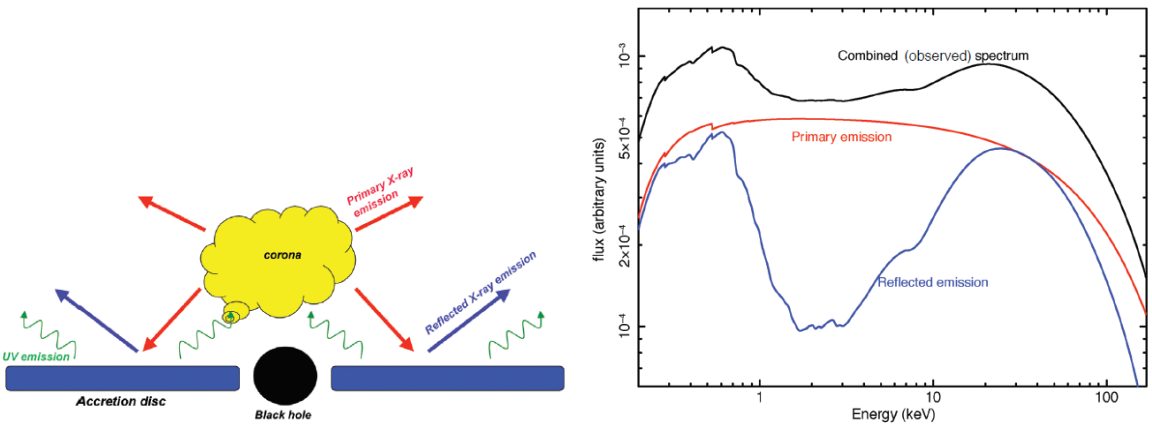

Figure 1.6: *Left panel*: Schematic representation of the inner disc region in AGNs. UV seed photons from the disc are inverse-Compton scattered to X-rays in the corona, which illuminates the disc thereby producing a disc reflection spectrum. *Right panel*: Spectral components corresponding to the emission regions on the left. Figure credit: Gallo (2011).

the 'soft excess'[7] (see Turner & Pounds 1989 for early findings), the origin of which remains an open research question (described in the following paragraphs). Furthermore, fluorescent emission by Fe Kα at 6.4 keV has been measured in many AGNs, with some displaying narrow unresolved lines ($\sigma_{\mathrm{K}\alpha} \lesssim 500$ km s^{-1}), indicating an origin via reflection from a slowly rotating, neutral medium (e.g. the torus), and others displaying extremely broad, asymmetric features that extend over $3-7$ keV, indicating an origin via reflection from material much closer to the SMBH that is subject to both general and special relativistic effects.

For AGNs exhibiting X-ray spectra with a soft excess and broad Fe Kα line profile[8], reflection of coronal X-rays off of the inner accretion disc (i.e. $r_{\mathrm{AD}} \lesssim 10-20\ r_g$) has been shown to describe these features well (e.g. Crummy et al. 2006), acting as a secondary

[7]Recall that the multi-temperature disc black body of AGNs peaks in the UV, and therefore cannot account for the soft excess, despite its black body-like appearance.

[8]These features are also often accompanied by a "hard excess" known as the Compton hump, which peaks at $\sim 20-30$ keV and is the result of Compton down-scattering of X-ray photons scattering off of the accretion disc and/or dusty torus (Lightman & White 1988).

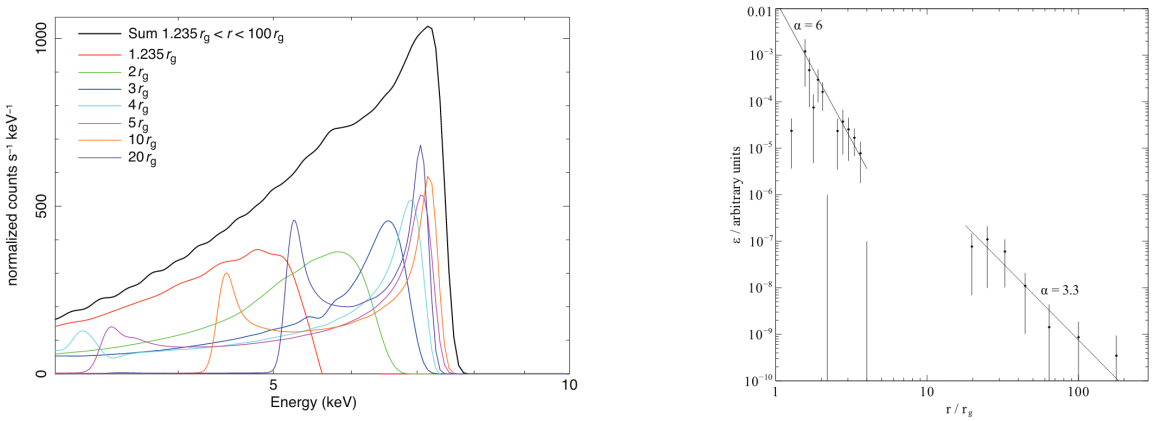

Figure 1.7: *Left panel*: Relativistically broadened Fe Kα line profile (black), with contributions from concentric annuli of the disc (colours). Annuli near the ISCO exhibit the most gravitationally redshifted and asymmetric line profiles due to general relativistic effects near the SMBH. Annuli at larger radii resemble a double-peaked Doppler broadened line profile, with asymmetry due to special relativistic effects. *Right panel*: The measured disc emissivity profile in the NLS1 1H 0707−495, done by computing the incident coronal flux for concentric disc annuli, breaking down the observed Fe Kα in the same manner as on the left. Here α represents the emissivity index, labelled in two regimes: (i) $\alpha = 6$ denotes the heavily illuminated inner disc region receiving enhanced X-ray flux due to general relativistic light-bending effects, and (ii) $\alpha = 3.3$ denotes the classical/Newtonian result of an infinite slab illuminated by an elevated point source. Figure credit: Wilkins & Fabian (2011).

X-ray emitter whose characteristic shape can be used to infer much about the conditions near the SMBH (see Figure 1.6). For example, if the accretion disc extends to the ISCO (i.e. is not truncated by some mechanism at larger radii) then it is possible to probe the black hole spin $a = Jc/GM_{\rm BH}^2$, where J is the angular momentum. Non-spinning black holes (i.e. Schwarzschild black holes with $a = 0$) will have $r_{\rm ISCO} = 6\ r_g$. Maximally-spinning black holes (i.e. Kerr black holes with $a = 0.998$) will have $r_{\rm ISCO} = 1.235\ r_g$, enabled by the significant rotation of spacetime due to frame-dragging in the ergosphere of Kerr black holes. The reflection spectrum produced in each scenario will differ dramatically due to the enhanced gravitational redshift imparted to the X-ray emission from the innermost

disc material of a Kerr black hole. This effect can be most easily observed by examining the Fe Kα line profile (Fabian et al. 1989). A Kerr black hole will produce an Fe Kα line profile that is highly asymmetric due to extreme general relativistic effects on the emitting disc material at the ISCO, with a prominent blueshifted 'horn' and extended redshifted 'wing' (see Figure 1.7, left). In fact, by breaking down contributions to the overall Fe Kα line profile in concentric annuli on the accretion disc, the disc emissivity (or illumination) profile $\epsilon(r) \propto r^{-\alpha}$, where r is the radius of an annulus on the accretion disc and α is the emissivity index, can be studied[9] (see Figure 1.7, right). These emissivity profiles typically display a broken power law shape that breaks at some radius $r_{\rm break}$, below which the disc is heavily illuminated due to general relativistic light-bending effects and beyond which the disc receives illumination as predicted by classical/Newtonian physics of an infinite slab illuminated by an elevated point source. The precise measurements of α and $r_{\rm break}$ reveal important information about the geometry and motion of the X-ray corona (e.g. Wilkins & Fabian 2012; Gonzalez et al. 2017). Detailed modelling of the reflection spectrum in AGNs has found evidence of radially extended slab-like coronae (e.g. Wilkins et al. 2014) with others finding evidence of vertically collimated, possibly relativistically beamed, coronae (e.g. Gallo et al. 2011; Wilkins & Gallo 2015a; Wilkins et al. 2017).

Similar to the reverberation mapping techniques applied to optical data to measure $M_{\rm BH}$, X-ray reverberation analyses have been used as a model-independent method with which we may probe the presence of highly ionised relativistically broadened reflection spectra

[9]In practice, reflection models applied to the X-ray data of AGNs encode the emissivity profile directly within the model computation. This makes measurements of the emissivity profile more straight-forward than via the direct breakdown of the Fe Kα line profile, though the latter method is still superior in those sources where it is feasible to apply (i.e. very high quality data).

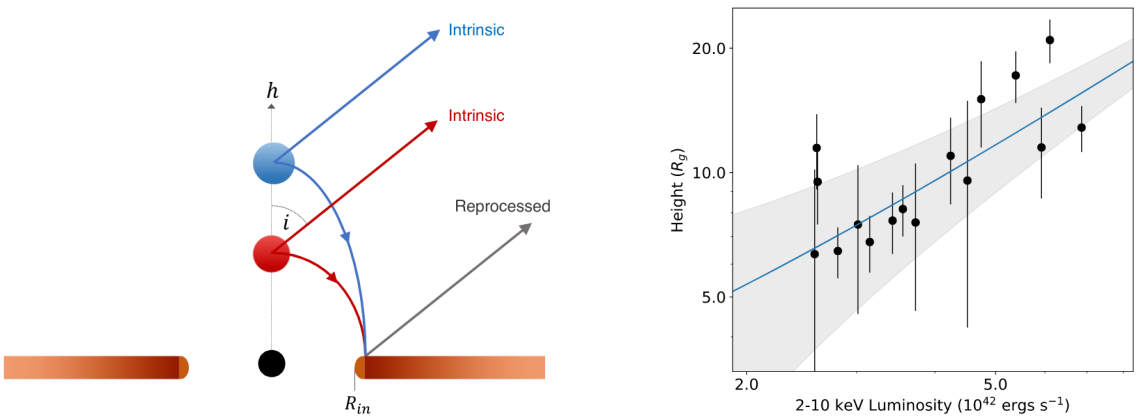

Figure 1.8: *Left panel*: Schematic representation of the point source corona in IRAS 13224−3809 increasing in luminosity (intrinsic) with increasing height, h, above the accretion disc, producing a correspondingly lagged disc reflection spectrum (reprocessed). *Right panel*: By measuring variable time lags between the intrinsic and reprocessed emission an X-ray corona with varying height above the accretion disc is found to produce higher X-ray luminosity at increased heights. Figure credit: Alston et al. (2020).

from the inner disc in numerous AGNs. In the reflection scenario (see Figure 1.8, left), X-rays emitted by the corona will arrive at the observer some time $\tau_{\rm C}$ (labelled 'intrinsic') before coherently reflected X-rays from the inner disc arriving at $\tau_{\rm R}$ (labelled 'reprocessed'). Measurements of the lag time between these two components, $\tau_{\rm lag} = \tau_{\rm R} - \tau_{\rm C}$, in large samples of AGNs have revealed $\tau_{\rm lag} \sim 100 - 1000$ s (e.g. Kara et al. 2016), highlighting the compactness of this region. In particular, a recent analysis of the NLS1 IRAS 13224−3809 by Alston et al. (2020) used variations in $\tau_{\rm lag}$ to infer rapid changes in the height[10] of a compact X-ray corona located above the disc along the BH spin axis. These lag variations were then mapped together with the corresponding X-ray luminosity of the source, finding that brighter X-ray luminosities correlated with increased coronal height about the disc,

[10]The coronal height in Figure 1.8 is calculated from the lag time between intrinsic and reprocessed emission by computing the response function of the disc material, which evolves with height, to a δ-function emission flare.

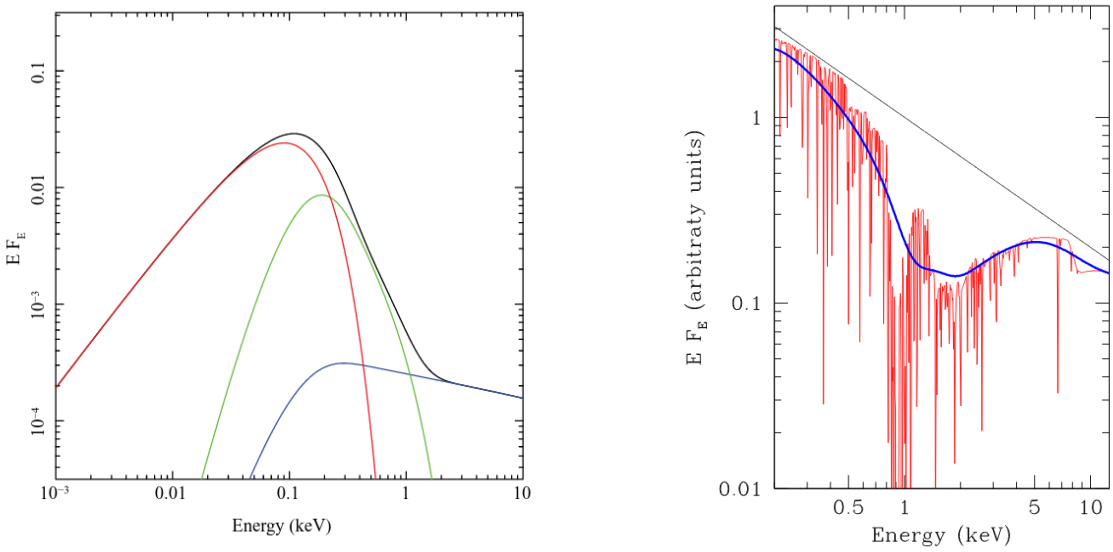

Figure 1.9: *Left panel*: Optical-to-X-ray AGN SED assuming a warm corona, or soft-Comptonisation, scenario (green curve) to explain the soft excess. The red curve denotes distant thermal disc emission with the blue curve as the coronal power law. Figure credit: Done et al. (2012). *Right panel*: AGN X-ray spectrum assuming an absorption scenario to explain the soft excess. The black curve represents the intrinsic (unabsorbed) coronal power law, which has been applied with a partially covering ionised absorber to produce the red curve. The blue curve is a smoothed version of the red, highlighting how an apparent soft excess is produced. Figure credit: Gierliński & Done (2004).

with the corona varying in height between $h \sim 6\ r_g$ to $h \sim 20\ r_g$ (see Figure 1.8, right).

Alternatively, however, some AGNs displaying a soft excess are not well fit by a power law plus reflection model, requiring instead (of reflection) a 'warm corona', or soft-Comptonisation, model (see Figure 1.9, left) (e.g. Porquet et al. 2004). This secondary X-ray corona may exist as the innermost portion of the disc, or as some atmosphere-like slab covering it, with enhanced optical thickness such that it emits a black body-like spectrum, thereby accounting for the shape of the soft excess. Indeed, such a description of the soft excess has been found to work very well for a number of AGNs (e.g. Petrucci et al. 2018).

Yet another description of the X-ray spectrum in AGNs invokes no additional emission

component(s) whatsoever, instead accounting for the significant spectral curvature via a partially covering and ionised obscuring cloud model (see Figure 1.9, right) (e.g. Gierliński & Done 2004). Such models find that by invoking the presence of orbiting gas clouds in the inner disc (similar to the discrete-clouds model of the BLR, albeit much closer to the SMBH), which become ionised due to the intense X-ray power law continuum and that provide some covering fraction $f_{\rm cov}$ over the corona, the X-ray spectrum can be simply reproduced without the need for additional extreme components.

It is likely that a combination of any of the aforementioned components exists in many AGNs, further complicating spectral fits performed when assuming a single underlying scenario. Indeed, during the occultation event observed by Gallo et al. (2021) in the RQ Type I AGN NGC 6814, the authors found that a partial covering scenario of some occulting cloud(s) could simply describe the event itself. The underlying continuum, however, could not be distinguished as either a power law plus reflection or power law plus soft-Comptonisation scenario, as both continuum models provided similar statistical fits.

1.5 Outflows

Until this point, we have discussed much about the accretion process in AGNs, representing the *inflow* of matter toward the central SMBH. AGNs of all types, however, also commonly exhibit *outflows* of matter. These outflows take one of two forms, as either a jet or a wind, with both types of outflow being capable of significantly altering the course of star formation in the host galaxy via AGN feedback.

1.5.1 Jets

We have already discussed how RL-AGNs possess powerful, tightly collimated, relativistic (i.e. up to $v_{\rm out} \sim c$) jets that govern many of the observed properties in such systems. Recalling Figure 1.3, radio observations reveal that RL-AGN SEDs are dominated by synchrotron emission from free electrons located in the jet beam, producing a broad low-frequency spectral component. Furthermore, relativistic electrons in the beam may inverse-Compton scatter their own synchrotron emission (i.e. synchrotron self Compton, SSC, or alternatively internal Compton, IC) or external seed photons (i.e. external Compton, EC), originating from, for example, the BLR or dusty torus, to X-ray and γ-ray energies, producing a secondary broad high-frequency spectral component. These two smooth, essentially featureless, components dominate the SED in most RL-AGNs, as the jet luminosity outshines the other spectral components due to luminosity enhancement as a result of relativistic beaming of the jet emission in systems where it is coincident (or at least nearly) with our line of sight viewing angle (e.g. Blandford & Königl 1979).

Regarding the physical mechanism(s) driving jets, several have been proposed. Early on, Blandford & Znajek (1977) suggested that energy and angular momentum may be extracted from the SMBH directly via magnetic fields anchored in the accretion disc and threaded through the SMBH, resulting in free electrons being accelerated to large distances by the poloidal magnetic field. Later, Blandford & Payne (1982) suggested that instead of extracting energy and angular momentum directly from the SMBH, it was possible to do so from the magnetized accretion disc. In this model, poloidal magnetic field lines of the inner

disc stream electrons liberated from the disc material out at high velocities, with collimation provided by toroidal field lines of the outer disc region. This model appears a somewhat natural consequence of the MRI disc theory.

In both described jet launching mechanisms a connection between the accretion disc and jet is fundamental (i.e. the disc-jet connection). At present, tantalizing hints toward this disc-jet connection have been reported (e.g. Merloni et al. 2003; Falcke et al. 2004; Körding et al. 2006), where it has been suggested that jets dominate systems accreting in the sub-Eddington regime (i.e. $L/L_{\rm Edd} \ll 1$, where $L_{\rm Edd} \simeq 1.26 \times 10^{38}\,(M_{\rm BH}/M_{\odot})$ erg s^{-1}), but that as the accretion rate rises to near or above the Eddington limit (i.e. $L/L_{\rm Edd} \gtrsim 1$) the brightening disc begins to quench the jet. Testing of the disc-jet connection is complicated by the fact that jetted objects tend not to display strong disc components while sources with intense disc emission tend not to display strong jets, aspects that significantly hinder a simultaneous characterisation of both structures.

In recent years, however, an increasing population of NLS1s have shown great promise in their potential to explore the disc-jet connection within. For example, recent analyses of I Zw 1 (Gallo et al. 2007; Wilkins et al. 2017) and Mrk 335 (Gallo et al. 2013; Wilkins & Gallo 2015a), both RQ-NLS1s, have exhibited what have been inferred as aborted jet launching events through dramatic variability in the structure of their X-ray coronae, afforded by the study of their strong disc reflection spectra. These events indicate that perhaps a partial fulfillment of the prerequisites for jet launching were met in these RQ AGNs, however, they seem to have failed to meet some as-of-yet unknown condition(s) to successfully produce a powerful outflow. Numerous RL-NLS1s have also been observed, with some even displaying

significant γ-ray emission in their jets (e.g. Abdo et al. 2009a,b; D'Ammando et al. 2012, 2015, see D'Ammando 2019 for a review), a finding that stands out among results that found only the most massive SMBHs are capable of producing RL-AGNs (e.g. Laor 2000). In such AGNs, strong disc emission is produced alongside powerful jets, placing these systems as top-tier candidates in which the disc-jet connection can be thoroughly explored. To date, however, a relatively minor presence of such studies exists in the literature, likely due to the fact that RL-NLS1s represent only a small portion ($\sim 7\%$; Komossa et al. 2006) of an already limited subclass of Type I AGNs. Nevertheless, there have been some indications that RL-NLS1s may exist as the young, low-mass counterpart to blazars (Foschini 2011).

1.5.2 Winds

AGN winds can be viewed as the less powerful, lower velocity (i.e. $v_{\rm out} \ll c$), diffuse (i.e. no collimation) counterparts to jets. A variety of winds have been observed in AGNs, with most of their differences fundamentally linked to the distance from the central SMBH at which they are inferred to be launched. This subsequently dictates all of the measured wind properties, such as the ionisation state $\xi = L_{\rm I}/n_{\rm H}r^2$ (where $L_{\rm I}$ is the luminosity of the ionising continuum, $n_{\rm H}$ is the hydrogen density, and r is the distance from the ionising continuum source) and velocity $v_{\rm out}$ of the outflowing matter.

A significant fraction (i.e. $\sim 50\%$) of AGNs have been found to exhibit mildly ionised (i.e. $\log\left(\xi/\text{erg cm s}^{-1}\right) \sim -1-3$), moderate column density (i.e. $N_{\rm H} \sim 10^{20}-10^{22}$ cm^{-2}) obscuring gas at large distances (i.e. ~ 1 pc) from the SMBH, the so-called warm absorbers (WAs) (e.g. Reynolds 1997; Blustin et al. 2005). In many of these systems, WAs are

measured to have blueshifts corresponding to $v_{\rm out} \sim 100 - 1000$ km s^{-1}, hence suggesting a wind origin, and are observed to evolve on both short (e.g. De Marco et al. 2020) and long timescales (e.g. Kaastra et al. 2014). The most rapid winds measured to date are known as ultra-fast outflows (UFOs), exhibiting extreme properties (i.e. $\log\left(\xi/\text{erg cm s}^{-1}\right) \gtrsim 4$, $N_{\rm H} \sim 10^{22} - 10^{24}$ cm^{-2}, $v_{\rm out} \sim 0.1 - 0.4c$) that indicate an origin of within $\sim 100 - 1000\ r_g$ of the SMBH. Despite their extremity, UFOs are apparently rather common, occurring in $\sim 30 - 40\%$ of AGNs based on blind-search sample studies with $N \approx 50$ (e.g. Tombesi et al. 2010; Gofford et al. 2013; Igo et al. 2020)[11]. The energy carried via winds driven by the central engine out into the host galaxy offer a significant source of AGN feedback (e.g. Fiore et al. 2017). Interestingly, the vast majority of AGNs that display strong evidence of UFOs also exhibit WAs. This frequent presence of the two wind structures suggests a common underlying driving mechanism linking WAs and UFOs, of which several have been proposed.

Similarly to how bright O-type stars are capable of driving winds, radiation pressure in atomic lines from the intense disc and X-ray emission has been shown capable of accelerating matter near the SMBH to sufficiently high velocities such that UFOs are produced. In such a scenario (e.g. Proga et al. 2000), the wind is launched perpendicular to a bright disc, becoming accelerated radially outward by the interior X-ray emission, producing an axially symmetric wind. The relative proportion of UV and X-ray luminosities will govern the exact geometry of the outflow, though in general a high velocity, highly ionised, low density interior wind surface will sheath a slower, less ionised, dense outflow (see Figure 1.10). The

[11]Sample sizes for each study are as follows: Tombesi et al. (2010) $N = 42$, Gofford et al. (2013) $N = 51$, Igo et al. (2020) $N = 58$.

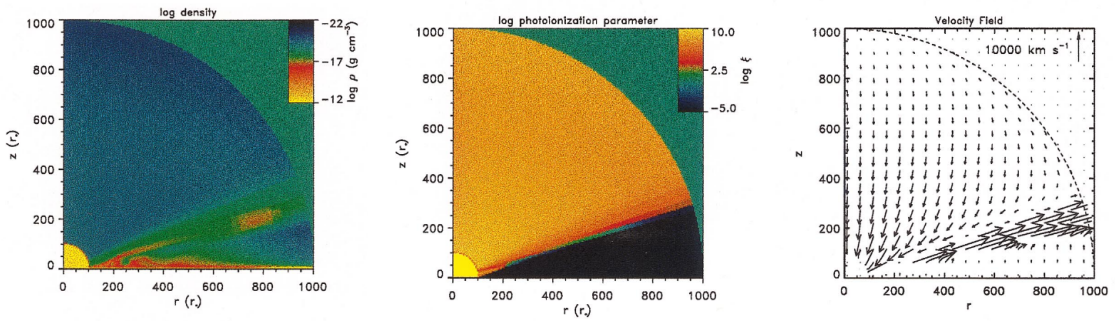

Figure 1.10: Selection of radiatively-driven wind properties, displaying density profile (left), ionisation gradient (middle), and velocity field (right) as a function of disc radius r and height above the disc z. In each panel, the circle bound by $r = 100\ r_g$ denotes the central engine, within which exists the X-ray source. A wind elevation angle of 15° off of the disc (i.e. opening angle of 75° from polar/spin axis) was used to simulate the wind geometry. Figure credit: Proga et al. (2000).

interior sheath is critical in this model in order to prevent overionisation of the outflowing material, which would result in outflow termination. This underlying line-driven launching mechanism is also able to account for the properties of WAs. Radiatively-driven wind models have been successfully applied to numerous AGNs, with a notable recent application being to IRAS 13224−3809, where it was found that increased X-ray luminosity led to both more rapid outflows (Chartas & Canas 2018) as well as over-ionisation of the outflowing material, resulting in a dissipation of the outflow (Pinto et al. 2018).

Alternatively, magnetocentrifugal acceleration of matter due to a rotating external magnetic field extracting energy and momentum from the disc (i.e. via the Blandford & Payne 1982 mechanism) has also been shown capable of producing both UFOs (Fukumura et al. 2010b) and WAs (Fukumura et al. 2010a). In this model, matter is accelerated along magnetic field lines from the disc, becoming photoionised by the central X-ray source, producing a wind structure of low-density, highly ionised matter near the SMBH spin axis that transi-

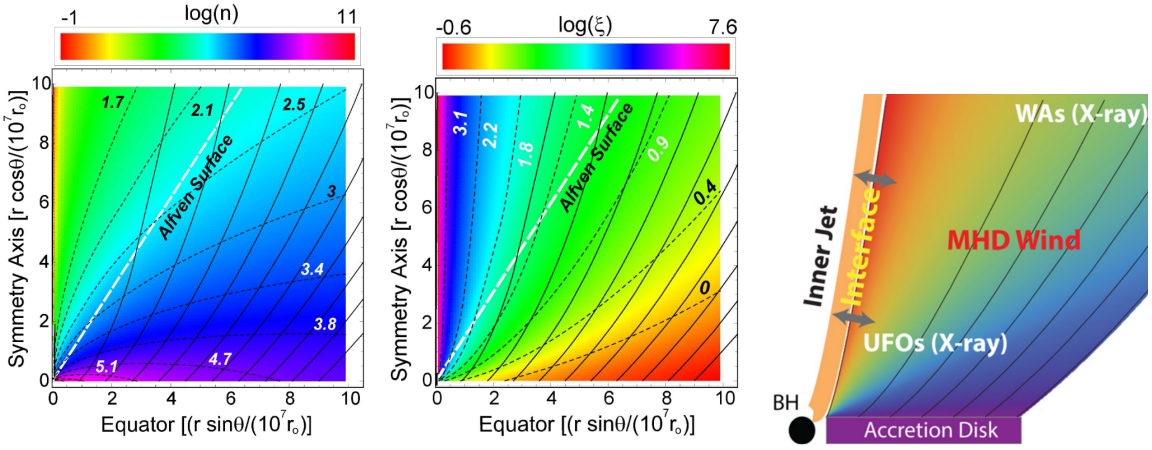

Figure 1.11: Selection of magnetically-driven wind properties, displaying density profile (left), ionisation gradient (middle), and wind geometry (right) as a function of disc radius (x-axis) and height above the disc (y-axis). In the left and middle panels, the origin represents the location of the SMBH and X-ray source. In all panels, solid black lines represent magnetic field lines stemming from the accretion disc. Figure credit: Fukumura et al. (2010a) (left and middle) and Fukumura et al. (2014) (right).

tions to high-density, low ionisation state matter along the disc surface (see Figure 1.11, left and middle). Notably, in this model UFOs are produced as the most interior region of this wind structure, with WAs existing at larger distances from the SMBH. The combined UFO and WA wind geometry may also be capable of confining and collimating a radio emitting plasma (i.e. jet) along the SMBH spin axis (see Figure 1.11, right), offering a unification of the high-velocity outflows from AGNs (Fukumura et al. 2014). At this time, however, magnetically-driven wind models have a sparse presence in the literature and they have not yet been widely applied to large samples of AGNs. Notably, such wind models have been applied to the archetypal UFO in the Type I AGN PG 1211+143 by Fukumura et al. (2015), wherein a superposition of various wind stream lines intersecting our line of sight viewing angle to the central engine was found to provide a good description of the data.

Finally, it may be that the UFOs observed in some AGNs can be explained as a natural consequence of the reflection scenario, as proposed by Gallo & Fabian (2011). In this model, resonant absorption of reflected X-rays occurring in a thin, hot atmosphere above the accretion disc can produce significantly blueshifted absorption features depending on the radius at which our line of sight viewing angle to the central engine intersects the atmosphere. This model foregoes the need for any extreme wind phenomenon, and has been shown to provide a good description of the previously described UFOs in both IRAS 13224−3809 (Fabian et al. 2020) and PG 1211+143 (Gallo & Fabian 2013).

As was the case with jets, winds are expected to have a close relationship with the inner disc environment. Parker et al. (2018a) conducted a literature search of AGNs with UFOs that were modelled assuming a reflection scenario and found that UFOs exhibited parameters consistent with radiatively-driven wind model predictions. However, this work is the sole study in which UFOs and the inner disc are so closely investigated together in a large sample of AGNs, and the authors only explored how the line of sight viewing angle and outflow velocity are related, leaving other parameter relationships unexplored.

With currently available X-ray telescopes, it remains difficult to uncover the exact nature of UFOs due to limited spectral resolution in the 7−10 keV band where they are detected. Of the three very different proposed scenarios capable of producing the observed high-energy absorption features, none have been found to be exceptionally more applicable than the others, as the differences in expected density and ionisation structures between the models cannot be adequately explored in the current data. It is indeed always possible that some sources exhibit UFOs that are the result of a mixture of the various scenarios. In any case,

the abilities of next-generation high-resolution X-ray spectra from future missions such as *XRISM* (XRISM Science Team 2020) and *Athena* (Nandra et al. 2013) promise significant advancements in revealing how UFOs are driven in AGNs

1.6 AGN feedback

Revealing how outflows in AGNs operate is a critically important aspect toward a more complete understanding of galactic evolution. Ferrarese & Merritt (2000) and Gebhardt et al. (2000) observed a very tight correlation between the velocity dispersion of stars in galactic bulges, $\sigma_\star$, and the mass of the central SMBH within such that $M_{\rm BH} \propto \sigma_\star^{4-5}$, the famous $M_{\rm BH} - \sigma_\star$ relation. These results were the first strong indication of co-evolution between the host galaxy and its SMBH. Mechanisms that account for this co-evolution have been proposed for both jets (e.g. Fabian et al. 2003; McNamara et al. 2005; Croton et al. 2006) and winds (e.g. Silk & Rees 1998; Fabian 1999; King 2005) as the result of AGN feedback, a process through which energy from the central engine is deposited back into the host galaxy via an outflow.

AGNs accreting at rates near the Eddington limit (i.e. $\lambda_{\rm Edd} = L_{\rm bol}/L_{\rm Edd} \sim 1$) exhibit radiative-mode feedback through winds, driven either via a radiation pressure (e.g. Proga et al. 2000) or magnetic (e.g. Fukumura et al. 2010a) mechanism. With typical outflow energies of $\sim 5 - 10\%$ $L_{\rm Edd}$ (e.g. Fabian 2012) winds are more than capable of unbinding and expelling gas from the bulge of the host galaxy. This is further highlighted by comparing the energy released during SMBH accretion ($E_{\rm BH}$) and the binding energy of the bulge gas

($E_{\rm gas}$), which finds that $E_{\rm BH} \sim 2\,000 \times E_{\rm gas}$ (King & Pounds 2015). Regarding the impact of this released energy on the host galaxy, Silk & Rees (1998) showed that for a wind launched by a SMBH accreting at the Eddington limit $M_{\rm BH} \propto \sigma_\star^5$ would naturally result, and Fabian (1999) later showed that $M_{\rm BH} \propto \sigma_\star^4$ for $\lambda_{\rm Edd} \sim 0.1$. Thus, both results reproduce the observed $M_{\rm BH} - \sigma_\star$ relation exceptionally well, making clear the significant impact that winds can have on galactic evolution. The expulsion of central engine gas also effectively halts further accretion onto the SMBH, thus offering a self-regulation on its own growth, leading to a co-evolution between the growth of the SMBH and of the galactic bulge.

Jets typically exist in systems with lower accretion rates (i.e. $\lambda \ll 1$), producing so-called kinetic-mode feedback. The strongest evidence of jet feedback can be found around the large central galaxies of galaxy clusters, such as NGC 1275 (Perseus A) in Abell 426 (the Perseus cluster). Hot gas in the intracluster medium (ICM) around NGC 1275 is falling back onto the galaxy via a cooling flow (Fabian 1994), the end result of which should be the formation of many new stars (i.e. a few $\times 100$ $M_\odot$ yr^{-1}, Fabian et al. 2006). No such star formation exists in NGC 1275 due to the fact that the deposited gas is in fact *not* cool (for early indications, see Gorenstein et al. 1978; Helmken et al. 1978), implying that it is somehow being maintained in its hot state. X-ray observations have revealed cavities and ripples in the ICM around NGC 1275 (e.g. Boehringer et al. 1993; Fabian et al. 2000, 2003, 2006; Hitomi Collaboration et al. 2016), evidence of shocks propagating through it that have been launched by some mechanism. Feedback via powerful jet activity has been shown capable of producing such ripples due to buoyant 'bubbles' of energetic jet ejecta rising through the colder host galaxy and ICM material (e.g. Fabian 2012). As the ejecta

moves through ICM, shock fronts are launched and heat the surrounding matter, producing the observed X-ray ripples. This jet feedback is therefore responsible for the production and maintenance of the hot ICM around NGC 1275, thus altering the evolution of the host galaxy, and possibly of the other nearby cluster galaxies immersed in the hot gas.

Whether via a jet (low-$\lambda_{\rm Edd}$, kinetic-mode) or wind (high-$\lambda_{\rm Edd}$, radiative-mode), the essential role of feedback is to disturb the giant molecular gas clouds (GMCs) in the host galaxy that would otherwise collapse and form stars[12], thus altering the evolution of the AGN host galaxy. Based on the information presented so far, the effect of feedback on GMCs would appear to be mostly negative (i.e. suppressing star formation), providing an effective mechanism through which galaxies transition from star-forming to quiescent (i.e. no new star formation). Feedback, however, can also have a positive (i.e. triggering star formation, e.g. Ishibashi & Fabian 2012; Silk 2013; Santoro et al. 2016) effect on the host galaxy stellar population, as shock propagation from both jets and winds leads to the compression of GMCs along the shock-front, thus triggering the formation of new stars. This positive feedback may be responsible for the observed 'inside-out' growth in massive galaxies (e.g. Bezanson et al. 2009).

It is important to note, however, that the precise role of AGN feedback on galactic evolution remains difficult to characterise. The described positive and negative roles of feedback are not necessarily mutually exclusive consequences of AGN-driven outflows, likely manifesting simultaneously within the host galaxy (e.g. Cresci et al. 2015; Carniani et al. 2016). Furthermore, AGN feedback may act negatively in regions along outflow trajectories, but

[12]The collapse of GMCs occurs naturally given they meet the appropriate criteria, which is when they exceed the Jeans mass $M_{\rm J} = (4\pi/3)\,\rho R_{\rm J}^3$, where ρ is the gas density and $R_{\rm J}$ is the cloud radius.

positively in other regions of the same host galaxy where energetic ejecta are not deposited (e.g. Cano-Díaz et al. 2012; Carniani et al. 2016). This is all to say that AGN feedback remains poorly understood, highlighting the importance of continued work on this still relatively young field. The contribution of the work presented in this thesis will be to examine how the AGN central engine is linked to the outflows responsible for feedback, and thus galaxy evolution in general.

1.7 Motivation of the present work

The previous sections have highlighted various insights we have gleaned about the central engine in AGNs over the past several decades, as well as what we have yet to form an adequate understanding of. In the following three chapters, I focus primarily on understanding how high-velocity outflows in AGNs relate to the inner disc environment via X-ray spectroscopy and, to a lesser extent, time series analysis.

There are two methodologies that may be used to investigate the connection between the AGN central engine and high-velocity outflows: (i) detailed analyses of targeted observation campaigns on singular sources to fully characterize the observed outflow(s) within and (ii) sample studies of numerous AGNs with and without outflows to explore population trends. Studies of type (i) provide test-beds in which we may explore the underlying physics of the observed phenomenon of interest, afforded by rigorous statistical treatments and state-of-the-art modelling techniques that can be tested prior to application on studies of type (ii). For instance, if we determine that a particular RL-AGN appears deficient in reflected X-ray

emission due to a beamed X-ray corona, we may then explore if a trend exists between reflected X-ray strength and radio power or jet presence in a sample of AGNs. Studies of type (ii) allow us to explore questions such as: Does the presence of a jet preclude the presence of a wind, or vice-versa? Can both outflows exist simultaneously in an AGN? Does each type of outflow exist preferentially within a particular subclass, or set of subclasses, of AGNs? How do AGNs with outflows compare to those that lack them?

In Chapters 2 and 3 I present the results of two studies highlighting how the jets in two RL-AGNs, III Zw 2 and IRAS 17020+4544, relate to the inner disc environment. In Chapter 4 I apply state-of-the-art physically motivated spectral models to the X-ray spectra of 20 AGNs aimed at uncovering how conditions of the inner disc relate to UFO properties. In Chapter 5, I conclude this work by discussing the successes achieved in the presented analyses, limitations on the inferences to be made based on the results, and future work that will be pursued in order to further our understanding of high-velocity outflows in AGNs.

Chapter 2

The changing source of X-ray reflection in the radio-intermediate Seyfert 1 galaxy III Zw 2

This work was originally published in the March 2018 issue of the Monthly Notices of the Royal Astronomical Society, Volume 475, Issue 1, pp. 128−138.

It is presented in unaltered form here.

2.1 Introduction

Active galactic nuclei (AGN) are responsible for some of the most energetic and luminous phenomena in the Universe. Emission from these objects spans a large range of the electromagnetic spectrum, from radio to γ-ray wavelengths. Since their identification by Seyfert (1943) AGN have been classified into numerous categories based on their observed luminosity in these different energy bands. Through the analysis of X-ray emission from these objects we are able to study the innermost regions of AGN, exploring the central engine thought to be responsible for a vast number of different features such as relativistic jets and observed reflection spectra off the accretion disc.

Of the various categories of AGN, a small set are radio-loud ($\sim 10 - 20$ per cent) possessing large amounts of radio emission and typically displaying relativistic radio jets. The formation of these jets, however, is not well understood, though it is believed to be connected to accretion disc structure and mass accretion rate (e.g. Merloni et al. 2003; Falcke et al. 2004; Körding et al. 2006). For example, Lohfink et al. (2013) were able to determine that for 3C 120, a broad-line radio galaxy (BLRG), the innermost region of the accretion disc became destroyed via some disc instability and was thus launched as a jet. By studying sources that exhibit large amounts of both radio and X-ray emission, such as radio loud Seyfert galaxies, it is possible to probe this disc-jet connection through analysis of the disc and jet emission simultaneously (e.g. Gallo et al. 2006; Kataoka et al. 2007; King et al. 2017).

III Zw 2A (PG 0007+106, Mrk 1501, $z = 0.089$, hereafter referred to as III Zw 2)

is the brightest of a three member galaxy group. It is a peculiar object that has proven particularly difficult to classify in the standard AGN categories due to its highly variable radio band emission (e.g. Aller et al. 1985; Falcke et al. 1999) coupled with a Seyfert I nucleus (e.g. Osterbrock 1977). Radio-loud AGN are typically housed in elliptical galaxies (e.g. Kirhakos et al. 1999), though early studies of III Zw 2 indicate a spiral morphology (e.g. Hutchings & Campbell 1983; Taylor et al. 1996). More recent studies using *Hubble Space Telescope* (*HST*) H-band images suggest an elliptical host galaxy (Veilleux et al. 2009). A tidal bridge with knots of star formation exists between III Zw 2 and its nearest group neighbour III Zw 2B (Surace et al. 2001) indicating an ongoing merger phase.

The radio emission from III Zw 2 is extremely variable, by as much as a factor of 20 (Aller et al. 1985) exhibiting a quasi-periodic activity cycle with period $P = 5.14 \pm 0.19$ yr (Li et al. 2010). Variability is also present in the optical (e.g. Lloyd 1984; Clements et al. 1995) and X-ray (e.g. Kaastra & de Korte 1988; Salvi et al. 2002) bands. The extended radio emission, however, is weak (e.g. Unger et al. 1987; Brunthaler et al. 2005), which is expected from a Seyfert I galaxy. Notably, the radio jet present in III Zw 2 is the first superluminal jet discovered in a Seyfert galaxy (Brunthaler et al. 2000). Exactly what causes the aforementioned immense radio variability is still a mystery. One explanation is that relativistic jets interacting with the interstellar medium (ISM) exciting molecular clouds near the central engine (Falcke et al. 1999). Alternatively, the X-ray variability may be leading the radio by approximately 13 months (Clements et al. 1995), suggesting changes in the inner disc region propagating outward altering the jet activity.

Salvi et al. (2002) studied the high-energy emission of III Zw 2 using archival data

from 1977 up to and including the *XMM-Newton* 2000 data. It was found that the X-ray spectrum was best described by a power law of slope $\Gamma \approx 1.7$ and an extremely broad Fe Kα line (FWHM $\sim$ 140000 km s^{-1}) at 6.44 keV with no evidence for a soft excess or intrinsic absorption. No short term variability was detected in the X-ray light curves analysed by Salvi et al. (2002), however, long term (year time scales) 10-times flux variations were found alongside correlated X-ray and radio variability. They interpret the radio to optical emission as synchrotron radiation that is self-absorbed in the radio/millimetre energy range, with the X-ray emission being produced by inverse Compton scattering of UV seed photons from the accretion disc by electrons in the corona that also produce synchrotron radiation.

The broad Fe Kα line found by Salvi et al. (2002) has motivated this work to further analyse the spectral feature using data from the *Suzaku* and *Swift* satellites. Broad emission lines are thought to originate from segments of the accretion disc nearest the black hole (e.g. Fabian et al. 1989). By studying the shape of these spectral features it is possible to obtain the emissivity profile (i.e. the pattern in which the disc is illuminated by the corona) (e.g. Wilkins & Fabian 2011) and through analysis of the emissivity profile subsequently determine the geometry of the corona (e.g. Wilkins & Fabian 2012; Gonzalez et al. 2017) even if the emission is directed toward (e.g. Wilkins et al. 2014) or away (e.g. Wilkins & Gallo 2015a) from the disc. The detection of a broad feature in the X-ray spectrum III Zw 2 can therefore potentially be used to constrain the geometry of the corona, further motivating the analysis of recent observations.

In this work we study the X-ray spectrum of III Zw 2 using all available data since the 2000 *XMM-Newton* observation (inclusive) in order to study the high-energy variability in an

effort to explain its peculiar nature. The paper is organized in the following arrangement. First, we present the data used in this study and discuss the data reduction techniques performed on the raw data (Section 2.2). We then present our analysis on both the long and short term variability of the X-ray data (Section 2.3). Section 2.4 displays the results of fitting the mean spectrum from each data set with simple phenomenological models before exploring more physically motivated spectral models. Finally, we discuss the results in greater detail (Section 2.5) and conclude (Section 2.6).

2.2 Observations & Data Reduction

In this paper we use archival data obtained from the *XMM-Newton* (Jansen et al. 2001), *Suzaku* (Mitsuda et al. 2007), and *Swift* (Burrows et al. 2005) satellites. Details of the observations are presented in Table 2.1.

Table 2.1: X-ray observations of III Zw 2 used in this work. *XMM-Newton* data corresponds to that taken by the EPIC pn detector. *Suzaku* include those taken by the two front-illuminated (FI) detectors, XIS0 and XIS3, and the HXD-PIN detector. Both XRT and BAT data from *Swift* were used and are shown below. Column (7) indicates the energy ranges used when performing broad band spectral fitting.

(1) Observatory	(2) Observation ID	(3) Start Date (yr.mm.dd)	(4) Duration (s)	(5) Exposure (s)	(6) Counts	(7) Energy Band (keV)
XMM-Newton EPIC pn	0127110201	2000.07.03	16311	10160	32835	$0.3-10$
Suzaku FI-XIS	706031010	2011.06.14	169080	81466	98392	$0.7-10$
Suzaku HXD-PIN				68980	16652	$15-25$
Swift XRT	00036363001	2007.06.21		4828		
	00036363002	2009.05.22		4284		
	00036363003	2009.09.03		404		
	00036363004	2010.02.01		75		
	00036363005	2010.02.07		5701		
	00036363006	2010.07.08		1128		
	00036363007	2010.07.08		2316		
	00036363008	2012.01.03		3284		
	00049402001	2013.05.16		618		
	00049402002	2016.11.07		172		
	00049402003	2017.02.08		1209		
	00049402004	2017.05.15		737		
	00093000001	2017.05.18		718		
	00093000002	2017.05.19		488		
	00049402006	2017.07.29		792		
	Total	2007−2017		26754	5361	$0.5-7$
Swift BAT			70 months		412	$15-150$

2.2.1 *XMM-Newton*

The EPIC pn (Strüder et al. 2001) camera was operated in small window mode with the thin filter for the duration of the III Zw 2 observation. The *XMM-Newton* Observation Data Files (ODFs) were processed using the *XMM-Newton* Science Analysis System (`SAS v15.0.0`). EPIC response matrices were generated using the `SAS` tasks `ARFGEN` and `RMFGEN`. The light curve was extracted from the resulting event lists, with no significant background flaring detected. Source photons were extracted from a 35″circular region centred on the source. Background photons were extracted from a 50″circular off-source region. MOS data were examined by Salvi et al. (2002) and determined to by consistent with those taken by the EPIC pn camera. We also determine that the MOS data is consistent with the EPIC pn data, though for simplicity here we use data from the EPIC pn camera exclusively.

2.2.2 *Suzaku*

Suzaku observed III Zw 2 in the XIS-nominal position, with the two front-illuminated CCDs (XIS0 and XIS3), the back-illuminated CCD (XIS1), and the HXD-PIN detectors. Cleaned event files from version 3 processed data were used to extract data products using `xselect`. For each XIS CCD, source photons were extracted from a 4′circular region centred on the source. Background photons were extracted from a 3′circular off-source region. Response files were generated using `xisrmfgen` and `xissimarfgen`. After determining that the XIS0 and XIS3 data were consistent the two were combined to create a single spectrum. XIS1 data were also found to be consistent with the FI detectors, though for simplicity here we use

only the XIS0+XIS3 combined data. In accordance with the findings presented in Nowak et al. (2011) we ignore the $1.88-1.92$ keV and $2.19-2.37$ keV ranges of the XIS0 and XIS3 spectra, and therefore of the combined spectrum, when performing spectral fits.

An HXD-PIN spectrum was extracted following standard procedures. The non-X-ray background (NXB) file corresponding to the observations was used to determine the common good-time interval between the NXB and the source data. The resulting PIN exposure was 68980 sec once corrected for detector dead time. The cosmic X-ray background (CXB) was modelled using the provided flat response files and the PIN background spectrum was created by merging the CXB and NXB background files. Examination of the PIN data yield a 11 per cent detection of the AGN between $15-25$ keV.

2.2.3 *Swift*

Fifteen observations of III Zw 2 were obtained with the Swift XRT in window timing mode between 2007 and 2017 (Table 2.1). Light curves and spectral data products were extracted with the online Swift-XRT data products generator[1] (Evans et al. 2009), which produces calibrated and background subtracted products.

The average exposure during each observation was 1784 sec, but individual exposures ranged from 74 sec to 5700 sec. Given the small counts in each exposure, the spectrum was generated from the combined fifteen observations over the ten-year span. The total combined exposure is 26754 sec and the source is detected between $0.5-7$ keV.

Also included in the analysis is the Swift-BAT spectrum that was generated from the

[1] http://www.swift.ac.uk/user_objects/

70-month survey[2] (Baumgartner et al. 2013).

2.2.4 General

All spectral fitting was done using `XSPEC v12.9.1` (Arnaud 1996). *XMM-Newton* EPIC pn and *Suzaku* XIS spectra were binned in accordance with the optimal binning technique described in Kaastra & Bleeker (2016) and implemented in the `Python` code made available by C. Ferrigno[3]. The average *Swift* source spectrum was grouped such that each bin contains a minimum of 20 counts. In the plots presented the spectra have been re-binned for display purposes. Model likelihoods were evaluated using the Cash (1979) statistic, modified in `XSPEC` as the C-statistic. Note that only the BAT data are Gaussian[4], however, C-statistics are presented here as well to simplify presentation. Parameters reported in the fits are in the rest frame of the source and errors on them correspond to a 90 per cent confidence level. The Galactic column density toward III Zw 2 of 5.39×10^{20} cm^{-2} (Kalberla et al. 2005) is kept fixed in all spectral fits. The reported fluxes in the relevant models are produced using the `XSPEC` model `cflux`. Since the *Suzaku* data were taken in XIS-nominal position the HXD-PIN and XIS cross-normalisation is fixed at 1.16. Henceforth, references to *XMM-Newton* data correspond to that taken by the EPIC pn camera, *Suzaku* to the combined XIS0+XIS3 data, and *Swift* to the XRT data. The PIN data are linked to the *Suzaku* data in all relevant fits, and similarly the BAT data are linked to the *Swift* data.

[2]https://swift.gsfc.nasa.gov/results/bs70mon/
[3]https://cms.unige.ch/isdc/ferrigno/developed-code/
[4]https://swift.gsfc.nasa.gov/analysis/threads/batspectrumthread

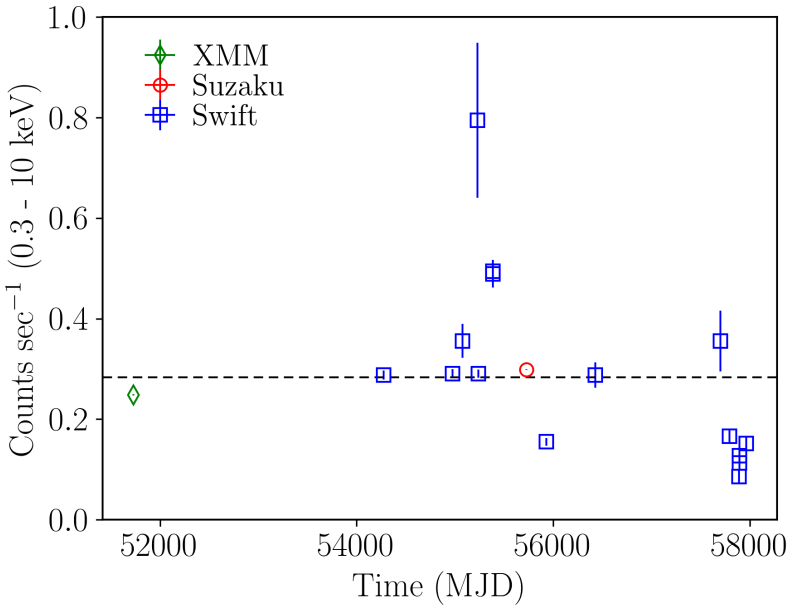

Figure 2.1: The $0.3-10$ keV combined long term light curve of III Zw 2 with data from all three satellites expressed in *Swift* count rate. Error bars are included on all data points though they are not visible in all cases as the symbol is larger. The average total count rate is plotted as the dashed horizontal line.

2.3 Variability

2.3.1 Long Term

Our analysis of III Zw 2 begins with examining its variability over the observations between July 2000 and July 2017 (Table 2.1). Figure 2.1 shows the combined long term $0.3-10$ keV light curve, which displays significant changes in count rate over the 17−year time span. Fitting the weighted mean count rate to the combined light curve (0.283 ± 0.001 counts s^{-1}) results in a fit statistic of $\chi^2_\nu = 35.47$. The fractional variability (Edelson et al. 2002) is $F_{\rm var} = 25 \pm 15$ per cent, further indicating the presence of long term X-ray variability in

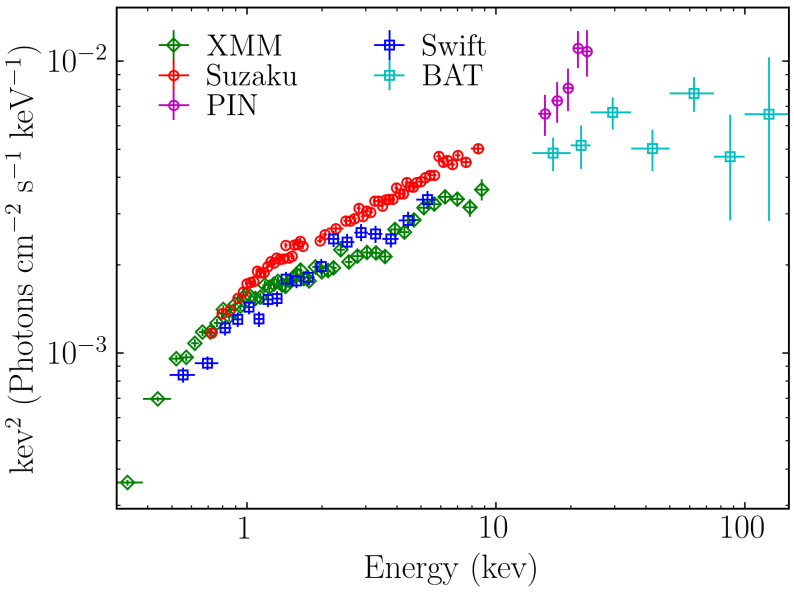

Figure 2.2: The unfolded spectra of III Zw 2 for all the data fit by a power law with slope $\Gamma = 0$ to examine the change in spectral shape over time. No significant spectral changes are observed.

III Zw 2.

In the *Swift* light curve the average count rate (0.228 ± 0.003 counts s^{-1}) produces a poor fit to the data ($\chi^2_\nu = 61.45$) and has a fractional variability of $F_{\rm var} = 86 \pm 17$ per cent. Due to the sparse data, however, these significant deviations from the average count rate and variability cannot be further explored. The mean spectrum of these *Swift* observations is therefore used for the remainder of the spectral fitting and analysis.

It is then necessary to examine spectral changes between the different observations, as shown in Figure 2.2. By unfolding the spectra against a power law model with slope $\Gamma = 0$ we are able to correct each spectrum for the effective area of its respective detector, allowing for a direct spectral comparison across different time epochs and instruments. The three

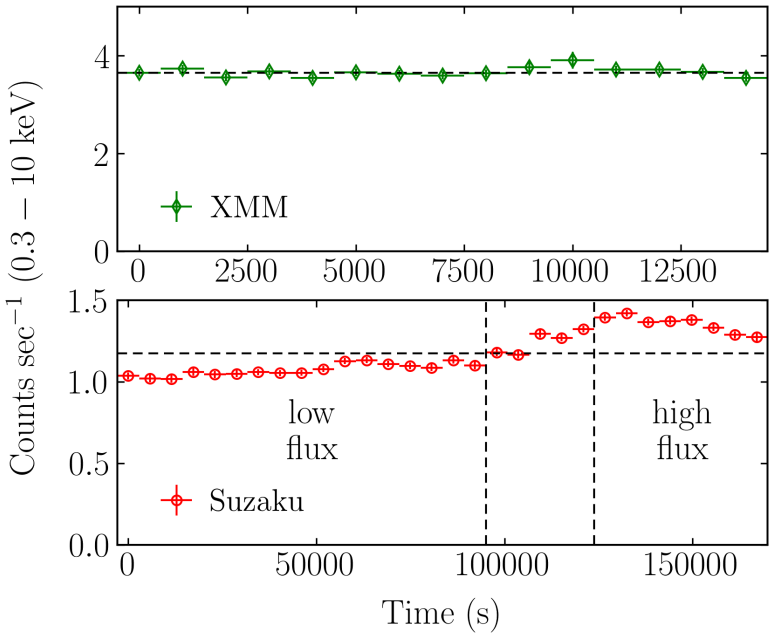

Figure 2.3: The $0.3 - 10$ keV short term light curves of III Zw 2 for the *XMM-Newton* (top panel) and *Suzaku* (bottom panel) observations. The *XMM-Newton* data have been binned in 1000 second bins and the *Suzaku* data have been binned according to the 96 minute orbital period of the satellite. Vertical lines in the bottom panel denote the low (left of first line) and high (right of second line) flux states of the *Suzaku* observation. Horizontal dashes lines represent the average count rates in each panel.

data sets appear to be in approximate agreement with each other. The *Suzaku* data exhibit a higher flux with similar slope to both the *XMM-Newton* and *Swift* data. The colour and marker scheme presented in Figure 2.2 (*XMM-Newton* - green diamond, *Suzaku* - red circle, PIN - magenta circle, *Swift* - blue square, and BAT - cyan square) is maintained throughout this work.

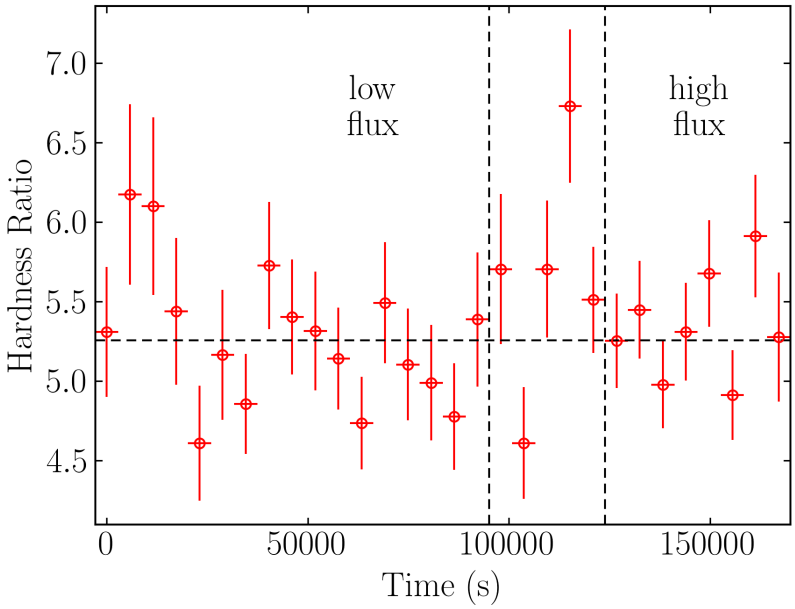

Figure 2.4: Hardness ratio (hard/soft) between the $0.5-1$ keV (soft) and $2-10$ keV (hard) energy bands of the *Suzaku* observation of III Zw 2. The dashed horizontal line represents the average ratio with vertical lines denoting the low (left of first line) and high (right of second line) flux states.

2.3.2 Short Term

The short term light curves for the *XMM-Newton* and *Suzaku* observations are shown in Figure 2.3. The *XMM-Newton* light curve is flat and featureless throughout. Calculating the fractional variability ($F_{\rm var} < 2.3$ per cent) and fitting the mean (3.65 ± 0.02 counts s^{-1}) to the light curve ($\chi^2_\nu = 0.85$) indicate no significant variability during this observation, requiring no further investigation. With this it is therefore acceptable to use the mean spectrum of the *XMM-Newton* data for the remainder of the spectral fitting and analysis.

The *Suzaku* observation is relatively flat for the first ~ 95 ks before rising slightly for the remainder of the observation (~ 75 ks). Computing the fractional variability ($F_{\rm var} = 12 \pm 2$

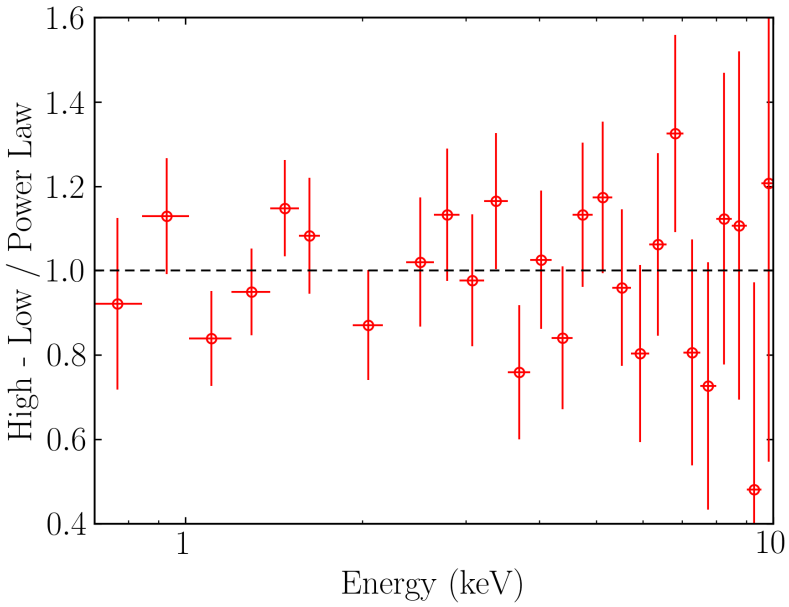

Figure 2.5: Spectral comparison of the high and low flux states for III Zw 2 during the *Suzaku* observation. Taking the difference between the high and low flux states and fitting with a power law of slope $\Gamma = 1.53$ finds no significant spectral differences between them, supporting analysis of only the mean spectrum for the *Suzaku* observation.

per cent) and fitting the mean (1.174 ± 0.004 counts s^{-1}) to the light curve ($\chi^2_\nu = 40.78$) state the significance of this short term variability. Considering the small increase in count rate we examine the hardness ratio between the $0.5 - 1$ keV and $2 - 10$ keV bands of the *Suzaku* data, shown in Figure 2.4. Fitting the hardness ratio to the mean (5.26 ± 0.07) finds moderate deviation ($\chi^2_\nu = 1.41$). No corresponding step in the hardness ratio is observed at ~ 95 ks as in the light curve.

The low flux state was taken to be the first 95 ks of the observation and the high flux state was taken to be all data after 124 ks. The resulting spectral difference (high-low) compared to a power law ($\Gamma = 1.53$) is shown in Figure 2.5. Here the spectra have been

re-binned to more clearly show any trends. There are no significant differences between the two flux states of the *Suzaku* data. Therefore, the mean spectrum of the *Suzaku* data is used for the remainder of the spectral fitting and analysis.

2.4 Fitting the Mean Spectrum

2.4.1 High Energy X-ray Spectrum

We begin our spectral analysis of III Zw 2 by studying the $2-10$ keV energy range for the mean spectrum of each observation. To start we fit a simple cut-off power law (denoted cpl) and narrow Gaussian (denoted zgN) to each data set, with the power law cut-off energy frozen at 300 keV (this value is maintained throughout the work presented as it was not found to improve the fit when left free to vary) and the Gaussian frozen at $E_{\mathrm{K}\alpha} = 6.4$ keV and width frozen at $\sigma_{\mathrm{K}\alpha} = 1$ eV. Good statistical fits to the *XMM-Newton* and *Suzaku* data were found, with the *Swift* data having the poorest fit quality. The parameter values are presented as Model (1) in Table 2.2 and the ratio residuals are displayed in the top panel of Figure 2.6a. Though the *XMM-Newton* and *Suzaku* fits produce Γ values more closely in agreement with one another, the large error on the *Swift* fit does mean that all three values are in agreement.

Table 2.2: The best fit parameters found by fitting the $2-10$ keV band of III Zw 2 for the three observations. In Model (1) the line energy of the Gaussian features is kept frozen at 6.4 keV and the width is kept frozen at 1 eV. In Model (2) both aforementioned parameters are left free to vary. The normalisation of the power law component is in units of photons keV^{-1} cm^{-2} s^{-1} at 1 keV.

Model	Data Set	Γ	$\mathrm{Norm}_{\mathrm{pl}}$ ($\times 10^{-3}$)	$E_{\mathrm{K}\alpha}$ (keV)	$\sigma_{\mathrm{K}\alpha}$ (keV)	$EW_{\mathrm{K}\alpha}$ (eV)	C/dof
(1) cpl+zgN	*XMM-Newton*	1.55 ± 0.04	$1.42^{+0.09}_{-0.08}$	6.4	0.001	42^{+47}_{-34}	103.40/102
	Suzaku	1.54 ± 0.02	1.90 ± 0.06			39^{+17}_{-16}	95.99/98
	Swift	1.71 ± 0.12	$1.88^{+0.30}_{-0.26}$			219^{+103}_{-124}	93.45/79
(2) cpl+zgB	*XMM-Newton*	$1.61^{+0.07}_{-0.06}$	$1.49^{+0.11}_{-0.10}$	6.26 ± 0.55	$0.96^{+0.71}_{-0.58}$	312^{+239}_{-312}	98.60/100
	Suzaku	1.54 ± 0.02	1.90 ± 0.06	$6.40^{+0.09}_{-0.05}$	< 0.158	39^{+17}_{-13}	95.98/96
	Swift	$1.79^{+0.14}_{-0.13}$	$2.03^{+0.35}_{-0.30}$	$6.30^{+0.16}_{-0.13}$	$0.22^{+0.21}_{-0.11}$	467^{+299}_{-262}	85.70/77

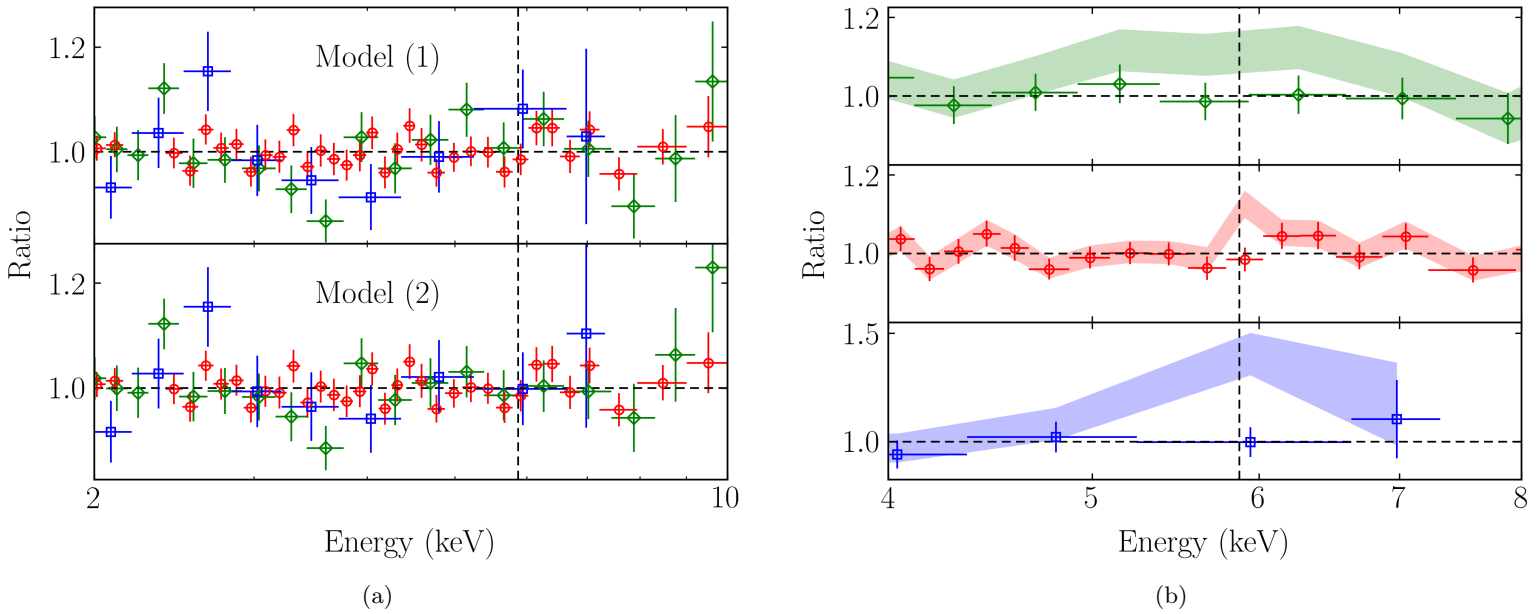

Figure 2.6: (a) The ratio residuals produced by Model (1), a cut-off power law and a narrow Gaussian centred at 6.4 keV, and Model (2), a cut-off power law and a broad Gaussian, as presented in Table 2.2 fit over the $2-10$ keV energy range. (b) A close-up of the $4-8$ keV energy range for the three data sets. Shaded regions denote the best fit of a cut-off power law to the $2-10$ keV energy range excluding $4-7$ keV. Empty markers denote the fit given by Model (2). Vertical lines in both (a) & (b) denote the rest frame Fe Kα line energy of 6.4 keV.

Freeing the line energy and width to allow fitting of a broad feature (denoted zgB) significantly improves the *XMM-Newton* and *Swift* fits, indicating the presence of a broad spectral feature at ~ 6.3 keV in these data. The *Suzaku* fit is unaffected by the free energy and breadth of the line and thus indicates a narrow feature at 6.4 keV in the data taken during this observation. The ratio residuals in the bottom panel of Figure 2.6a show this cut-off power law and broad Gaussian fit, with the parameter values presented as Model (2) Table 2.2.

Figure 2.6b provides a focus on the $4-8$ keV energy range of the three data sets. Here a comparison is presented between a fit comprised of a cut-off power law fitting over the $2-10$ keV energy range excluding $4-7$ keV (i.e. to fit only the continuum) and Model (2) shown in Table 2.2. The difference in the width of the Fe Kα emission line feature in the three observations is clearly shown here. The broad line in the *XMM-Newton* data is in stark contrast with the very narrow feature found in the *Suzaku* data, suggesting interesting behaviour occurring in this already peculiar object (discussed in Section 2.5).

2.4.2 Broadband X-ray Spectrum

Extrapolating Model (2) from Table 2.2 to the broadband X-ray energy range appropriate for each data set produces the ratio residuals shown in Figure 2.7. The *XMM-Newton* data display clear soft (< 2 keV) residuals, suggesting the presence of a second component contributing to the spectrum. The *Suzaku* data do not show significant deviation from this extrapolated fit, though the data are truncated at 0.7 keV, leaving out a large portion of where the soft excess would be. The PIN data above ~ 20 keV are poorly fit, showing

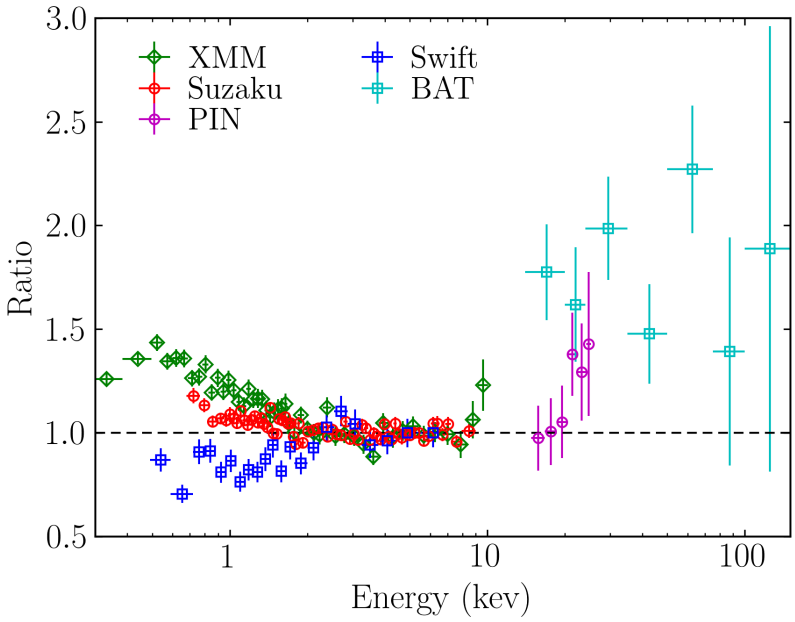

Figure 2.7: The ratio residuals produced by extrapolating Model (2) from Table 2.2 over the entire appropriate energy range for each data set. Clear low (< 2 keV) and high (> 20 keV) energy residuals are shown.

some curvature in the data toward higher energies. The model overestimates the *Swift* data below ~ 2 keV with the BAT data being almost entirely underestimated, suggesting a more shallow broadband spectrum than found by Model (2) in the $2 - 10$ keV range.

Refitting Model (2) to the broadband energy range of each data set vastly reduces the ratio residuals in all data sets, as shown in the top panel of Figure 2.8, with parameter values shown as Model (3) in Table 2.3. The *XMM-Newton* and *Suzaku* broadband fits are comparatively worse than the $2 - 10$ keV fits suggesting a more complex model is necessary while the *Swift* data is fit with approximately the same mediocrity. The width of the Gaussian feature in the *XMM-Newton* fit has increased significantly, while the slope has simultaneously steepened, further indicating presence of a broad spectral feature and/or

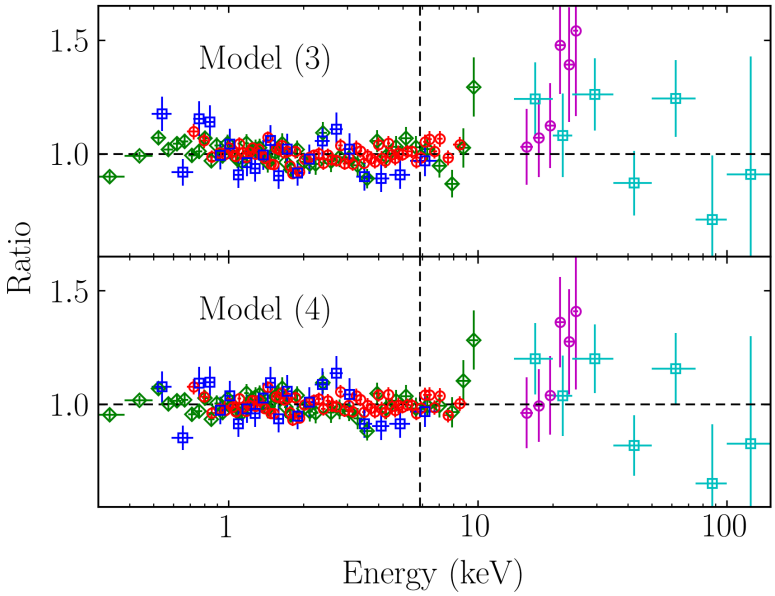

Figure 2.8: The ratio residuals produced by Model (3), a cut-off power law and broad Gaussian, and Model (4), a cut-off power law, broad Gaussian, and black body, presented in Table 2.3 fit over the appropriate energy ranges for each data set. Comparing the top and bottom panels shows similar fit quality, with the Model (4) displaying improved low energy residuals. Vertical lines in both the top and bottom panels denote the rest frame Fe Kα line energy of 6.4 keV.

soft excess emission.

Table 2.3: The best fit parameters found by fitting the appropriate energy range for each of the three data sets of III Zw 2. The *XMM-Newton* broadband energy range is $0.3-10$ keV, *Suzaku* + PIN is $0.7-10$ keV and $15-25$ keV, and *Swift* + BAT is $0.5-7$ keV and $15-150$ keV. The normalisation of the power law component is in units of photons keV^{-1} cm^{-2} s^{-1} at 1 keV. The normalisation of the black body component is in units of L_{39}/D_{10}^2 where L_{39} is the source luminosity in uints of 10^{39} erg s^{-1} and D_{10} is the distance to the source in units of 10 kpc.

Model	Data Set	Γ	Norm_{pl} ($\times 10^{-3}$)	$E_{\text{K}\alpha}$ (keV)	$\sigma_{\text{K}\alpha}$ (keV)	$EW_{\text{K}\alpha}$ (eV)	kT (eV)	Norm_{bb} ($\times 10^{-6}$)	C/dof
(3) cpl+zgB	*XMM-Newton*	1.80 ± 0.02	1.78 ± 0.02	$6.67^{+0.74}_{-0.82}$	$2.49^{+1.55}_{-0.81}$	1812^{+527}_{-695}	-	-	160.02/131
	Suzaku + PIN	1.58 ± 0.01	2.03 ± 0.02	$6.41^{+0.13}_{-0.05}$	< 0.215	47^{+20}_{-25}			192.67/156
	Swift + BAT	1.57 ± 0.02	1.61 ± 0.04	$6.28^{+0.18}_{-0.16}$	$0.17^{+0.17}_{-0.11}$	251^{+169}_{-148}			247.74/202
(4) cpl+zgB+bb	*XMM-Newton*	$1.66^{+0.05}_{-0.04}$	$1.59^{+0.07}_{-0.06}$	$6.34^{+0.52}_{-0.47}$	$1.02^{+1.01}_{-0.41}$	408^{+382}_{-354}	173^{+13}_{-14}	$8.41^{+2.40}_{-2.59}$	138.69/129
	Suzaku + PIN	1.53 ± 0.03	1.89 ± 0.07	$6.40^{+0.08}_{-0.05}$	< 0.152	38^{+20}_{-18}	234^{+40}_{-51}	$4.93^{+1.94}_{-1.95}$	175.23/154
	Swift + BAT	1.54 ± 0.03	$1.52^{+0.07}_{-0.08}$	$6.28^{+0.18}_{-0.16}$	$0.18^{+0.17}_{-0.11}$	254^{+125}_{-146}	144^{+56}_{-52}	$5.76^{+4.15}_{-3.20}$	238.85/200

Given the apparent soft excess in Figure 2.7 the data were tested for the presence of a second spectral component by adding a black body component (denoted bb) to the previous model, producing the ratio residuals shown in the bottom panel of Figure 2.8 and the model parameters shown as Model (4) in Table 2.3. All three data sets show significant improvements to the quality of fit with the addition of a black body component to the model, though the *Swift* data are least affected by this additional spectral component. *XMM-Newton* exhibits the steepest spectrum of the three, with the *Suzaku* and *Swift* fits showing agreement in photon index.

Considering the time separation of 11−years between the *XMM-Newton* and *Suzaku* observations, the fits in Table 2.3 can be interpreted as an evolution of the spectral shape of III Zw 2 due to the normalisation of the power law. During the *XMM-Newton* observation, the lower power law normalisation would have exhibited a more significant low energy component (black body) while during the *Suzaku* observation a high power law normalisation would have acted to effectively over-power this second, weaker component. Further investigation of the spectrum of III Zw 2 requires two-component physically motivated models.

The results from phenomenological broadband fits above indicate a second component present in the spectra. To account for this physically, a reflector (e.g. the torus, accretion disc, etc.) illuminated by the hard X-ray source (corona or jet) can be modelled using the `XSPEC` model `xillver` (García et al. 2014).

A cold distant reflector (i.e. the torus) was modelled with `xillver` by setting the iron abundance to $A_{\rm Fe} = 1.0$ and the ionisation parameter to $\log \xi = 0.0$ erg cm s^{-1}. Results from superluminal motion of the radio jet in III Zw 2 require the inclination of the object to

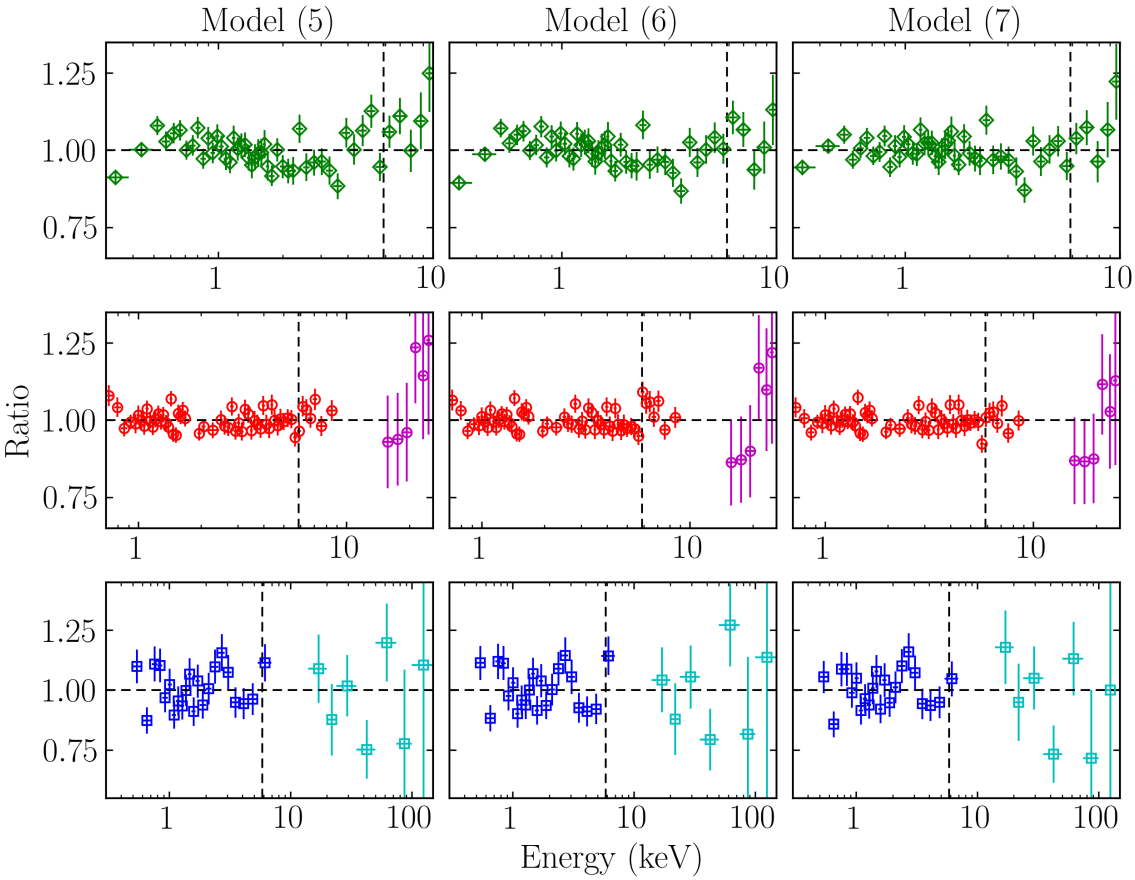

Figure 2.9: The ratio residuals produced by the models presented in Table 2.4 fit over the appropriate energy ranges for each data set. Model (5) describes a cut-off power law and cold distant reflector, Model (6) a cut-off power law and blurred cold reflector, and Model (7) a cut-off power law and blurred ionised reflector. Comparing the three models shows very similar fit quality overall. Vertical lines in the panels denote the rest frame Fe Kα line energy of 6.4 keV.

be $\leq 41^{\circ}$ (Brunthaler et al. 2000). With this we freeze the disc inclination at $i = 20^{\circ}$ for all three data sets. Additionally, inclination was found to be poorly constrained when free to vary and does not improve the fit quality. The ratio residuals produced by the best fit model of a cold distant reflector are shown in the first column of Figure 2.9 and the corresponding parameter values in Model (5) of Table 2.4.

Table 2.4: Best fit model parameters for cold distant, Model (5), blurred cold, Model (6), and blurred ionised, Model (7), reflection. Inclination angle is kept frozen at $i = 20°$ in agreement with previous radio studies. The iron abundance was kept frozen at solar abundance $A_{\rm Fe} = 1.0$ and ionisation parameter was kept frozen at $\log \xi = 0.0$ erg cm s^{-1} to best simulate a distant cold reflector (ie. the torus) in Models (5) & (6). The iron abundance and ionisation parameter are left free to vary in Model (7). Subscript p indicates that a parameter has been pegged at a limit.

Model	Data Set	Γ	$\log F_{\rm pl}$ (erg cm^{-2} s^{-1})	q	$A_{\rm Fe}$	$\log \xi$ (erg cm s^{-1})	$\log F_{\rm ref}$ (erg cm^{-2} s^{-1})	R	C/dof
(5)	*XMM-Newton*	1.78 ± 0.02	-10.48 ± 0.02	-	1.0	0.0	$-10.99^{+0.10}_{-0.12}$	$0.31^{+0.03}_{-0.04}$	181.17/133
	Suzaku + PIN	1.61 ± 0.01	-10.20 ± 0.02				$-11.11^{+0.10}_{-0.13}$	$0.12^{+0.01}_{-0.02}$	175.47/158
	Swift + BAT	1.65 ± 0.04	-10.36 ± 0.05				$-11.08^{+0.14}_{-0.22}$	$0.22^{+0.03}_{-0.05}$	241.39/204
(6)	*XMM-Newton*	1.81 ± 0.02	-10.53 ± 0.02	3	1.0	0.0	$-10.91^{+0.07}_{-0.09}$	$0.42^{+0.03}_{-0.04}$	168.99/133
	Suzaku + PIN	1.64 ± 0.02	-10.24 ± 0.03				$-10.98^{+0.11}_{-0.16}$	$0.18^{+0.02}_{-0.03}$	190.25/158
	Swift + BAT	1.65 ± 0.05	-10.36 ± 0.06				$-11.10^{+0.17}_{-0.28}$	$0.20^{+0.04}_{-0.06}$	245.93/204
(7)	*XMM-Newton*	1.64 ± 0.02	-10.40 ± 0.02	$2.65^{+0.37}_{-0.38}$	$4.78^{+3.04}_{-0.70}$	$2.80^{+0.34}_{-0.08}$	$-11.04^{+0.10}_{-0.12}$	$0.23^{+0.02}_{-0.03}$	142.77/130
	Suzaku + PIN	$1.62^{+0.02}_{-0.04}$	-10.21 ± 0.02	$-10.00^{+10.37}_{p}$	$0.51^{+0.25}_{-0.01p}$	$1.40^{+0.62}_{-0.66}$	$-10.94^{+0.10}_{-0.16}$	$0.19^{+0.02}_{-0.03}$	170.68/155
	Swift + BAT	$1.63^{+0.08}_{-0.04}$	$-10.33^{+0.04}_{-0.09}$	$0.51^{+4.45}_{-10.51p}$	$5.02^{+4.98p}_{-3.09}$	< 2.48	$-11.15^{+0.14}_{-0.12}$	$0.28^{+0.05}_{-0.04}$	237.18/201

The *Suzaku* fit is described by a bright power law that outshines a weaker reflection component. The *XMM-Newton* fit shows a more steep but less prominent power law allowing more of the curvature intrinsic to the reflection spectrum to be seen in the average spectrum. Overall the data are fit well by this cold distant reflection model, though the broad lines found in the phenomenological models of *XMM-Newton* and *Swift* are not typically the result of reflection from this type of material, prompting further modelling. Alternate models to `xillver`, like `reflionx` (Ross & Fabian 2005) and `pexmon` (Nandra et al. 2007) were also attempted to model a cold reflector scenario. No one model seemed superior and we describe only the `xillver` fits here.

A blurred cold reflector was simulated by convolving the cold distant `xillver` reflection model with the blurring kernel `kdblur` (based off of Laor 1991 and first described by Fabian et al. 2002). As in Model (5) the iron abundance and ionisation parameter are kept frozen at $A_{\rm Fe} = 1.0$ and $\log \xi = 0.0$ erg cm s^{-1}, respectively. The emissivity index in `kdblur` was kept frozen at $q = 3.0$ in accordance with a distant reflector. A maximally spinning Kerr black hole is assumed and as such the inner radius of the accretion disc was kept frozen at $R_{\rm in} = 1.235 r_g$ and the outer radius of the disc was kept frozen at $R_{\rm out} = 400 r_g$, where $r_g = GM/c^2$. The blurring inclination was linked to the inclination of the reflection component (i.e. frozen at $i = 20°$). Allowing these parameters to vary freely does not enhance the fit. The best fit model ratio residuals to a blurred cold reflector are displayed in the second column of Figure 2.9 with the corresponding parameter values shown as Model (6) in Table 2.4.

The addition of a blurring kernel to the cold reflection model yields a significantly im-

proved fit to the *XMM-Newton* data while the *Suzaku* data are poorly fit. Conclusions about the physical system remain unchanged: the *Suzaku* data are best described by a bright power law that outshines the reflection component whereas the *XMM-Newton* and *Swift* data exhibit a weaker power law component allowing curvature intrinsic to the reflection spectrum to be seen. We now explore the effect of iron abundance, ionisation parameter, and emissivity index on the fit quality to these data.

The broad lines observed in the spectra of the *XMM-Newton* and *Swift* observations are indicative perhaps of blurred ionised reflection (i.e. off of the inner region of the accretion disc). Modelling such reflection with `xillver` convolved with `kdblur` requires allowing iron abundance, ionisation parameter, and emissivity index to be left free to vary. The best fit model of a blurred ionised reflector is presented in Model (7) of Table 2.4 with the ratio residuals shown in the bottom panel of Figure 2.9.

Similar to the case of the previous models the *Suzaku* fit shows a strong power law component relative to reflection, with the *XMM-Newton* and *Swift* fits finding slightly weaker power laws comparatively. Notably we find a poorly fit Fe Kα line in the *Suzaku* data set with this blurred ionised model. We find that the broadened line of the *XMM-Newton* data is best fit by this model, indicating the presence of relativistic line broadening due to emission originating from material in the accretion disc nearest the black hole (Cunningham 1975; Fabian et al. 1989; Laor 1991). The reflection fraction (R) remains constant across the three data sets, suggesting the same amount of primary X-ray emission reaching the reflector in each observation. Most noteworthy are the extreme differences in iron abundance, ionisation parameter, and emissivity index between the *XMM-Newton* and *Suzaku* data sets.

The *XMM-Newton* data is best fit by a super-solar abundance and highly ionised reflector whereas the *Suzaku* data correspond to a sub-solar abundance and less ionised reflector. Statistically this blurred ionised reflection model is the best fitting model for the *XMM-Newton* and *Swift* data sets, though for the *Suzaku* data it offers no statistically significant improvement over the cold distant reflection scenario.

Comparing the results from Models (5), (6), and (7) we note that the *XMM-Newton* data are better fit by reflection off of the inner accretion disc (Model 7) and that the *Suzaku* data are best fit by reflection off the torus (Model 5), prompting an interesting discussion as to the cause of this spectral difference over the course of only 11−years.

Based on the best-fit model for each spectrum the observed $0.5-10$ keV flux is approximately 1.18×10^{-11} ergs cm^{-2} s^{-1} and is comparable within ~ 15 per cent between the epochs. The $10-100$ keV Swift BAT flux is approximately 2.48×10^{-11} ergs cm^{-2} s^{-1}. The intrinsic $2-10$ keV and $10-100$ keV luminosities are approximately 1.61×10^{44} ergs s^{-1} and 4.83×10^{44} ergs s^{-1}, respectively, assuming a standard cosmology with $H_0 = 70$ km s^{-1} Mpc^{-1} and $\Omega_\Lambda = 0.73$.

2.4.3 The X-ray Source

The *XMM-Newton* data of III Zw 2 is found to be best fit by Model (7), a cut-off power law and blurred ionised reflector. This model describes relativistically broadened emission originating from a highly ionised, super-solar abundance accretion disc that is being illuminated by a primary X-ray source some height above the disc (i.e. a corona or jet).

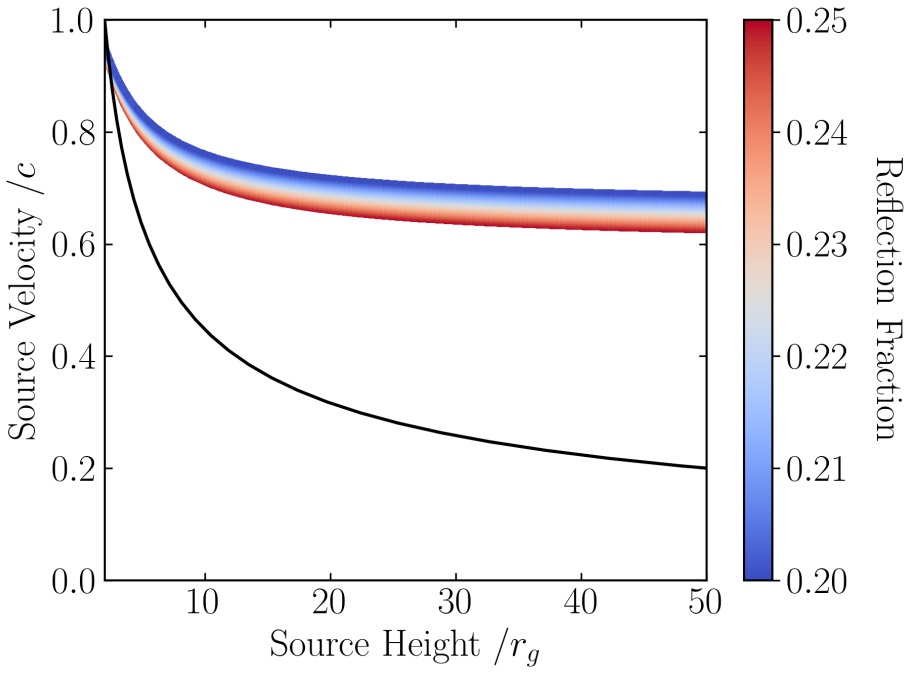

Figure 2.10: The source height and source velocity parameter space given the reflection fraction of the best fit Model (7), a cut-off power law and blurred ionised reflector, to the *XMM-Newton* data of III Zw 2 assuming a lamppost X-ray source. The black line represents the escape velocity of the black hole.

Gonzalez et al. (2017) performed general relativistic (GR) ray tracing simulations studying the illumination pattern of the accretion disc (i.e. emissivity profile) for various corona geometries and velocities, constructing an approximation for the reflection fraction, R, produced by point source coronae (i.e. the lamppost model) given the source height and source velocity (see Section 5.1 therein).

Assuming the lamppost model here we use this approximation of R to compute the source height and source velocity parameter space that produces the reflection fraction value in Model (7) of $R = 0.23^{+0.02}_{-0.03}$. These results are shown in Figure 2.10 as the shaded region with the black curve corresponding to the escape velocity from the black hole in III

Zw 2 using the mass estimate $M_{\rm BH} = (1.84 \pm 0.27) \times 10^8 M_\odot$ (Grier et al. 2012).

It is found that for all source heights $z > 2.4 r_g$ the source velocity exceeds the escape velocity of the black hole. This results in an anisotropically emitting X-ray source moving away from the black hole and accretion disc system. A constraint on the source height cannot be made, however, for the source heights explored ($z = 2 - 50 r_g$) the source velocity can be constrained as $v > 0.6c$.

2.5 Discussion

III Zw 2 is an interesting radio-intermediate Seyfert 1 galaxy. Its radio emission has been studied numerous times revealing extreme, possibly periodic, variability and the presence of a superluminal radio jet. The high-energy emission, however, has been studied far less with data being more sparse than at radio wavelengths. Here we have presented a thorough analysis of the X-ray spectrum of III Zw 2 obtained from the *XMM-Newton*, *Suzaku*, and *Swift* satellites.

All of the models presented throughout Section 2.4 provide good statistical fits to the data sets analysed here. Model (3) of Table 2.3 was built upon by adding a black body emitter to produce Model (4), which significantly improved all of the fits, indicating a two-component spectrum. The addition of this second, soft component altered the slope of the power law (Γ) such that all three data sets were in agreement. Interestingly, it was found that the *XMM-Newton* data were best fit by a broad ($\sigma_{\rm K\alpha} \approx 1$ keV) emission line at $E_{\rm K\alpha} \approx 6.3$ keV whereas the *Suzaku* data were best fit by a narrow ($\sigma_{\rm K\alpha} \approx 1$ eV) emission

line at $E_{\mathrm{K}\alpha} \approx 6.4$ keV. The *Swift* data, however, are best explained as a mid-point between these two extremes, with parameter values resembling a blend of the other fits, which seems reasonable since *Swift* data are combined over 17−years.

By simulating physically motivated models of reflection off of either the torus or accretion disc we were able to determine that the *XMM-Newton* data were best fit by a blurred ionised reflector and that the *Suzaku* data were best fit by a cold distant reflector. Here again the best fit to the *Swift* data appears to be an amalgamation of these two very different fits, with parameter values residing between the lower and upper bounds provided by the *XMM-Newton* and *Suzaku* fits. Combining the super-solar iron abundance and high ionisation parameter values of the *XMM-Newton* fit suggests emission coming from an accretion disc illuminated by an X-ray emitting corona (e.g. Fabian et al. 2009, 2013; Gallo et al. 2015). The *Suzaku* fit, however, indicates a reflector with solar iron abundance that is not subject to the intense gravitational effects associated with being near the black hole as evidenced by the lower ionisation parameter. From this we infer that the *XMM-Newton* data were taken during a period when the reflected X-ray emission of III Zw 2 was due to reflection off of the inner accretion disc whereas the *Suzaku* data were taken during a period of reflection off of the distant dusty torus surrounding the innermost region of the AGN, with the *Swift* data representing data taken during the transition between these two phases. The behaviour seems akin to that of changing-look AGN that appear to switch from Seyfert 1 to Seyfert 2 in the optical and X-ray (e.g. LaMassa et al. 2015). However, unlike that class of AGN, III Zw 2 does not exhibit a marked change in the X-ray flux from 2001 to 2011.

The most significant result in the work presented here is the discovery that a cold distant

reflector provides the best fit to the *Suzaku* data, while a blurred ionised reflector produced the best fit to the *XMM-Newton* data. This suggests that the source of the reflection completely changed over the course of only 11−years between these observations though the illuminating hard X-ray source has remained relatively constant as evidenced by the comparable flux. Considering only the *XMM-Newton* and *Suzaku* data in combination with results from radio light curve analysis we hypothesise the cause of the strange behaviour exhibited by III Zw 2 is due to a precessing radio jet, as first mentioned by Brunthaler et al. (2003, 2005), being described in more detail later by Li et al. (2010). Brunthaler et al. (2003, 2005) discuss a periodicity of approximately five years of the radio emission from III Zw 2 and mention a precessing jet as a potential explanation to the observations. In their description the jet would need to be interacting with a molecular torus on a five year cycle, though no evidence of a molecular torus was found. Li et al. (2010) measured a quasi-periodic cycle in the radio light curve with period $P = 5.14 \pm 0.19$ years, supporting the approximation provided by Brunthaler et al. (2003). In addition, Clements et al. (1995) were able to determine an approximate 13−month lag between X-ray and radio variability.

The spectral differences observed between the two epochs can be explained as the radio jet precessing in such a way as to illuminate the inner disc region during the *XMM-Newton* observation producing the broad Fe Kα line and blurred ionised reflection spectrum, and then illuminating the torus during the *Suzaku* observation and producing signatures of a cold distant reflector in the X-ray spectrum.

This evidence, while not conclusive, is supportive of a precessing radio jet interacting with a changing reflector producing the different X-ray spectra measured by *XMM-Newton* in

2000 and *Suzaku* in 2011. Furthermore, the evidence of a tidal bridge with star forming knots between III Zw 2 and III Zw 2B found by Surace et al. (2001) is indicative of an ongoing merger phase which provides a plausible mechanism that could result in disc instabilities, in turn producing a precessing accretion disc that would influence the behaviour of the radio jet.

Very recently, Liska et al. (2017) showed via general relativistic magnetohydrodynamics (GRMHD) simulations that precessing accretion discs can in fact propagate radio jets along their spin axis, producing jets that precess with the disc. The interaction between III Zw 2 and III Zw 2B may have resulted in a precessing accretion disc, thus causing the radio jet to precess along with it, producing the spectral results presented here.

The blurred reflection model for the *XMM-Newton* data yield a low reflection fraction ($R \approx 0.23$) that is suggestive of a primary source that is anisotropically illuminating away from the accretion disc. This is plausible if the primary source is the base of the jet, which would be consistent with the radio jet in this source. Following the determination of R from source height and source velocity in Section 5.1 of Gonzalez et al. (2017) the measured R value implies a source velocity of $v > 0.6c$ for source heights of $z = 2 - 50r_g$. This velocity is comparable to the radio jet velocity $v = 0.874c$ (Chen et al. 2012) supporting the connection between the X-ray source and radio jet.

The observed spectral changes found here are perhaps reminiscent of the state transitions seen in X-ray binaries (XRBs). During epochs when the jet is on (i.e. the low/hard state) spectra from XRBs are described by emission from an optically thin, geometrically thick accretion disc. Once the jet has turned off (i.e. the high/soft state) the spectra from these

objects are described by a traditional optically thick, geometrically thin standard accretion disc. Here we are unable to determine conclusively such a relationship between the radio jet and accretion disc as we lack simultaneous radio and X-ray observations. Additionally, the time scales for which such processes would occur in AGN are orders of magnitude greater than those of X-ray binaries and would therefore not be expected.

Alternative interpretations of the data include disc truncation (e.g. Lohfink et al. 2013) and ionisation changes in the disc (e.g. Bonson et al. 2015; Gallo et al. 2015). In a disc truncation scenario the inner portion of the accretion disc would be lost due to launching, ejecting the material via a jet. This, however, would almost certainly cause flux changes as a portion of the reflector is lost. With the essentially constant flux between the *XMM-Newton* and *Suzaku* observation it is unlikely that a disc truncation scenario would produce the observed spectral differences.

Changes in the ionisation of the accretion disc would be associated with changes in the source flux. If the disc is exposed to a primary source that is brightening one may see a correlation between the flux and ionisation parameter. However, if light bending of the primary source is important (e.g.Miniutti & Fabian 2004) then a correlation between brightness and ionisation may not be obvious. Nevertheless, the flux during the *XMM-Newton* and *Suzaku* observations was comparable and unlikely to result in significant changes in the ionisation that would alter the appearance of the broad emission line.

Alternatively, increased Comptonisation due to a variable, patchy corona could alter the shape of the reflection spectrum (i.e. broad line) (e.g. Wilkins & Gallo 2015b). If a patchy corona were covering a large fraction of the central disc then the blurred emission would

be further Comptonised as it traverses the corona. In this scenario, the corona could be more obscuring during the Suzaku observation and hence Comptonise the broad line that is evident during the XMM observation. This may be consistent with the slightly high power law flux observed in 2011.

2.6 Conclusions

III Zw 2 is a peculiar radio-intermediate Seyfert 1 galaxy that exhibits extreme variability in its radio emission. The most recent set of X-ray observations have been used to perform a spectral analysis on the X-ray spectrum, which has been studied far less than the radio emission.

We find evidence of a soft excess in all data sets with a broad Fe Kα line required in the *XMM-Newton* and *Swift* data, but only a narrow line in the *Suzaku* data.

Physical models of a cold distant reflector (i.e. the torus) and blurred ionised reflector (i.e. the inner region of the accretion disc) were fit to the data, finding the *XMM-Newton* data best described by a blurred ionised reflector (i.e. the accretion disc) and the *Suzaku* data being best fit by a cold distant reflector (i.e. the torus).

The spectral difference observed in the *XMM-Newton* and *Suzaku* data sets, which occurred over the 11−years between observations, is hypothesized as the result of a precessing radio jet illuminating the inner disc region in 2000 and interacting with the dusty torus in 2011.

However, other possible explanations exist. Continued monitoring in the radio and X-

ray wavelengths as well as deep pointed observations with *XMM-Newton* and *NuSTAR* will help better understand the nature of the X-ray variability.

Chapter 3

Characterising continuum variability in the radio-loud narrow-line Seyfert 1 galaxy IRAS 17020+4544

This work was originally published in the August 2020 issue of the Monthly Notices of the Royal Astronomical Society, Volume 496, Issue 3, pp. 3708−3824.

It is presented in unaltered form here.

3.1 Introduction

Evidence suggests that every massive galaxy likely harbours a super-massive black hole (SMBH) at its centre. Active galactic nuclei (AGN) are those galaxies where the SMBH is actively accreting material from the surrounding environment. This accretion process may result in the formation of an accretion disc (Shakura & Sunyaev 1973), enabling maximally efficient conversion of matter into radiation which thereby produces the most luminous continuous sources of emission in the Universe that in many cases outshines the entire stellar component of the AGN host galaxy.

AGN are luminous emitters across the entire electromagnetic spectrum, exhibiting significant variability in flux and spectral state over time. In the X-ray band AGN can be broadly described as having a two-component spectral model, dominated by a blackbody-like component at lower energies (i.e. $\lesssim 1$ keV) and a power-law component over a broader high-energy band (i.e. > 2 keV). This simple model is often modified significantly, such as by absorption in the host galaxy and/or contributions from X-ray reflection off of the accretion disc, greatly complicating the inferences that can be made about the physical environment surrounding the SMBH when modelling the X-ray spectrum. In order to alleviate some of these modelling complications various model-independent techniques have been brought to the fore-front of AGN research, with notable success. An important caveat of such techniques, however, is the need for large quantities of high quality data, sometimes limiting their use to well-sampled, bright sources.

Narrow-line Seyfert 1 galaxies (NLS1s) are a type of AGN that frequently exhibit ex-

treme, complex behaviour for a number of different properties. These AGN were originally classified as those displaying Hβ emission lines with full-width half-maximum values (FWHM) of < 2000 km s^{-1} (Goodrich 1989), as well as strong Fe II and weak [O III] emission (Osterbrock & Pogge 1985). The FWHM of these Hβ features, originating from the broad-line region (BLR) which is dominated by orbital motion governed by the gravitational potential of the central SMBH, suggest smaller black hole masses ($M_{\rm BH} < 10^8\ M_{\odot}$) for the NLS1 population (e.g. Peterson et al. 2000). Other optical-regime works have revealed accretion rates in these AGN to be between $L/L_{\rm Edd} \approx 0.1 - 1$ (Boroson & Green 1992), in some cases even surpassing the Eddington limit, indicating an extreme central environment.

Radio studies of NLS1s have found that a large majority are undetected across radio wavelengths (i.e. radio-silent) or exhibit low levels of emission (i.e. radio quiet; RQ). A small fraction ($\sim$ 7 per cent) are defined as being radio-loud (RL) (Komossa et al. 2006) possessing powerful, relativistic jets. There is, however, some ambiguity surrounding radio-loudness as a parameter and its usefulness in characterising and / or classifying AGN as there are now examples of previously claimed radio-silent sources being detected at 37 GHz indicating jet activity (Lähteenmäki et al. 2017, 2018).

In the X-ray regime, NLS1s typically display steep spectra (i.e. X-ray power-law photon index $\Gamma \gtrsim 2$), the presence of a significant soft excess, and rapid, sometimes large amplitude, variability (e.g. Boller et al. 1996; Brandt et al. 1997; Komossa et al. 2017; Gallo 2018). The steep X-ray spectrum may be indicative of a cooler or lower density primary corona than is found in other types of AGN while the strong soft excess might arise from a large contribution of X-ray reflection off of the accretion disc.

One of the many open questions in AGN research seeks to uncover the connection between the accretion disc and radio jet (i.e. disc-jet connection). Previous works have suggested that in states of sub-Eddington, radiatively inefficient accretion, emission is dominated by the jet and that once the source enters a higher, more efficient accretion state the disc emission begins to quench that of the jet (e.g. Merloni et al. 2003; Körding et al. 2006). Coupling the strong disc emission and evidence of jet activity in the RL-NLS1 population offers a unique test-bed in which a connection between these two components may be explored.

For instance, the structure of the X-ray power-law source (i.e. corona) in AGN has historically been represented as a compact 'point-source' geometry that resides some height above the accretion disc. Recently, however, there have been results indicating signatures of coronal geometries that are low in height and significantly extended over the inner disc as well as signatures of vertically collimated coronae that are outflowing at some velocity. In Mrk 335 (Wilkins & Gallo 2015a) and I Zw 1 (Wilkins et al. 2017), two examples of RQ-NLS1s, events that can be described as aborted jet launches have been suggested, wherein an originally extended corona became vertically collimated (gaining some outflow velocity) before collapsing into a more compact geometry.

Many NLS1s also display clear signatures of emission from the inner accretion disc, such as a soft excess at low energies $\lesssim 1$ keV and relativistically broadened Fe K emission in the $6 - 7$ keV band originating from material at the inner most edge of the disc (Laor 1991). Reverberation analysis techniques have been used as a model-independent tool to reveal time-lags between the soft excess and coronal emission in numerous AGN (e.g. Kara

et al. 2016). In some cases a high-frequency lag is detected such that emission from the soft excess lags behind the continuum, supporting the idea of a reflection-based origin for the soft excess. Such features are also observable in the lag-energy spectra, constructed by plotting the aforementioned reverberation lags as a function of energy, where they show large time lags for the soft excess and Fe K emission band compared with the continuum, indicating a common origin (e.g. Zoghbi et al. 2010; Kara et al. 2016). In some sources, however, the soft excess has been interpreted as evidence of a secondary cooler, optically thick X-ray corona (e.g. Done et al. 2012).

RL-NLS1s therefore pose a promising population of AGN in which the disc-jet connection can be rigorously tested, owing to the recent evidence of launching X-ray coronae and strong reflected emission from the accretion disc.

IRAS 17020+4544 (also known as: B3 1702+457, J170330.38+454047.1) is a nearby ($z = 0.0604$)[1] RL-NLS1 that has been studied numerous times at radio wavelengths with a sparse presence in X-ray astronomy literature. Radio surveys have found the source to be classified as a compact steep-spectrum object (CSS) with a turnover frequency at < 150 MHz (Snellen et al. 2004) exhibiting a sub-relativistic or misaligned jet on parsec scales (Doi et al. 2011; Giroletti et al. 2017). Berton et al. (2018), however, reported a flat in-band spectral index while also finding a steep broad band index, suggesting significant radio variability. Early work (Leighly et al. 1997; Komossa & Bade 1998) discovered the presence of warm absorbers (WAs) in the X-ray spectrum, with recent studies (Longinotti et al. 2015; Sanfrutos et al. 2018) confirming their presence alongside ultra-fast outflows of high column

[1]Obtained from the NASA/IPAC Extragalactic Database (NED) at https://ned.ipac.caltech.edu/

density, highly ionised material. The high-energy X-ray spectrum (i.e. $0.3 - 10$ keV) has not yet been examined.

In this work we will focus on the analysis of four *XMM-Newton* EPIC pn observations of IRAS 17020+4544 presenting timing and spectral analyses exploring the observed variability. The paper is organised as follows. In Section 3.2 we present details of the observations and data reduction. Section 3.3 presents the various timing methods used to characterise the observed variability using model-independent approaches. In Section 3.4 we model the X-ray spectrum using spectral models motivated by the timing results. We discuss further the implications of our results in Section 3.5, concluding in Section 3.6.

3.2 Observations & Data Reduction

In this paper we use archival data obtained from the *XMM-Newton* (Jansen et al. 2001) X-ray observatory. Details of the four observations used in this analysis are presented in Table 3.1.

The EPIC pn (Strüder et al. 2001) camera was operated in small window mode with the medium filter applied for the duration of all four observations. Throughout this work we abbreviate the observation IDs as in column (2) of Table 3.1. The *XMM-Newton* Observation Data Files (ODFs) were processed using the *XMM-Newton* Science Analysis System (SAS) version 15.0.0 creating event lists with the EPCHAIN task. While producing the event list products we used the conditions $0 \leq$ PATTERN ≤ 4 and FLAG $== 0$. Source photons were extracted from a $35''$ circular region centred on the source. Background photons were

Table 3.1: *XMM-Newton* EPIC pn observations of IRAS 17020+4544 used in this work. The columns are: (1) observation ID, (2) abbreviated name referenced throughout the manuscript, (3) start date of observation, (3) observation duration, and (4) final exposure time including background flaring corrections.

(1) Obs. ID	(2) Abbrev.	(3) Start Date [yyyy-mm-dd]	(4) Duration [ks]	(5) Exp. [ks]
0206860101	2004.101	2004-08-30	21.8	13.5
0206860201	2004.201	2004-09-05	21.5	12.9
0721220101	2014.101	2014-01-23	82	56.2
0721220301	2014.301	2014-01-25	84	56.0

extracted from a 50″ circular off-source region. The timing and spectral products were each extracted from the resulting event lists using the EVSELECT task, finding evidence of significant high-energy (> 10 keV) background flaring in both 2004 observations and mild background activity during the 2014 observations; none of the observations displayed any evidence of pile-up according to the EPATPLOT output. Corrected light curves for each observation were produced using the SAS task EPICLCCORR. Spectra for each observation were produced with response matrices generated using the SAS tasks RMFGEN and ARFGEN. When producing the spectra we extracted good-time intervals (GTIs) using the TABGTIGEN task, excluding times where the background level at > 10 keV exceeded 0.3 counts s^{-1}, the 'quiescent' background counts before and after the flaring. The final exposures after extracting the GTIs are listed as column (5) of Table 3.1.

We use a Galactic column density of $N_{\rm H} = 2.20 \times 10^{20}$ cm^{-2} from Willingale et al. (2013)[2], which reports a combined atomic and molecular column density of hydrogen, and

[2]Browser based tool for calculating Galactic column density available at http://www.swift.ac.uk/analysis/nhtot/index.php

use Wilms et al. (2000) abundances throughout our spectral modelling. We also assume a cosmology with $H_0 = 70$ km s^{-1} Mpc^{-1}, $q_0 = 0$, and $\Lambda_0 = 0.73$. All reported spectral model parameter errors are at the 90 per cent confidence level, unless otherwise stated. All energy values are in the observed frame, unless otherwise stated.

3.3 Timing Analysis

3.3.1 Exploring the light curves

For each of the four observations a broad band $0.3 - 10$ keV background-subtracted light curve was made using bins of 200 s, as shown in the top row of Figure 3.1. Increased levels of background activity can be seen at the end of both 2004 epochs, with 2004.201 additionally exhibiting increased background levels during the middle of the observation. The first $\sim$ 20 ks of 2014.101 also exhibit increased background levels. These times were filtered out using the GTI criteria described in Section 3.2 when making the spectra for these observations. We checked and confirmed that the timing products are unaffected by these periods of increased background activity, and therefore we include them in all of the following timing analyses. The mean source count rate of each broad band light curve is shown as column (2) in Table 3.2, which globally varies within ~ 35 per cent of its mean of 7.7 ± 1.0 counts s^{-1}.

The variability in the broad band light curves can be quantitatively assessed by computing the fractional variability as in Vaughan et al. (2003), shown as column (3) in Table 3.2. Epoch 2014.101 stands out as having the lowest fractional variability while 2014.301

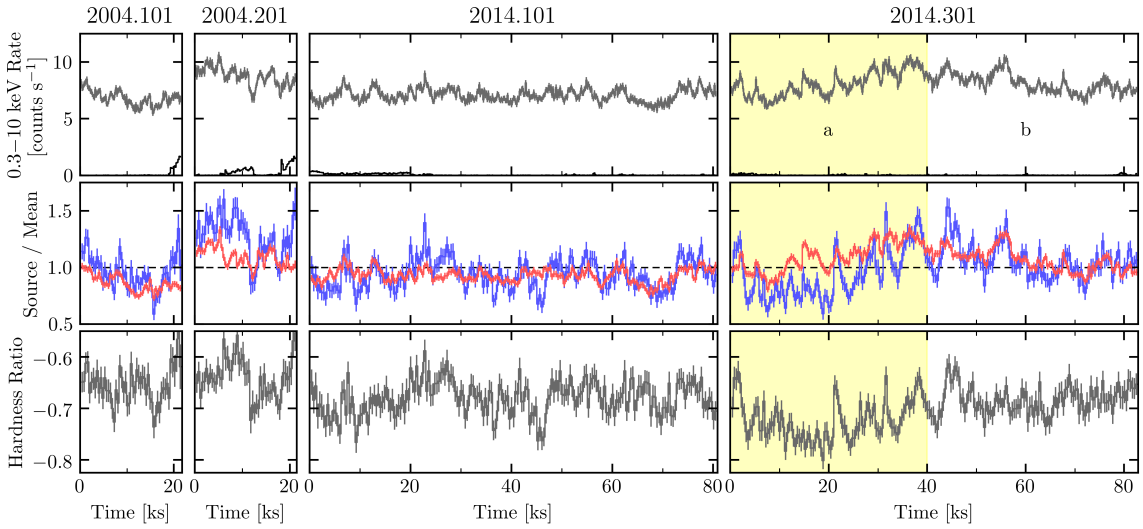

Figure 3.1: *Top row* − The broad band $0.3-10$ keV EPIC pn background-subtracted light curves binned by 200 s (grey curves) for each of the *XMM-Newton* observations, with the background light curves shown as the black curves. *Middle row* − The soft ($S = 0.3-1$ keV; red curves) and hard ($H = 2-10$ keV; blue curves) EPIC pn source light curves binned by 400 s. Each light curve has been divided by the mean source count rate across all observations in the corresponding energy band allowing for direct comparisons of variability in each band. *Bottom row* − The hardness ratios $HR = (H - S) / (H + S)$ for each observation using the same 400 s binned light curves as the middle row. In each of the 2014.301 panels the first 40 ks are highlighted in yellow.

displays significantly more variable behaviour than any other epoch. Both 2004 observations display a mild dimming over time while sharing similar levels of variability. These levels of variability are not extreme when compared to the large-amplitude short-term variability observed in other NLS1s.

To explore energy-dependent variability we extracted soft (S) and hard (H) band light curves using $0.3-1$ keV and $2-10$ keV, respectively, and computed the hardness ratio $HR = (H - S) / (H + S)$ between them, as shown in the middle (normalised light curves) and bottom (hardness ratios) rows of Figure 3.1. To reduce the size of the error bars we re-binned the data into 400 s time bins. It is clear that the hard band is significantly

Table 3.2: General light curve properties for each of the five epochs using time bins of 400 s. The columns are: (1) observation abbreviation, (2) the mean $0.3-10$ keV source count rate, (3) the fractional variability ($F_{\rm var}$) of the $0.3-10$ keV light curve, and (4) the mean hardness ratio ($HR = (H-S)/(H+S)$) between the $0.3-1$ keV and $2-10$ keV light curves.

(1) Epoch	(2) Mean Rate [counts s^{-1}]	(3) $F_{\rm var}$ [per cent]	(4) Mean HR
2004.101	6.82 ± 0.01	8.7 ± 0.3	-0.655 ± 0.003
2004.201	8.76 ± 0.02	8.7 ± 0.3	-0.641 ± 0.003
2014.101	7.100 ± 0.003	6.9 ± 0.2	-0.680 ± 0.001
2014.301a	8.11 ± 0.01	12.9 ± 0.2	-0.724 ± 0.002
2014.301b	8.171 ± 0.008	9.6 ± 0.2	-0.685 ± 0.002

more variable than the soft band in all observations, having $F_{{\rm var},H} = 14 \pm 1$ compared to $F_{{\rm var},S} = 7.8 \pm 0.7$ globally. Visual inspection reveals hints of correlated variability between the soft and hard bands, to be examined further in a following section. The hardness ratios remain relatively constant throughout each observation, exhibiting variations of $\sim$ 20 per cent globally, with the mean value for each epoch given as column (4) of Table 3.2. Epoch 2014.301 exhibits the most significant hardness ratio deviation of any epoch, where a dip at $\sim$ 20 ks is observed, after which the hardness ratio increases gradually for the remainder of the observation.

The increased fractional variability and changing hardness ratio of 2014.301 indicate significantly different behaviour during this observation when compared to the other epochs. Since the apparent spectral state change in 2014.301 is only present during the first 40 ks we segmented this observation into two 40 ks long segments, hereafter referred to as 2014.301a for the first 40 ks and 2014.301b for the remaining 40 ks.

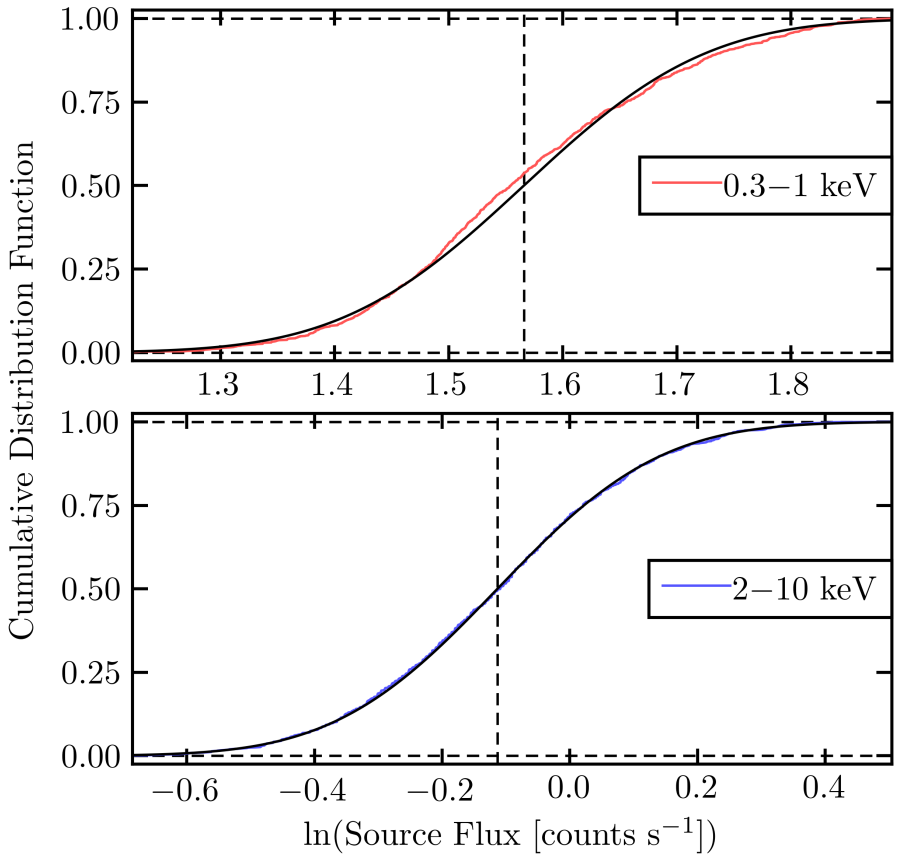

Figure 3.2: The natural logarithm of the soft ($0.3-1$ keV; top panel) and hard ($2-10$ keV; bottom panel) source flux distributions using light curves binned by 200 s. In each panel the black solid line represents the best-fit normal distribution to the data and the vertical black dashed line represents the mean flux.

Analysing the flux distributions of a time series can uncover the nature of the variability of that time series. The observed variability in all accreting systems follows a stochastic process which is typically considered *stationary* on the timescale of the observations. All accreting systems are observed to display a log-normal flux distribution (e.g. Uttley et al. 2005; Alston 2019, and references therein). A significant deviation from a stationary process was first observed in Alston et al. (2019), where a non-log-normal flux distribution and a

time-dependent power spectral density (PSD) were observed (see also Alston 2019). To explore the possibility of non-stationarity in IRAS 17020+4544 we analysed the log-flux distributions of the soft and hard energy bands using 200 s binned light curves, shown as the empirical cumulative distribution functions (ECDFs)[3] in Figure 3.2. The log-flux distributions were each fit with a normal distribution, and the normality of both bands were evaluated by performing Kolmogorov-Smirnov (KS) and Anderson-Darling (AD) (Anderson & Darling 1952) tests. We found that for the soft band $p_{\rm KS} = 0.027$ and $p_{\rm AD} = 3.6 \times 10^{-7}$ whereas for the hard band $p_{\rm KS} = 0.99$ and $p_{\rm AD} = 0.89$. These results may suggest that variability in the soft band is due to physical changes in the system while hard band variability is explained by stochastic variations in the emission process. This interpretation is complicated by the unknown impact of the warm absorption in this source, which significantly affects the soft band below ~ 2 keV, on the soft-band flux distribution. Furthermore, it is possible that the ~ 210 ks total observing time is insufficient in providing enough data to adequately sample the flux distributions.

Many RQ-NLS1s have been shown to enter a softer spectral state when they are at their brightest (i.e. 'softer-when-brighter' trend). To check for such a trend here we constructed a series of hardness ratio versus flux (hereafter simply hardness-flux) plots, shown in Figure 3.3. We fit each epoch with its corresponding mean hardness ratio as well as with a linear model with free to vary slope and intercept, finding that the linear model provided a significantly better fit (> 99 per cent confidence level) in every epoch. The best-fit models are given as column (2) of Table 3.3, where in column (3) it is clear that none of the fits

[3]We use ECDFs here rather than histograms to avoid arbitrarily binning the data in the flux domain.

Table 3.3: The best-fit models to the hardness-flux and flux-flux plots using 400 s binned light curves with the soft band (S) as $0.3-1$ keV and the hard band (H) as $2-10$ keV. The columns are: (1) observation abbreviation, (2) best-fit linear model to hardness-flux plot using $F_{\rm C}$ as the combined flux in the soft and hard bands, (3) the χ^2 value of the given hardness-flux equation, (4) best-fit linear and power-law models to the flux-flux plot using $F_{\rm S}$ as the soft band flux and $F_{\rm H}$ as the hard band flux, and (5) the χ^2 value of the given flux-flux equation for the indicated degrees of freedom, dof. Errors are not displayed due to the very poor fit qualities, however we note that all parameters have relative errors of ~ 5 per cent other than the hardness-flux slope estimates which have relative errors of ~ 50 per cent.

(1) Epoch	(2) Hardness-Flux Equation	(3) Fit Quality χ^2/dof	(4) Flux-Flux Equation	(5) Fit Quality χ^2/dof
2004.101	$HR = 0.022F_{\rm C} - 0.77$	111/50	$F_{\rm S} = 1.51F_{\rm H} + 2.83$	258/50
			$F_{\rm S} = 4.34F_{\rm H}^{0.32}$	256/50
2004.201	$HR = 0.021F_{\rm C} - 0.78$	125/49	$F_{\rm S} = 1.44F_{\rm H} + 3.60$	266/49
			$F_{\rm S} = 5.05F_{\rm H}^{0.30}$	264/49
2014.101	$HR = 0.022F_{\rm C} - 0.80$	458/198	$F_{\rm S} = 1.17F_{\rm H} + 3.47$	746/198
			$F_{\rm S} = 4.63F_{\rm H}^{0.22}$	753/198
2014.301a	$HR = 0.022F_{\rm C} - 0.86$	363/98	$F_{\rm S} = 2.26F_{\rm H} + 3.32$	889/98
			$F_{\rm S} = 5.61F_{\rm H}^{0.38}$	865/98
2014.301b	$HR = 0.010F_{\rm C} - 0.75$	193/98	$F_{\rm S} = 2.36F_{\rm H} + 2.86$	570/98
			$F_{\rm S} = 5.23F_{\rm H}^{0.45}$	568/98

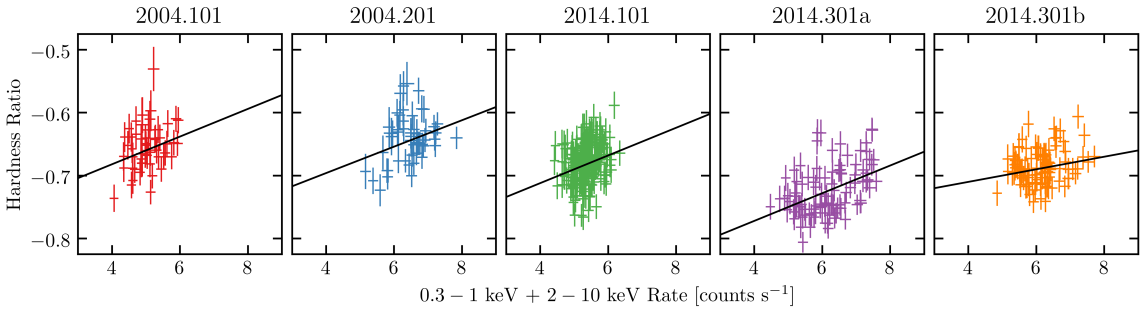

Figure 3.3: Hardness-flux plot using $0.3-1$ keV and $2-10$ keV light curves binned by 400 s as the soft and hard light curves, respectively. In each panel the black solid line displays the best-fit model to the hardness-flux relation, with corresponding equations given in Table 3.3.

provide statistically good descriptions of the data with $\chi^2/dof \gtrsim 2$ in all epochs. Despite the poor fit qualities we note that the 'softer-when-brighter' trend is not observed here, in fact the opposite is true: increased flux levels correspond to harder spectra. Furthermore, 2014.301b exhibits a slope that is significantly different from the other epochs, which all share a common slope value of ~ 0.022. This may suggest that a significant physical change in the central region may have taken place during the 2014.301b epoch.

Flux-flux plots have been used as another model-independent timing tool capable of characterising the nature of spectral variability. By plotting the soft versus hard flux we can explore the relationship between these two energy bands directly, as shown in Figure 3.4. We note that in order to avoid arbitrarily binning in the flux-flux plane we only bin the light curves in the time domain. We fit each epoch with both linear (free to vary slope and intercept) and power-law (free to vary normalisation and index) models in order to distinguish the variability as either variations of the hard continuum in the presence of an additional constant component or changes in the hard continuum photon index, respectively

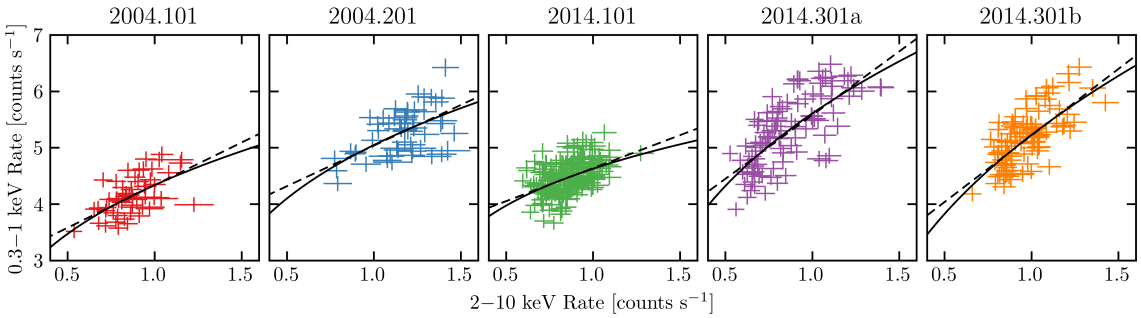

Figure 3.4: Flux-flux plots using $0.3-1$ keV and $2-10$ keV light curves binned by 400 s as the soft and hard light curves, respectively. In each panel the black dashed line displays the best-fit linear model while the black solid line displays the best-fit power-law model, with corresponding equations given in Table 3.3.

(Taylor et al. 2003). The best-fit linear and power-law models are given as column (4) in Table 3.3, where in column (5) it is clear that again none of the fits provide statistically good descriptions of the data with $\chi^2/dof \gtrsim 3$ in all epochs for both models. While a power-law fit is found to the better description overall, suggesting that the spectra exhibit varying photon index values throughout the observation epochs thus providing a straightforward explanation for the hardness ratio variability, we note that the poor fit qualities obtained indicate that the variability observed is due to more than simply a spectral power-law normalisation change and / or pivot. We note that the 2014.301 epochs are much steeper in both model descriptions than the previous three epochs. A power-law plus constant fit (to account for a changing photon index in the presence of an additional constant component) was attempted and found to provide a marginally better fit to the data, though the parameters could not be constrained in any meaningful way and are thus not presented here.

In Table 3.2 we note that the fractional variability increases during the 2014.301a soft state. To explore this further we split each observation into 10 ks segments, binning each

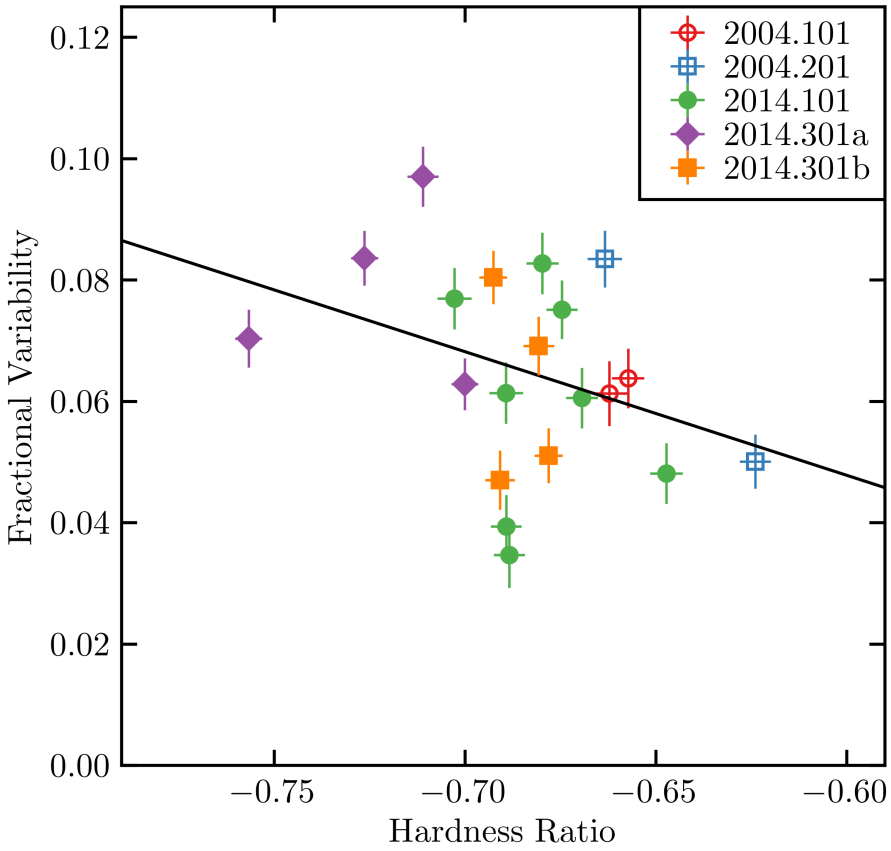

Figure 3.5: The mean fractional variability versus mean hardness ratio of 10 ks light curve segments using 400 s binned light curves for each epoch. The best-fit linear model $F_{\rm var} = [-0.2 \pm 0.1]\,HR + [-0.07 \pm 0.09]$ is shown as the solid black line.

by 400 s, and computed the fractional variability of the broad band as well as the hardness ratio between the soft and hard bands for each epoch. The results are shown in Figure 3.5, where the best-fit linear model was found to be $F_{\rm var} = [-0.2 \pm 0.1]\,HR + [-0.07 \pm 0.09]$ yielding a fit quality of $\chi^2/dof = 272/2$. The fit reveals a trend of decreased variability during harder spectral states, though the fit quality is very poor.

Finally, noting the increased variability in the hard band compared to the soft band,

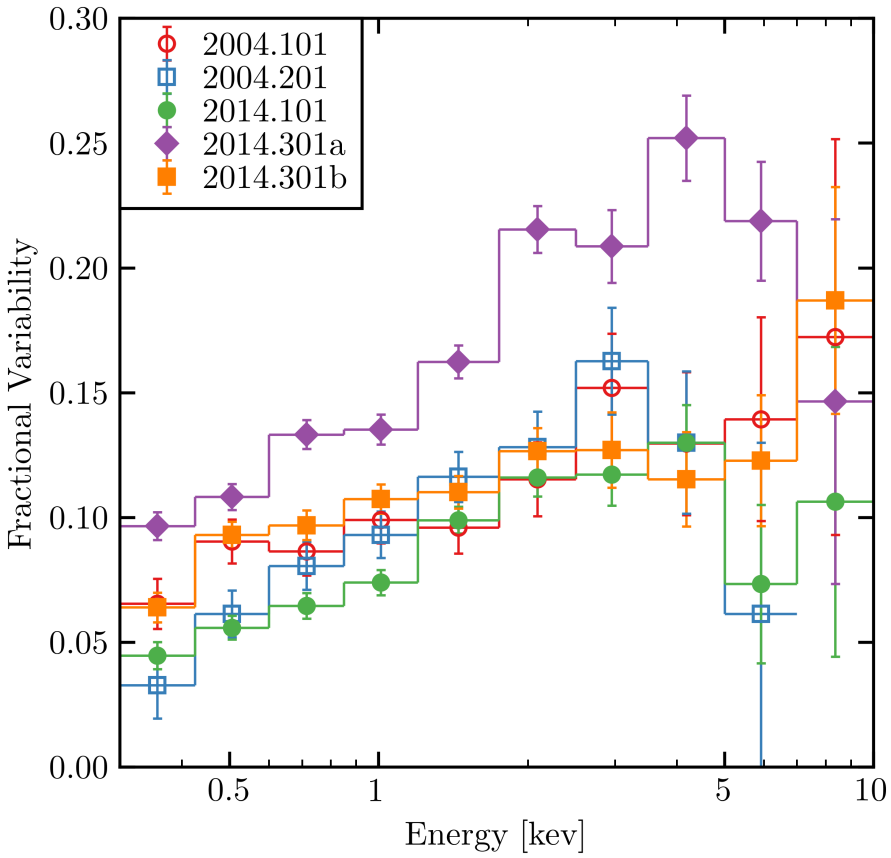

Figure 3.6: The fractional variability versus energy spectra using light curves binned by 400 s.

we computed fractional variability spectra for each of the five epochs in various energy bins (approximately evenly spaced in energy, combining high-energy bins to reduce error size), shown in Figure 3.6. Immediately notable is the consistent shape of the spectra, which all display a trend of increasing variability with energy. Other RQ-NLS1s typically exhibit fractional variability spectra that appear peaked at low energies or are relatively flat across all energies (e.g. Markowitz et al. 2003) which have been interpreted as evidence of a dominant disc component or a dominant power-law changing only in normalisation,

respectively. While four of the epochs exhibit similar levels of variability across the entire energy range, 2014.301a displays significantly higher variability at all energies while also more steeply increasing in variability up to $\sim$ 5 keV, where the level drops to more like those at other epochs.

To ensure that differing light curve lengths between the epochs did not produce the observed differences in the fractional variability spectra, we computed the spectra based on 20 ks segments for each epoch. Comparing the mean spectrum of that segmented analysis with the mean spectrum of the presented analysis in Figure 3.6 found them to be completely consistent.

3.3.2 Frequency-space products

The results so far have been useful to reveal general properties of the various observation epochs. In order to probe the temporal variability of the data in a more detailed manner we must move into frequency based analysis methods. To do this we followed the various prescriptions outlined in Uttley et al. (2014), and we summarize the steps here. In this section we focus solely on the two 2014 observations as they are free from significant background flaring and allow for the analysis of the low-frequency regime.

3.3.2.1 Combined analysis

We first computed the $0.3 - 10$ keV PSD for the combined 2014 observations. For each epoch, we generated a broad band ($0.3 - 10$ keV) light curve binned by 200 s. We then performed a discrete Fourier transform (DFT) on each broad band light curve, allowing for

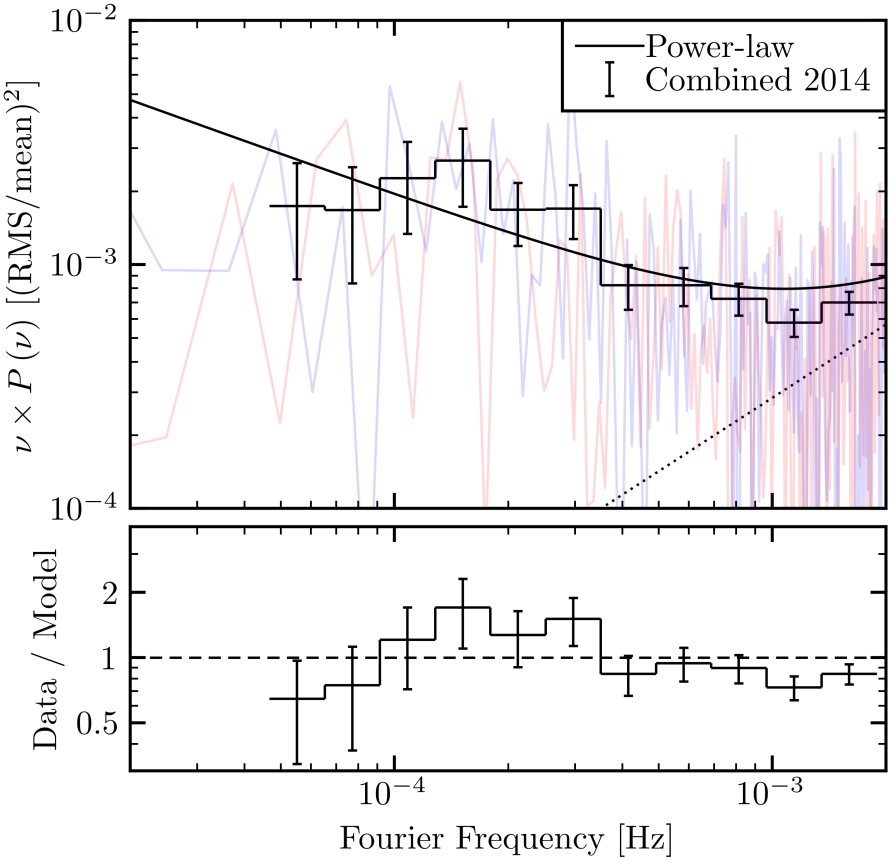

Figure 3.7: *Top panel* – The broad band (0.3 – 10 keV) power spectral density (PSD) using 200 s binned light curves for the combined 2014 epochs, with the raw PSDs for the 2014.101 (red) and 2014.301 (blue) epochs also shown. The Poisson noise level is shown as the dotted line. The solid line displays the best-fit power-law model to the raw PSDs of the 2014 epochs. *Bottom panel* – Ratio residuals when dividing the PSD by the best-fit power-law to the 2014 data.

a subsequent calculation of the PSD (i.e. RMS normalized square of the periodogram) in each observation. We then combined the two PSDs and binned the result in frequency-space using a geometric binning factor of 1.4, which is shown in Figure 3.7. We excluded frequencies lower than $3/T$ Hz, where T is the light curve length, in order to ensure that any periodic signals are detected at least three times and to avoid the impact of red-noise

leakage.

At frequencies $\gtrsim 10^{-3}$ Hz the source signal is dominated by the Poisson (i.e. white) noise. The overall shape of the PSD resembles those seen in other Type 1 AGN (e.g. González-Martín & Vaughan 2012) where a possible flattening is observed below $\sim 1.5 \times 10^{-4}$ Hz. To test the significance of this flattening we simultaneously fit the raw (i.e. not frequency binned) PSDs from both epochs with a power-law and a bending power-law model, using the Whittle statistic to evaluate the model likelihoods. Following the methods in Vaughan (2010) we performed the likelihood ratio test (LRT) to compare the two models, finding that the bending power-law model provides $T_{\rm LRT}^{\rm obs} = 3.45$ when compared to the power-law model, finding a break frequency in the PSD of $\nu_{\rm break} \approx 2 \times 10^{-5}$ Hz. However, fitting with the bending power-law model did not constrain the low-frequency slope well and thus it was frozen at $\alpha_{\rm L} = -0.465$, which itself was found to be the best-fit value for this parameter when sampling values between -1 and 0.

In order to evaluate the significance of the fit improvement offered by the bending power-law model we ran Markov Chain Monte Carlo (MCMC) simulations (5 chains of $50,000$ iterations) to draw from the posterior parameter distributions of the power-law fit, which were subsequently used to simulate posterior predictive PSDs. These simulated PSDs were then fit by both the power-law and bending power-law models in order to simulate a distribution of $T_{\rm LRT}^{\rm sim}$. Simulating $N = 2500$ PSDs from the posterior distribution of power-law parameters returned a posterior predictive p-value of $p = 0.063$ when comparing $T_{\rm LRT}^{\rm obs}$ to $T_{\rm LRT}^{\rm sim}$, which itself follows a χ_1^2 distribution. This indicates a modest fit improvement for the inclusion of a bend when simultaneously fitting the raw PSDs but cannot be concluded

Table 3.4: Parameter estimates (90 per cent confidence intervals) for simultaneous fitting of raw PSDs using a power-law model $P(\nu) = N\nu^{-\alpha} + C$. The columns are: (1) fit parameter, (2) mean value from MCMC simulations, and (3) and (4) being the 5 per cent and 95 per cent bounds from the MCMC simulations, respectively. A superscript ^{f} denotes a model parameter that was kept fixed to the listed value during fitting.

(1) Parameter	(2) Mean	(3) 5 per cent	(4) 95 per cent
Normalisation, N	1.1×10^{-5}	4.1×10^{-6}	2.7×10^{-5}
Slope, α	1.56	1.44	1.69
Poisson noise, C	0.264^f		

as statistically significant. Furthermore, the parameter values for the bending power-law model were unable to be meaningfully constrained and thus we do not discuss this model beyond this point. The 90 per cent confidence intervals for the power-law parameters are given in Table 3.4 (the Poisson noise level was held constant at the computed noise level during the fitting procedure).

The ubiquitous additional constant component found in the flux-flux analysis may be a sign of X-ray reflection off of the accretion disc. This reflector may also be detected via time-lag analysis of two light curves with one being from an energy band dominated by the primary emission and the other being from an energy band dominated by the reflected emission. We therefore computed the combined lag-frequency spectrum to study the time-lag between the soft and hard bands. For each epoch, we generated soft ($0.3 - 1$ keV) and hard ($1 - 4$ keV) light curves binning by 200 s. We then performed a DFT on each light curve, taking the complex conjugate of the soft light curve DFT and multiplying it by the hard light curve DFT to produce a complex valued product, the cross-spectrum, binning in frequency-space using a geometric binning factor of 1.4. The argument of this complex

valued binned cross-spectrum is the phase $\phi(\nu_i)$, which gives the phase-lag between the soft and hard light curves in the bin at frequency ν_i[4]. From this, we compute the time-lag at frequency ν_i as $\tau(\nu_i) = \phi(\nu_i) / (2\pi\nu_i)$. To further increase our signal-to-noise we chose to combine the two 2014 observations to produce a single lag-frequency spectrum. This involved combining the cross-spectra of the two light curves from each epoch, and then proceeding with the remaining steps outlined above as normal. The resultant combined lag-frequency spectrum is shown in the bottom panel of Figure 3.8, with the corresponding raw coherence plotted in the top panel. As with the PSDs, here we exclude frequencies lower than $3/T$ Hz.

The combined lag-frequency spectrum exhibits large positive lags in the low-frequency range of $(4.66 - 12.8)\times10^{-5}$ Hz and negative lags in the high-frequency range of $(1.79 - 3.51)\times 10^{-4}$ Hz. We are unable to explore beyond 10^{-3} Hz due to very low coherence at frequencies greater than this. Notable is the fact that at no point is the coherence > 0.80, which is at odds with many other AGN that have had their lag-frequency spectra evaluated finding coherence values of ~ 1 over a broad frequency range. High levels of coherence indicate a simple linear transform between the low- and high-energy input light curves, which may be expected in a strictly reverberation scenario wherein the light curve variability is preserved. The level of incoherence observed here thus indicates a non-linearity in the transform, which may simply be due to Poisson noise. However, given the observed differences in flux distribution between the low- and high-energy regimes the low coherence here may be an independent piece of evidence that suggests physical differences in the emission processes corresponding

[4]In this work ν_i is taken to be the bin mid-point frequency.

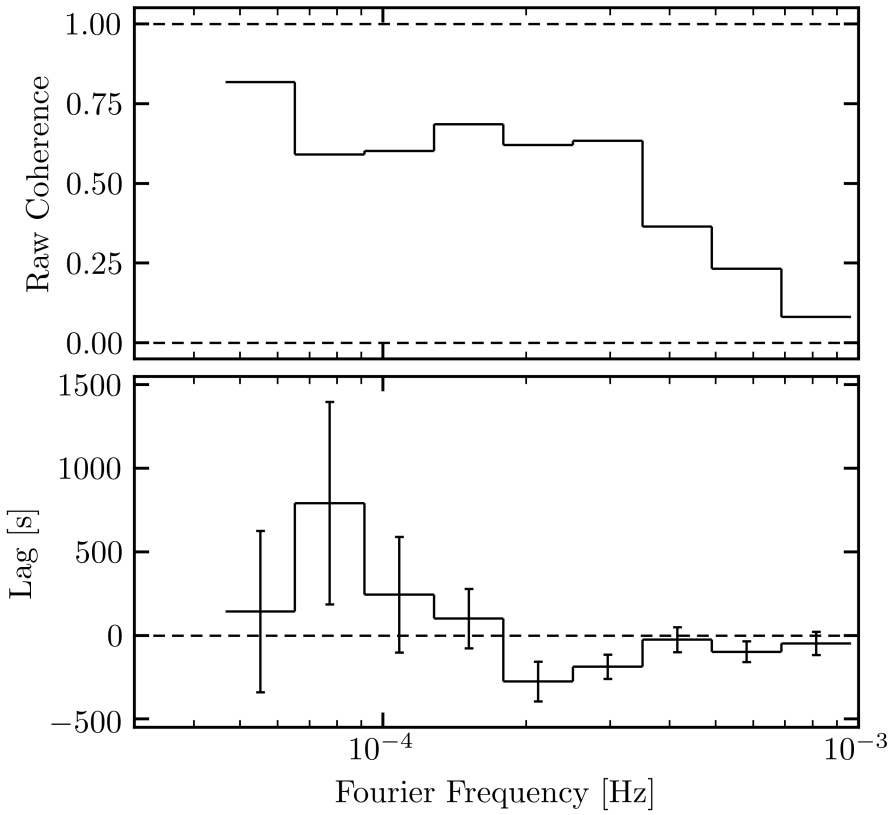

Figure 3.8: *Top panel* − The raw coherence of the soft (0.3−1 keV) and hard (1−4 keV) light curves, binned by 200s, for the combined 2014 epochs. *Bottom panel* − The lag-frequency spectra computed using the same light curves are shown, where positive lags indicate soft band leading the hard, and negative lags indicate soft band lagging the hard.

to these different energy bands. The negative lags present in the lag-frequency spectrum indicate that hard band variations take place first and are 'echoed' by the soft band some time later (i.e. the lag value). With our selected soft and hard band energy range this therefore provides evidence of the reverberation of coronal emission off of the accretion disc.

Lag-energy spectra were computed in the defined low- and high-frequency bands. We first generated light curves binned by 200 s for each observation in energy bands that give an

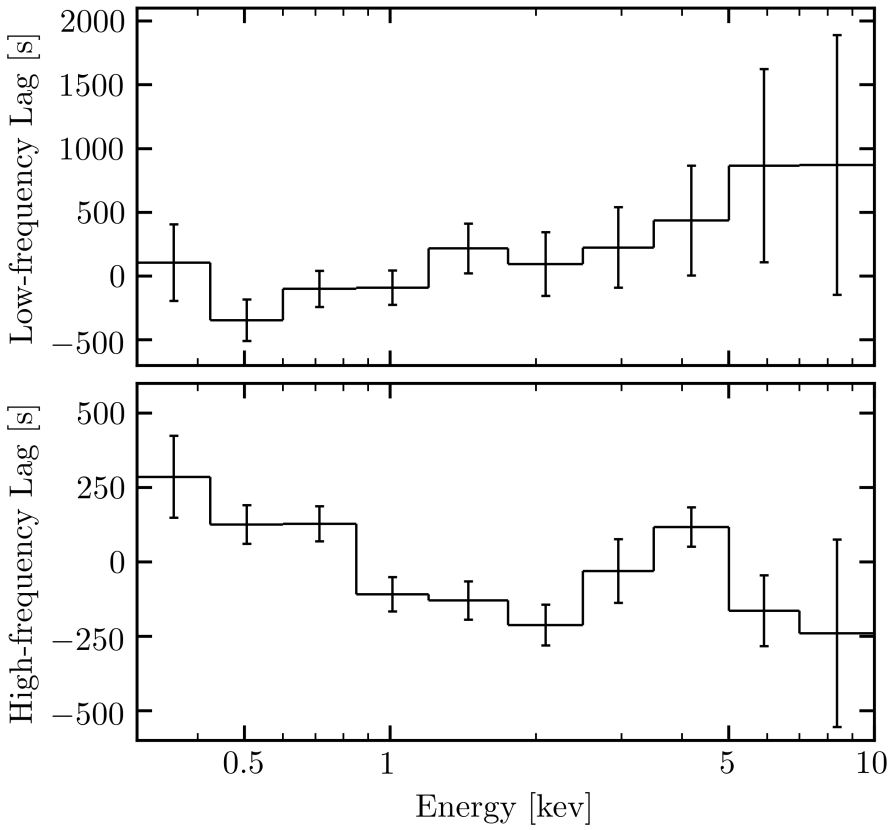

Figure 3.9: The combined low-frequency $(4.66 - 12.8) \times 10^{-5}$ Hz (top panel) and high-frequency $(1.72 - 3.51) \times 10^{-4}$ Hz (bottom panel) lag-energy spectra using 200 s binned light curves with $0.3 - 10$ keV as the reference band.

approximately equally sampled log-energy-space. For each energy band we subtracted the band-of-interest light curve (i.e. those bound by the energy bin edges) from the reference broad band light curve ($0.3 - 10$ keV) and computed the cross-spectrum between the two. We then averaged the cross-spectrum in the desired frequency band over the two 2014 observations. With this single cross-spectrum we then computed the lag between the band-of-interest and reference band in the desired frequency range. The resultant low- and high-frequency lag-energy spectra are shown in Figure 3.9. It is important to keep in mind that

in these lag-energy plots the lag value on the y-axis is not important, rather, the separation between data points is the quantity of interest. This is due to the zero-point being arbitrary as the lag value depends on the dominant spectral component over the broad band which itself is defined differently at each data point due to the aforementioned band-of-interest subtraction.

The low-frequency lag-energy spectrum presents a shape attributed to the propagation of mass accretion rate changes in the disc through the corona (Lyubarskii 1997; Kotov et al. 2001; Arévalo & Uttley 2006). In this scenario the outer, low-energy regions of the corona receive these fluctuations before the inner, high-energy regions, thus explaining the observed approximately log-linear relation. Our defined low-frequency band does include two lag values consistent with zero, however, when restricting the analysis to the single bin with a strictly positive lag we retrieved the same lag-energy spectral shape with larger errors.

The high-frequency lag-energy spectrum presents a shape attributed to X-ray reflection, where the reflected emission (i.e. soft excess at < 2 keV and relativistically broadened Fe K at $4-7$ keV) changes after the coronal emission (i.e power-law at $2-4$ keV), hence explaining the large lags at < 1 keV and $3 - 5$ keV and minimal lags at ~ 2 keV. Notable is the fact that $5 - 7$ keV, which contains the Fe Kα emission complex, does not show an increased lag relative to $3.5 - 5$ keV, rather it is significantly decreased. This perhaps suggests that we are not sampling long enough time-scales to observe reverberation of the Fe Kα emission. Indeed reducing our high-frequency range to lower frequencies finds a corresponding slight increase in the $5 - 7$ keV lag, though a peak in this energy band is never found, thus we

present only the wide frequency-band results. This peculiar aspect of the high-frequency lag-energy spectrum is also observed in IRAS 13224−3809 (Kara et al. 2016). Given the interpretation of the high-frequency lag-energy spectrum we are therefore motivated to test a reflection model in our spectral analysis based on this model-independent timing analysis result.

We note that our combined-epoch lag results are consistent with those presented in Kara et al. (2016), wherein the reverberation lag in this source was first reported.

Lastly, we calculated the low- and high-frequency (absolute) covariance spectra, which are useful in determining the shape of variable spectral component(s). This was done by using essentially the same base procedure as the lag-energy analysis, making use of the same light curves in the same energy bands with $0.3 - 10$ keV as the reference band. Instead of computing the lags from the cross-spectrum we calculated the covariance as in Uttley et al. (2014). The results are shown in Figure 3.10 where both the low- and high-frequency spectra display similar shapes, which suggests a similar varying component across a broad range of time-scales. The shape itself may be interpreted as that resulting from a variable power-law, where the multiple absorption effects impacting this source act to reduce the observed power-law emission in the low-energy regime while at higher energies the natural fall-off of the power-law produces a similar effect in the covariance spectra. We note tentatively here that the low-frequency spectrum appears peaked toward lower energies than the high-frequency spectrum, suggesting a softer power-law varying on longer timescales than a secondary harder power-law that varies more rapidly. We revisit this in Section 3.4 where we explore the broad band spectral properties.

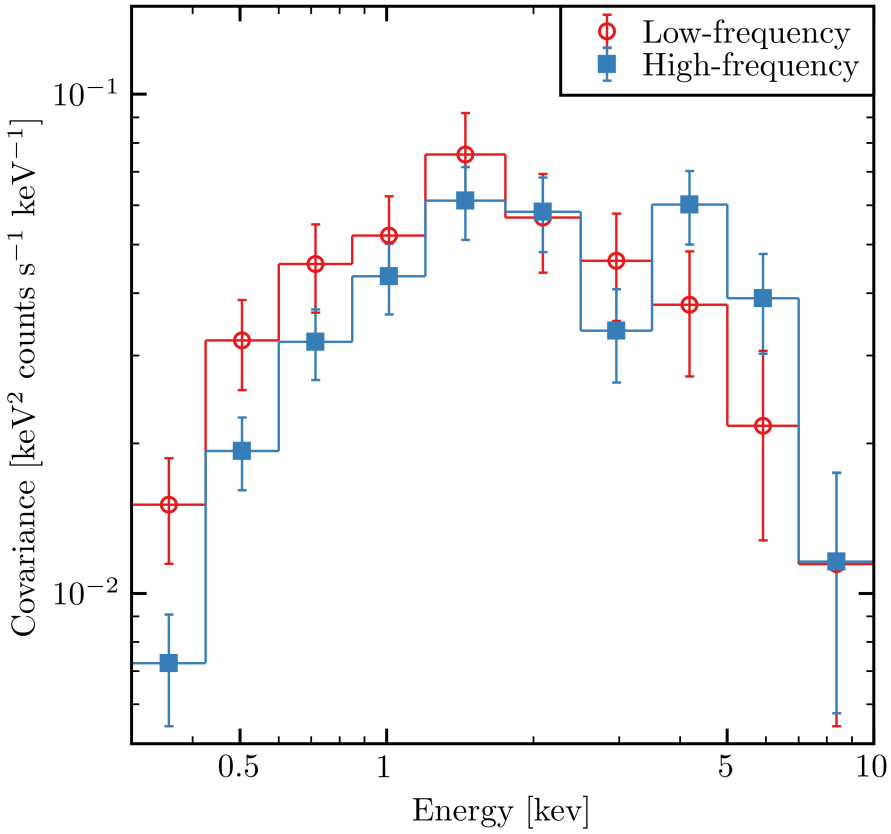

Figure 3.10: The combined low-frequency $(4.66 - 12.8) \times 10^{-5}$ Hz (red open circles) and high-frequency $(1.72 - 3.51) \times 10^{-4}$ Hz (blue filled squares) absolute covariance spectra using 200 s binned light curves with $0.3 - 10$ keV as the reference band. We plot these spectra in $EF_{\rm E}$ units in order to directly compare the covariance shape to spectral component shapes.

3.3.2.2 Time-resolved analysis

Motivated by the unique behaviour of 2014.301, especially during 2014.301a, we extracted the frequency-space timing products in a time-resolved manner analysing differences between 2014.101, 2014.301a, and 2014.301b. This required splitting each 2014 observation into 40 ks segments, reducing the light curve length by half which therefore means that we were unable to probe the low-frequency band and were restricted to analysing only the high-

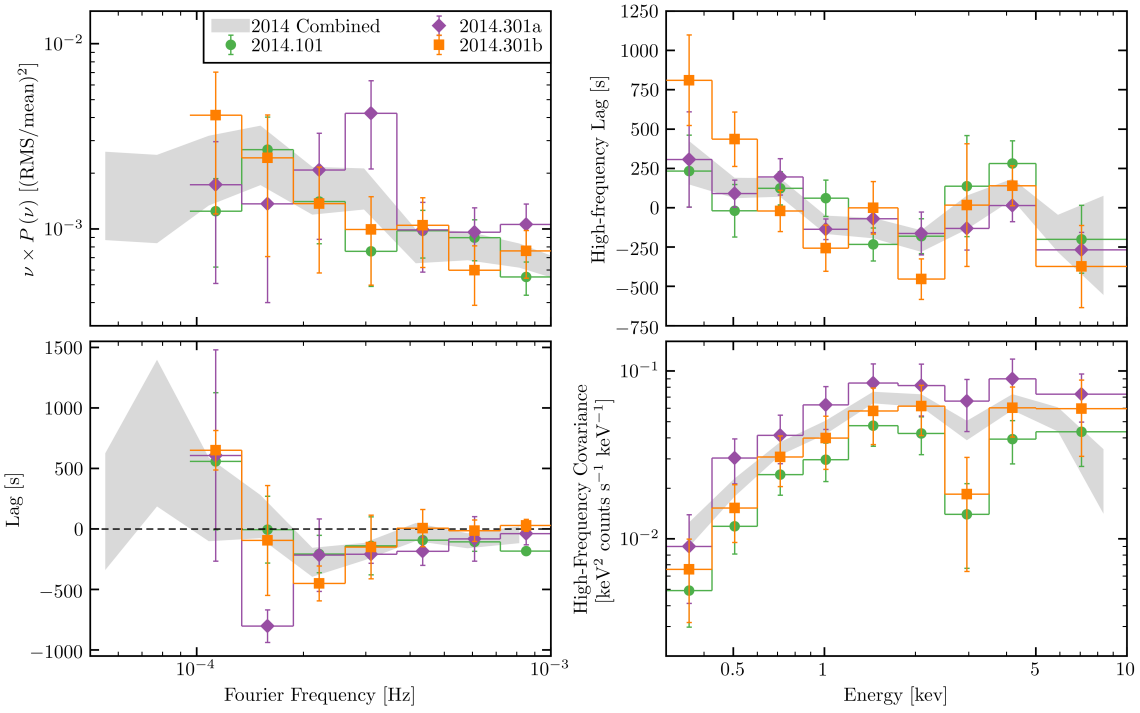

Figure 3.11: *Top left* – PSDs for 2014.101 (green circles), 2014.301a (purple diamonds), and 2014.301b (orange squares). *Bottom left* – Lag-frequency spectra for the same epochs in the left panel. *Top right* – High-frequency $(1.79 - 3.51) \times 10^{-4}$ Hz lag-energy spectra for same three epochs as other panels. *Bottom right* – Absolute covariance spectra extracted from the same high-frequency band as the lag-energy spectra for the same three epochs as in the other panels, plotted in $EF_{\rm E}$ units. The grey filled region in each panel displays relevant quantity obtained when combining the 2014 data sets.

frequency regime. We combined both segments of 2014.101 in order to reduce clutter in the figures, taking note that all following analyses found that both segments of 2014.101 behaved similarly. Frequency products were binned in frequency-space using a geometric binning factor of 1.4. We note that the two highest energy bins in the combined analysis were merged here as individually they returned very large errors on the computed quantities.

We started by computing broad band $0.3 - 10$ keV PSDs for the three epochs, shown in the top left panel of Figure 3.11. The PSD shapes for all epochs are quite similar, with the

exception of the bin centred at $\sim 3 \times 10^{-4}$ Hz, for which 2014.301a displays increased power. Evaluating the significance of this deviation found it to be statistically insignificant when fitting the raw PSDs and comparing parameters, which is perhaps not surprising given that the differences between the PSDs do not exceed the 2σ level. We also computed the ratio between the 2014.301a epoch and the other two, which did not find the deviations seen in Figure 3.11 to be statistically significant, again likely owing to the large error bars.

Next we computed the lag-frequency spectra, applying the same methodology described in the previous section, which are shown in the bottom left panel of Figure 3.11. All three epochs exhibit negative lags in the $(2-4) \times 10^{-4}$ Hz band, which agrees with the combined analysis results. Interestingly, 2014.301a exhibits a larger negative lag at a lower frequency than any other epoch, suggesting a marked change in the behaviour of the source during this epoch, although the change does not exceed the 2σ level. We note that this observed change in the shape of the lag-frequency spectrum is reminiscent of the results presented by Alston et al. (2020), where ~ 2 Ms of data on the RQ-NLS1 IRAS 13224−3809 were used to map a moving corona. The results here may therefore suggest a coronal height increase during the 2014.301a epoch. Other RQ-NLS1s such as I Zw 1 (Wilkins et al. 2017) and Mrk 335 (Wilkins & Gallo 2015a) have also shown evidence of moving coronae in the context of failed jet launching scenarios. Alternative interpretations for this result are unclear as the frequency at which reverberation lags are detected is thought to be governed by $M_{\rm BH}$ in systems where X-ray reflection is substantial.

The lag-energy spectra were extracted from the same $(1.79-3.51) \times 10^{-4}$ Hz band as in the combined analysis, and are shown in the top right panel of Figure 3.11. All three epochs

exhibit spectra closely resembling the combined result across the entire energy range. We note, however, a slight shape change in the spectral shape over time. In 2014.101 similar lags for energies $\lesssim 1$ keV and $3.5-5$ keV are found. If we interpret the high-frequency lag-energy spectrum as a signature of reverberation this suggests that the emission in these two energy-bands originate at similar distances from the hard X-ray corona, which leads the reverberated emission. In 2014.301b the low-energy lag is significantly increased relative to the high-energy lag. Indeed by taking $\Delta\tau = \tau_{0.3-0.85} - \tau_{2.5-5}$ we find that $\Delta\tau_{2014.101} = 0 \pm 203$, $\Delta\tau_{2014.301a} = 257 \pm 141$, and $\Delta\tau_{2014.301b} = 330 \pm 120$ indicating a significant change in the time delay between these two energy bands.

Absolute covariance spectra were also constructed for each epoch using the same high-frequency range as the lag-energy, with the results shown in the bottom right panel of Figure 3.11. All three epochs exhibit the same shape as the combined high-frequency result, indicating the same spectral component is varying in each epoch but with different levels of variability, where in fact the normalisations of the spectra mimic the fraction variability results in column (3) of Table 3.2. We note that the only source of deviation in shape between the epochs is in the bin centred at ~ 3 keV, which exhibits increased levels of variability in 2014.301a. As aforementioned the shape of these covariance spectra suggest a straight-forward explanation to the hardness ratio dip observed in 2014.301a as the simple variability of the power-law component.

3.4 Spectral Analysis

All spectral fitting was done using XSPEC version 12.10.0c (Arnaud 1996) and all spectra were grouped using the HEASOFT task FTGROUPPHA with the GROUPTYPE=OPT flag to bin the spectra as described in Kaastra & Bleeker (2016). We evaluate the goodness-of-fit of our models by following the method of Kaastra (2017) making use of Cash (C) statistics (Cash 1979) to evaluate model likelihoods. In order to make proper use of C-statistics we are required to use the total (i.e. source plus background) spectrum in each epoch, which differs from the commonly used background-subtracted spectral modelling approach. To do this we simultaneously modelled the total and background spectra[5], which allowed for the contribution of the background emission to be 'modelled-out' of the total spectrum. The fits presented in this section were therefore performed by fitting the five total and five background spectra, linking the total and background spectra for each epoch.

3.4.1 Modelling the broad band continuum

When performing our spectral fits we first fit the background spectra, starting off with each being fit by a broken power-law. This was found to be insufficient in describing the overall shape of the background spectra, requiring the addition of known instrumental emission and absorption features of the EPIC pn detector at corresponding energies using the GAUSS model. The background extraction region in each epoch was not found to contain any other X-ray sources and thus we do not add any other components to account for the background

[5]We followed the guide to source and background modelling at https://heasarc.gsfc.nasa.gov/xanadu/xspec/manual/node40.html

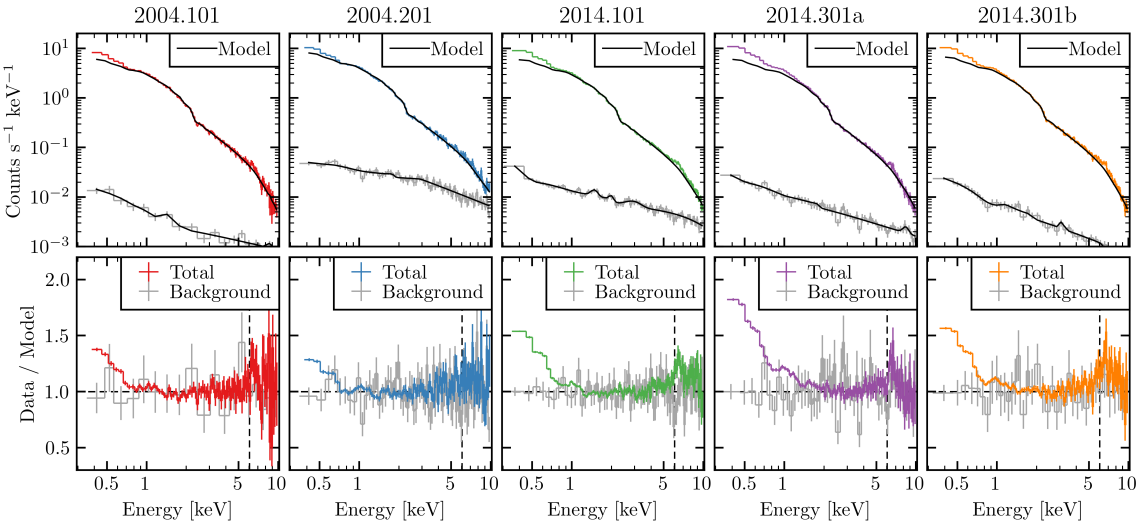

Figure 3.12: *Top row* − Coloured (grey) curves are the total (background) spectrum in each epoch with the solid black lines denoting the absorbed power-law ($\Gamma = 2.35 \pm 0.03$) fit over $2-4$ keV (full broad band background model, see text for details). *Bottom row* − Coloured (grey) curves denote the ratio residuals of the total (background) spectrum in each epoch when divided by the model displayed in the top row of the corresponding column. Vertical lines in each bottom panel denote the observed frame Fe Kα emission line energy, which has a rest frame energy of 6.4 keV.

emission. After accounting for the continuum shape and instrumental features the fit quality to the background was sufficiently good (i.e. additional components did not improve the fit in a statistically significant way) such that we froze all background model parameters to the fitted values found in this step for the remainder of the spectral modelling. We do not present the background model parameters here, though the fits are presented in Figure 3.12 alongside the total spectrum fits.

After an adequate background model was obtained for each epoch the total spectra were then fit by including the background components in addition to the desired source model components. We initially modelled the continuum by fitting the $2-4$ keV band with an absorbed power-law using the CUTOFFPL model, accounting for Galactic absorption

along our line of sight with TBABS. However, this source is known to have significant warm absorption (Leighly et al. 1997; Longinotti et al. 2015; Sanfrutos et al. 2018) that is accounted for here by using the XSPEC implementation of the SPEX (Kaastra et al. 1996) model XABS (Steenbrugge et al. 2003) provided by Parker et al. (in prep.). We inserted the warm absorbers in order of significance according to Sanfrutos et al. (2018), finding that beyond three components the fit did not improve significantly. We initially kept the warm absorber parameters (i.e. column density, ionisation parameter, turbulent velocity, and outflow/inflow velocity) fixed to the values derived in Sanfrutos et al. (2018). Due to the flux variability observed throughout Section 3.3 we left each power-law model component to have a free to vary normalisation, while linking the photon index across the epochs and freezing the cut-off energy at $E_{\rm cut} = 300$ keV (all fits were found to be insensitive to this parameter). We found a photon index of $\Gamma = 2.35 \pm 0.03$ and show the ratio residuals (i.e. data divided by the model residuals) for this fit in Figure 3.12 where we extrapolate across the broad $0.3 - 10$ keV band.

All five spectra show evidence of a soft excess below ~ 1.5 keV, with the strength of this excess being variable over the observations on long and short time scales. Both 2004 epochs exhibit weaker soft excesses than either of the 2014 epochs, with 2014.301a displaying the strongest soft excess of any data set while 2014.101 and 2014.301b appear intermediate. The excess emission observed around the Fe K emission complex at $6 - 7$ keV appears persistent on long and short time scales, though 2004.201 does not visually reveal its presence due to lower spectral quality.

In the following, we outline the approach and motivation for allowing certain spectral

parameters to be free to vary during the fitting procedure. The final model, with parameter values and 90 per cent confidence intervals, are reported in Table 3.5.

Based on the reverberation evidence obtained from Section 3.3 and the signatures presented in the residuals (i.e. soft excess and broad Fe K emission) we were motivated to fit our data with an additional reflection component. We used RELXILLD version 1.2.0 (García et al. 2014) to account for relativistically blurred emission originating from the highly ionised inner accretion disc region, with an initial parameter setup as follows. The emissivity profile of the disc (approximated as a once-broken power-law in RELIXLLD) was set such that the inner index $q_{\rm in}$ was free to vary while the break radius was frozen at $R_{\rm break} = 6\ r_g$ (i.e. the innermost stable circular orbit (ISCO) of a Schwarzschild black hole), where $r_g = GM/c^2$, and the outer index was frozen at $q_{\rm out} = 3$. We froze the black hole spin at $a = 0.998$, freezing the inner disc radius at $R_{\rm in} = R_{\rm ISCO,0.998} = 1.235\ r_g$ and the outer disc radius at $R_{\rm out} = 400\ r_g$. The iron abundance and disc density were initially frozen at $A_{\rm Fe} = 1$ and $\log N = 15$ cm^{-3}, respectively. The remaining RELXILLD parameters of disc inclination i and ionisation parameter $\log \xi$ were left free to vary. We allowed the flux of the power-law and reflection components to be free to vary between epochs, with all other parameters linked across all epochs, and used the power-law model as the emission source illuminating the accretion disc (i.e. $\Gamma_{\rm RELXILLD} = \Gamma_{\rm CUTOFFPL}$). The resulting fit returned $C = 1761$ for $dof = 893$ and presented significant residuals around the Fe K emission complex and higher energies, while the soft excess was well accounted for.

The evidence from Section 3.3 indicates a significant spectral state change during 2014.301a and thus we allowed Γ to be free to vary in this epoch only, returning $\Delta C = -329$ for 1

additional free parameter. The photon index for 2014.301a at this stage in the fitting procedure is significantly softer than the average. Taking into account the global hardness ratio variations of ~ 20 per cent we then tested allowing Γ to be free to vary in all epochs, returning $\Delta C = -127$ for 3 additional free parameters. Epoch 2014.301a maintained the softest power-law, with the other epochs displaying similar photon index values. This intermediate model provides a mediocre fit to the data with a relatively simple explanation for the spectral variability.

Accretion disc density has recently been shown to be anti-correlated with $M_{\rm BH}$, with low-mass systems such as NLS1s more frequently exhibiting $\log N > 15$ cm^{-3} (Jiang et al. 2019). We first tested for the possibility of non-solar iron abundance in our data by allowing $A_{\rm Fe}$ to be free to vary, finding a best-fit value consistent with a solar abundance while not providing a significant fit improvement. Due to this we kept $A_{\rm Fe} = 1$ frozen throughout the remainder of the spectral fitting. To test for the presence of a high-density disc we allowed $\log N$ to be free to vary, returning $\Delta C = -130$ for 1 additional free parameter. The disc density found by this fit is significantly higher than the standard accretion disc density, falling in line with other high-density discs found in NLS1s.

Truncated accretion discs with $R_{\rm in} > R_{\rm ISCO}$ have been suggested in RL AGN wherein the inner part of disc becomes unstable and subsequently is ejected along the jet resulting in a radio flare and truncated disc (e.g. Lohfink et al. 2013). Here we tested for inner disc truncation by allowing $R_{\rm in}$ to be free to vary, returning $\Delta C = -10$ for 1 additional free parameter. This fit does not find a significantly truncated disc, only being $\sim 1\ r_g$ beyond the ISCO of a maximally spinning Kerr black hole of, though the improvement is substantial.

We also tested the impact of a free to vary break radius in the once-broken emissivity profile of the disc. This parameter was found to modestly improve the fit quality returning $\Delta C = -5$ for 1 additional free parameter and produced comparable values for the other free parameters as when it was fixed. We therefore kept the value fixed at $R_{\rm break} = 6\ r_g$ for the remainder of the spectral modelling. Black hole spin was also set to be free to vary, though we found no significant fit improvements in doing so and therefore keep it fixed at $a = 0.998$ for the remainder of the spectral modelling.

We have only reported detailed results for the reflection scenario, although several alternative models based on other physical scenarios were also tested for their ability to describe the data. Our best-fit model using the reflection scenario so far was found to have $C/dof = 1165/887$. In RL sources the contribution to the X-ray spectrum by the radio jet may be modelled via a double power-law continuum, wherein the X-ray corona is responsible for producing the softer power-law while the harder power-law is representative of the jet emission. We therefore applied a double power-law model here but found it to be a poor fit with $C/dof = 1475/887$. We also tried a soft-Comptonisation model using COMPTT (Titarchuk 1994) wherein the soft excess can be explained by an optically thick 'warm' corona while the high energy emission is due to the standard hot corona, a scenario that has been successfully applied to RQ sources (e.g. Petrucci et al. 2018). We found, however, that such a model was also substantially worse than the reflection scenario returning a best fit of $C/dof = 1392/889$. We do not report any of the parameters of these alternative models as they were found to be statistically worse fits to the data.

3.4.2 Iron emission features

All of the fits discussed up to this point have had significant excess residuals present in the Fe K emission complex around $6-7$ keV, despite this region having already been treated by the reflection component in our model. In order to account for the poorly fit feature(s) present in this region we tested two cases: (i) a series of intrinsically narrow emission features to emulate Fe I, XVII, XVII emission features, and (ii) a single broad Fe K emission feature. We found that in case (i) by inserting lines at 6.4, 6.7, and 6.97 keV using the ZGAUSS model with narrow widths of $\sigma = 10$ eV and free to vary normalisation linked across all epochs the fit returned $\Delta C = -84$ for 3 additional free parameters. Notably, line normalisation increased with line energy, perhaps suggesting that a single broad, asymmetric line profile would be a more fitting description. Nevertheless, we also tested accounting for the potentially narrow emission features with the presence of an additional reflection component originating at much larger distances, emulating outer disc / toroidal emission, via the XILLVER (García & Kallman 2010) model, though we found no significant fit improvement in doing so. For case (ii) we inserted a broad line with free to vary energy, width, and normalisation that were linked across all epochs. This fit returned $\Delta C = -130$ for 3 additional free parameters, providing a significantly better description of the Fe K emission region than the three narrow lines and returning a line energy of $E \approx 6.8$ keV and line width of $\sigma \approx 0.5$ keV. Evaluating the ratio residuals produced by this broad line, however, revealed that the symmetric nature of the Gaussian profile over-estimated the the low-energy side of the line.

The evidence for an asymmetric line profile, which indicates relativistically broadened

line emission, prompted the use of the LAOR model. We allowed the line energy, emissivity index, and inner radius of the disc to be free to vary, linking the outer disc radius and disc inclination to the corresponding RELXILLD parameters. Upon fitting the spectra it was found that the emissivity index was not statistically differentiable from $q = 3$, and thus this parameter was kept fixed to that value. The resulting fit returned $\Delta C = -130$ for 3 additional free parameters, thus being equivalent to a single broad Gaussian, with much of the asymmetry in those residuals eliminated. We tested allowing the energy and normalisation of the line to be free to vary between the epochs, but found no significant improvements to the fit when doing so and therefore kept these parameters linked across all epochs. We report the results obtained using the LAOR model though there was no statistical benefit in using this emission line model over, for example, the DISKLINE model which returned similar parameter values.

With the fit described so far we noted the presence of significant residuals at ~ 1 keV in all of the spectra. The cause for such deviations from the model may have been due to either (i) the presence of excess Fe L emission or (ii) improperly modelled warm absorption due unknown RGS to EPIC pn cross calibration. We first tested case (i) by inserting a second LAOR component at ~ 1 keV with free to vary energy and normalisation, each linked across all epochs, linking all other parameters to those of the Fe K feature found above, resulting in $\Delta C = -68$ for 2 additional free parameters. The fit is significantly improved in this energy band with the addition of this Fe L feature, though some significant residuals are still present. Testing case (ii) did not require a second emission feature but instead we allowed the column density and ionisation parameter of each of the three warm absorbers

to be free to vary, which resulted in $\Delta C = -132$ for 6 additional free parameters. This significantly improved the residuals across the entire low-energy band. We considered it possible, however, that a truly present Fe L feature has now been washed out artificially by the free warm absorbers. To test this we combined both cases (i) and (ii) by inserting an Fe L feature using a LAOR component while simultaneously allowing the warm absorbers to each have free to vary column density and ionisation parameter, returning $\Delta C = -164$ for 8 additional free parameters. The evidence presented here suggests that Fe L may in fact be present in the spectra, although the warm absorbers produce a significantly greater impact on the fit quality and account for the majority of the deviations from the model.

3.4.3 The final fit

We therefore arrived at two best-fit models, one in which low-energy deviations are accounted for by allowing the warm absorber parameters to be free to vary and one in which excess Fe L emission is present. In order to evaluate the goodness-of-fit for each scenario we used the method presented in Kaastra (2017), computing the expected C-statistic and its variance ($C_{\rm E}$, $C_{\rm V}$), where we found that ($C_{\rm E}$, $C_{\rm V}$) = (907 ± 13.5) for the 10 simultaneously fit spectra. The excess Fe L emission scenario resulted in $C = 871$ for 876 degrees of freedom, while the free to vary warm absorber model returned $C = 900$ for 878 degrees of freedom. Comparing these to the expected C-statistic and its variance finds that the inclusion of Fe L emission can be rejected at a 2σ level, whereas the varying warm absorber model cannot be rejected even at the 1σ level. We report this final best-fit model and its parameters in Table 3.5, with the ratio residuals shown in Figure 3.13.

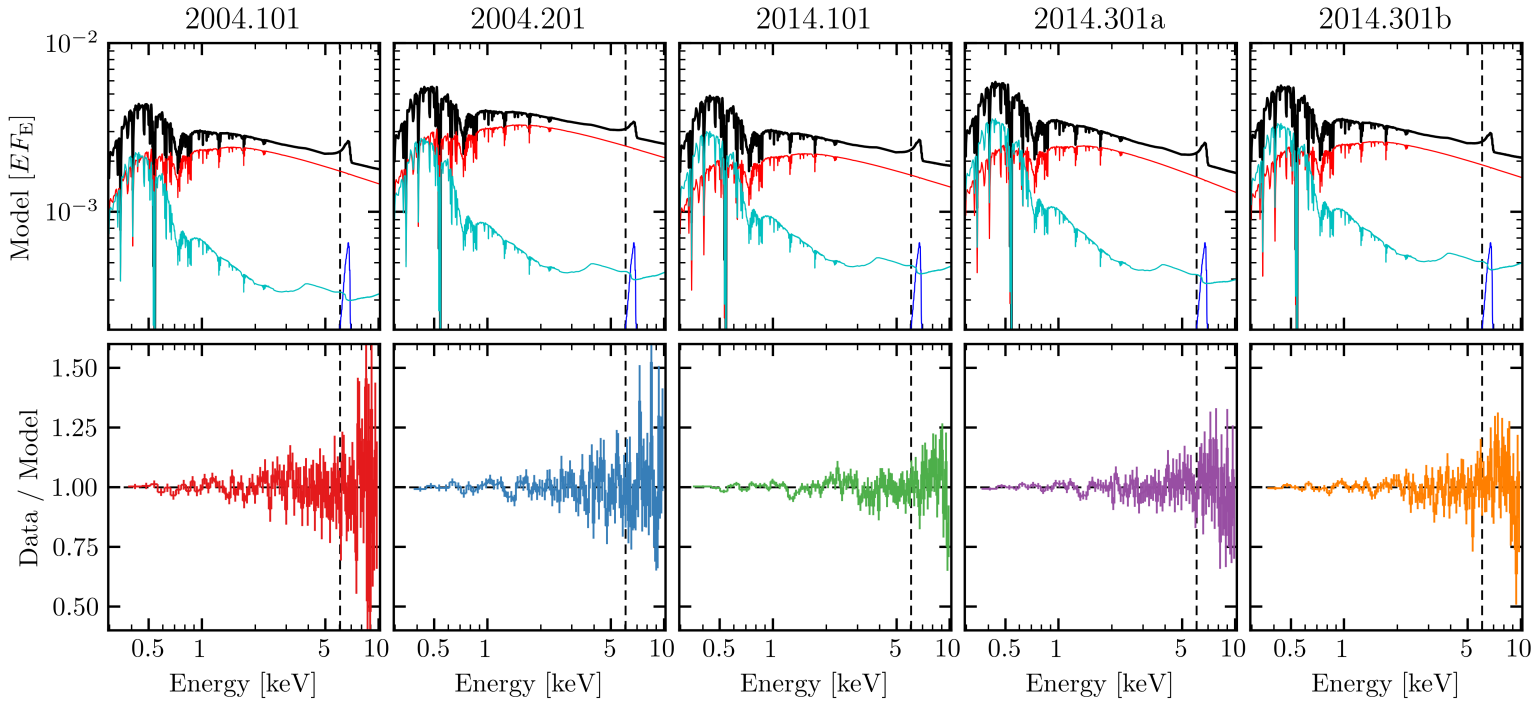

Figure 3.13: *Top row* – Total model (black) and model components: power-law (red), reflection (cyan), and broad Fe emission line (blue). The curves are plotted in EF_E units of keV^2 photons cm^{-2} s^{-1} keV^{-1}. *Bottom row* – Coloured (grey) curves denote the ratio residuals of the total (background) spectrum in each epoch when divided by the model displayed in the top row of the corresponding column. Vertical lines in each panel denote the observed frame Fe Kα emission line energy, which has a rest frame energy of 6.4 keV.

Table 3.5: Fit parameters and errors (i.e. 90 per cent confidence intervals) for the final reflection model. Parameters flagged with a ^{f} were kept frozen to the listed value and those flagged with a ^{l} were kept linked to the indicated parameter throughout the fitting procedure.

Model Component	Parameter	Fit Value				
		2004.101	2004.201	2014.101	2014.301a	2014.301b
TBABS	$N_{\rm H}/10^{20}$ cm^{-2}			2.20^f		
XABS1	$N_{\rm H}/10^{20}$ cm^{-2}			13^{+1}_{-2}		
	$\log(\xi/\mathrm{erg\ cm\ s^{-1}})$			1.50 ± 0.07		
	$v_{\rm turb}$/km s^{-1}			60^f		
	$v_{\rm outflow}$/km s^{-1}			140^f		
	z			0.0604^f		
XABS2	$N_{\rm H}/10^{20}$ cm^{-2}			$10^{+0.9}_{-1.6}$		
	$\log(\xi/\mathrm{erg\ cm\ s^{-1}})$			0.9 ± 0.1		
	$v_{\rm turb}$/km s^{-1}			1000^f		
	$v_{\rm outflow}$/km s^{-1}			110^f		
	z			0.0604^f		
XABS3	$N_{\rm H}/10^{20}$ cm^{-2}			$6.6^{+1.6}_{-2.5}$		
	$\log(\xi/\mathrm{erg\ cm\ s^{-1}})$			< -1.8		

	$v_{\rm turb}$/km s^{-1}			110^f		
	$v_{\rm outflow}$/km s^{-1}			140^f		
	z			0.0604^f		
CFLUX1	$E_{\rm min}$/keV			0.1^f		
	$E_{\rm max}$/keV			100^f		
	$\log\left(F/\text{erg cm}^{-2}\text{ s}^{-1}\right)$	-10.54 ± 0.02	$-10.41^{+0.01}_{-0.02}$	-10.58 ± 0.02	-10.51 ± 0.02	-10.51 ± 0.02
CUTOFFPL	Γ	2.32 ± 0.02	2.29 ± 0.02	2.30 ± 0.02	2.39 ± 0.02	2.31 ± 0.02
	$E_{\rm cut}$/keV			300^f		
CONST	R	$0.49^{+0.15}_{-0.09}$	$0.45^{+0.14}_{-0.08}$	0.73 ± 0.20	$0.72^{+0.20}_{-0.15}$	$0.68^{+0.20}_{-0.13}$
CFLUX2	$E_{\rm min}$/keV			$E^l_{\rm min,\ CFLUX1}$		
	$E_{\rm max}$/keV			$E^l_{\rm max,\ CFLUX1}$		
	$\log\left(F/\text{erg cm}^{-2}\text{ s}^{-1}\right)$			$\log F^l_{\rm CFLUX1}$		
RELXILLD	$q_{\rm in}$			$7.0^{+0.6}_{-0.2}$		
	$q_{\rm out}$			3^f		
	$R_{\rm break}/r_g$			6^f		
	a			0.998^f		
	$i/^\circ$			24^{+3}_{-4}		
	$R_{\rm in}/r_g$			$2.5^{+0.4}_{-0.2}$		

	$R_{\rm out}/r_g$	400^f
	z	0.0604^f
	Γ	$\Gamma^l_{\rm CUTOFFPL}$
	$\log\left(\xi/\mathrm{erg\ cm\ s^{-1}}\right)$	$2.71^{+0.06}_{-0.01}$
	$A_{\rm Fe}$	1^f
	$\log N/\ \mathrm{cm^{-3}}$	> 18.9
ZASHIFT	z	0.0604^f
LAOR	$E_{\rm rest}/\mathrm{keV}$	7.1 ± 0.1
	q	3^f
	$R_{\rm in}/r_g$	10^{+10}_{-4}
	$R_{\rm out}/r_g$	$R^l_{\rm out,\ RELXILLD}$
	$i/^\circ$	$i^l_{\rm RELXILLD}$
	$N/10^{-5}$ photons $\mathrm{s^{-1}\ cm^{-2}}$	1.3 ± 0.3

Despite achieving a statistically acceptable fit to the data, significant high-energy residuals remain throughout the epochs. Especially notable are the residuals in the 2014 epochs, which all show slight excesses at ~ 8 keV before decreasing toward higher energies. Strong emission features that would account for this curvature are not known, and were therefore not explored. Blue-shifted Fe K absorption features at energies > 7.1 keV have been reported in numerous AGN (e.g. Tombesi et al. 2010; Gofford et al. 2013; Igo et al. 2020), and indeed evidence of ultra-fast outflows from other RGS based analyses (Longinotti et al. 2015; Sanfrutos et al. 2018) having already been detected in this source with velocities of $\sim 0.05 - 0.1c$. Longinotti et al. (2015) reported finding marginal evidence of blue-shifted Fe K absorption that would correspond to an outflow of $\sim 0.3c$. We performed a search for such features in each epoch by stepping an inverted narrow (i.e. $\sigma = 10$ eV) Gaussian component between $7.1 - 10.5$ keV in the source frame, allowing energy and normalisation to be free to vary. We obtained similar absorption feature energies as Longinotti et al. (2015), though we found a statistically insignificant fit improvement for their inclusion ($\Delta C = -14$ for 10 additional free parameters) and therefore do not include them in the reported model.

The covariance spectra produced in Section 3.3 were then explored quantitatively by using the reported best-fit broad band spectral model. Covariance spectra for the low- and high-frequency combined analysis were loaded into XSPEC via the FTFLX2XSP tool after accounting for detector effective area in each energy band, and subsequently fit with the model in Table 3.5. During the fitting procedure we initially allowed only the normalisation of each component to be free to vary, which showed that the power-law component was sufficient on its own in fitting the the covariance spectra. This fit, however, was quite

poor ($\chi^2/dof \approx 1.5$) in describing both data sets and therefore we allowed the power-law photon index to be free to vary between the two frequency regimes, finding the data to be over fit ($\chi^2/dof \approx 0.7$) but with residuals significantly improved across all energies. The low-frequency data were best-fit by a power-law with $\Gamma = 2.37 \pm 0.12$ while the high-frequency data returned $\Gamma = 2.02 \pm 0.07$. This suggests a possible two-corona scenario where the harder power-law varies on shorter timescales, corresponding to a compact coronal structure, than a more slowly varying soft power-law, corresponding to a more extended geometry. The absence of a detected reflection component suggests that it may be varying on significantly longer timescales than those explored here. Fitting the time-resolved high-frequency covariance spectra returned the same hard power-law as the combined analysis, albeit with varying normalisations.

With this interesting result we attempted to fit our broad band data sets with a two-corona scenario by restricting the power-law photon indices to be within ± 10 per cent of the aforementioned values. Doing so found no statistically significant fit improvement when including the hard power-law from the high-frequency covariance fit, recovering only the soft power-law from the low-frequency covariance fit. Indeed this soft power-law agrees very well with the best-fit model presented in Table 3.5, suggesting it dominates the observed emission.

We note in Section 3.3 that the changing lag-frequency spectrum observed during the 2014.301a epoch may be interpreted as evidence of a moving corona, specifically an increase in height above the accretion disc. Ray-tracing simulations exploring accretion discs illuminated by compact coronal geometries predict a decrease in $q_{\rm in}$ for an increase in source

height (e.g. Wilkins & Fabian 2012; Gonzalez et al. 2017), however, we found no statistically significant fit improvement when allowing $q_{\rm in}$ for the 2014.301a epoch to be free to vary independently of the other epochs.

3.5 Discussion

In this work we have presented the first detailed timing and spectral analyses on the four *XMM-Newton* EPIC pn observations of the RL-NLS1 IRAS 17020+4544. We have found that the source flux varies by $\sim$ 35 per cent and the hardness ratio by $\sim$ 20 per cent over the 10 yr period spanned by the observations. We note that the flux levels reported here in Table 3.3 are essentially unchanged from those measured by Leighly (1999a) using *ASCA* data from 1995, revealing low levels of long-term variability over $\sim$ 20 yr. These characteristics are not extreme when compared to other NLS1s, such as Mrk 335 (Gallo et al. 2018) and IRAS 13224−3809 (Alston et al. 2019), which have been shown to exhibit significant short- and long-term variability. The first 40 ks of the second 2014 observation were found to be significantly softer than at any other time, prompting the segmentation of this observation into two epochs in which separate timing and spectral analyses were performed in an effort to uncover the cause of such a spectral state change.

Further abnormalities were found in the behaviour of IRAS 17020+4544 with respect to its variability properties when compared to the bulk of its RQ-NLS1 counterparts, displaying a 'harder-when-brighter' trend rather than 'softer-when-brighter', increasing fractional variability with energy rather than being peaked at low energies or flat, and a possible

non-stationary process evident only at low energies. The 'harder-when-brighter' trend observed here is similar to the trends observed in I Zw 1 (RQ-NLS1; Gallo et al. 2004, 2007) and IRAS 16318−472 (RL-NLS1; Mallick et al. 2016), where the authors also reported similar trends of increasing fractional variability with energy in both sources, leading to a suggested variable power-law in both photon index and normalisation to explain the variability in those objects. Our flux-flux analysis of the various observation epochs of IRAS 17020+4544 agrees with this simple variable power-law explanation. We note, however, that the observed 'harder-when-brighter' trend is generally more often observed in blazars (e.g. Bhatta et al. 2018; Singh et al. 2019; Zhang et al. 2019), particularly during flaring episodes, than in Seyfert-type AGN. Since IRAS 17020+4544 and IRAS 16318−472 are both jetted sources it is plausible that the jet emission is influencing and/or connected to the X-ray emission. Indeed an aborted jet scenario was proposed for I Zw 1 (Gallo et al. 2007; Wilkins et al. 2017) wherein flaring of the hard X-ray corona was best explained as an episode of vertical collimation and outflow, which may be interpreted as the X-ray corona acting as the base of a jet. Moreover, Foschini et al. (2015) found that when normalising by black hole mass the jet properties of RL-NLS1s aligned well with those of flat-spectrum radio quasars (FSRQs) and BL Lac objects, appearing to be the low-power tail of the more powerful, higher black hole mass blazar-type sources.

Frequency-domain methods applied to the light curves revealed many similarities with other RQ-NLS1s, with the PSD here being well fit by a simple power-law description, though no break frequency could be constrained, and the lag-frequency spectra exhibiting a strong high-frequency reverberation signature, providing evidence of X-ray reflection

that is frequently found in other NLS1s (e.g. Zoghbi et al. 2010; Kara et al. 2016). Using this high-frequency reverberation lag we estimated the mass of the SMBH in IRAS 17020+4544 using the relationships derived in De Marco et al. (2013) relating the frequency of the reverberation lag and the absolute value of the reverberation lag to the black hole mass. The lag-frequency spectrum in Figure 3.8 has a clearly defined negative lag at $(\nu,\ |\tau|) = \left(2.12 \times 10^{-4}\ \text{Hz},\ 270\ \text{s}\right)$, allowing for the black hole mass estimation to be performed using the aforementioned $\nu - M_{\rm BH}$ and $|\tau| - M_{\rm BH}$ relations, finding $2.34 \times 10^7\ M_\odot$ and $5.82 \times 10^7\ M_\odot$, respectively. Previous $M_{\rm BH}$ estimates for IRAS 17020+4544 have been as low as $3.1 \times 10^6\ M_\odot$ (Berton et al. 2015) to as high as $5.4 \times 10^7 M_\odot$ (Berton et al. 2016), with Nikołajuk et al. (2009) finding $1.08 \times 10^7\ M_\odot$. Our estimates here therefore broadly agree with the high-mass estimates of previous studies, which themselves are typical mass estimates for NLS1s, usually on the order of a few $\times 10^7\ M_\odot$ (e.g. Berton et al. 2015). We then used the empirical relationship derived by McHardy et al. (2006) between bolometric luminosity and black hole mass to estimate the PSD break frequency. The mean of our mass estimates calculated here via the combined lag-frequency spectrum is $M_{\rm BH} = 4.08 \times 10^7\ M_\odot$. Using the LUMIN function in XSPEC on our best-fit spectral model we found $L_{2-10} = 5.84 \times 10^{43}$ erg s^{-1}. Duras et al. (2020) recently reported bolometric corrections to the X-ray luminosity including those based on $M_{\rm BH}$, which can be used to estimate this value as $L_{\rm bol} = 16.86 \times L_{2-10} = 9.85 \times 10^{44}$ erg s^{-1}. These quantities provide an estimated PSD break frequency of $\nu_{\rm break} \approx 9.43 \times 10^{-6}$ Hz, which is below the lowest sampled frequency available with these data, explaining why we were unable to properly constrain this parameter during the attempted bending power-law fits.

The timing analysis results provided strong evidence of a variable power-law spectral component in the presence of some reflection component, motivating the use of such a two-component model in the spectral modelling. We found the five epochs to be best-fit by a scenario in which the power-law component was variable in both normalisation and photon index across all epochs, with its emission being reflected off of a highly ionised, high density accretion disc truncated just outside the ISCO of a maximally spinning Kerr black hole. Excess residuals were still present in the Fe K and Fe L energy bands, with the broad Fe K emission feature being well fit by a Gaussian feature with similar parameters to those measured by Leighly (1999b) using *ASCA* data from 1995, revealing a persistent, broad Fe K emission line. When fitting this feature with a Gaussian line profile we found $E \approx 6.8$ keV and $\sigma \approx 0.5$ keV, translating into a FWHM of $v \approx 50,000$ km s^{-1}, which would correspond to $r = GM/v^2 \approx 35\ r_g$ assuming that the emission is produced by an accretion disc 'hot-spot' on a Keplerian orbit around the central SMBH.

We attempted to fit the residuals using the DISKLINE model which revealed an emission region consistent with an annulus between $10 - 45\ r_g$, though these values were not well constrained. Using our lag-derived mean $M_{\rm BH}$ estimate we approximate an expected reverberation lag of ~ 7 ks for material at this radius, however, the high-frequency lag-energy spectrum of Figure 3.9 reveals no such lag at the corresponding energy.

The absence of a detected reverberation lag in the $5 - 7$ keV band is puzzling as it suggests that the emission feature is not responding to continuum variations. Physically this may correspond to a simple scenario where the emission region is in reality significantly further away from the inner disc region than our derived emission line parameters would

suggest. Indeed it was found that a distant reflection scenario (i.e. off of the torus) fits a significant portion of the Fe K band deviations from our intermediate continuum fit, however, a broad emission line provided a substantial statistical improvement over this scenario. Alternatively, the ultra-fast outflows detected in the RGS spectra of this source may produce a shielding wind structure that prevents the coherent propagation of continuum variations to the inferred 'hot-spot' radius. It is also possible that the origin of the excess Fe K band emission is due a more complex reflection scenario in which the reflection spectrum of the accretion disc is Comptonised by an extended corona covering the inner disc (e.g. Petrucci et al. 2001; Wilkins & Gallo 2015b). Wilkins & Gallo (2015b) showed that Comptonisation of the accretion disc reflection spectrum by an extended patchy corona can produce an enhanced blue 'horn' of the Fe Kα emission feature while also artificially increasing the recovered inner disc radius relative to the input value on the simulated spectrum. Furthermore, the ionisation state the disc material is expected to follow a gradient which may be poorly fit when assuming a fixed value for the entirety of the disc, as was done here in using the RELIXLLD model. The origin of the Fe K excess emission remains difficult to constrain based on the currently available data.

As described in Section 3.4 the best-fit model was achieved by allowing the RGS-derived warm absorber parameters to be free to vary, with the excess Fe L emission scenario ruled out when evaluating the goodness-of-fit. Despite this, we tested the validity of such a scenario by comparing our observed line normalisation ratio $N_{\rm L}/N_{\rm K} = (L/K)_{\rm O}$ to the theoretical predictions of Kallman (1995), where it was found that for a gas with ionisation parameter $\log \xi \approx 2.5$ being photoionised by a power-law with photon index $\Gamma = 2.5$ the theoretically

expected line ratio is $(L/K)_{\rm T} \approx 1.6$. When we inserted an additional Fe L feature without allowing the warm absorbers to be free to vary we found that the observed line ratio was $(L/K)_{\rm O} = 3.2 \pm 0.6$, and when the warm absorber parameters were freed this changed to $(L/K)_{\rm O} = 2.9 \pm 0.8$. In both cases the line ratio does not agree with the theoretically predicted value. We also note that the best-fit line energies of these Fe K and Fe L features are significantly higher than their rest-frame energies and not as theoretically predicted by Kallman (1995). This result may by due to the asymmetry of the blurred line profile which was added after the power-law and blurred ionised reflector had fit the continuum. These components may have already fit the present red-shifted 'wing' of the line, leaving only the blue-shifted 'horn' of the feature to be fit by the separate emission features described here, resulting in the higher line energies reported.

The nature of the variability was further explored by applying our best-fit spectral model to the covariance spectra, where we found that the low-frequency spectrum was well described by a soft power-law ($\Gamma \approx 2.4$) while the high-frequency spectrum required a significantly harder power-law ($\Gamma \approx 2.0$). This is interpreted as evidence of a two-corona scenario, in which a compact, hard corona varies more rapidly than an extended, soft corona that varies more slowly. Evidence of this complex coronal geometry has been reported in RQ-NLS1s such as 1H 0707−495 (Kara et al. 2013) as well as in the flaring states of I Zw 1 (Gallo et al. 2007; Wilkins et al. 2017) and Mrk 335 (Wilkins & Gallo 2015a). This extended coronal geometry may in fact be responsible for producing the observed excess Fe K band emission via the aforementioned Comptonisation of the accretion disc reflection spectrum. Here we are unable to significantly detect the hard power-law component in the

spectrum, perhaps indicating that it is significantly weaker than the soft power-law. It may also be true that the currently available data are not of sufficient quality to apply such a model consisting of a double power-law plus highly ionised, relativistically blurred reflection spectrum modified by multiple warm absorbers, where there are significant degeneracies between the numerous free parameters of the multiple spectral components.

The radio emission in this source indicates the presence of a radio jet, although whether it is a sub-relativistic or misaligned jet remains unknown (Doi et al. 2011; Giroletti et al. 2017). Gonzalez et al. (2017) showed that for beamed X-ray coronae the reflection fraction will be $R < 1$ and presented a method to compute the height and velocity of the outflowing corona given the reflection fraction from spectral modelling. The best-fit model parameters in Table 3.5 therefore suggest a beamed corona in IRAS 17020+4544. Considering that the 2004 and 2014 best-fit parameters give different reflection fraction values between the two observing periods, but are consistent with epochs within those periods, we took the mean reflection fraction values for each, giving $R = 0.47^{+0.17}_{-0.10}$ for 2004 and $R = 0.71^{+0.22}_{-0.18}$ for 2014. We compared these source parameter curves to the escape velocity required to overcome the gravitational potential of the black hole in IRAS 17020+4544 by taking the mean of the mass estimates obtained from our combined lag-frequency spectrum as $M_{\rm BH} = (4.08 \pm 1.74) \times 10^7\ M_{\odot}$. This revealed the combinations of source parameters that will result in an observable outflow. The results are shown in Figure 3.14, where the X-ray corona is shown to be capable of outflowing from the system for source heights as close as $\sim 3\ r_g$ in 2004 but at larger heights of $\sim 7\ r_g$ in 2014. If we invoke the X-ray corona as the base of the radio jet then these results can be interpreted in two ways: (i) the X-ray source has

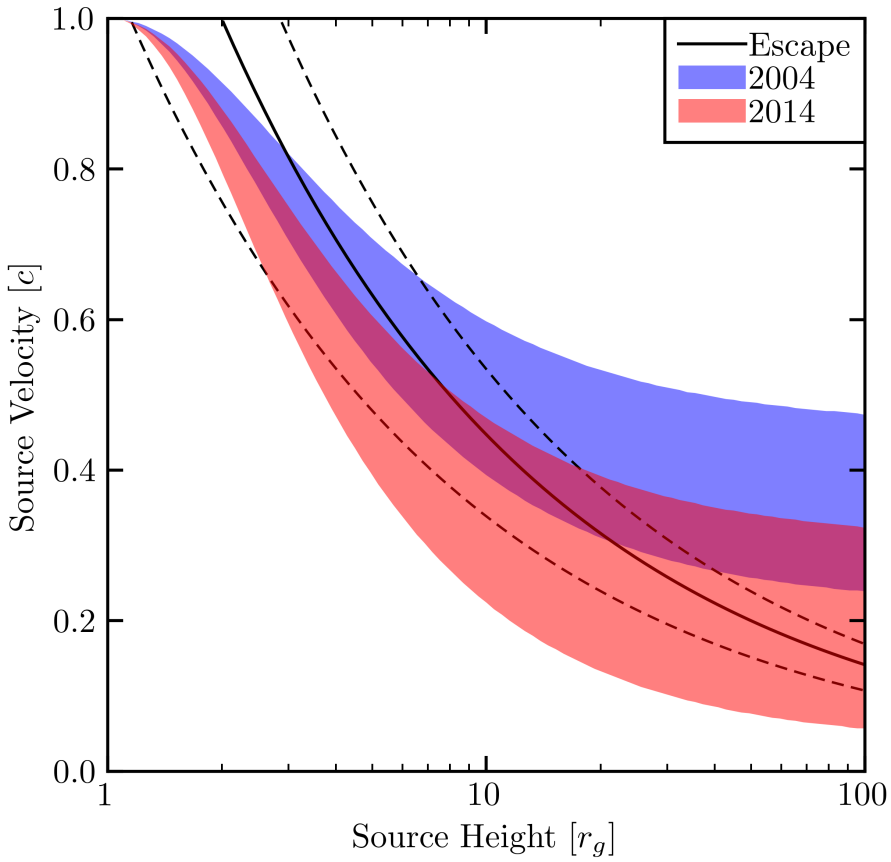

Figure 3.14: The coronal parameters required to enable escape from the black hole environment. The black solid line represents the velocity needed at each height to escape the gravitational potential of a maximal spin ($a = 0.998$) Kerr black hole of mass $(4.08 \pm 1.74) \times 10^7\ M_\odot$, with the dashed lines corresponding to the lower and upper mass limits. The blue and red filled regions represent the source parameters estimated using the range of reflection fraction values obtained from the spectral fits for the 2004 ($R = 0.47^{+0.17}_{-0.10}$) and 2014 ($R = 0.71^{+0.22}_{-0.18}$) data sets, respectively.

increased in height between the two epochs, or (ii) the X-ray source has significantly slowed over the 10 yr period and maintained a constant source height. These two scenarios would have very different impacts on the emissivity profile of the accretion disc. For example, in case (i) the source has increased in height, resulting in less emission incident on the inner

disc, thereby lowering $q_{\rm in}$. In case (ii), the source will have become more weakly collimated, thereby allowing more emission to be gravitationally bent back toward the accretion disc thus increasing $q_{\rm in}$. When attempting to fit such scenarios to the data here we were unsuccessful in sufficiently constraining the parameters such that meaningful statistical differences could be determined, and thus they are not presented here. We note that the sub-relativistic scenario (i.e. $\beta \lesssim 0.9c$) suggested in previous radio studies agrees with the results here, where the maximum velocity attained resulting in an outflow is $\sim 0.8c$.

3.6 Conclusion

We found that IRAS 17020+4544, a RL-NLS1 with a sub-relativistic radio jet, is in many ways comparable to RQ counterparts, while also showing significant differences regarding variability trends.

Notable differences include a 'harder-when-brighter' trend, increasing variability with energy, and evidence of possible non-stationarity at low energies. The hardness-flux relationship and fractional variability spectra are found to be similar to other sources, both RQ and RL, that show evidence of jet activity. In such sources a variable power-law, both in normalisation and photon index, is shown to be sufficient in explaining the observed trends.

Similarities with RQ sources are found with the confirmation of a reverberation lag, providing evidence of significant disc reflection in the X-ray spectrum of a RL source, as well as a standard PSD that can be well described by a simple power-law. Computation of the low- and high-frequency covariance spectra suggests that a variable power-law dominates

the observed flux variability across a wide range of time-scales, with a compact hard corona being variable on shorter timescales than an extended soft corona which varies on longer timescales.

The evolution of all timing products as the source enters a soft spectral state was explored, finding significantly increased variability across all energies, in both the fractional variability and covariance spectra, as well as a shifted lag-frequency spectrum to lower frequencies. These pieces of evidence indicate a significant spectral state change, potentially explained by a moving X-ray corona.

Simultaneous spectral modelling of all five epochs was performed with parameters motivated by the timing results. We find that a variable power-law in the presence of a relativistically blurred, highly ionised reflector is sufficient in explaining the X-ray spectra. The spectra also display evidence of significant excess Fe K emission beyond the included reflection model, perhaps from an orbiting hot-spot in the accretion disc at $r \approx 35\ r_g$.

IRAS 17020+4544 provides another look into a very limited class of AGN: a RL, jetted NLS1 with strong disc emission in the X-ray spectrum. Such sources provide important testing grounds for disc-jet connection theories. Here we show that, as in a handful of other NLS1s, the power-law spectral component produced by the X-ray corona may be linked to the radio jet base.

Chapter 4

On ultra-fast outflows and their relationship to the inner disc environment in active galactic nuclei

---

This work is being prepared for publication in the

Monthly Notices of the Royal Astronomical Society.

4.1 Introduction

The accretion of matter onto a supermassive black hole (SMBH) at the centre of a massive galaxy produces the most luminous continuous source of electromagnetic radiation in the Universe, known as an active galactic nucleus (AGN). AGNs generally exhibit relatively flat spectral energy distributions (SEDs) from radio to γ-ray energies, with ~ 10 per cent (for early findings see Kellermann & Pauliny-Toth 1966; Shapiro & Weinreb 1966) exhibiting significantly enhanced radio emission (i.e. radio-loud) compared to the bulk population (i.e. radio-quiet). Those that are radio-loud often possess large-scale (i.e. many orders of magnitude larger than the AGN central engine), tightly collimated, relativistically beamed radio jets that provide an important source of feedback capable of significantly altering the course of star formation in the host galaxy both positively (e.g. Silk 2005) and negatively (e.g. Croton et al. 2006).

The extreme environment that is produced near a SMBH while it is actively accreting is perhaps best studied at X-ray wavelengths, where spectroscopic and variability analyses of the X-ray emission from AGNs have enabled an indirect exploration of the ongoing physical processes therein. Such works have revealed the presence of an X-ray corona within $\sim 10\ r_g$, where $r_g = GM/c^2$, of the SMBH (for a recent example see Alston et al. 2020), whose emission takes the form of a power law with $F(E) \propto E^{-\alpha}$, where the photon index $\Gamma = \alpha + 1 \approx 1.8 - 2$ (e.g. Nandra & Pounds 1994; Dadina 2008; Beckmann et al. 2009; Ricci et al. 2017). Some fraction of this coronal power law emission illuminates the accretion disc, which subsequently produces a characteristic disc reflection spectrum (Fabian et al.

1989). The short time-scale, large amplitude variability of the X-ray luminosity observed in many AGNs suggests a compact, possibly variable coronal structure (e.g. Wilkins & Gallo 2015a; Wilkins et al. 2017; Alston et al. 2020), where in some cases an extended atmosphere-like coronal geometry is inferred (e.g. Kara et al. 2013; Wilkins et al. 2014). Relativistically broadened Fe K emission lines are best explained as the result of a highly ionised, relativistically blurred inner disc reflection spectrum, which may also account for the peculiar "soft excess" observed at $\lesssim 2$ keV in many AGNs (Crummy et al. 2006).

This two-component power law plus reflection model, however, is often significantly modified by the presence of gas and dust along our line of sight to the SMBH. At energies $\lesssim 2$ keV, high-resolution X-ray observations have found that $\sim 50\%$ of AGNs exhibit spectra rich in complex emission and absorption by matter photoionised by the central X-ray source (for early results see Turner et al. 1993; Reynolds 1997; George et al. 1998). Bulk motion of this matter has been measured as well, with typical outflow velocities of $v_{\rm out} \sim 100 - 1000$ km s^{-1}, with ionisation states ranging from $\log \xi \sim -1 - 3$ erg cm s^{-1} and hydrogen equivalent column densities of $N_{\rm H} \sim 10^{20} - 10^{22}$ cm^{-2} (e.g. Reynolds 1997; Blustin et al. 2005; McKernan et al. 2007). In some cases, these so-called warm absorbers (WAs) may be partially covering the central X-ray source, possibly accounting for the soft excess without the need for an extreme reflection component (Gierliński & Done 2004).

With the advent of high-resolution X-ray spectroscopy in the high-energy X-ray band, absorption features at $7-10$ keV have been reported in $\sim 30-40$ per cent of sampled AGNs (e.g. Tombesi et al. 2010 hereafter T10; Gofford et al. 2013 hereafter G13; Igo et al. 2020 hereafter I20). Attributing these features to absorption by Fe XXVI requires extreme inferred

outflow velocities of $v_{\rm out} \sim 0.01 - 0.5c$, so-called ultra-fast outflows (UFOs). UFOs have been successfully modelled as highly ionised ($\log \xi \gtrsim 3.5$ erg cm s^{-1}), high column density ($N_{\rm H} \gtrsim 10^{22}$ cm^{-2}) photoionised absorbers originating within $\sim 100 - 1000\ r_g$ of the SMBH. Such structures have been shown to provide an important source of AGN feedback into the host galaxy capable of significantly altering the course of star formation within (e.g. Silk & Rees 1998; Fabian 1999; King 2005; Tombesi et al. 2012; Wagner et al. 2013; Gofford et al. 2015).

At this time, various aspects regarding the nature of UFOs remain unknown or difficult to ascertain. For example, there is no consensus as to how UFOs are launched and accelerated, though several driving mechanisms have been shown equally capable of reproducing observed features. Early works were based on theory developed to model spherically symmetric winds driven by line opacity in O-type stars (i.e. radiatively- or line-driven winds; e.g. Castor et al. 1975). Murray et al. (1995) then showed that an axially symmetric adaptation of line-driven winds could be applied to AGNs, however, requiring an *ad hoc* implementation of obscuring matter between the central X-ray source and wind structure in order to prevent overionisation, and hence dissipation, of the wind[1]. Later, Proga et al. (2000) produced a model of a self-shielding line-driven disc wind, solving the puzzle of how to drive a wind with X-rays without destroying it in the process. In this model, material is launched from a bright disc $\sim 100 - 1000\ r_g$ from the central X-ray source, becoming radially accelerated by the X-ray emission due to photon capture in the lines. An interior (i.e. poloidally facing) wind sheath comprised of low density, high ionisation, rapidly outflowing matter is

[1]While later studies have addressed this in a self-consistent manner (see text) it remains an important issue of this model that must be accounted for when attempting to explain winds in this way.

formed, protecting the more dense, less ionised, more slowly outflowing wind[2]. Geometry of the wind is then governed by relative UV/X-ray contributions to the radiation field, with poloidal winds resulting from brighter discs and equatorial winds resulting from brighter X-ray sources. More luminous sources would then be capable of driving more rapid outflows in this model (e.g. Gofford et al. 2015; Chartas & Canas 2018), that is, until some threshold is breached at which over-ionisation of the outflowing matter can no longer be prevented by the self-shielding interior wind sheath, resulting in wind cessation (e.g. Pinto et al. 2018).

Alternatively, magnetically-driven winds have also been proposed via the mechanism outlined by Blandford & Payne (1982) in which angular momentum is extracted from the accretion disc, resulting in a launching of material perpendicular to the disc surface, being accelerated along the field lines (e.g. Contopoulos & Lovelace 1994). Such a model has been used to explain outflowing WAs (e.g. Fukumura et al. 2010a) and UFOs (e.g. Fukumura et al. 2010b) as part of the same large-scale wind structure, with difference in ionisation state, column density, and outflow velocity due to distance of a particular wind stream line from the SMBH, with observed absorber properties a result of our line of sight observing angle through the overall wind structure. This model has been successfully applied to the prototypical UFO observed in the QSO PG 1211+143 (Fukumura et al. 2015). Unification between winds and jets has also been suggested under this magnetically-driven outflow model, in which the wind structure is capable of confining a jet plasma along the SMBH polar axis, providing both a collimation and acceleration mechanism (e.g. Fukumura et al. 2014).

[2]A more physical interpretation of such a discrete sheath may be that of a stratified wind structure.

Gallo & Fabian (2011) proposed a scenario in which UFOs may require no outflow whatsoever, instead showing that resonant absorption through a hot, co-rotating plasma above the accretion disc may provide a less extreme explanation of the proposed UFOs, utilizing instead a natural extension of the reflection scenario. Here, increasing line of sight viewing angles from face-on to edge-on orientations would result in a increased observed cross section through the disc atmosphere, resulting in more heavily blueshifted and deeper absorption features. This model was found to provide a good description of the reported UFOs in both IRAS 13224−3809 (Fabian et al. 2020) and PG 1211+143 (Gallo & Fabian 2013), both of which were previously explained through one (or both) of the aforementioned UFO driving mechanisms.

Fundamental in all three of the above UFO scenarios is a direct relationship with the central engine, specifically the inner disc environment. To date, however, there has been no work conducted on modelling the X-ray spectra of a sample of AGNs using a reflection scenario while simultaneously evaluating UFO parameters in an effort to explore parameter correlations. Parker et al. (2018a) performed a literature search of sources that have been individually treated in this manner, finding that radiatively-driven winds offer a good description of UFOs, though that analysis was limited to exploring how outflow velocity relates to line of sight inclination angle.

In general, the existing literature examining the properties of UFOs can be split into two main methods of study: (i) blind searches for UFOs through large samples of AGNs to determine population statistics such as what portion of the AGN population exhibits UFOs (e.g. T10, G13, I20), and (ii) deep analyses on individual AGNs aimed at fully characterising

the observed UFO(s) (see Parker et al. 2018a and references therein). In studies of type (i), a simple phenomenological model (i.e. an absorbed power law) is typically applied to a restricted portion of the X-ray spectrum (i.e. generally high-energy $2-10$ keV to avoid low-energy spectral complexity from additional model components such as WAs) for the sample of AGNs. Such analyses are efficient at finding plenty of evidence of possible UFOs, as found in the literature. The simplicity of the applied models in type (i) studies, however, restricts the analysis to a very narrow scope of parameter correlations that can be examined. Type (ii) studies, on the other hand, are effective at applying the most detailed modelling techniques available, but lack, by definition, the ability to probe the UFO driving mechanism(s) over a wide range of the AGN parameter space. Furthermore, it is unfortunate that current X-ray missions do not provide spectra of sufficient spectral resolution to effectively distinguish the very different proposed wind driving mechanisms, often finding that the fine-tuning of any of the three described UFO scenarios can lead to approximately equivalent statistical fits.

In this work, we attempt to merge the two methodologies. We took advantage of the sample-based results from T10, G13, and I20 to select AGNs found to exhibit strong evidence of UFOs. We then applied a physically motivated power law plus reflection spectral model (including photoionised emission and/or absorption where needed) to their X-ray spectra, evaluated data deviations from the best-fit model under this scenario, and simultaneously fit the detected UFOs. This allowed us to explore what relationships, if any, exist between the UFO and inner disc environment via the simultaneous characterisation of the inner disc and UFO parameters in a sample of 20 AGNs.

4.2 Sample Selection

Our sample was compiled based on those AGNs found to exhibit strong evidence of UFOs as reported by T10, G13, and/or I20[3]. However, in order to simplify the modelling complexity we included only radio-quiet Type 1 AGNs (i.e. those that have been classified as Seyfert 1, 1.2, 1.5 or narrow-line Seyfert 1 AGNs) that are generally more easily modelled by a simple power law plus reflection scenario (i.e. no changing look AGNs and no sources in which a warm corona / soft-Comptonisation component has been shown to dominate the soft X-ray band)[4]. Furthermore, we considered only those AGNs with reported UFO velocity $v_{\rm UFO} \gtrsim 0.01c$. We note that PG 1448+273 is the only AGN included here that does not originate from T10, G13, nor I20; Kosec et al. (2020) recently reported a UFO with $v_{\rm UFO} \sim 0.1c$ in this source, therefore we included it in this work.

With a list of candidate AGNs exhibiting strong evidence of UFOs, we then selected specific archival *XMM-Newton* observations for each source in a manner dependent on the analysis from which it was selected. Sources cross-listed in T10 had the exact same observations analysed here. G13 used exclusively *Suzaku* data, which lacks the desired low-energy coverage down to 0.3 keV crucial to constraining the spectral models used in this work. Therefore, we chose to analyse the two longest exposures available in the *XMM-Newton* archive for cross-listed sources. This was done in order to minimise the possibility of not finding any UFO due to the known rapid variability of such features. For sources cross-listed in I20, we

[3]We selected only those sources with "likely" outflows from I20, omitting those with "possible" outflows.

[4]This choice therefore excludes: ESO 323−G77, NGC 4151, NGC 4395, and Ton S180 as they exhibit more complex X-ray spectra.

also selected the two longest exposures available for each source in the *XMM-Newton* archive. Despite I20 being similarly based on exclusively archival *XMM-Newton* data, that work focussed on time variability to detect UFOs, necessitating the combination of all observations for an individual source, thus providing no direct observation-specific information.

The final sample of sources and observations used in this work can be found in Table 4.1, with relevant observational information and source parameters presented.

Table 4.1: The sample of AGNs analysed in this work. The columns are: (1) source name, (2) *XMM-Newton* observation ID, (3) start date of observation, (4) net exposure, (5) net counts, (6) source redshift, (7) SMBH mass, (8) Galactic hydrogen equivalent column density, (9) colour excess due to Galactic reddening, and (10) reference(s) where high-energy absorption features were reported (1: T10, 2: G13, 3: I20, and K20: Kosec et al. 2020). Observations marked with a superscript p exhibit significant levels of pile-up (i.e. > 2 per cent).

(1) Source Name	(2) Obs. ID	(3) Obs. Date [yyyy-mm-dd]	(4) Exposure [ks]	(5) Counts $[\times 10^5]$	(6) Redshift $[z]$	(7) Mass $[\log(M_{\rm BH}/M_\odot)]$	(8) Gal. Abs. $[N_{\rm H}/10^{20}\ {\rm cm}^{-2}]$	(9) Colour Excess $[E_{\rm B-V}/{\rm mag}]$	(10) UFO Ref.
1H 0419−577	0148000201	2002-09-25	11.9	0.24	0.10400	8.58	1.34	0.015	1
1H 0707-495	0511580101^p	2008-01-29	106.7	3.50	0.04057	6.31	6.55	0.113	3
	0653510601	2010-09-19	110.1	4.91					
Ark 120	0147190101	2003-08-24	76.2	20.2	0.03271	8.18	14.6	0.126	1
IC 4329A	0147440101	2003-08-06	87.3	22.7	0.01605	8.34	5.56	0.059	1, 3
IRAS 13224−3809	0780561501^p	2016-07-20	127.5	1.83	0.06580	6.76	6.78	0.072	3
	0792180101^p	2016-07-26	125.8	2.20					
IRAS 13349+2438	0096010101	2000-06-20	29.6	1.02	0.10764	7.74	1.07	0.013	3
	0402080301	2006-07-16	46.8	1.35					
MR 2251−178	0670120201	2011-11-11	93.3	18.0	0.06398	8.01	2.67	0.036	2
	0670120401	2011-11-15	92.0	15.9					
Mrk 79	0400070201	2006-09-30	14.0	2.13	0.02219	7.72	6.73	0.071	1, 3
Mrk 205	0124110101	2000-05-07	15.3	0.51	0.07085	8.32	3.45	0.042	1, 3
Mrk 290	0400360601	2006-05-04	15.3	0.81	0.02958	7.39	1.75	0.013	1
Mrk 509	0130720101	2000-10-25	20.6	3.20	0.03440	8.15	5.04	0.059	1, 3
	0306090201	2005-10-18	59.8	17.1					
	0306090401	2006-04-25	48.5	14.2					
Mrk 766	0304030301	2005-05-25	68.9	5.79	0.01293	6.25	1.89	0.019	1, 2, 3
	0304030501	2005-05-29	65.1	9.11					
Mrk 841	0205340401	2005-07-17	18.1	1.20	0.03642	8.52	2.43	0.033	1, 3
NGC 3516	0401210601	2006-10-10	46.8	5.96	0.00884	7.50	3.92	0.048	1, 2
NGC 3783	0112210101	2000-12-28	26.1	4.12	0.00973	7.47	13.8	0.12	1, 2
NGC 4051	0109141401	2001-05-16	74.1	19.2	0.00234	6.24	1.19	0.013	1, 2, 3
	0157560101^p	2002-11-22	44.7	2.13					
PDS 456	0721010401	2013-09-15	102.9	2.01	0.18400	8.91	33.3	0.53	2, 3
	0721010601	2014-02-26	119.7	1.69					
PG 1211+143	0112610101^p	2001-06-15	49.5	1.39	0.08090	7.61	3.02	0.034	1
PG 1448+273	0741280201	2017-01-25	56.6	1.07	0.06500	6.97	2.96	0.029	K20
Swift J2127.4+5654	0693781701	2012-11-04	94.6	5.08	0.01440	7.18	91.4	1.532	2
	0693781801	2012-11-08	93.4	6.03					

4.3 Data Reduction

This work makes exclusive use of archival data obtained from the *XMM-Newton* (Jansen et al. 2001) X-ray telescope. Data products were extracted from the Observation Data Files (ODFs) of each observation using the Science Analysis System (SAS) version 17.0.0. Below we describe the processing steps for each instrument used in this work.

4.3.1 EPIC pn data

For each observation listed in Table 4.1 we produced EPIC pn (Strüder et al. 2001) event lists using the SAS task EPCHAIN. Source counts were extracted from a circular region centred on the source position (obtained from the NASA/IPAC Extragalactic Database) of radius 35″, and background counts were extracted from an off-source circular region on the same detector chip of radius 50″. Good time intervals (GTIs) were produced for each observation using the TABGTIGEN task and were selected based on the observation-specific quiescent background level, filtering out times of flaring for which the background count rate exceeded the mean quiescent background count rate. The majority of the analysed observations displayed insignificant levels of pile-up[5] of ≤ 2 per cent, as determined by the output of the EPATPLOT task. Several observations, however, did display moderate levels of pile-up, which have been highlighted in Table 4.1. Despite this, we found it impractical to correct for

[5]Pile-up occurs in sources with flux levels high enough such that during the time between CCD event read-out cycles multiple incoming photons are deposited onto any particular pixel. The effect is thus to 'pile-up' the photon energies as the detector records the combined energy of the multiple photons as due to a single event. The spectral hardening due to pile-up effects is detrimental to accurate parameter estimation from any applied models, however, correcting the effect via the exclusion of bright source-centred pixels can degrade spectral quality too severely for use beyond the most simple phenomenological models.

the effect of pile-up in those observations due to the large source exclusion region needed in order to reduce the pile-up level to ≤ 2 per cent, often requiring > 20 per cent of the source extraction region to be excluded, significantly impacting spectral quality and consequently parameter estimation of observed absorption features (see Appendix A for details). The following observations exhibited the listed single event pile-up levels: 1H 0707−495 0511580101 2.4 per cent, IRAS 13224−3809 0780561501 2.2 per cent and 0792180101 2.8 per cent, NGC 4051 0157560101 3.5 per cent, PG 1211+143 0112610101 2.9 per cent.

We then produced the time-averaged X-ray spectrum of each observation using the EVSELECT task with the conditions $0 \leq$ PATTERN ≤ 4 and FLAG $== 0$, generating response matrices and ancillary files using the SAS tasks RMFGEN and ARFGEN, respectively. Rather than bin the X-ray spectra using a 'standard' minimum-counts-per-bin based approach, we chose to "optimally" bin the data using the method described by Kaastra & Bleeker (2016) via the FTGROUPPHA task with GROUPTYPE=OPT. This binning scheme improves vastly upon historically applied methods by taking into consideration detector resolution, source count rate, as well as mean photon energies in each detector resolution element (see Kaastra & Bleeker 2016 for details). Our decision to optimally bin the X-ray spectra here, however, subsequently required the use of the Cash statistic (Cash 1979) (hereafter C) when fitting the data to evaluate model likelihoods. This choice of statistic was necessary as optimally binned spectra are allowed to produce energy bins with $N < 20$ counts, making commonly used χ^2 statistics invalid. Moreover, C is a Poissonian statistic, thus making it more appropriate for use in X-ray astronomy over Gaussian-based χ^2 in general. Indeed, even in the high-count regime Humphrey et al. (2009) showed that C performed better that χ^2, arguing for

more widespread use of C. Finally, the use of C here means that the standard background spectrum subtraction from the total spectrum that is usually performed in X-ray spectral analyses is invalid here, due to the Poissonian nature of C[6]. Instead, the background spectrum of a given observation was modelled in conjunction with the total spectrum of that observation.

All X-ray spectral fits were performed using the HEASOFT spectral fitting package XSPEC v12.10.0c (Arnaud 1996). We assumed a cosmology with $H_0 = 70$ km s^{-1} Mpc^{-1}, $q_0 = 0$, and $\Lambda_0 = 0.73$ and assumed Wilms et al. (2000) ISM abundances. All reported spectral model parameter errors are at the 90 per cent confidence level, unless otherwise stated.

4.3.2 Optical Monitor data

We also processed all available Optical Monitor (OM) (Mason et al. 2001) data for each observation in Table 4.1 using the SAS task OMICHAIN. The resultant combined source list files were then used to extract the source flux in all available filters using the OM2PHA task, supplying the source coordinates with a position tolerance of $30''$, decreasing the tolerance when multiple detections were made near the source position.

All available filters for each observation were corrected for Galactic reddening by converting the colour excess values tabulated by Willingale et al. (2013) to the appropriate total extinction value, A_λ, in each filter according to the method described in Cardelli et al. (1989), assuming $R_V = 3.1$.

[6]This is important as the difference between two Poisson distributions, represented by the total and background spectra here, does not produce a Poisson distribution, and thus the resultant 'source' spectrum cannot by properly modelled using C.

4.4 Methodology

4.4.1 Broad band X-ray spectral modelling

First, the use of C as a fit statistic in this work necessitated modelling[7] the extracted background spectrum of each observation rather than simply subtracting it from the total spectrum, the usual procedure in AGN X-ray literature. This process has the added benefit of potentially reducing the number of false-positive UFO detections that may otherwise occur in the case of background over-subtraction at high-energies, which is especially relevant in those AGNs with steep X-ray spectra or overall low source flux. We modelled the background spectrum of each observation assuming a black body (BB) plus broken power law (BKNPO) continuum across $0.3 - 10$ keV as well as emission features (GAUSS) placed at 1.5 keV, to account for instrumental Al Kα, and at $\sim$ 8.5 keV, to account for instrumental Ni Kα, Cu Kα, and Zn Kα. The aforementioned background lines are expected emission features based on the internal "quiescent" background of the EPIC pn detector[8]. This translates into an XSPEC background model syntax of BB+BKNPO+GAUSS+GAUSS. Once an acceptable background spectral fit was obtained, we froze the background model parameters and included it in the total spectral model, modelling the source spectrum according to the method described below.

Our modelling of the source spectrum makes use of physically motivated spectral models

[7]We followed the background modelling steps outlined at https://heasarc.gsfc.nasa.gov/xanadu/xspec/manual/node40.html

[8]Internal quiescent background features obtained from https://xmm-tools.cosmos.esa.int/external/xmm_user_support/ documentation/uhb/epicintbkgd.html.

under the assumption of a power law continuum that illuminates the accretion disc, producing a multi-component X-ray spectrum comprised of a power law, relativistic inner-disc reflection, and further reflection from more distant material (i.e. the torus). We chose to model such disc reflection scenarios with RELXILLD version 1.2.0 and XILLVERD (García et al. 2016) for the inner- and outer-disc regimes, respectively, modelling the power law emission with the CUTOFFPL model[9]. Our use of the high-density variant of RELXILL was motivated by the results of Jiang et al. (2019), wherein low-mass SMBHs with masses $\lesssim 10^8\ M_\odot$ were found to be better fit by higher disc densities $\log n_e > 10^{15}$ cm^{-3}. We accounted for Galactic absorption due to both neutral and molecular hydrogen using the results of Willingale et al. (2013), applying the TBABS model component to the data, freezing the column density parameter to the tabulated value for all fits (see Table 4.1 column 6). We set the $0.1 - 100$ keV luminosity of the power law and RELXILLD components to be equal to each other by applying a CLUMIN model component to each and linking the luminosity values. We then added a multiplicative CONSTANT to the RELXILLD model in order to evaluate the reflection fraction as $R_{0.1-100\ \mathrm{keV}} = L_{\mathrm{RELXILLD}}/L_{\mathrm{CUTOFFPL}} = L_{\mathrm{R}}/L_{\mathrm{PL}}$. In XSPEC the syntax of our base broad band spectral model therefore consisted of: TBABS × (CLUMIN × CUTOFFPL+CONSTANT × CLUMIN × RELXILLD+XILLVERD). See Table 4.2 (top) for a summary of base model parameter information.

Many of the AGNs studied here are known to exhibit significant intrinsic absorption, neutral and/or ionised, and/or photoionised emission. We therefore performed a literature search on each object in order to obtain initial parameter values for these additional compo-

[9]We kept $E_{\mathrm{cut}} = 300$ keV fixed during all spectral fits, as it was unconstrained in all cases due to the 10 keV high-energy limit of *XMM-Newton* .

Table 4.2: Model parameter descriptions for the various XSPEC spectral model components. The top table segment contains the base model components, while additional components (i.e. ZTBABS, XABS, and PION) are shown in the bottom segment. XABS and XABSUFO are essentially the same model, only differing in their allowed parameter ranges.

Model	Parameter	Units	Description
TBABS	$N_{\rm H}$	$\rm cm^{-2}$	Galactic column density obtained from Willingale et al. (2013).
CLUMIN	$L_{0.1-100\rm keV}$	erg $\rm s^{-1}$	$0.1-100$ keV luminosity of convolved model.
	z	–	AGN host galaxy redshift.
CUTOFFPL	Γ	–	Power law photon index, i.e. $F(E) \propto E^{-\Gamma}$.
	$E_{\rm cut}$	keV	E-folding energy of exponential turnover.
RELXILLD	$R_{0.1-100\rm keV}$	–	Reflection fraction, i.e. $R \equiv L_{\rm R}/L_{\rm PL}$.
	$q_{\rm in}$	–	Inner emissivity profile index, i.e. $\epsilon(r) \propto r^{-q_{\rm in}}$.
	$q_{\rm out}$	–	Outer emissivity profile index, i.e. $\epsilon(r) \propto r^{-q_{\rm out}}$.
	$r_{\rm break}$	r_g	Emissivity profile break radius at which $q_{\rm in}$ transitions to $q_{\rm out}$.
	a	–	Black hole spin parameter.
	θ	degrees	Disc inclination angle.
	$r_{\rm in}$	r_g	Disc inner radius.
	$r_{\rm out}$	r_g	Disc outer radius.
	$\log \xi$	erg cm $\rm s^{-1}$	Disc ionisation parameter.
	$A_{\rm Fe}$	$A_\odot$	Disc iron abundance relative to solar.
	$\log n_e$	$\rm cm^{-3}$	Disc density.
	z	–	AGN host galaxy redshift.
XILLVERD	θ	degrees	Disc inclination angle.
	$\log \xi$	erg cm $\rm s^{-1}$	Disc ionisation parameter.
	$A_{\rm Fe}$	$A_\odot$	Disc iron abundance relative to solar.
	$\log n_e$	$\rm cm^{-3}$	Disc density.
	z	–	AGN host galaxy redshift.
	N	–	Model normalisation, i.e. $N \equiv 10^{20}\,(n_e \xi/4\pi)$.
ZTBABS	$N_{\rm H}$	$\rm cm^{-2}$	AGN host galaxy column density.
	z	–	AGN host galaxy redshift.
XABS/ XABSUFO	$\log \xi$	erg cm $\rm s^{-1}$	WA/UFO ionisation parameter.
	$N_{\rm H}$	$\rm cm^{-2}$	WA/UFO column density.
	$v_{\rm turb}$	km $\rm s^{-1}$	WA/UFO turbulent velocity.
	z	–	WA/UFO redshift, i.e. $v_{\rm out} \equiv (z - z_{\rm AGN})c$.
PION	$\log \xi$	erg cm $\rm s^{-1}$	Photoionised emitter ionisation parameter.
	n_e	$\rm cm^{-3}$	Photoionised emitter density.
	$A_{\rm O}$	$A_\odot$	Photoionised emitter oxygen abundance.
	$A_{\rm Fe}$	$A_\odot$	Photoionised emitter iron abundance.
	z	–	Photoionised emitter redshift, i.e. $v_{\rm out}$.
	N	–	Model normalisation.

nents in each object, as obtaining absorption parameters directly from the RGS spectrum of each observation (where applicable) was outside the scope of this work. We preferentially took parameter values from analyses that were performed on the specific observations examined here (see Table 4.1 column 2). In some cases the presence of the additional components was visually identifiable in the X-ray spectrum, however, no literature values were available. In such instances we added components until subsequent additions made no statistically significant improvements to the fit. For objects showing significant intrinsic absorption we therefore modified our base model by adding a neutral absorber in the source frame, via ZTBABS and/or ionised absorption via the XSPEC implementation of the SPEX (Kaastra et al. 1996) model XABS (Steenbrugge et al. 2003) provided by Parker et al. (2019). For objects exhibiting significant photoionised emission we used the XSPEC implementation of the SPEX model PION[10] (Miller et al. 2015; Mehdipour et al. 2016), again provided by Parker et al. (2019)[11]. See Table 4.2 (bottom) for a summary of additional model parameter information.

The base model, and any necessary additions, was then fit to the $0.3 - 10$ keV X-ray spectrum of each observation in Table 4.1. We initially allowed the following parameters to be free to vary during the fitting procedure: CLUMIN − luminosity $L_{0.1-100\ \mathrm{keV}}$; CUTOFFPL − photon index Γ; CONST − $R_{0.1-100\ \mathrm{keV}}$; XILLVERD − normalisation N_{X}. The following parameters were therefore initially frozen to their listed values: RELXILLD − inner emissivity index $q_{\mathrm{in}} = 6$, outer emissivity index $q_{\mathrm{out}} = 3$, emissivity break radius $r_{\mathrm{break}} = 6\ r_g$, black hole spin $a = 0.998$, inner disc radius $r_{\mathrm{in}} = r_{\mathrm{ISCO},\ a=0.998} = 1.235\ r_g$, outer disc ra-

[10] We kept the gas density parameter of PION fixed to default value of $n_e = 10^{-4}$ cm^{-3} during all spectral fits, as it was unconstrained in all cases.

[11] XSPEC implementations of both XABS and PION are available at https://www.michaelparker.space/xspec-models.

dius $r_{\rm out} = 400\ r_g$, disc inclination $\theta = 30°$, ionisation parameter $\log \xi_{\rm R} = 2$ erg cm s^{-1}, iron abundance $A_{\rm Fe} = 1$, and disc density $\log n_e = 15$ cm^{-3}. We linked the Γ values of RELXILLD and XILLVERD to that of CUTOFFPL. All equivalent parameters of the XILLVERD component were linked to those of the RELXILLD component, except for the following parameters which were kept frozen to the listed values in all fits: $\log \xi = 0$ erg cm s^{-1}, $A_{\rm Fe} = 1$, and $\log n_e = 15$ cm^{-3}. Additional neutral absorption, ionised absorption, and photoionised emission components that were included according to the literature on each object had their parameters initially fixed to the literature values.

Once an initial fit was obtained, we tested the significance of allowing each of the following parameters to be free to vary during the fitting: $q_{\rm in}$, a, θ, $\log \xi$, $A_{\rm Fe}$, and $\log n_e$. We note that for any source in which a was allowed to be free to vary, $A_{\rm Fe}$ was also allowed to be free to vary, in accordance with the findings of Reynolds (2014). For objects in which additional components were included, we then allowed select parameters of those components to be free to vary: ZTBABS − column density $N_{\rm H,AGN}$; XABS − ionisation parameter $\log \xi_{\rm WA}$, column density $N_{\rm H,WA}$; PION − ionisation parameter $\log \xi_{\rm P}$, normalisation $N_{\rm P}$. Ionised absorbers modelled with XABS had their turbulent and outflow velocities frozen to literature values, or in cases where this information was not available were fixed to 100 km s^{-1} and rest in the source frame, respectively. Photoionsed emission components modelled with PION had their turbulent and outflow velocities fixed to 100 km s^{-1} and rest in the source frame, respectively, and had their elemental abundances fixed to solar abundances.

For those objects with multiple observations, we modelled the spectra from all observations in Table 4.1 simultaneously, linking several parameters of the base spectral model

between all observations of the same object, namely: a, $r_{\rm in}$, $r_{\rm out}$, θ, $A_{\rm Fe}$, and $\log n_e$ (and $N_{\rm H}$ of ZTBABS, if applicable). Other parameters were allowed to be free to vary and unlinked between the multiple observations so long as the fit improvement in doing so was statistically significant; otherwise, they were kept linked between the multiple observations. This procedure afforded tighter constraints on key parameters of the reflection model for those objects with multiple observations, helping to reduce the known degeneracies of the listed parameters. Comments on the spectral fits for all sources are given in Appendix C.

4.4.2 Monte Carlo simulations

Once a best-fit broad band spectral model was obtained for a particular observation, the significance of data deviations from that model were evaluated via an $N = 1000$ iterations Monte Carlo simulation. First, we simulated a realisation of the best-fit spectral model to the data via the FAKEIT NONE command in XSPEC, using the observation exposure time to determine the photon statistics. Following the method of Markowitz et al. (2006), however, an intermediate step was performed such that after simulating this original Monte Carlo realisation of the best-fit model, the model was re-fit to the synthetic data to create an intermediate model. This intermediate model was then used to simulate a new Monte Carlo realisation in the same manner as described above. This second realisation of the best-fit model, produced by the intermediate model, was then accepted as the $i^{\rm th}$ Monte Carlo iteration, with the original synthetic spectrum not considered. This procedure was performed in order to account for the uncertainty of the null hypothesis of the best-fit model (see Section 4.3.3 of Markowitz et al. 2006 for details). We repeated the above steps for

each of the $N = 1000$ Monte Carlo iterations.

These simulated spectra were then used to produce a Monte Carlo distribution of stochastic fit improvements ΔC, to be used when evaluating the significance of the data deviations from the best-fit model. For each of the $N = 1000$ synthetic spectra, we inserted a narrow ($\sigma = 10$ eV) Gaussian feature, starting at 2 keV and stepping by 0.1 keV through to 10 keV (observed energies), with the line normalisation free to vary between positive and negative values. At each step, the stochastic fit improvement, ΔC, for the inclusion of the narrow Gaussian was recorded. This produced 81000 ΔC measurements for each observation, producing a Monte Carlo distribution of ΔC based on stochastic fluctuations from the $N = 1000$ realisations of the best-fit spectral model.

Finally, the significance of deviations in the observed spectrum from its best-fit spectral model were evaluated by using a similar process as described above, stepping a narrow ($\sigma = 10$ eV) Gaussian feature through $2 - 10$ keV (observed energies) by 0.1 keV and evaluating the fit improvements for a range of positive and negative line normalisation values, using 20 steps in each direction[12]. The Monte Carlo significance, S, of the fit improvement to observed data produced in each step above was then obtained by computing the 50th, 90th, 95th, and 99th percentiles of the Monte Carlo ΔC distribution and categorising into one of four bins: 50th $\leq S <$ 90th, 90th $\leq S <$ 95th, 95th $\leq S <$ 99th, and 99th $\leq S$.

This produced a final result consisting of data deviation significance contours spanning $2 - 10$ keV spaced every 0.1 keV. We determined those observations displaying "strong" evi-

[12]The exact range of line normalisation used for each observation was based on the flux level and feature depth.

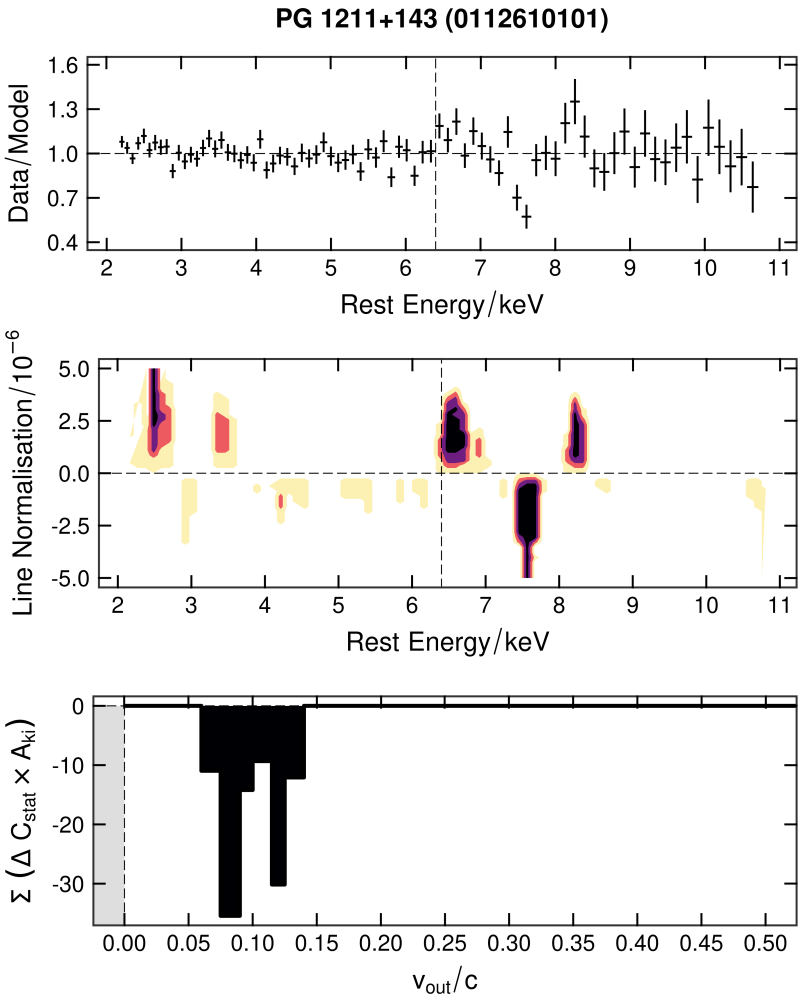

Figure 4.1: *Top panel*: Ratio residuals of the best-fit model to the X-ray spectrum of PG 1211+143 during observation 0112610101, displaying an absorption feature at $\sim$ 7.6 keV. The vertical dashed line represents the Fe Kα emission line at 6.4 keV (top and middle panels). *Middle panel*: Significance, S, contours of the data deviations from the best-fit model (see Section 4.4.2 for details). Colour-coding of S contours based on the Monte Carlo ΔC distribution percentiles is as follows: yellow - 50th $\leq S <$ 90th, orange - 90th $\leq S <$ 95th, purple - 95th $\leq S <$ 99th, and black - 99th $\leq S$. *Bottom panel*: The outflow velocity curve, as determined by the "comb" search through the contours in the middle panel (see Section 4.4.3.1 for details). Shaded regions indicate the same significance levels as in the middle panel. Peaks at $v_{\rm out} = 0.08c$ and $v_{\rm out} = 0.1175c$ indicate the presence of a UFO with $v_{\rm out} \sim 0.1c$.

dence of high-energy absorption features as those with negative line normalisation contours in the $7-10$ keV band corresponding to $S \geq 95$ per cent. An example of the results of this procedure is shown in Figure 4.1 (top and middle panels), where we display the significant detection of the well-known UFO in PG 1211+143. Additional plots of this procedure are included in Appendix B, with the results for all sources shown in Appendix D.

4.4.3 Fitting the absorption features

4.4.3.1 Preliminary velocity determination

Prior to the application of a physically motivated spectral model to determine the wind parameters, we chose to first estimate the outflow velocity by performing a "comb" search through the contours. From the National Institute of Standards and Technology (NIST) Atomic Spectra Database[13] (Kramida et al. 2020) we retrieved a series of Fe XXV and Fe XXVI absorption lines (see Table 4.3), recording the rest energy and Einstein coefficient of each line. As the Monte Carlo simulations had an energy stepping of 0.1 keV, we binned the "comb" features by taking the mean of all line energies and Einstein coefficients for transitions within 0.1 keV of each other. The "comb" was then shifted through the contours of each observation, covering an outflow velocity range in the source frame up to $0.5c$ using a step size of $0.005c$. For each velocity step, Monte Carlo significance contours with $S \geq 95$ per cent and whose energy corresponded to one of the "comb" features had their fit improvement ΔC summed, applying a weight to each fit improvement by the Einstein coefficient for its corresponding line in the "comb". Finally, the statistical significance of the total weighted

[13]The NIST database can be accessed at https://www.nist.gov/pml/atomic-spectra-database.

Table 4.3: All Fe absorption lines used in the grid to determine the best-fit UFO velocity.

Ion	Transition	Rest energy $[E_{\rm rest}/{\rm keV}]$	Einstein coefficient $\left[A_{\rm ki}/10^{13}\ {\rm s}^{-1}\right]$
Fe XXV	Heα	6.668	44.2
		6.700	45.7
Fe XXVI	Lyα	6.952	29.3
		6.973	29.6
Fe XXV	Heβ	7.872	1.50
		7.881	12.4
Fe XXVI	Lyβ	8.246	7.83
		8.253	7.86
Fe XXV	Heγ	8.292	0.60
		8.295	5.05
Fe XXV	Heδ	8.485	0.31
		8.487	2.54
Fe XXVI	Lyγ	8.701	3.20
Fe XXVI	Lyδ	8.909	1.61

fit improvement at each velocity step was compared to the χ^2_ν distribution for $\nu = 1 + N_{\rm lines}$ degrees of freedom, where $N_{\rm lines}$ is the number of lines in the "comb" that were found to coincide with contours of $S \geq 95$ per cent. The significance level for each tested outflow velocity was categorised into the same bins as for the Monte Carlo significance contours, using the same colour scheme[14]. This procedure allowed for the determination of statistically significant outflow velocities without the use of any physical spectral model. An example of the results of this procedure are shown in Figure 4.1 (bottom panel). Additional plots of this procedure are shown in Appendix B, with results for all sources shown in Appendix D.

[14]Note that while the Monte Carlo significance contours and outflow velocity significance levels are represented by the same colours and percentiles, they do not represent the same information. Monte Carlo significance contours highlight at what significance level the data deviations from the best-fit spectral model exceed the stochastic noise variability from the $N = 1000$ iterations. Outflow velocity significance levels highlight the statistical significance of including corresponding absorption lines from the "comb" that align with features in the Monte Carlo significance contours.

Before moving on, however, we tested the ability of our "comb" in recovering a known input outflow velocity by performing as series of simulations using a high flux example of our base spectral model. We simulated $N = 1000$ spectra assuming: $L_{\mathrm{PL\ 0.1-100\ keV}} = 10^{43}$ erg s^{-1}, $\Gamma = 2$, $R_{\mathrm{0.1-100\ keV}} = 1.3$, $q_{\mathrm{in}} = 6$, $q_{\mathrm{out}} = 3$, $r_{\mathrm{break}} = 6\ r_g$, $a = 0.998$, $r_{\mathrm{in}} = 1.235\ r_g$, $r_{\mathrm{out}} = 400\ r_g$, $\theta = 30°$, $\log \xi_{\mathrm{R}} = 1.5$ erg cm s^{-1}, $A_{\mathrm{Fe}} = 1$, $\log n_e = 15$ cm^{-3}, and $N_{\mathrm{XILLVERD}} = 7.5 \times 10^{-5}$ at a redshift of $z = 0.01$. Using these spectra we performed the same procedure outlined in Section 4.4.2 to produce a stochastic ΔC distribution for the described base model.

Then, we applied a UFO to the base model using a modified XABS model tailored to typical UFO parameters[15], which we will refer to as XABSUFO to avoid confusion with the WAs, inputting parameters approximating the mean values determined by Tombesi et al. (2011) and Gofford et al. (2015): $\log \xi_{\mathrm{UFO}} = 4$ erg cm s^{-1}, $N_{\mathrm{H,UFO}} = 5 \times 10^{22}$ cm^{-2}, and $v_{\mathrm{turb}} = 2000$ km s^{-1} for three outflow velocities $v_{\mathrm{UFO}} = 0.05c,\ 0.15c,\ 0.25c$. For each of the three outflow velocities we simulated $N = 1000$ realisations of the now wind-applied base models, removed the wind model component, re-fit the now wind-less base model, and performed the procedure outlined in Section 4.4.2 treating each of the $N = 1000$ wind-applied spectra as a "real" observation with which to evaluate the contours against the MC distribution produced in the previous step (i.e. described in previous paragraph).

With this procedure, we were then able to perform $N = 1000$ "comb" searches through the simulated spectra for each input outflow velocity $v_{\mathrm{UFO}} = 0.05c,\ 0.15c,\ 0.25c$, enabling a thorough test of the "comb" search method and its ability to recover the known input

[15]This model is available at https://www.michaelparker.space/xspec-models.

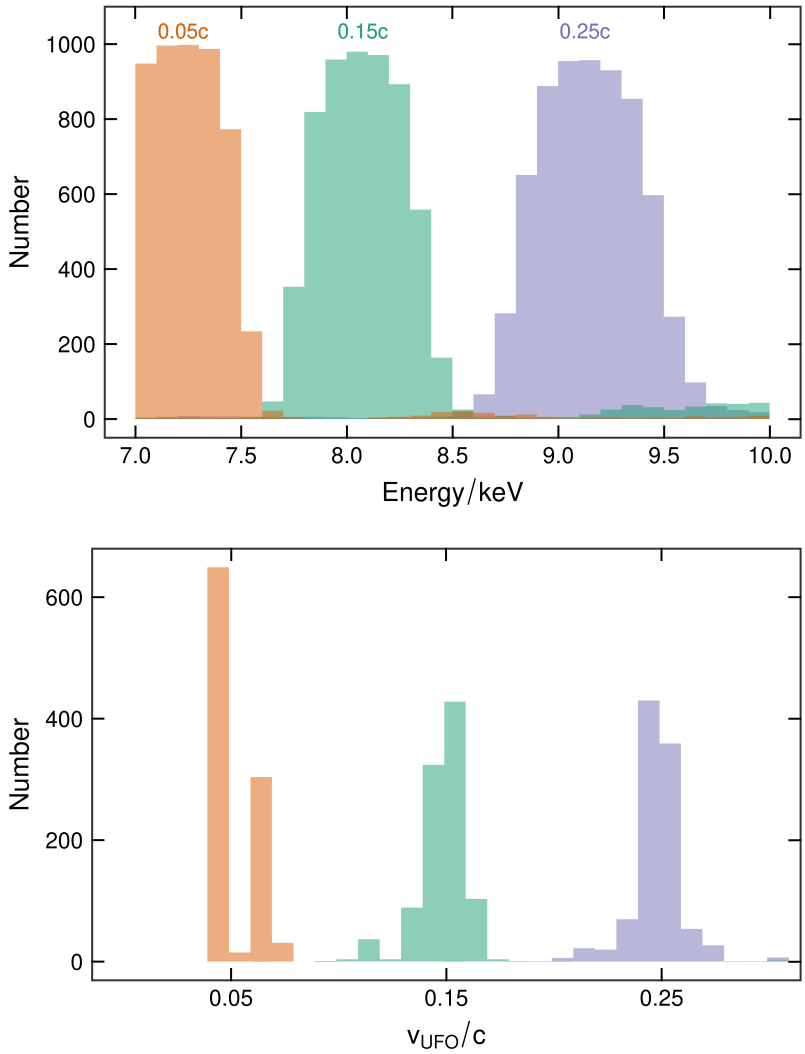

Figure 4.2: *Top panel*: Detected UFOs with $\geq$ 95 per cent Monte Carlo significance from the velocity determination simulations (see text for details) based on input velocities $v_{\rm UFO} = 0.05c,\ 0.15c,\ 0.25c$. *Bottom panel*: The corresponding retrieved $v_{\rm UFO}$ values based on the detected features in the top panel. Corresponding colour in each panel represents the same simulation.

outflow velocity. The results, shown in Figure 4.2, clearly display that we are able to recover the input outflow velocity within $\Delta v_{\rm out} \sim \pm 0.02c$ independent of the input outflow velocity. This result is significant for a multitude of reasons. First, it shows that despite the

XABSUFO model indeed including the higher transitions of Fe listed in Table 4.3, for relatively standard wind parameters we are not able to significantly detect these features. Therefore, a spectrum exhibiting absorption features at higher energies consistent with Heγ, Heδ, Lyγ, and/or Lyδ may in fact be exhibiting a separate wind component entirely. Second, we find that even at the highest outflow velocities, which push the absorption features near the *XMM-Newton* EPIC pn band pass upper limit, we are able to detect the features with high precision. Therefore, absorption features near the 10 keV upper limit can still be reported with a high degree of confidence.

4.4.3.2 Application of a physical outflow model

Once a set of statistically significant outflow velocities were determined for each observation, we then applied a physically motivated photoionised absorption spectral model to the data using XABSUFO. For each unique statistically significant outflow velocity (i.e. those not found to be within $\Delta v_{\rm out} = \pm 0.02c$ of each other) we inserted an XABSUFO component initially fixed at the measured velocity, with $\log \xi$ and $N_{\rm H}$ left free to vary and $v_{\rm turb} = 2000$ km s^{-1} kept fixed. Once an acceptable fit was obtained, we then tested the fit improvement of allowing $v_{\rm UFO}$ to be free to vary. Then, the fit improvement of allowing $v_{\rm turb}$ to be free to vary was assessed. In many sources, multiple highly significant velocity solutions were found in the velocity determination curves. In such cases, we evaluated the fits obtained when allowing the multiple XABSUFO components to have parameters free to vary independently of one another as well as when $\log \xi_{\rm UFO}$, $N_{\rm H,UFO}$, and $v_{\rm turb}$ of the multiple components were linked together. In most instances, linking the multiple XABSUFO

components (except in $v_{\rm UFO}$) provided an equally good fit quality as leaving the components free to vary independently. The results of this fitting procedure are listed in Table 4.4, with corresponding reflection parameters and any additional model component parameters are listed in Table 4.5 and Table 4.6, respectively.

We make special note of the low-log $\xi_{\rm UFO}$ components in 1H 0707−495 and IRAS 13224−3809. While the significance contours and velocity determination curves did not exhibit strong evidence of such components, we found that when applying an XABSUFO component to the spectra the low-log $\xi_{\rm UFO}$ was always found. Furthermore, the significance contours and velocity determination curves of 1H 0707−495 were exceptionally broad, and therefore we found it necessary to include two (linked) XABSUFO components to describe what appears as a single feature. Even with extremely high $v_{\rm turb} > 20\ 000$ km s^{-1} a single component was not able to adequately describe the detected feature. We conduct forthcoming analyses including these UFOs, though we note that the results do not change significantly when they are omitted.

Table 4.4: Source (1) and observation (2) followed by the best-fit UFO parameters from the XABSUFO model in columns (3)-(6). Column (7) lists the fit improvement ΔC to the best-fit reflection model for the inclusion of the relevant UFO with a number of additional free parameters $N_{\rm fp}$. Column (8) lists the fit statistic C and degrees of freedom dof of the final best-fit model (corresponding reflection parameters are in Table 4.5 with additional model parameters in Table 4.6). Parameter values followed by a superscript t indicate linkage between an equivalent parameter value. Parameter values followed by a superscript f were frozen to the value during fitting. Errors followed by a superscript p indicate that the corresponding parameter value reached the lower/upper limit of the model parameter range. Errors represent 90 per cent confidence intervals on parameter values.

Source Name	Obs. ID	$\log \xi_{\rm UFO}$	$N_{\rm H,UFO}$	$v_{\rm turb}$	$v_{\rm UFO}$	$\Delta C/N_{\rm fp}$	C/dof
		$\left[\text{erg cm s}^{-1}\right]$	$\left[\times 10^{24}\ \text{cm}^{-2}\right]$	$\left[\times 10^{3}\ \text{km s}^{-1}\right]$	$[c]$		
1H 0419−577	0148000201	4.0 ± 0.3	$0.09^{+0.09}_{-0.04}$	2^{f}	-0.08 ± 0.01	$-10/3$	146/162
		4.0^{t}	0.09^{t}	2^{t}	-0.400 ± 0.007	$-3/1$	
1H 0707−495	0511580101	3.25 ± 0.06	$0.010^{+0.002}_{-p}$	9 ± 2	$-0.02^{+0.01}_{-0.02}$	$-127/4$	260/182
		$4.17^{+0.02}_{-0.03}$	$0.9^{+0.1}_{-0.2}$	9^{t}	$-0.101^{+0.006}_{-0.007}$	$-268/3$	
		4.17^{t}	0.9^{t}	9^{t}	$-0.185^{+0.006}_{-0.008}$	$-64/1$	
	0653510601	$3.25^{+0.16}_{-0.07}$	$0.012^{+0.005}_{-0.001}$	10 ± 3	-0.03 ± 0.02	$-478/4$	213/182
		$4.20^{+0.02}_{-0.03}$	$0.9^{+1.0}_{-0.2}$	10^{t}	$-0.118^{+0.009}_{-0.010}$	$-128/3$	
		4.20^{t}	0.9^{t}	10^{t}	$-0.173^{+0.008}_{-0.009}$	$-13/1$	
IRAS 13224−3809	0780561501	$3.21^{+0.09}_{-0.21p}$	$0.022^{+0.006}_{-0.007}$	17 ± 3	$-0.11^{+0.02}_{-0.03}$	$-531/4$	206/174

		$4.19^{+0.10}_{-0.09}$	$9.98^{+0.01}_{-0.02}$	17^{t}	$-0.221^{+0.006}_{-0.010}$	$-157/3$	
	0792180101	$3.3^{+0.1}_{-0.2}$	$0.021^{+0.019}_{-0.008}$	21 ± 3	$-0.12^{+0.02}_{-0.04}$	$-262/4$	202/174
		$4.20^{+0.16}_{-0.06}$	9.97 ± 0.02	21^{t}	-0.227 ± 0.007	$-293/3$	
IRAS 13349+2438	0096010101	4.35 ± 0.08	$1.5^{+5.9}_{-0.9}$	9^{+7}_{-3}	$-0.137^{+0.010}_{-0.009}$	$-67/4$	172/164
	0402080301	$4.25^{+0.07}_{-0.04}$	$1.5^{+4.1}_{-0.7}$	13^{+4}_{-3}	$-0.137^{+0.007}_{-0.006}$	$-136/4$	237/183
MR 2251−178	0670120201	$4.6^{+0.1}_{-0.4}$	$0.10^{+0.15}_{-0.08}$	2^{f}	$-0.288^{+0.009}_{-0.015}$	$-10/3$	269/193
		4.6^{t}	0.10^{t}	2^{t}	-0.345 ± 0.005	$-13/1$	
	0670120401	$4.3^{+0.3}_{-0.2}$	$0.04^{+0.16}_{-0.02}$	2^{f}	-0.337 ± 0.005	$-24/3$	241/193
Mrk 79	0400070201	$4.5^{+0.4}_{-0.7}$	$0.10^{+0.03}_{-0.09}$	2^{f}	-0.09 ± 0.01	$-4/3$	192/177
Mrk 205	0124110101	$4.7^{+0.2}_{-0.1}$	$1.1^{+1.4}_{-0.9}$	2^{f}	-0.094 ± 0.009	$-12/3$	134/152
Mrk 509	0130720101	$4.95^{+0.05p}_{-0.5}$	$0.5^{+0.3}_{-0.4}$	2^{f}	$-0.168^{+0.006}_{-0.005}$	$-12/3$	185/189
		4.95^{t}	0.5^{t}	2^{t}	$-0.29^{+0.01}_{-0.02}$	$-8/1$	
	0306090401	$4.1^{+0.3}_{-0.2}$	$0.02^{+0.03}_{-0.01}$	2^{f}	$-0.21^{+0.01}_{-0.02}$	$-6/3$	200/196
		4.1^{t}	0.02^{t}	2^{t}	$-0.308^{+0.009}_{-0.007}$	$-13/1$	
Mrk 766	0304030301	4.6 ± 0.1	$0.26^{+0.44}_{-0.08}$	2^{f}	$-0.044^{+0.008}_{-0.012}$	$-15/3$	284/187
		4.6^{t}	0.26^{t}	2^{t}	$-0.264^{+0.007}_{-0.008}$	$-24/1$	

	0304030501	$4.5^{+0.2}_{-0.3}$	$0.12^{+0.16}_{-0.04}$	2^{f}	-0.085 ± 0.008	$-12/3$	362/187
		4.5^{t}	0.12^{t}	2^{t}	$-0.270^{+0.008}_{-0.011}$	$-14/1$	
Mrk 841	0205340401	4.5 ± 0.2	0.3 ± 0.1	2^{f}	$-0.04^{+0.01}_{-0.02}$	$-13/3$	177/179
		4.5^{t}	0.3^{t}	2^{t}	$-0.287^{+0.008}_{-0.007}$	$-9/1$	
NGC 3516	0401210601	$3.24^{+0.06}_{-0.03}$	$0.016^{+0.003}_{-0.001}$	2^{f}	$-0.018^{+0.004}_{-0.005}$	$-337/3$	288/186
		$4.5^{+0.2}_{-0.1}$	$0.10^{+0.03}_{-0.07}$	2^{t}	-0.162 ± 0.008	$-9/3$	
		4.5^{t}	0.08^{t}	2^{t}	$-0.300^{+0.006}_{-0.007}$	$-8/1$	
NGC 3783	0112210101	$4.5^{+0.2}_{-0.3}$	$0.10^{+0.17}_{-0.08}$	2^{f}	$-0.095^{+0.009}_{-0.012}$	$-16/3$	216/178
NGC 4051	0109141401	$4.87^{+0.09}_{-0.14}$	$0.33^{+0.27}_{-0.05}$	2^{f}	-0.019 ± 0.005	$-29/3$	358/211
	0157560101	$4.1^{+0.2}_{-0.1}$	$0.2^{+0.2}_{-0.08}$	2^{f}	$-0.156^{+0.007}_{-0.006}$	$-25/3$	356/180
PDS 456	0721010401	4.4 ± 0.1	$0.7^{+0.8}_{-0.4}$	17^{+5}_{-7}	-0.28 ± 0.01	$-83/4$	243/182
		4.4^{t}	0.7^{t}	17^{t}	-0.45 ± 0.02	$-8/1$	
PG 1211+143	0112610101	$4.48^{+0.09}_{-0.07}$	10^{+1}_{-2}	8^{+8}_{-3}	$-0.095^{+0.007}_{-0.012}$	$-87/4$	206/177
PG 1448+273	0781430101	$4.1^{+0.2}_{-0.1}$	$0.5^{+0.4}_{-0.2}$	7^{+6}_{-4}	$-0.09^{+0.009}_{-0.008}$	$-53/4$	172/160

Table 4.5: Source (1) and observation (2) followed by the best-fit continuum parameters from the CLUMIN × CUTOFFPL+CONSTANT × CLUMIN × RELXILLD+XILLVERD base model in columns (3)-(12). Parameter values followed by a superscript t indicate linkage between an equivalent parameter value. Parameter values followed by a superscript f were frozen to the listed value during fitting. Errors followed by a superscript p indicate that the corresponding parameter value reached the lower/upper limit of the model parameter range. Errors represent 90 per cent confidence intervals on parameter values.

Source Name	Obs. ID	CLUMIN	CUTOFFPL	CONST	RELXILLD						XILLVERD
		$\log L_{0.1-100\mathrm{keV}}$ [erg s^{-1}]	Γ	$R_{0.1-100\mathrm{keV}}$	q_{in}	a	θ [degrees]	$\log \xi$ [erg cm s^{-1}]	A_{Fe}	$\log n_e$ [cm^{-3}]	N_{X} [$\times 10^{-5}$]
1H 0419−577	0148000201	$44.43^{+0.08}_{-0.07}$	$1.74^{+0.05}_{-0.03}$	$5.2^{+0.9}_{-0.7}$	$8.7^{+0.9}_{-1.2}$	0.998^{f}	68^{+2}_{-4}	$1.3^{+0.2}_{-0.3}$	2.9 ± 0.4	15^{f}	–
1H 0707−495	0511580101	$44.45^{+0.05}_{-0.07}$	2.88 ± 0.02	0.36 ± 0.07	$4.8^{+0.6}_{-0.8}$	0.998^{f}	78.7 ± 0.4	$2.03^{+0.06}_{-0.03}$	$8.6^{+1.0}_{-0.7}$	$19.0^{+p}_{-0.1}$	–
		44.45^{t}	2.88^{t}	$1.27^{+0.08}_{-0.10}$	4.8^{t}	0.998^{t}	78.7^{t}	$0^{+0.04}_{-p}$	8.7^{t}	19.0^{t}	–
	0653510601	$44.63^{+0.3}_{-0.09}$	3.17 ± 0.01	$0.27^{+0.04}_{-0.02}$	5.4 ± 0.6	0.998^{t}	78.7^{t}	$2.31^{+0.01}_{-0.10}$	8.7^{t}	19.0^{t}	–
		44.63^{t}	3.17^{t}	$1.8^{+0.1}_{-0.2}$	5.4^{t}	0.998^{t}	78.7^{t}	0^{t}	8.7^{t}	19.0^{t}	–
IRAS 13324−3809	0780561601	$46.71^{+0.09}_{-0.14}$	2.89 ± 0.03	$1.9^{+0.4}_{-0.3}$	$10.0^{+p}_{-0.5}$	0.998^{f}	$87.2^{+0.3}_{-0.4}$	$1.44^{+0.20}_{-0.07}$	$4.6^{+0.5}_{-0.6}$	$19.0^{+p}_{-0.2}$	–
		46.71^{t}	2.89^{t}	$5.3^{+0.4}_{-0.9}$	10.0^{t}	0.998^{t}	87.2^{t}	$0^{+0.07}_{-p}$	4.6^{t}	19.0^{t}	–
	0792180101	46.8 ± 0.2	2.86 ± 0.03	$1.7^{+0.3}_{-0.2}$	10.0^{t}	0.998^{t}	87.2^{t}	1.44^{t}	4.6^{t}	19.0^{t}	–
		46.8^{t}	2.86^{t}	$4.5^{+0.3}_{-0.9}$	10.0^{t}	0.998^{t}	87.2^{t}	0^{t}	4.6^{t}	19.0^{t}	–
IRAS 13349+2438	0096010101	$45.5^{+0.5}_{-0.2}$	3.03 ± 0.06	$4.6^{+0.5}_{-0.9}$	10^{+p}_{-4}	$0.6^{+0.2}_{-0.1}$	65^{+3}_{-1}	$0^{+0.02}_{-p}$	$1.70^{+0.6}_{-0.7}$	$19.0^{+p}_{-0.2}$	–
	0402080301	$45.47^{+0.01}_{-0.14}$	2.71 ± 0.06	$3.0^{+0.4}_{-0.6}$	10^{t}	0.6^{t}	65^{t}	0^{t}	1.7^{t}	19.0^{t}	–
MR 2251−178	0670120201	$45.26^{+0.30}_{-0.05}$	$1.844^{+0.009}_{-0.008}$	0.36 ± 0.02	$2.1^{\pm}0.6$	0.998^{f}	26 ± 3	$1.30^{+0.07}_{-0.09}$	$0.5^{+0.05}_{-p}$	15^{f}	–
	0670120401	$45.18^{+0.09}_{-0.01}$	$1.829^{+0.011}_{-0.008}$	0.36 ± 0.02	2.1^{t}	0.998^{t}	26^{t}	1.30^{t}	0.5^{t}	15^{t}	–
Mrk 79	0400070201	$44.0^{+0.3}_{-0.06}$	2.00 ± 0.03	$0.8^{+0.3}_{-0.1}$	$5.7^{+0.6}_{-0.4}$	0.998^{f}	45^{+8}_{-6}	$2.2^{+0.2}_{-0.1}$	1^{f}	$19.0^{+p}_{-0.2}$	8^{+3}_{-2}
Mrk 205	0124110101	$44.7^{+1.1}_{-0.2}$	$2.05^{+0.03}_{-0.02}$	0.5 ± 0.1	6^{f}	0.998^{f}	65^{+6}_{-12}	$0^{+0.2}_{-p}$	1^{f}	15^{f}	6^{+60}_{-4}
Mrk 509	0130720101	44.8 ± 0.2	$2.00^{+0.04}_{-0.03}$	$0.50^{+0.05}_{-0.04}$	5.7 ± 0.7	$0.97^{+0.01}_{-0.02}$	16^{+1}_{-7}	1.2 ± 0.2	$0.6^{+0.3}_{-0.1}$	15^{f}	23^{+7}_{-6}
	0306090401	44.59 ± 0.03	2.19 ± 0.02	$0.49^{+0.05}_{-0.04}$	6.6 ± 0.2	0.97^{t}	16^{t}	$1.4^{+0.3}_{-0.1}$	0.6^{t}	15^{t}	9 ± 2
Mrk 766	0304030301	43.4 ± 0.2	2.39 ± 0.05	$2.7^{+0.8}_{-0.7}$	$6.1^{+0.2}_{-0.3}$	0.998^{f}	17^{+6}_{-4}	$2.29^{+0.07}_{-0.14}$	$0.5^{+0.05}_{-p}$	$17.9^{+0.1}_{-0.5}$	10^{+3}_{-2}
	0304030501	$43.5^{+0.2}_{-0.1}$	$2.45^{+0.04}_{-0.09}$	$2.4^{+0.3}_{-0.8}$	6.1 ± 0.2	0.998^{t}	17^{t}	2.3 ± 0.2	0.5^{t}	17.9^{t}	7 ± 2
Mrk 841	0205340401	$44.40^{+0.50}_{-0.05}$	1.96 ± 0.02	0.53 ± 0.08	$3.7^{+0.8}_{-1.0}$	0.998^{f}	33^{+9}_{-8}	$1.30^{+0.09}_{-0.25}$	$0.5^{+0.3}_{-p}$	15^{f}	6 ± 3
NGC 3516	0401210601	$43.47^{+0.26}_{-0.03}$	$2.30^{+0.03}_{-0.05}$	$0.78^{+0.06}_{-0.12}$	$5.0^{+0.2}_{-0.3}$	$0.978^{+0.008}_{-0.009}$	27^{+2}_{-3}	$1.69^{+0.03}_{-0.24}$	$2.8^{+0.2}_{-0.4}$	15^{f}	33^{+5}_{-6}
NGC 3783	0112210101	$43.67^{+0.15}_{-0.03}$	1.93 ± 0.03	$0.51^{+0.12}_{-0.06}$	$4.9^{+2.5}_{-0.4}$	0.998^{f}	37^{+5}_{-4}	$2.3^{+0.1}_{-0.2}$	$0.5^{+0.2}_{-p}$	$19.0^{+p}_{-0.2}$	35^{+2}_{-4}
NGC 4051	0109141401	$42.18^{+0.05}_{-0.02}$	$2.07^{+0.02}_{-0.01}$	$0.51^{+0.07}_{-0.05}$	$7.0^{+0.3}_{-0.2}$	0.87 ± 0.03	26^{+2}_{-3}	$2.68^{+0.04}_{-0.11}$	$3.2^{+0.3}_{-0.5}$	$18.86^{+0.14p}_{-0.09}$	17^{+2}_{-1}
	0157560101	$41.26^{+0.05}_{-0.07}$	2.20 ± 0.02	$2.9^{+0.3}_{-0.5}$	$5.1^{+0.3}_{-0.4}$	0.87^{t}	26^{t}	$0.69^{+0.02}_{-0.33}$	3.2^{t}	18.86^{t}	9^{+2}_{-1}
PDS 456	0721010401	$46.1^{+0.4}_{-0.2}$	$2.8^{+0.02}_{-0.03}$	$4.2^{+0.5}_{-0.4}$	5.3 ± 0.6	0.998^{f}	72^{+2}_{-4}	$0.71^{+0.04}_{-0.12}$	$4.6^{+0.5}_{-0.4}$	$19.0^{+p}_{-0.1}$	–
PG 1211+143	0112610101	$46.3^{+0.7}_{-1.7}$	$2.57^{+0.03}_{-0.04}$	$3.0^{+0.4}_{-0.5}$	$7.2^{+0.9}_{-0.7}$	0.998^{f}	72^{+2}_{-1}	$0^{+0.7}_{-p}$	$2.4^{+0.7}_{-0.8}$	$19.0^{+p}_{-0.2}$	–
PG 1448+273	0781430101	$44.20^{+0.14}_{-0.09}$	$2.80^{+0.09}_{-0.06}$	$4.5^{+0.8}_{-1.0}$	$7^{\pm}1$	0.998^{f}	72 ± 2	$0^{+0.2}_{-p}$	1^{f}	$19.0^{+p}_{-0.2}$	–

Table 4.6: Source (1) and observation (2) followed by the best-fit parameters of any additional model component(s). Intrinsic neutral absorption column density $N_{\rm H,AGN}$ by ZTBABS is given in column (3). Photoionised emission by PION is given in columns (4)-(5). Warm absorption by XABS is given in columns (6)-(9). Parameter values followed by a superscript t indicate linkage between an equivalent parameter value. Parameter values followed by a superscript f were frozen to the listed value during fitting. Errors followed by a superscript p indicate that the corresponding parameter value reached the lower/upper limit of the model parameter range. Errors represent 90 per cent confidence intervals on parameter values.

Source Name	Obs. ID	ZTBABS	PION		XABS			
		$N_{\rm H,AGN}$	$\log \xi_{\rm P}$	$N_{\rm P}$	$\log \xi_{\rm WA}$	$N_{\rm H,WA}$	$v_{\rm turb}$	$v_{\rm WA}$
		$[\times 10^{20}$ cm$^{-2}]$	[erg cm s^{-1}]		[erg cm s^{-1}]	$[\times 10^{21}$ cm$^{-2}]$	[km s^{-1}]	[km s^{-1}]
1H 0419−577	0148000201	–	–	–	1.6 ± 0.4	$2.1^{+1.7}_{-0.9}$	100^{f}	0^{f}
IRAS 13349+2438	0096010101	–	–	–	$2.44^{+0.12}_{-0.09}$	25^{+5}_{-4}	361^{f}	-578^{f}
					-0.2 ± 0.2	6.1 ± 0.6	267^{f}	-524^{f}
	0402080301	–	–	–	2.38 ± 0.05	42 ± 5	361^{t}	-578^{t}
					$-0.3^{+0.1}_{-0.2}$	$6.3^{+0.6}_{-0.5}$	267^{t}	-524^{t}
MR 2251−178	0670120201	–	$2.00^{+0.21}_{-0.08}$	$1.4^{+0.6}_{-0.4}$	4.0 ± 0.2	13^{+6}_{-3p}	1000^{f}	0^{f}
					$3.0^{+p}_{-0.2}$	3^{+2}_{-1}	100^{f}	0^{f}
					$2.16^{+0.09}_{-0.10}$	$5.2^{+0.7}_{-1.1}$	100^{f}	-470^{f}
					0.9 ± 0.1	1.4 ± 0.2	100^{f}	-480^{f}
	0670120401	–	2.00^{t}	1.4^{t}	$3.9^{+0.3}_{-0.2}$	10^{+5}_{-p}	1000^{t}	0^{t}
					$3.0^{+p}_{-0.1}$	3 ± 2	100^{t}	0^{t}
					$2.11^{+0.06}_{-0.08}$	$6.5^{+0.7}_{-2.0}$	100^{t}	-470^{t}

					$0.5^{+0.1}_{-0.2}$	1.2 ± 0.1	100^{t}	-480^{t}
Mrk 79	0400070201	–	–	–	-0.9 ± 0.6	$0.9^{+0.3}_{-0.4}$	100^{f}	0^{f}
Mrk 509	0130720101	–	–	–	$2.0^{+0.2}_{-0.3}$	$1.2^{+0.4}_{-0.5}$	70^{f}	0^{f}
	0306090401	–	–	–	2.3 ± 0.2	1.4 ± 0.3	70^{t}	0^{t}
					$0.5^{+0.6}_{-1.5}$	$0.2^{+0.2}_{-0.1}$	170^{f}	-120^{f}
Mrk 766	0304030301	–	$2.60^{+0.05}_{-0.15}$	$2.2^{+0.2}_{-0.3}$	$2.01^{+0.03}_{-0.07}$	$12.1^{+0.5}_{-1.3}$	100^{f}	-340^{f}
					$-1.36^{+0.16}_{-0.08}$	$2.2^{+0.2}_{-0.1}$	100^{f}	-340^{f}
	0304030501	–	2.60^{t}	$3.5^{+0.3}_{-0.4}$	$1.99^{+0.02}_{-0.05}$	12.1 ± 0.5	100^{t}	-340^{t}
					$-1.5^{+0.2}_{-0.1}$	$2.2^{+0.1}_{-0.2}$	100^{t}	-340^{t}
Mrk 841	0205340401	–	–	–	$3.0^{+p}_{-0.2}$	9^{+5}_{-7}	50^{f}	0^{f}
					$1.6^{+0.4}_{-0.5}$	$1.8^{+2.1}_{-0.5}$	50^{f}	0^{f}
NGC 3516	0401210601	$4.7^{+0.7}_{-0.6}$	–	–	$2.98^{+0.02p}_{-0.06}$	13 ± 3	400^{f}	-800^{f}
					$1.90^{+0.06}_{-0.11}$	21^{+1}_{-2}	50^{f}	-1600^{f}
					1.01 ± 0.07	$3.0^{+0.5}_{-0.7}$	50^{f}	-200^{f}
NGC 3783	0112210101	–	–	–	$3.00^{+p}_{-0.04}$	21^{+7}_{-6}	120^{f}	-480^{f}
					$2.16^{+0.08}_{-0.09}$	16 ± 2	50^{f}	-460^{f}
					$0.4^{+0.2}_{-0.3}$	2.4 ± 0.5	50^{f}	-1070^{f}
					$-0.5^{+0.6}_{-0.5}$	$0.8^{+0.6}_{-0.3}$	790^{f}	-1100^{f}
NGC 4051	0109141401	–	$2.47^{+0.05}_{-0.04}$	$5.7^{+1.0}_{-0.7}$	2.96 ± 0.04^{p}	15^{+4}_{-3}	100^{f}	0^{f}

	0157560101	–	$2.79^{+0.05}_{-0.09}$	4.5 ± 0.4	$1.5^{+0.8}_{-0.2}$	$0.5^{+0.5}_{-0.3}$	100^{f}	0^{f}
PDS 456	0721010401	–	–	–	$0.11^{+0.08}_{-0.10}$	4.2 ± 0.4	100^{f}	0^{f}
PG 1211+143	0112610101	–	–	–	$2.34^{+0.11}_{-0.07}$	$5.2^{+1.0}_{-0.7}$	1000^{f}	-21540^{f}
					$-1.0^{+0.5}_{-0.1}$	$1.4^{+0.4}_{-0.3}$	100^{f}	-23170^{f}
PG 1448+273	0781430101	4^{+4}_{-3}	–	–	$-1.3^{+1.5}_{-0.6}$	$1.1^{+0.5}_{-0.7}$	50^{f}	0^{f}

4.5 Analysis & Results

We now have a full characterization of the X-ray spectra for the 20 Type 1 AGNs in our sample using a physically motivated spectral model based on an assumed power law plus reflection scenario. We report strong evidence of UFOs ($S \geq 95$ per cent) in 16 of those AGNs, with 14 also having simultaneous optical/UV spectral coverage from the OM detector, which was used to explore further correlations with UFO parameters.

In addition to the various measured parameters from the spectral models, for each observation we computed the total X-ray luminosity in the $0.1-100$ keV band as $L_{\rm X} = L_{\rm PL} + L_{\rm R}$, where $L_{\rm PL}$ is the power law luminosity measured by CLUMIN and $L_{\rm R} = R \times L_{\rm PL}$ is the reflected X-ray luminosity computed using the reflection fraction R. We then computed the Eddington ratio $\lambda_{\rm Edd}$ in order to probe the accretion rate of each AGN during each observation. Brightman et al. (2013) found that $\Gamma = (0.32 \pm 0.05) \log \lambda_{\rm Edd} + (2.27 \pm 0.06)$, where Γ is the power law photon index. However, Waddell & Gallo (2020) showed that $\lambda_{\rm Edd} = 10 \times L_{\rm X}/L_{\rm Edd}$, where $L_{\rm Edd} \simeq 1.26 \times 10^{38}\ M_{\rm BH}$ erg s^{-1}, provided an equivalent characterisation of the accretion rate. Here we used the latter method to evaluate $\lambda_{\rm Edd}$, though we note that none of the results presented henceforth change significantly if we instead use the method of Brightman et al. (2013). All SMBH mass estimates were obtained from Ponti et al. (2012), with the exception of PG 1448+273, which comes from Vestergaard & Peterson (2006), and Swift J2127.4+5654, which comes from Malizia et al. (2008).

To ensure that individual sources were not dominating any observed trends due to enhanced variability in the parameters of a particular AGN, we evaluated correlations based

on the mean value of each parameter. This means that sources in which a UFO was detected in multiple observations had the mean UFO parameter values computed across all such observations. In some instances, multiple UFOs were detected in a source, therefore requiring the UFO parameters to be averaged across all detected UFOs, and across all observations if multiple observations reported multiple UFOs. In the forthcoming plots we also display the raw parameter values, as listed in Table 4.4 and Table 4.5.

In Figure 4.3 we present all measured parameter correlations in the form of correlation matrices. In the following paragraphs we briefly discuss the lower-significance results (i.e. Pearson correlation coefficients r corresponding to p-values of $p \leq 0.1$), presenting detailed analyses of only those correlations corresponding to $p < 0.01$ in subsequent sections.

Several parameters appear to be 'key' when evaluated based on their strong correlation to many of the parameters we explored (shown in brackets beside parameter name and variable, using X-ray-only parameter measurements, total of 13, as in the left panel of Figure 4.3): disc inclination θ (10), accretion rate $\log \lambda_{\rm Edd}$ (9), UFO column density $\log N_{\rm H,UFO}$ (8), photon index Γ (8), total X-ray luminosity $\log L_{\rm X}$ (7), reflection fraction R (7), and inner emissivity index $q_{\rm in}$ (7). Boroson & Green (1992) argued that accretion rate was the most likely explanation for the coined 'Eigenvector 1' parameter space in their sample of 87 AGNs, where strong correlations between the widths and strengths of Hβ, Fe II, and [O III] were found. Later, Wang et al. (1996) showed strong correlations with X-ray luminosity via the photon index at low energies (i.e. $\lesssim 2.5$ keV) also belonged to the Eigenvector 1 parameter space. Many of our correlations in Figure 4.3 therefore appear consistent with Eigenvector 1 (i.e. $\log \lambda_{\rm Edd}$, Γ, $\log L_{\rm X}$). We note that several of the parameters exhibiting many strong

correlations are very closely linked to the other parameters (e.g. $\lambda_{\rm Edd} \propto \Gamma$ according to Brightman et al. 2013; also $\lambda_{\rm Edd} \propto L_{\rm X}$ according to Waddell & Gallo 2020), sometimes by definition (e.g. $L_{\rm X} \equiv (1+R) \times L_{\rm PL}$). Therefore, it is likely than many inherent degeneracies exist between the explored parameters. This is also true for many of the reflection model parameters, where parameter estimation has been shown to be unreliable for several key parameters (i.e. inner emissivity index $q_{\rm in}$, spin a, ionisation parameter $\log \xi_{\rm R}$; Bonson & Gallo 2016), though we closely followed the recommendations (when applicable) of Reynolds (2014) in an attempt to alleviate as many of these issues as possible. Still, we find it intriguing that disc inclination and UFO column density so strongly and plentifully correlate with other parameters. We leave discussion of these particular parameters in the context of an alternative (i.e. slim) accretion disc model interpretation to Section 4.6. Finally, black hole spin, disc ionisation parameter, and UFO outflow velocity were found to correlate with virtually no other parameters in the sample. The lack of correlations here suggest either that these parameters are poorly sampled in our work (i.e. do not cover an appropriate range of their parameter space), that they are measured inaccurately / improperly (e.g. Bonson & Gallo 2016), and / or that they exhibit more complex (i.e. than linear) relationships with other parameters.

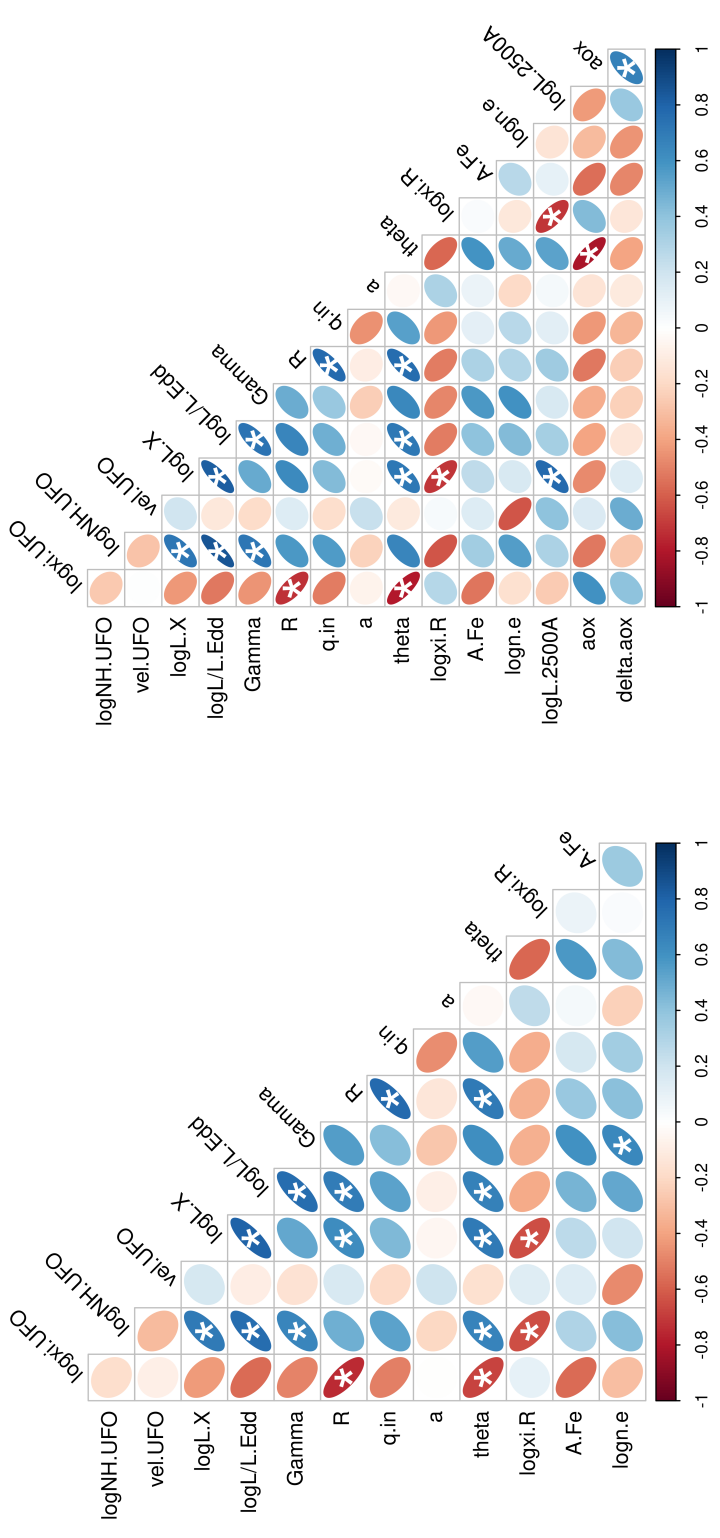

Figure 4.3: *Left panel:* Pearson correlation coefficients r of all tested parameters for those sources with UFO detections. Negative/positive ellipse direction indicate anti-correlation/correlation. Darker red/blue colours and more elliptical shapes indicate stronger anti-correlations/correlations. Ellipses marked with a white $*$ indicate a(n) (anti-)correlation corresponding to $p < 0.01$. *Right panel:* Same as left, now using the subset of sources with UFO detections that also had OM data available for analysis. In both panels, $v_{\rm UFO}$ is computed using the mean of the highest UFO velocities in each source (see 4.5.3 for details).

In general, the inclusion of optical/UV data for 14 of the 16 AGNs with UFOs in the sample does not significantly change the correlations discussed above (comparing left and right panels of Figure 4.3). Of the three additional parameters afforded by this multi-wavelength data (see Section 4.5.4 for their definitions), we find that $\alpha_{\rm OX}$ (7) is most abundantly correlated, while $L_{2500\text{Å}}$ (3) and $\Delta\alpha_{\rm OX}$ (3) are much less so. Many of the $\alpha_{\rm OX}$ correlations in fact closely follow those with accretion rate and disc inclination angle, with $\alpha_{\rm OX}$ itself being very tightly correlated with inclination ($r = 0.81$, $p = 0.0004$). These results are also discussed in the context of slim accretion discs in Section 4.6, likely pointing towards very disc-dominated SEDs in those extreme AGNs.

4.5.1 UFO ionisation state

We first explored correlations with UFO ionisation state, measured by $\log \xi_{\rm UFO}$ from the XABSUFO model. Both reflection fraction R ($r = -0.75$, $p = 0.0009$) and disc inclination θ ($r = -0.68$, $p = 0.004$) were found to exhibit strong anti-correlations with $\log \xi_{\rm UFO}$ (Figure 4.4).

An increase in R may be interpreted as a reduction in the coronal height and/or a reduction in coronal beaming (e.g. Gonzalez et al. 2017). With the ionising coronal X-ray emission being increasingly directed toward the inner disc due to the extreme light-bending near the SMBH for larger values of R, a reduction in $\log \xi_{\rm UFO}$ may be expected as a natural consequence of this geometry. Furthermore, reflection-dominated scenarios with $R > 1$ would produce a softer ionising continuum than power law-dominated scenarios with $R < 1$, in which case the illumination of the UFO material by the softer reflection-dominated

continuum would naturally lead to a reduction in $\log \xi_{\rm UFO}$.

Edge-on systems (i.e. larger values of θ) may exhibit lower $\log \xi_{\rm UFO}$ values as a result of the structure of the UFO itself. Typical launching radii of $\sim 100\ r_g$ with large opening angles would result in an increased wind cross section along our line of sight viewing angle for larger θ. As a result, material on the innermost layer of the UFO (i.e. directly illuminated by the X-ray source) would become the most highly ionised while material in deeper layers would have correspondingly reduced $\log \xi_{\rm UFO}$ as a result of the additional absorption and scattering of the ionising continuum from interior layers, producing the observed trend.

Notably, 1H 0707−495 is a clear outlier in the $\log \xi_{\rm UFO} - R$ anti-correlation (see Figure 4.4, left), finding $\log \left(\xi_{\rm UFO}/\text{erg cm s}^{-1}\right) \sim 4.0$ for $R \sim 1.9$. The X-ray corona in this AGN has been interpreted as significantly radially extended (e.g. Kara et al. 2013; Wilkins et al. 2014). Such a coronal geometry would result in a partially covered inner disc region, thereby leading to the Comptonization of the X-ray reflection spectrum itself. This scenario has been shown to artificially reduce R when using standard reflection models (Wilkins & Gallo 2015b), offering a plausible explanation as to the outlying nature of 1H 0707−495 in this space.

Mrk 205 does not conform with the $\log \xi_{\rm UFO} - \theta$ anti-correlation (see Figure 4.4, right), where we found that $\log \left(\xi_{\rm UFO}/\text{erg cm s}^{-1}\right) \sim 4.7$ for $\theta \sim 65°$. As one of the lowest quality spectra in the entire sample (see column (5) of Table 4.1), requiring numerous model parameters to be kept fixed to their initially assumed values, and with only a single spectrum used to characterise all of spectral properties of the source, the results of Mrk 205 may be suffering from low data quality.

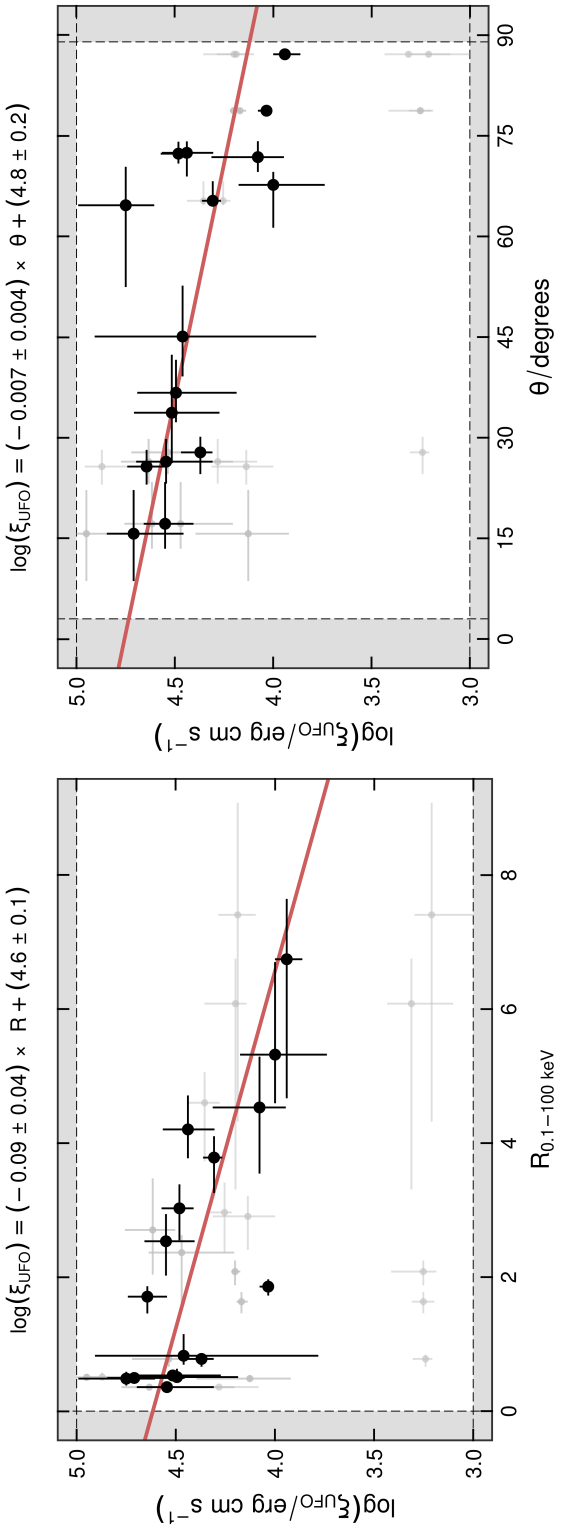

Figure 4.4: *Left panel:* UFO ionisation parameter $\log \xi_{\rm UFO}$ plotted as a function of reflection fraction $R_{0.1-100\ \rm keV}$. A strong anti-correlation is observed, with a Pearson correlation coefficient of $r = -0.75$ corresponding to a p-value of $p = 0.0009$. *Right panel:* Same as left, now plotting disc inclination angle θ as the independent variable. A strong anti-correlation is observed, with $r = -0.68$ corresponding to $p = 0.004$. In both panels, the grey data points represent measured parameter values for individual observations, the grey shaded regions bordered by dashed lines indicate parameter ranges not available in the spectral models, and the best-fit linear regression to the data is plotted as the red solid line with regression equation given above the top axis. Regression parameters are estimated at the 90 per cent confidence level.

4.5.2 UFO column density

UFO column density, measured by $N_{\rm H,UFO}$ from the XABSUFO model and logarithmically rescaled to $\log N_{\rm H,UFO}$, was found to be strongly associated with accretion rate $\log \lambda_{\rm Edd}$ ($r = 0.77$, $p = 0.0005$), total X-ray luminosity $\log L_{\rm X}$ ($r = 0.71$, $p = 0.002$), disc inclination θ ($r = 0.66$, $p = 0.005$), power law photon index Γ ($r = 0.65$, $p = 0.006$), and disc ionisation parameter $\log \xi_{\rm R}$ ($r = -0.64$, $p = 0.007$) (see Figures 4.5, 4.6, and 4.7).

Gofford et al. (2015) estimated the upper limit on the UFO mass outflow rate as $\dot{M}_{\rm UFO}^{\rm max} \propto L_{\rm ion}$, where $L_{\rm ion}$ is the ionising continuum illuminating the wind, which in this work is represented by $L_{\rm ion} = L_{\rm X}$, suggesting we have found that more luminous AGNs drive more massive outflows owing to the strong $\log N_{\rm H,UFO} - \log L_{\rm X}$ correlation (see Figure 4.5, right). In addition, those authors estimated the UFO mass outflow lower limit as $\dot{M}_{\rm UFO}^{\rm min} \propto N_{\rm H,UFO}$, suggesting that more massive outflows exist in systems with higher accretion rates owing to the strong $\log N_{\rm H,UFO} - \log \lambda_{\rm Edd}$ correlation (see Figure 4.5, left).

We additionally note that a very strong $\log L_{\rm X} - \log \lambda_{\rm Edd}$ correlation exists in the sample, with $r = 0.80$ and $p = 0.0002$ (see Figure 4.3), indicating that the most luminous AGNs are also those with the most extreme accretion rates. This trend remained when we computed $\lambda_{\rm Edd}$ using the Brightman et al. (2013) relationship, which is exemplified by the strong $\log \lambda_{\rm Edd} - \Gamma$ correlation ($r = 0.77$, $p = 0.0006$; see Figure 4.3) and thus explains the $\log N_{\rm H,UFO} - \Gamma$ correlation (see Figure 4.6, right).

As with the $\log \xi_{\rm UFO} - \theta$ anti-correlation found earlier, the $\log N_{\rm H,UFO} - \theta$ correlation (see Figure 4.6, left) can be explained by the structure of the UFO, with increasing viewing

angles intersecting an increasing portion of the UFO. This may be expected from all three of radiatively-driven winds, MHD-driven winds, and disc-atmosphere absorption scenarios.

Finally, assuming a radiatively-driven UFO scenario, highly ionised discs may provide a matter reservoir with lower line opacity, thus being more inefficient in capturing momentum of the ionising radiation. Conversely, discs providing low-ionisation matter may exhibit more massive outflows due to the enhanced momentum capture of the launched matter. Therefore, the observed $\log N_{\rm H,UFO} - \log \xi_{\rm R}$ anti-correlation (see Figure 4.7) may suggest an overall radiative driving mechanism for UFOs in AGNs.

NGC 4051 possessed the lowest $L_{\rm X}$ measured of all sources in the sample, with $L_{\rm X} \sim 2 \times 10^{42}$ erg cm^{-2} s^{-1}, yet has a moderate UFO column density with $N_{\rm H,UFO} \sim 2.7 \times 10^{23}$ cm^{-2}, presenting a significant outlier in the $\log N_{\rm H,UFO} - \log L_{\rm X}$ trend. We note that despite a factor of ~ 3.2 difference between $L_{\rm X}$ of the two analysed observations, $N_{\rm H,UFO}$ differs by only a factor of ~ 1.6.

IRAS 13224−3809 lies far above the $\log N_{\rm H,UFO} - \log \xi_{\rm R}$ trend line, with $N_{\rm H,UFO} \sim 5 \times 10^{24}$ cm^{-2} and $\xi_{\rm R} \sim 13$ erg cm s^{-1}. We note that this source required a double reflector scenario as in Jiang et al. (2018), with one reflector measured to have $\xi_{\rm R} \sim 25$ erg cm s^{-1} and the other $\xi_{\rm R} \sim 1$ erg cm s^{-1} (the RELXILLD lower limit), in order to model two distinct ionisation zones of the accretion disc. We took the mean $\xi_{\rm R}$ value between the two reflection components as the parameter value to be used in the correlation analyses (as was done with 1H 0707−495, the other source requiring a double reflector model). However, a model incorporating a gradient of ionisation with radius of the disc would more accurately represent such a scenario (e.g. the RELXILL_ION variant). We used a double reflector scenario here in

order to more easily compare with the literature on IRAS 13224−3809, though this approach may result in a biased or inaccurately measured disc ionisation state.

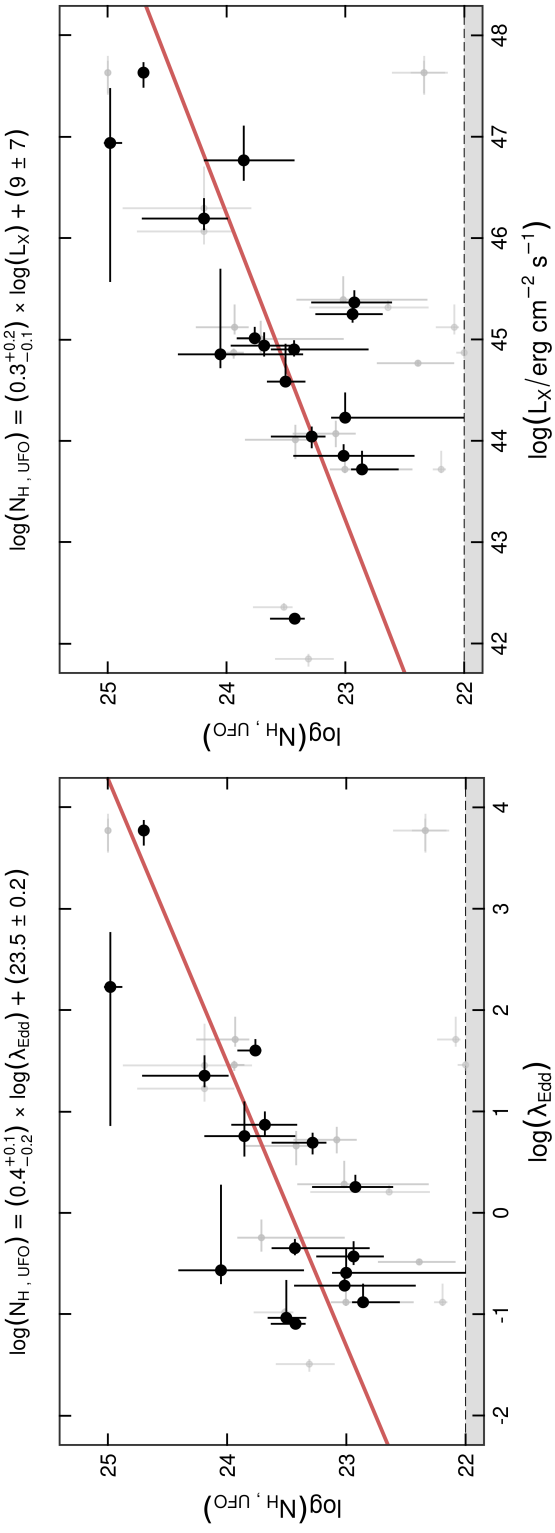

Figure 4.5: *Left panel*: UFO column density $\log N_{\rm H,UFO}$ plotted as a function of Eddington accretion rate $\log \lambda_{\rm Edd}$. A strong correlation is observed, with a Pearson correlation coefficient of $r = 0.77$ corresponding to a p-value of $p = 0.0005$. *Right panel*: Same as left, now plotting X-ray luminosity $\log L_{\rm X}$ as the independent variable. A strong correlation is observed, with $r = 0.71$ corresponding to $p = 0.002$. In both panels, the grey data points represent measured parameter values for individual observations, the grey shaded regions bordered by dashed lines indicate parameter ranges not available in the spectral models, and the best-fit linear regression to the data is plotted as the red solid line with regression equation given above the top axis. Regression parameters are estimated at the 90 per cent confidence level.

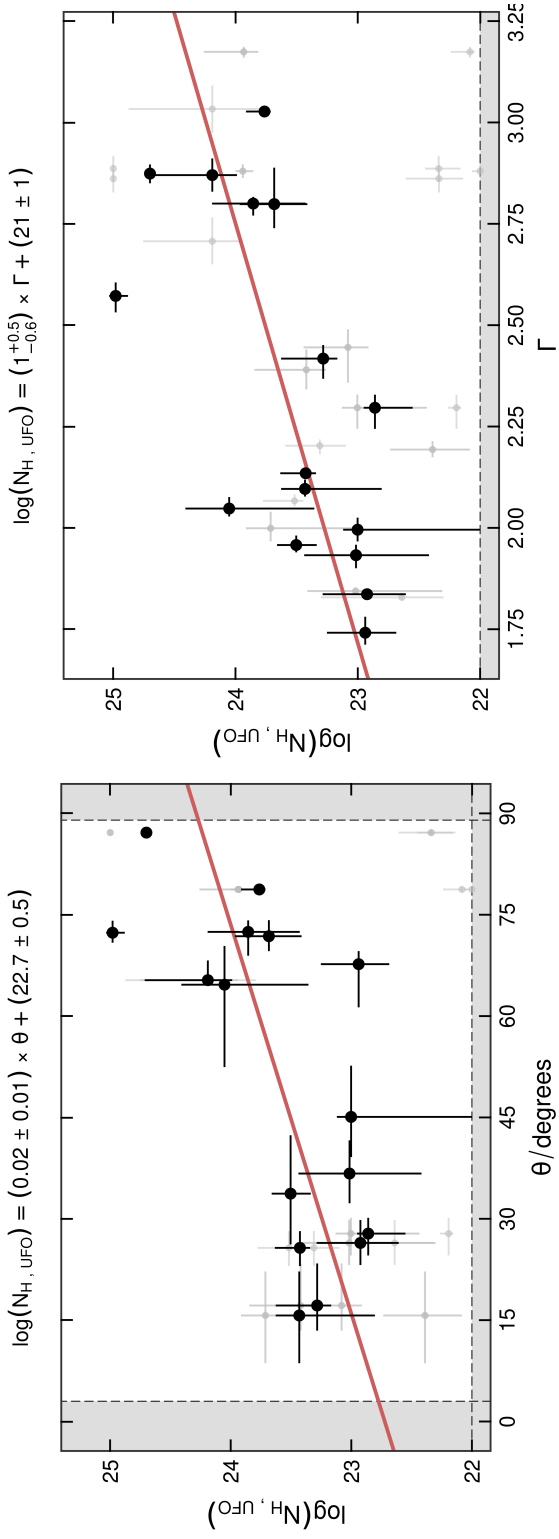

Figure 4.6: *Left panel:* Same as Figure 4.5, now plotting disc inclination angle θ as the independent variable. A strong correlation is observed, with $r = 0.66$ corresponding to $p = 0.005$. *Right panel:* Same as left, now plotting power law photon index Γ as the independent variable. A strong correlation is observed, with $r = 0.65$ corresponding to $p = 0.006$.

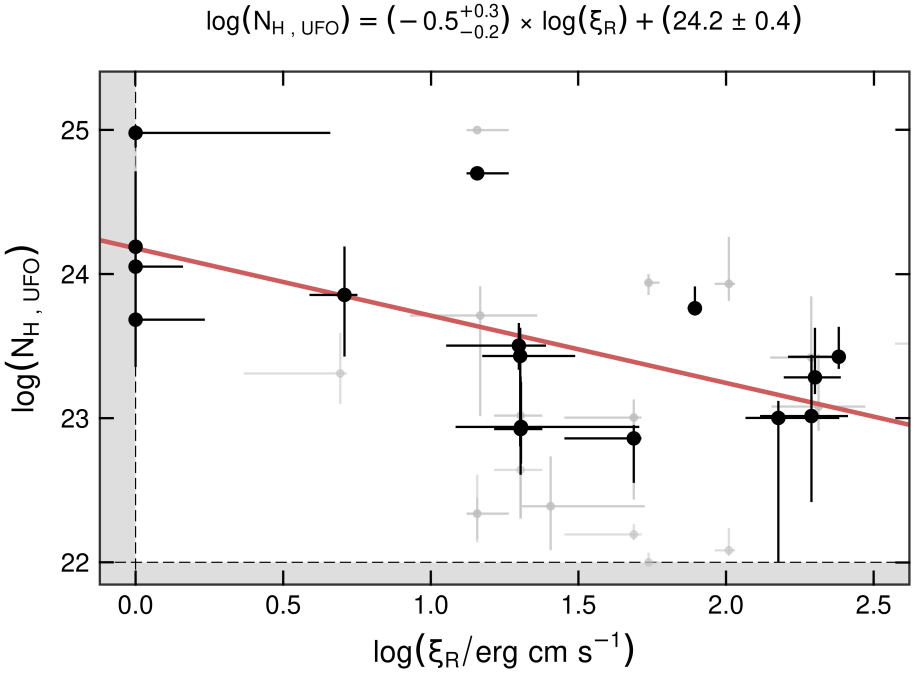

Figure 4.7: Same as Figure 4.5, now plotting disc ionisation parameter $\log \xi_{\rm R}$ as the independent variable. A strong anti-correlation is observed, with $r = -0.64$ corresponding to $p = 0.007$.

4.5.3 UFO velocity

The final UFO parameter of interest that we examined was the outflow velocity $v_{\rm UFO}$. When examining for correlations with $v_{\rm UFO}$ we computed three values to compare with the various other parameters: (1) the mean of the *lowest* velocity UFOs for each source, (2) the mean velocity among *all* UFOs for each source, and (3) the mean of the *highest* velocity UFOs for each source[16]. These various evaluations of $v_{\rm UFO}$ were done in order to probe whether

[16]Sources with multiple observations had their lowest (method 1) / highest (method 3) mean UFO velocities taken across the lowest/highest velocity UFO from each observation. Sources with a single observation did not require computation of a mean velocities for methods (1) and (3). Sources with a single UFO used that velocity regardless of applied method.

different driving mechanisms may dictate how the lowest versus highest velocity UFOs in each source are produced. In the end, we chose to use method (2), the mean $v_{\rm UFO}$ among *all* UFOs for each source, to explore parameter correlations (i.e. this is the method used to produce the $v_{\rm UFO}$ correlations in Figure 4.3).

Interestingly, $v_{\rm UFO}$ was not found to correlate strongly with any parameter, regardless of the method used to evaluate it[17]. While a moderate correlation with disc density $\log n_e$ ($r = -0.47$, $p = 0.06$ using the mean of the highest velocity UFOs in each source) was found, that relationship is difficult to properly characterise due to the measured $\log n_e$ values occupying only the extremities of the available model parameter space (i.e. parameters were often either pegged at $\log n_e = 15$ cm^{-3} or, if it was found necessary to be left free to vary, $\log n_e = 19$ cm^{-3}).

We considered that the lack of strong correlations with $v_{\rm UFO}$ may be due to a possible mixture of the various driving mechanisms, each displaying their own trends that become lost when combining them together. The $v_{\rm UFO} - \theta$ parameter space was then used to probe the possible presence of different UFO driving mechanisms (i.e. radiation pressure, MHD, and disc-atmosphere absorption) in our sample, in a manner similar to Parker et al. (2018a).

The radiatively-driven wind predictions were computed based on the simplified model used by Parker et al. (2018a). We similarly used $r_{\rm launch} = 10$, $r_{\rm curve} = 300$, $v_{\rm inf} = 0.5c$, and $R_{\rm v} = 1000$. We varied the final wind inclination, $\theta_{\rm final}$, and acceleration coefficient, β, in order to explore the parameter space coverage of this model. We used three test cases: $(i_{\rm final},\ \beta)_{\rm low} = (45°,\ 0.5)$, $(i_{\rm final},\ \beta)_{\rm mid} = (65°,\ 1)$, and $(i_{\rm final},\ \beta)_{\rm high} = (85°,\ 1.5)$ which

[17]In Figure 4.3 we show the results of $v_{\rm UFO}$ correlations computed using the mean of the highest UFO velocities in each source.

represent winds with a small opening angle and low acceleration, moderate opening angle and moderate acceleration, and large opening angle and high acceleration, respectively.

The MHD-driven wind predictions were produced by Fukumura et al. (2010b) to model the outflow in APM 08279+5255. The authors simulated outflows assuming source properties of $\lambda_{\rm Edd} = 0.5$, $\Gamma = 2$, and $\alpha_{\rm OX} = -2$ (see Section 4.5.4 for details on $\alpha_{\rm OX}$). Their $\lambda_{\rm Edd}$ and Γ values are not unrepresentative of our sample, although $\alpha_{\rm OX}$ is significantly more negative than in our sample ($\langle\alpha_{\rm OX}\rangle \approx -1.38$, see Table 4.7). Still, our goal here was to examine whether sources displayed general trends coincident with the predictions of the MHD wind model, with more rigorous modelling left for future works. As the authors only explored $\theta \in [30, 80]$, we extrapolated this curve to inclinations below 30° using a line with slope equal to the slope between the preceding two data points[18].

Finally, the disc-atmosphere absorption model predictions were approximated by computing the maximum blueshift of the intrinsic line energy of the RELLINE (Dauser et al. 2012) model for various inclinations. For this, we assumed $a = 0.998$ and $q_{\rm in} = 6$, which are standard values for each parameter that also represent our sample well ($\langle a\rangle \approx 0.96$ and $\langle q_{\rm in}\rangle \approx 6.2$, see Table 4.5). This procedure was used for the same purpose by Parker et al. (2018a).

Comparing the model predictions of the $v_{\rm UFO} - \theta$ plane for all three absorption scenarios to the sample measurements, we found that many of the UFOs in our sample can be well explained by more than one driving mechanism (Figure 4.8). In highly inclined systems, the disc-atmosphere absorption model offers a simple wind-less explanation for many of the

[18]In private communication, K. Fukumura suggested that this was an acceptable approximation, as wind velocity is expected to decrease with θ.

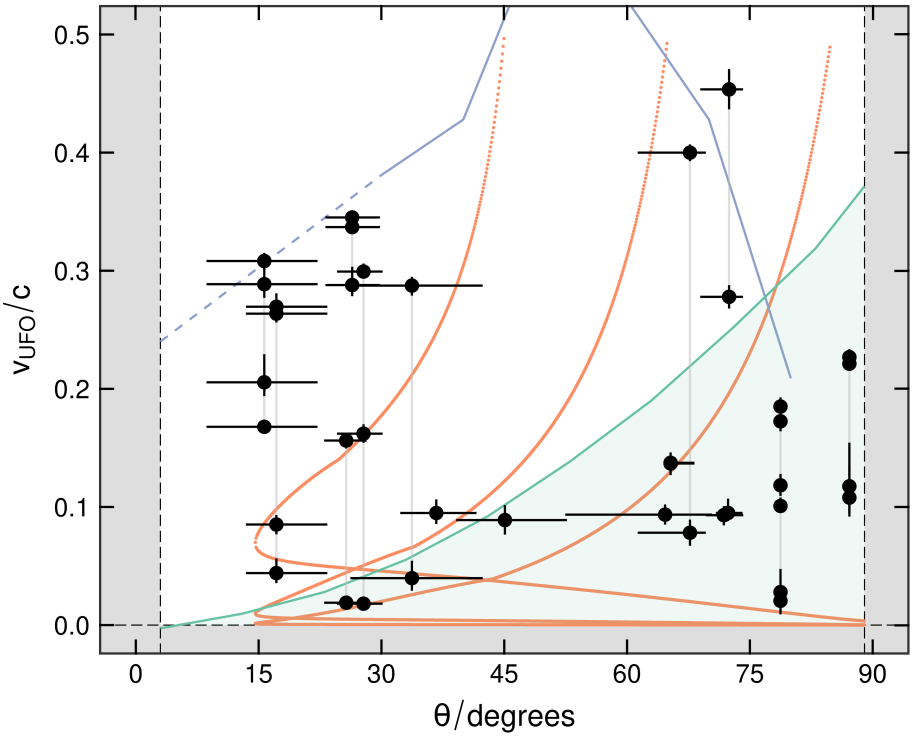

Figure 4.8: All measured UFO velocities from the sample. Vertical grey lines connect all UFOs detected in the same source. Orange curves represent the low, mid, and high radiatively-driven wind model predictions from left to right, respectively (see text for details). The blue curve represents the MHD-driven model prediction. The green curve represents the disc-atmosphere absorption model prediction, which is an upper-limit that is represented by the filled green region below the curve. The vertical grey shaded regions bordered by dashed lines indicate parameter ranges not available in the spectral models.

UFOs. In more face-on systems (i.e $\theta \lesssim 30°$), the MHD-driven wind model predicts the highest velocity UFOs in this regime of the sample. This is consistent with the wind geometry predicted by the MHD wind model, where the highest velocity stream lines are oriented nearest the SMBH spin axis. However, the three radiatively-driven model predictions used here cover a very wide range of the $v_{\rm UFO} - \theta$ parameter space, offering a plausible driving mechanism for many of the measured UFOs. Indeed, close inspection of the overlaid radiatively-driven wind models finds that several sources with multiple UFOs have their winds well represented by a single curve (e.g. Mrk 841, NGC 3516, NGC 4051). In general, it is difficult to distinguish the most plausible driving mechanism across the entire AGN population probed by our sample, with low-θ systems exhibiting UFOs apparently spanning the region bound by the radiatively- and MHD-driven wind models, but not necessarily agreeing well with one or the other particularly well, and with high-θ systems having UFOs plausibly explained as either radiatively-driven winds or as resonant absorption from a disc atmosphere, requiring no wind. We elaborate more on the interpretations of this parameter space in Section 4.6.

4.5.4 Optical/UV correlations

We have also analysed the available OM data (Table 4.7) for 14 of the 16 AGNs found to exhibit UFOs, providing several key parameters with which to characterise the optical/UV to X-ray SED. A commonly used characterisation of the optical/UV and X-ray wavebands

is the spectral index $\alpha_{\rm OX}$ (Tananbaum et al. 1979), defined as:

$$\alpha_{\rm OX} = \frac{\log\left(L_{\rm 2keV}/L_{2500\text{Å}}\right)}{\log\left(\nu_{\rm 2keV}/\nu_{2500\text{Å}}\right)} = 0.384\log\left(\frac{L_{\rm 2keV}}{L_{2500\text{Å}}}\right). \quad (4.1)$$

To estimate $L_{\rm 2keV}$, we computed the source-frame $F_{\rm 2keV}$ in XSPEC using the PEGPWRLW model, accounting for Galactic absorption using the values listed in Table 4.1.

Then, we estimated the source-frame $F_{2500\text{Å}}$ in the following manner. In those observations where the available OM filters spanned over source-frame 2500 Å, we simply performed a linear interpolation between the two nearest filters and estimated the flux accordingly. In those observations where multiple available OM filters were long/short of 2500 Å in the source frame, we extrapolated the linear fit of the two nearest filters to estimate the flux. Finally, those observations taken with only a single OM filter had their source-frame 2500 Å flux estimated by fitting the single OM filter data to the mean QSO SED from Richards et al. (2006), evaluating $F_{2500\text{Å}}$ accordingly. We then corrected the $F_{2500\text{Å}}$ estimates of each source by the Galactic reddening values listed in Table 4.1.

Table 4.7: The optical/UV data for each observation in Table 4.1, where available. The columns are: (1) source name, (2) *XMM-Newton* observation ID, and (3) available optical/UV filters, (4) specific luminosity at 2 keV, (5) specific luminosity at 2500 Å, (6) UV-to-X-ray slope $\alpha_{\rm OX}$, (7) deviance of $\alpha_{\rm OX}$ from the Vagnetti et al. (2013) relationship, and (8) method used estimate $L_{2500\text{Å}}$: I − interpolation, E − extrapolation, and S − mean QSO SED of Richards et al. (2006) (see text).

(1) Source Name	(2) Obs. ID	(3) Available Filters	(4) $\log L_{2\rm keV}$ [erg s^{-1} Hz^{-1}]	(5) $\log L_{2500\text{Å}}$ [erg s^{-1} Hz^{-1}]	(6) $\alpha_{\rm OX}$	(7) $\Delta\alpha_{\rm OX}$	(8) Est. Method
1H 0419−577	0148000201	W2, W1, U, B, V	25.99	29.94	−1.52	−0.12	I
1H 0707-495	0511580101	W1	24.97	28.75	−1.45	−0.22	S
	0653510601	W2, M2, W1, U, B, V	24.90	28.96	−1.56	−0.29	I
IRAS 13224−3809	0780561501	W1	24.74	28.87	−1.58	−0.33	S
	0792180101	W1	24.90	28.87	−1.52	−0.27	S
IRAS 13349+2438	0096010101	W2	25.99	29.30	−1.27	+0.04	S
	0402080301	W1	26.06	29.58	−1.35	0	S
MR 2251−178	0670120201	W2, M2, W1, U, B, V	26.60	29.55	−1.14	+0.21	I
	0670120401	W2, M2, W1, U, B, V	26.56	29.55	−1.15	+0.20	I
Mrk 79	0400070201	W2, M2, W1, B	24.75	28.47	−1.43	−0.23	I
Mrk 509	0130720101	W2, M2	25.92	29.35	−1.32	0	E
	0306090401	W2, M2, W1	26.12	29.41	−1.26	+0.06	I
Mrk 766	0304030501	W2, M2, W1, U, B	25.00	27.62	−1.00	+0.08	I
NGC 3516	0401210601	U	24.70	28.23	−1.35	−0.19	S
NGC 3783	0112210101	W2	25.10	28.46	−1.29	−0.09	S
NGC 4051	0109141401	W2, M2, W1	23.81	26.87	−1.17	−0.19	I
	0157560101	W2, M2, W1, U, B	23.05	26.94	−1.49	−0.50	I
PDS 456	0721010401	W2, M2, W1, U, B, V	26.79	30.62	−1.47	+0.02	I
PG 1211+143	0112610101	W2, M2, W1, U	25.73	29.89	−1.59	−0.20	I
PG 1448+273	0741280201	W2	25.28	29.16	−1.49	−0.20	S

Both flux densities were then converted into the respective specific luminosity of interest using the redshift and comoving distance values for each source obtained from the NASA/IPAC Extragalactic Database. Then, $\alpha_{\rm OX}$ was calculated accordingly. Using our $L_{2500\text{Å}}$ estimates we also computed the expected $\alpha_{\rm OX}$ value according the $\alpha_{\rm OX} - L_{2500\text{Å}}$ relationship from Vagnetti et al. (2013) of $\alpha_{\rm OX,V13} = (-0.135 \pm 0.015) \log L_{2500\text{Å}} + (2.645 \pm 0.446)$. This allowed for the relative X-ray strength to be evaluated as $\Delta\alpha_{\rm OX} = \alpha_{\rm OX} - \alpha_{\rm OX,V13}$ for each source. We note that we did not correct the $L_{\rm 2keV}$ and $L_{2500\text{Å}}$ estimates for intrinsic source absorption, a choice in line with the methodology of sample studies involving $\alpha_{\rm OX}$ (e.g. Vagnetti et al. 2013). The results of these steps are listed in Table 4.7.

Before evaluating correlations between our optical/UV parameters ($L_{2500\text{Å}}$, $\alpha_{\rm OX}$, and $\Delta\alpha_{\rm OX}$) and UFO parameters, we sought to confirm the well known $\alpha_{\rm OX} - L_{2500\text{Å}}$ anti-correlation using our sample. We found a weak anti-correlation such that $r = -0.43$ giving $p = 0.13$ (see Figure 4.3, right). The best-fit linear regression to our sample found $\alpha_{\rm OX} = (-0.07 \pm 0.08) \log L_{2500\text{Å}} + (1 \pm 2)$, in very broad agreement with the Vagnetti et al. (2013) results based on the 90 per cent confidence intervals of our regression parameter estimates. The significant scatter inherent in the $\alpha_{\rm OX} - L_{2500\text{Å}}$ relationship combined with our small sample size does not lead us to believe that our sample significantly differs from the well-established relationship. In fact, NGC 4051 lies significantly below the fit from Vagnetti et al. (2013) ($\langle L_{2500\text{Å}} \rangle = 26.91$ erg s^{-1} Hz^{-1}, $\langle \alpha_{\rm OX} \rangle = -1.33$, $\langle \Delta\alpha_{\rm OX} \rangle = -0.35$) which may be due to an unaccounted host galaxy starlight contribution to the optical/UV data.

We found that $L_{2500\text{Å}}$, unlike $L_{\rm X}$, does not correlate strongly with any UFO parameter (see Figure 4.3, right). This suggests that the disc emission does not play a pivotal role in

driving the outflows, thereby suggesting that radiatively driven winds may not be the origin of many UFOs measured here. Instead, $\alpha_{\rm OX}$ was found to exhibit a moderate correlation with $\log \xi_{\rm UFO}$ ($r = 0.60$, $p = 0.023$) and a moderate anti-correlation with $\log N_{\rm H,UFO}$ ($r = -0.52$, $p = 0.055$) (see Figure 4.3, right). Neither correlation met our $p < 0.01$ criterion, and thus they are not plotted here.

Regarding the moderate $\log \xi_{\rm UFO} - \alpha_{\rm OX}$ correlation, we note that AGNs with less negative $\alpha_{\rm OX}$ values exhibit SEDs in which the optical/UV and X-ray emission are more comparable, while those with more negative $\alpha_{\rm OX}$ values are increasingly dominated by the disc UV emission. Therefore, while $L_{2500\text{Å}}$ does not strongly relate to the UFO directly, the relative proportion of optical/UV to X-ray emission does, such that more disc dominated systems correspond to less intensely ionised UFOs. This is an expected result in all three absorption scenarios, as more disc dominated systems possess softer ionised continua, thus reducing the overall ionisation of the material in the vicinity of the SMBH.

Finally, we note that the weak $\log N_{\rm H,UFO} - \alpha_{\rm OX}$ anti-correlation produces a best-fit regression slope consistent with zero within the 90 per cent confidence interval. Nevertheless, such a correlation may be expected based on the previously determined $\log N_{\rm H,UFO} - \lambda_{\rm Edd}$ correlation. Increased accretion rate leads to an increasingly disc-dominated SED, thus resulting in more negative $\alpha_{\rm OX}$ values, a trend that is observed very weakly in our sample ($\alpha_{\rm OX} - \lambda_{\rm Edd}$ anti-correlation from Figure 4.3 gives $r = -0.40$, $p = 0.157$). The $\log N_{\rm H,UFO} - \alpha_{\rm OX}$ anti-correlation and $\log N_{\rm H,UFO} - \lambda_{\rm Edd}$ correlation may therefore be multirwavelength counterparts confirming the same general trend of more dense winds in more rapidly accreting AGNs.

4.6 Discussion

The results of our analysis highlight a variety of interesting relationships between the X-ray emitting region and UFOs in AGNs. Before exploring physical scenarios in which we may place our results into context, we first discuss differences between our results and previous analyses, specifically for cross-listed sources in T10 as G13 and I20 are not directly comparable due to the use of *Suzaku* data and lack of observation-specific information, respectively.

4.6.1 Comparison to previous work, future improvements

A total of 17 of the 30 *XMM-Newton* observations analysed here are cross-listed with T10, having significantly detected UFOs reported therein, yet here we only found UFOs in 13 of them. Ark 120, IC 4329A, and Mrk 290 all lack UFOs based on our analysis on single observations of each, and one observation of Mrk 509 apparently does not exhibit any UFO evidence despite not being significantly different than the two that do.

It is clear, then, that (i) the different statistical treatment of the data, (ii) implementation of a physically motivated spectral model, and/or (iii) use of the broad band $0.3-10$ keV X-ray spectrum have/has significantly impacted the interpretation of absorption features in the $7-10$ keV band. Regarding (i), this seems the most likely explanation for the discrepancy with Ark 120, for which T10 reported $v_{\rm UFO}=0.269c$ while here we find no such feature. This UFO apparently visually corresponds to exactly one data point in T10, a data point which is not present in our Ark 120 spectrum due to the different data treatment.

Regarding (ii) and (iii), the examination of the ratio residuals plot of Mrk 290 in T10 finds broad band spectral curvature that remains in their best-fit model, suggesting the presence of an unaccounted for spectral component, which we assume here is the reflection spectrum (plus any additional photoionised emitters and/or absorbers). Indeed, the inclusion of such additional components finds no such ratio residuals in our best-fit model of Mrk 290, and hence no UFO. These differences highlight the importance of a rigorous statistical treatment of the data and application of physically motivated broad band X-ray spectral models in the reliable detection of UFOs.

The above discussion, however, is still very much applicable to our work here. We assumed a reflection scenario for all of our sources, which may not be an adequate representation of the underlying physical scenario in all cases. For example, Petrucci et al. (2018) tested the warm corona / soft-Comptonization model, wherein an optically thick X-ray corona accounts for the AGN soft excess, on numerous AGNs including 1H 0419−577 and Mrk 509. In fact, the authors analysed the same *XMM-Newton* observations of those AGNs that were used in this work and found the warm corona model to describe the data reasonably well ($\chi^2/dof \lesssim 1.3$). That is not to say our reflection assumption is invalid, but in some instances it may not be an accurate or complete representation of the X-ray spectrum. We note that Mrk 509 was found to be best-fit with $A_{\rm Fe} \approx 0.6$, a result that produces a reflection spectrum that predominantly fits the soft excess, similar to the warm corona. The reflection spectrum in Mrk 509 may then be trying to mimic an underlying warm corona, which has a black body-like appearance at low energies $\lesssim 2$ keV. MR 2251−178, Mrk 766, Mrk 841, and NGC 3783 were also found to be best-fit by $A_{\rm Fe} \approx 0.5$, perhaps indicating

that in these sources a warm corona model may be more appropriate, as a physical origin for $A_{\rm Fe} < 1$ in AGN accretion discs is not clear.

Furthermore, our absorption model of choice, XABS, appears to produce significantly higher $N_{\rm H,UFO}$ values than have been found in other works. For example, Tombesi et al. (2011) found a median column density of $N_{\rm H,UFO} \approx 5 \times 10^{22}$ cm^{-2} and Gofford et al. (2015) found $N_{\rm H,UFO} \approx 6 \times 10^{22}$ cm^{-2}, both using XSTAR (Kallman & Bautista 2001), while we found $N_{\rm H,UFO} \approx 3 \times 10^{23}$ cm^{-2}, 6 and 5 times larger, respectively. This effect therefore led to our models measuring significantly enhanced $L_{\rm X}$ values in many of the sources in our sample. We will apply the XSTAR photoionisation code to our sample of sources, to check for consistency between the measured parameters, in a future work.

Future work on this subject may therefore improve upon this work in a number of ways. For example, the inclusion of additional physical scenarios, such as soft-Comptonization and partial covering absorption, can be implemented. At that point, however, using *XMM-Newton* data alone would be insufficient in distinguishing the models, and therefore the addition of simultaneous high-energy *NuSTAR* (Harrison et al. 2013) coverage would be necessary in order to enhance our ability to disentangle the various models as well as more accurately measure their parameter values. Future missions, such as *XRISM* (XRISM Science Team 2020) and *Athena* (Nandra et al. 2013), will substantially improve our ability to resolve high-energy absorption features, enabling characterisations of UFOs that are currently not possible with available observatories.

4.6.2 Multi-component winds

For 9 of the 16 AGNs found to exhibit UFOs in this analysis we found that the inclusion of multiple UFO components was required in order to best fit the data. Some of those systems only required outflow velocity to be free to vary among the multiple components, whereas others required distinctly different ionisation states and column densities for the multiple components. One interpretation of these results may be that we are observing the stratification of the UFO structure in each such AGN. In the stratified wind geometry, our single line of sight passes through multiple layers of the UFO. This scenario would have our view through the wind intersect a variety of different acceleration zones or wind stream lines whose properties are dependent on the distance of the wind material from the SMBH, resulting in different measured ionisation states, column densities, and outflow velocities.

Interestingly, for 1H 0419−577, Mrk 766, and NGC 3516 we found that the low-velocity winds with $v_{\rm UFO} < 0.2c$ aligned with radiatively-driven model predictions in the $v_{\rm UFO} - \theta$ parameter plane, while the high-velocity winds with $v_{\rm UFO} > 0.2c$ in those same AGNs aligned more with MHD-driven model predictions. In these systems it may be that we are observing a variety of winds produced by different driving mechanisms.

Fukumura et al. (2014) suggested a scenario in which a single underlying MHD driving mechanism unifies WAs, UFOs, and jets in AGNs, wherein WAs exist a large radii and UFOs at smaller radii closer to the SMBH, with jets accelerated along the SMBH spin axis confined by the structure of the high-pressure wind. The authors showed that this model was capable of producing the observed jet properties of 3C 111 by confinement through

the combined WA and UFO wind structure. Radio observations of Mrk 766 have found evidence of a low-power parsec-scale jet in this RQ-NLS1 (e.g. Doi et al. 2013). The Z-shaped NLR in NGC 3516 has been argued as a possible side-effect of a precessing jet scenario (Veilleux et al. 1993; Arribas et al. 1997), though to date no radio confirmation of such a scenario has been made. Furthermore, the results of recent analyses on other radio-quiet AGNs (e.g. I Zw 1 Gallo et al. 2007; Wilkins et al. 2017; Mrk 335 Gallo et al. 2013; Wilkins & Gallo 2015a), have revealed what have been inferred as aborted jet-launching events, suggesting significant magnetic field structure and variability. Therefore, in those AGNs with low inclination angles and high-velocity UFOs, an underlying MHD driving mechanism that links WAs, UFOs, and jets may be the most plausible scenario. Indeed, while a jet *can* be produced in such a scenario, it is not necessitated by the model, thereby naturally accounting for the fact that some of these AGNs display jet activity while others do not. Testing this idea more thoroughly will require studies in which rigorously verified UFOs in low-inclination AGNs are detected alongside low-power jets in samples of both RL- and RQ-AGNs, which in turn may lead to modelling techniques that explore jets in AGNs by examining wind properties.

4.6.3 Extremities of accretion

Throughout the discussion of our results so far, we have assumed a standard accretion disc prescription (i.e. Shakura & Sunyaev 1973), which has been used to describe the discs in AGNs of all types for decades. This geometrically *thin*, optically thick disc model is especially relevant in systems with sub-Eddington accretion rates ($\lambda_{\rm Edd} \ll 1$). However,

for systems accreting near ($\lambda_{\rm Edd} \approx 1$) or above ($\lambda_{\rm Edd} \gg 1$) the Eddington rate, departures from the standard disc theory become significant, such that the accretion disc may become a *slim* or even *thick* disc, respectively (e.g. Abramowicz et al. 1980, 1988). In such systems, the extreme accretion rate results in radiation pressure supported disc in which the disc "puffs up", resulting in $H/r \leq 1$ and $H/r \sim 1$ for slim and thick discs, respectively, where H is the disc height at radius r, where for thin discs $H/r \ll 1$. The main mode of cooling in thin discs is radiation, while in slim and thick discs advection dominates the cooling as emission from the disc is unable to escape the accreting material before it falls onto the SMBH, making these systems radiatively inefficient.

The discussion of these alternative disc models is relevant to our sample of AGNs studied here, for which there are eight each with $\lambda_{\rm Edd} < 1$ and $\lambda_{\rm Edd} > 1$. Particularly, 1H 0707−495, IRAS 13224−3809, IRAS 13349+2438, PDS 456, PG 1211+143, and PG 1448+273 exhibit the most extreme accretion rates in the sample with $\lambda_{\rm Edd} \gtrsim 1$. We therefore discuss the observed parameter correlations for these objects in the context of a slim/thick disc scenario.

Many of the measured X-ray reflection and UFO parameter correlations share a moderate or strong dependence on $\lambda_{\rm Edd}$ (see Figure 4.3). We generally found that the aforementioned sources tended to have: high $L_{\rm X}$, steep Γ, large R, high $q_{\rm in}$, large θ, low $\log \xi_{\rm R}$, high $A_{\rm Fe}$, high $\log n_e$, high $L_{2500\text{Å}}$, and steep $\alpha_{\rm OX}$. These findings clearly exemplify the extreme nature of this subset of highly accreting AGNs as they occupy non-standard parameter spaces. Assuming a lamp-post coronal geometry and increasing the disc scale height to that of a slim/thick disc, we argue that as the inner disc region becomes more toroidal a natural enhancement of light bending scenario would take place. This would therefore lead

to increased R and $q_{\rm in}$. The described geometry may also result in a shielding of the outer disc by a toroidal inner disc, thereby reducing the observed $\log \xi_{\rm R}$. The enhanced inflow of matter in such systems may also naturally lead to high $\log n_e$ as well as super-solar $A_{\rm Fe}$ in the immediate vicinity of the SMBH. Measurements of θ in such systems using standard disc models could become significantly biased to larger values as a result of these effects. Indeed, simulations of the reflection spectra from slim accretion discs by Taylor & Reynolds (2018) showed that enhanced Fe Kα blue wings are expected in the slim disc scenario for $\theta = 60°$. When attempting to fit such features with standard reflection models this may lead to overestimation of θ, which may be the case here as all of these highly accreting systems are measured to have θ near or in excess of the Type I AGN upper limit of $\sim 60°$.

Furthermore, we note that the aforementioned AGNs exhibited UFOs with the lowest $\log \xi_{\rm UFO}$ and largest $N_{\rm H,UFO}$, with all of them also requiring significantly larger $v_{\rm turb}$ values than the assumed $v_{\rm turb} = 2000$ km s^{-1}, which itself was found to fit the other sources well. These AGNs displayed absorption features remarkably similar to one another yet distinctly different from the other AGNs, and we note that they preferentially occupied the region bound by the disc-atmosphere absorption model upper-limit $v_{\rm UFO}$ estimate. We recall from Section 4.1 that both IRAS 13224−3809 (Fabian et al. 2020) and PG 1211+143 (Gallo & Fabian 2013) were found to be well-fit by the disc-atmosphere absorption model in previous works, perhaps hinting at a common origin for the absorption features among these six sources. In a slim disc scenario, a significantly enhanced disc atmosphere may exist such that this description of UFOs becomes relevant. Taylor & Reynolds (2018) also showed that fitting slim disc simulated spectra with standard reflection models found absorption-

like features in approximately the energy band of interest for UFO studies, highlighting the ambiguity of interpreting UFOs in the spectra of these sources.

Finally, AGNs with slim/thick discs have SEDs that are dominated by the disc emission. Our subset of extreme accretors here are consistent with this, all exhibiting enhanced $L_{2500\text{Å}}$ and steeper α_{OX} relative to the rest of the sample.

While individually none of the results conclusively point toward the existence of non-standard accretion discs in these six extreme AGNs, taken together they strongly advocate the need for more wide-spread application of alternative disc models in order to explore this avenue more fully. For instance, exploring how slim disc model parameters evolve with accretion rate in a sample of AGNs would precisely reveal when deviations from the standard accretion disc theory of Shakura & Sunyaev (1973) become so significant such that standard spectral models no longer accurately represent source properties. This presents an interesting avenue of future investigation.

4.7 Conclusions

We have found several strong indicators of a close relationship between the X-ray emitting region in AGNs and UFOs. Wind ionisation was found to be strongly (i.e. $p < 0.01$) anti-correlated with disc reflection fraction and inclination angle. Column density of the wind was found to be strongly correlated with accretion rate, X-ray luminosity, disc inclination angle, power law photon index, and disc ionisation.

We are unable to conclusively determine a common radiation pressure or MHD driving

mechanism for the winds among all AGNs in the sample. High-velocity outflows with $v_{\rm UFO} > 0.2c$, especially at low disc inclination angles of $\theta \lesssim 30^{\circ}$, are found to be most likely driven by an MHD mechanism. The lack of any strong correlation between disc UV luminosity and the wind parameters further suggests a non-radiation pressure driving mechanism in the sample. Disc-atmosphere absorption effects cannot be ruled out as a potentially wind-less origin for absorption features in systems where $v_{\rm UFO} < 0.2c$ and $\theta \gtrsim 30^{\circ}$.

Six AGNs in our sample (1H 0707−495, IRAS 13224−3809, IRAS 13349+2438, PDS 456, PG 1211+143, and PG 1448+273) are found to be extreme accretors with $\lambda_{\rm Edd} \gtrsim 1$, in general agreement with their respective literature. They consistently occupied extreme regions across all measured parameter spaces and displayed wind properties akin to one another but different from the rest of the sample (i.e. deeper, broader features). A slim or thick disc scenario in these AGNs is discussed as a plausible underlying physical difference separating these sources from the others. In these non-standard accretion disc systems, a disc-atmosphere absorption scenario may be more likely due to the enhanced vertical structure of slim/thick discs.

Our results generally tend to find larger UFO column densities than those reported in previous works (i.e. $5-6$ times larger). This bias will be explored via the application of an alternate photoionisation code prior to journal submission.

Future works will need to examine larger samples of AGNs in order to fill more of the unexplored and/or poorly sampled parameter spaces presented here (e.g. BH spin parameter a and disc density $\log n_e$, both of which tended towards extreme values in our sample). In-depth analyses of the six extreme accretors involving the application of alternative disc

models are necessary to probe such a scenario in those AGNs, where a wind-less absorption origin of the observed features via the reflection spectrum may be more likely.

Chapter 5

Conclusions

5.1 Summary of results

The results presented in Chapters $2-4$ have shed some light on a number of interesting connections between high-velocity outflows in AGNs and the central engine that they are powered by. In Chapter 2, we showed that the beamed X-ray source in III Zw 2 has an outflow velocity greater than the escape velocity that is also consistent with the radio jet velocity. This led us to the interpretation of the X-ray corona acting as the jet base. Precession of the jet was then suggested as a plausible explanation for the extreme changes observed in the reflection spectrum, which transitioned from a relativistically blurred, highly ionised reflector into a distant, neutral reflector over $\sim$ 11 yr. We suggested that this behaviour approximately aligned with the estimated precession period of ~ 5 yr by Li et al. (2010) from radio observations.

X-ray observations of the jetted RL-NLS1 IRAS 17020+4544 were analysed in Chapter 3, where we found a mixture of properties typical of both RQ- and RL-AGNs. A harder-when-brighter trend was found, which is not commonly found in Seyferts, but is frequently attributed to jet variability in the X-ray band for blazars. Short- and long-term variability

was dominated by luminosity variations of a soft power law continuum ($\Gamma_{\rm avg} \approx 2.3$) and its relative flux compared to the reflection spectrum ($R_{2004} \approx 0.5$ to $R_{2014} \approx 0.7$). X-ray reverberation and covariance spectra provided model-independent support of the spectral modelling interpretations. Rapid lag changes attributed to coronal height variations and hardening covariance spectra with increased frequency were interpreted as tentative evidence of an extended, slowly varying corona coexisting with a compact, rapidly fluctuating corona, the latter of which may be the jet base. Mild coronal beaming was found as well as evidence suggesting that the X-ray source may have slowed and/or increased in height over 11 yr. The coronal outflow velocity was found to be consistent with the sub-relativistic jet interpreted from radio observations by Doi et al. (2011).

UFOs in 16 RQ-AGNs were evaluated for their relationship(s) with the central engine in Chapter 4. We found various strong dependencies of the wind parameters on the coronal and inner disc properties. Wind ionisation state was found to anti-correlate with both the reflection fraction and disc inclination. Column density of the wind was found to correlate with accretion rate, X-ray luminosity, power law photon index, and inclination, though it anti-correlated with disc ionisation state. In general, low-inclination AGNs displayed high-velocity winds that appeared consistent with an MHD driving mechanism. For the most inclined systems, the inferred extreme accretion rates in six AGNs may produce non-standard discs (i.e. slim/thick discs), wherein a wind-less disc-atmosphere absorption scenario was suggested as more likely, although a number of parameter biases when fitting such non-standard accretion scenarios with standard models made interpreting these incompletely, or incorrectly, treated systems difficult. The observed lack of any optical/UV correlations

with UFO properties suggested that a radiation pressure driving mechanism may not be the dominant one, though the existence of such winds could not be ruled out.

5.2 Current and planned work for the near-future

A clear connection between AGN outflows and the central engine has been showcased in the presented work. Naturally, a number of unanswered questions regarding the highlighted topic remain, the answers to which are critical to enhancing our understanding of AGNs and black hole physics. Below I break down ongoing and future work that will more intensely investigate these questions.

5.2.1 The disc-jet connection and RL-RQ dichotomy

In Chapter 1 we briefly discussed how the RL-RQ dichotomy in AGNs remains an area of open research, and that one promising avenue through which we may explore the underlying differences (and/or similarities) between RL- and RQ-AGNs is through NLS1s, where the disc-jet connection can be closely examined. Using the Karl G. Jansky Very Large Array (JVLA) operating at 5 GHz, Berton et al. (2018) characterised the radio emission of 74 NLS1s, including IRAS 17020+4544, finding that RL-NLS1s with flat radio spectra exhibited properties consistent with being low-luminosity blazar equivalents. We believe that these sources offer prime laboratories in which we can explore how the disc and jet interact. Building off of the Berton et al. (2018) sample and the results of Chapter 3, we are currently examining all of those NLS1s that have archival *XMM-Newton* observations (11 RL, 15 RQ). Our goal is to employ simple phenomenological models across both pop-

ulations, comparing the mean properties of each and examining for differences that may suggest methodologies better suited to exploring those differences. Spectral analyses, for example, will probe whether the power law continuum in RL-NLS1s dominates the X-ray band more substantially than in RQ-NLS1s and if it possesses a harder photon index on average, results that would both suggest a jet origin. Furthermore, if RL-NLS1s are indeed young blazar counterparts that have not undergone extended periods of jet activity, perhaps they will exhibit enhanced obscuration in the X-ray band owing to the gas and dust surrounding the central region that has not yet been cleared out by the jet. Interestingly, D'Ammando (2020) found that for a sample of 8 γ-ray emitting RL-NLS1s that no intrinsic absorption existed in those systems, offering evidence against the young-AGN hypothesis for such systems. We will additionally examine for differences in the variability trends and optical/UV-X-ray SED of RL- and RQ-NLS1s. Some of the questions we aim to answer are: Is a harder-when-brighter trend more frequently observed in RL-NLS1s that have jet-like power law continua? Are RL-NLS1s with enhanced radio emission less variable than RQ-NLS1s and RL-NLS1s with more intermediate radio emission due to a more dominant jet component? Do RL-NLS1s occupy a distinctly different $\alpha_{\rm OX}$ parameter space? These can be readily explored with simple models and straightforward analyses using archival data. However, more X-ray observations of a larger population of RL-NLS1s are a necessity, as the currently available sample is extremely limited.

Regarding particularly promising AGNs warranting deep X-ray observations in which the disc-jet connection may be explored, Mrk 783 is a RL-NLS1 with radio loudness that places it just above the classification threshold ($RL \sim 23$; Berton et al. 2015). Congiu et al.

(2017) reported one of most extended examples of NLS1 radio emission at $z < 0.1$ in this object, with relic emission stretching ~ 13 kpc from the centre of the galaxy nucleus in both directions, highly atypical for a NLS1. This was interpreted as the result of intermittent jet activity by the authors due to the S-like shape of the relic emission. Congiu et al. (2020) then followed-up with new radio and optical observations, finding evidence of a secondary point-like component in the galaxy ~ 1.5 kpc from the AGN. This secondary source was inferred as a companion galaxy in the late stages of an ongoing merger event with Mrk 783. The authors also showed that jet precession provided another plausible origin for the S-shaped extended radio structure. Both the intermittent jet activity and jet precession scenarios may have been induced by the merger event, according to the authors.

This dynamic central engine in Mrk 783 surely presents an invaluable opportunity to explore the X-ray behaviour during either: (i) an intermittent jet activity cycle, or (ii) a precessing jet scenario similar to what we have inferred in III Zw 2 (Chapter 2). We have therefore successfully proposed the first ever *XMM-Newton* observation (70 ks) of Mrk 783 for the Twentieth Announcement of Opportunity Cycle 20 (AO-20), scheduled to be taken during the May 2021 to April 2022 observing period. Examination of the very limited ($\sim$ 11 ks) archival *Swift* data revealed significant variability on monthly time scales (i.e. by a factor of ~ 3), with shorter time scales impossible to explore due to the cadence of archival data. We were also unable to distinguish the best-fit model of the X-ray spectrum as either a (somewhat) standard power law modified by a single standard WA ($\Gamma \sim 1.7$ with $\log\left(\xi_{\rm WA}/\text{erg cm s}^{-1}\right) \sim 2$ and $N_{\rm H,WA} \sim 5 \times 10^{21}$ cm^{-2}) or as a blazar-like power law with low high-energy turnover indicating a cool X-ray corona ($\Gamma \sim 1.4$ and $E_{\rm cut} \sim 50$ keV).

These models imply completely different conditions in the central engine, and with our new observation, offering the deepest X-ray view of Mrk 783 on record, we will be able to apply any of the techniques presented throughout Chapters 2−4 to aid in conclusively determining the underlying physical scenario operating in this interesting (possibly jetted) RL-NLS1. This AGN is especially intriguing as it lies on the boundary between RL and RQ, and therefore offers a rare opportunity to explore the disc-jet connection in a system where both contributions should be comparable.

Future observations of III Zw 2 are also warranted based on the results of Chapter 2. III Zw 2 would in fact be a prime candidate for multi-wavelength monitoring, assuming that jet precession is indeed the underlying mechanism responsible for producing the extreme changes measured in the reflection spectrum. Utilizing simultaneous radio, infrared, optical/UV, and X-ray observations made every four months over two years, for example, the significant spectral changes as the jet precesses from minimal to maximal pointing along our line of sight could be mapped in detail. Of course, a more reasonable and necessary starting point prior to any multi-wavelength observing campaign would be future X-ray observations timed approximately when a radio flare is anticipated, and examining for whether the inner disc is visible during such a time. There is absolutely the possibility that the jet does not precess in this source, but that the inner disc observed in 2000 was instead launched as part of the jet some time later leaving only a distant reflector to be measured by the 2011 observation. Such a scenario would then present interesting new explorations of the X-ray spectrum: is a distant reflector still dominating the reflected emission, suggesting that the inner disc has not yet had time to reassemble? Does a reflection component with

mild/intermediate properties exist, suggesting that the inner disc is in the process of reforming? Regardless of the exact scenario, future X-ray monitoring of III Zw 2 would provide new high-quality data with which the disc-jet connection in AGNs could be closely studied in this peculiar source.

5.2.2 Extreme accretors and UFOs

Lastly, a variety of works can build upon what we have found in Chapter 4, the most immediately interesting perhaps being more detailed examination of the highly accreting systems 1H 0707−495, IRAS 13224−3809, IRAS 13349+2438, PDS 456, PG 1211+143, and PG 1448+273. Several of these systems are well studied in the literature and are known to be exceptionally intriguing, having therefore amassed very large data sets available for immediate analysis. A short-term goal would be to examine a particular AGN, such as 1H 0707−495 with ~ 1.45 Ms of archival data, by applying models for radiatively-driven winds, MHD-driven winds, and disc-atmosphere absorption scenarios to the data during various source states (e.g. high- versus low-flux states, soft versus hard spectral states, etc.). This would then reveal how the wind properties respond to the various changes taking place in the X-ray emitting region, as was done for IRAS 13224−3809 by Pinto et al. (2018). Those authors concluded that a radiative driving mechanism may be responsible for producing the UFOs in that AGN, suggesting that the wind responded to increased X-ray luminosity by becoming overionised and subsequently dissipating. That scenario, however, becomes difficult to reconcile with the fact that IRAS 13224−3809 varies in X-ray flux by a factor of $\sim 10-100$ over the course of only a few hours, implying that a high-density wind with mass

outflow rate comparable to the accretion rate must dissipate and then completely reassemble within at least a similar time scale. The authors did not explore how an MHD-driven wind would apply to this system: can a magnetic driving mechanism account for the observed UFO variability without the dissipation and reassembly of the wind? More recently, Fabian et al. (2020) suggested that IRAS 13224−3809 exhibits no wind whatsoever, instead finding that the disc-atmosphere absorption model sufficiently described the variable absorption features. They proposed that the absorption variability is due to rapid fluctuations of the disc conditions within $\lesssim 7$ r_g of the ISCO. Indeed, Gallo & Fabian (2013) came to a similar conclusion for the absorption feature in PG 1211+143. May it be that highly accreting systems possess discs of enhanced vertical structure (i.e. slim/thick discs) that produce the observed variable high-energy absorption features we interpret as UFOs? Analysis of these extreme accretors using multiple absorption scenarios coupled with physically motivated alternative accretion disc models to characterise the observed features will enable powerful new interpretations of the high-energy absorption features in these systems.

Future analysis of the sample of AGNs presented in Chapter 4 will also implement the Reflection Grating Spectrometer (RGS; den Herder et al. 2001) on-board *XMM-Newton*, which possess significantly enhanced spectral resolution (i.e. $E/\Delta E \approx 100-500$) at energies $\lesssim 2$ keV compared to the EPIC-pn camera (i.e $E/\Delta E \approx 20$) used in our presented analysis. Using the results we have obtained so far, in conjunction with high-resolution modelling of the low-energy RGS data to measured warm absorber properties simultaneously with the UFOs, we can begin to draw relationships between the various regions of outflowing

material in these systems[1]. Furthermore, use of the $3-79$ keV high-energy band observed by *NuSTAR* (Harrison et al. 2013) will help to constrain model parameters by more accurately measuring the relative contribution of the power law, relativistic reflection, and distant reflection components to the observed spectrum (i.e. measuring the reflection fraction), owing to the Compton hump at $\sim 20-30$ keV which is not observable with *XMM-Newton*. Simultaneous *XMM-Newton* and *NuSTAR* archival observations exist for only a handful of the sources analysed in Chapter 4, making such a project suitable once more such observing campaigns have been completed on the AGNs of interest.

In summary, we have planned and are planning a number of future works that will continue to probe how high-velocity outflows in AGNs are connected to the central engine. In this document I have presented work that has so far produced an excess of new and interesting questions compared to answers; such is the way of science.

5.3 The next generation of X-ray observatories

XRISM and *Athena* are forecasted to launch in 2022/23 and 2031, respectively, and promise a bright future for AGN X-ray astronomy, though some significant hurdles need to be overcome in the coming years in order to make full use of their capabilities. For instance, the *XRISM* Resolve instrument will have a constant energy resolution of ~ 7 eV across the entire broad band energy range ($\sim 0.3-12$ keV), an improvement of $\sim 10-30$ times over the EPIC pn camera onboard *XMM-Newton* (XRISM Science Team 2020). The *Athena* X-ray Integral Field Unit (X-IFU) will have a spectral resolution at 6 keV of ~ 2.5 eV, an

[1]Note that only one AGN with a detected UFO in our sample *did not* have a warm absorber (Mrk 205).

improvement of ~ 60 times over the EPIC pn camera (Nandra et al. 2013). Such leaps in spectral resolution, while transformative to our ability to measure various spectral features, expose glaring shortcomings of our current state-of-the-art spectral models best-practices. This issue was exemplified during the analysis of Perseus cluster observations taken by *Hitomi* (the *XRISM* predecessor) before its untimely demise (e.g. Hitomi Collaboration et al. 2018). Unprecedented spectral resolution revealed that model choice and fitting technique produced effects comparable or in excess of statistical or instrumental uncertainty. To put this into perspective, spectra measured by the EPIC pn camera of *XMM-Newton* are often insensitive to the application of collisionally ionised versus photoionised plasma models, let alone to the differences between treatments embedded in the codes of either type. Moreover, those *Hitomi* observations found that improvements to our current spectral models actually require new atomic data from laboratory measurements in order to accurately measure the plethora of observed features in the new high-quality spectra that are unresolved by current X-ray observatories. Future missions will therefore require significant advances of the implemented plasma physics throughout our present-day suite of spectral models.

To illustrate these points in the relevant context of UFOs, we recall the 14 ks *XMM-Newton* EPIC pn exposure of Mrk 79 (see Chapter 4), where an absorption feature at ~ 7.65 keV was found, which corresponded to a 2.6σ deviation from the best-fit power law plus reflection model (Figure 5.1, left column). Applying a photoionised plasma model to account for this possible UFO, however, only resulted in a fit improvement of $\Delta C = -4$ for 3 additional free parameters, which is statistically insignificant at face-value, though was included in our analysis due to its high Monte Carlo significance ($S \geq 95\%$). Using the most

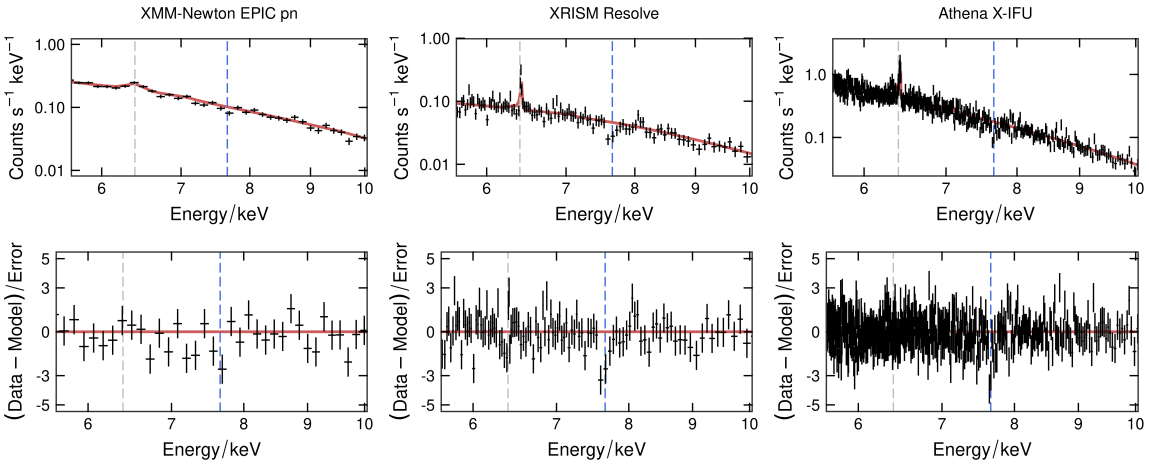

Figure 5.1: *XMM-Newton* EPIC pn observed spectrum (top left) and data deviations from the best-fit power law plus reflection model (bottom left) for the 14 ks exposure of Mrk 79. *XRISM* Resolve and *Athena* X-IFU simulated results are shown in the middle and right columns, respectively. The red line in each panel represents the base model, with grey and blue vertical dashed lines representing Fe Kα emission at 6.4 keV and the observed absorption feature, respectively. The absorption feature is detected at the $> 3\sigma$ significance level in both simulated spectra, while the current data find it to be at the $< 3\sigma$ level.

recent response matrix available for the *XRISM* Resolve instrument, we a simulated 14 ks exposure of the best-fit power law plus reflection plus UFO model, binning the spectrum by imposing a minimum signal-to-noise ratio of 5 for each bin, and found a similar absorption feature that now corresponds to a 3.3σ deviation when the UFO model component is removed (Figure 5.1, middle column), resulting in a fit improvement of $\Delta C = -26$ when it is re-applied. Performing the same simulation using the most recent *Athena* X-IFU response matrix found a 3.9σ deviation (Figure 5.1, right column) that results in $\Delta C = -68$ when fit. These simple tests demonstrate that even short exposures of moderately bright AGNs using future X-ray missions will be capable of detecting UFOs at significance levels requiring exposures $5 - 10$ times longer with current observatories. This opens the realm of time-

resolved UFO spectral analysis to a vast population of AGNs which will revolutionize our understanding of how the wind responds to variations in the X-ray emission of the inner disc region. Furthermore, the unprecedented spectral resolution in the high-energy band pass inhabited by UFOs will enable tighter constraints on key wind parameters, such as ionisation state, which will in turn significantly improve the inferred energetics and location of these extreme outflows.

5.4 Closing remarks

This work represents an important step toward reaching meaningful conclusions about how AGNs produce some of the most rapid outflows observed anywhere in the Universe, which are capable of completely altering the evolution of the AGN host galaxy by inhibiting or enhancing star formation. We have found that by observing the X-ray emission from systems exhibiting jets and winds that a close relationship between these structures and the inner accretion disc environment exists. Ongoing and future studies will build upon the findings presented here, eventually making use of the incredible capabilities of upcoming X-ray missions that will dramatically enhance our ability to study these outflows.

Appendix A

The effect of pile-up

Here we outline a brief investigation on the effect of pile-up in our sample from Chapter 4 using a case study of PG 1211+143 (see Figure A.1). This source displayed $3 \pm 0.5\%$ pile-up of single events and $9 \pm 0.9\%$ pile-up of double events when using the GTI-corrected (i.e. background flaring removed) events to produce the spectrum, falling outside of our $< 2\%$ pile-up criterion. In an attempt to alleviate the effect of pile-up on the spectrum we excluded annuli centred on the source position from the final extraction region of increasing radius until the results of the SAS task EPATPLOT gave 0% pile-up (of at least single events) within error. This procedure found that such a result was achieved once the central $r_{\rm ex} = 15''$ of the source-centred extraction region were excluded, translating to $\sim 18\%$ of the $r_{\rm src} = 35''$ source extraction region being removed. Applying this pile-up correction to the data reduced the spectral data counts by a factor of ~ 5.5, from $139,469$ in the uncorrected data to $25,154$ in the corrected data.

The resulting raw/uncorrected and pile-up corrected spectra are shown in Figure A.1 (top panel). We fit each spectrum across the $2-4$ keV rest-frame band, where the power law is expected to dominate the known strong reflection spectrum in this source, with an absorbed (Galactic column density) power law model, linking the photon index between both

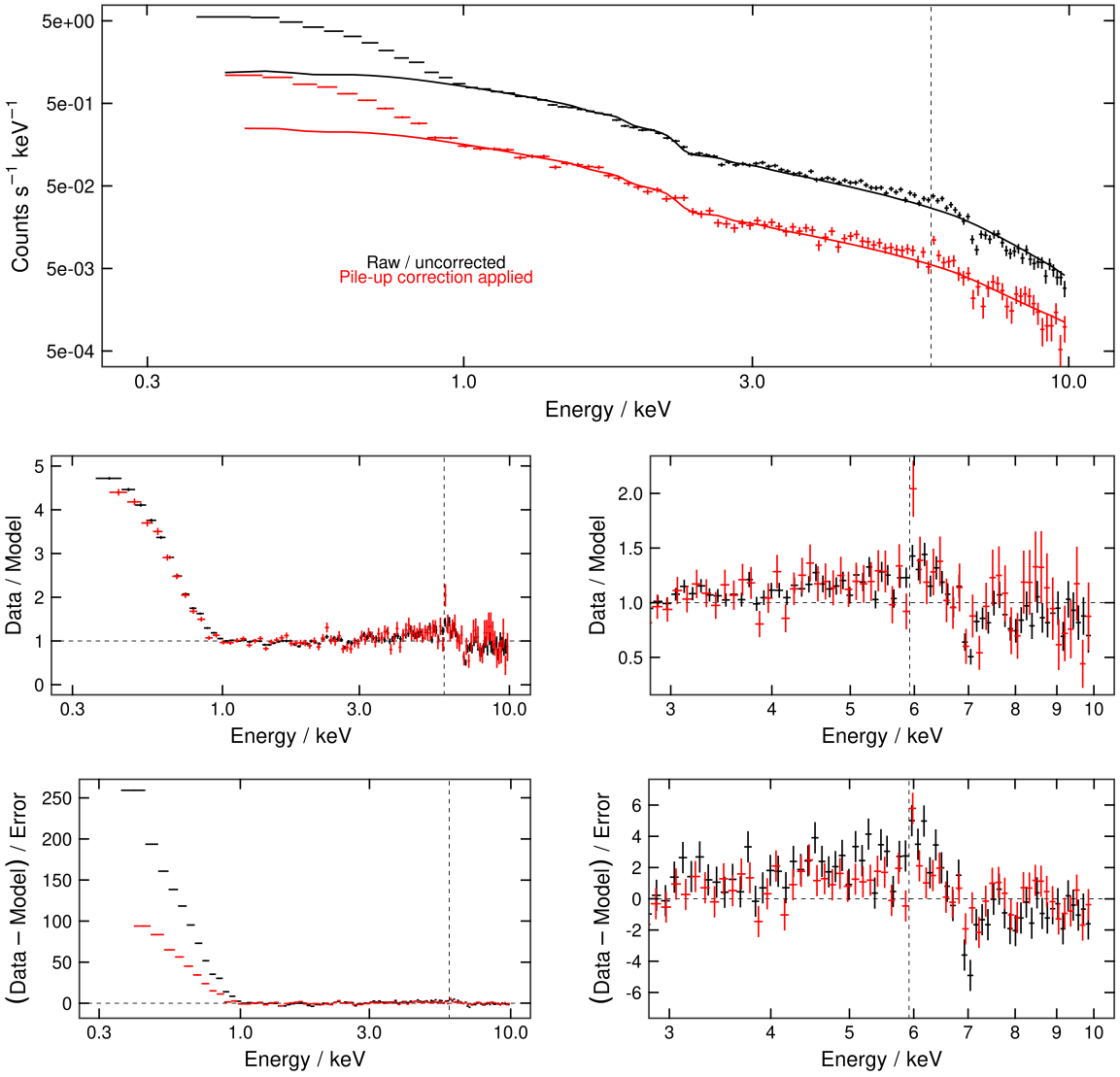

Figure A.1: *Top panel*: Raw/uncorrected (black points) and pile-up corrected (red points) *XMM-Newton* EPIC-pn spectra of PG 1211+143, which have been fit with a power law model (solid lines) over the $2-4$ keV (rest-frame) band with free to vary normalisation and linked photon index ($\Gamma = 1.81$). *Middle panels*: Broad band ($0.3-10$ keV, left) and high-energy ($3-10$ keV, right) zoom-in of the data ratio residuals to the power law model in the top panel. *Bottom panels*: Broad band ($0.3-10$ keV, left) and high-energy ($3-10$ keV, right) zoom-in of the significance level of data deviations from the power law model in the top panel (y-axis denotes $n\sigma$ deviations of the data from the model). In all panels the black dashed vertical line indicates the redshifted rest-frame energy of the Fe Kα emission line at 6.4 keV.

spectra, finding $\Gamma = 1.81$. When photon index was allowed to be free to vary between the two spectra we found that for the uncorrected spectrum $\Gamma = 1.83 \pm 0.04$ and for the corrected spectrum $\Gamma = 1.74 \pm 0.10$, corresponding to a fit improvement of $\Delta C \approx 2$ for 1 additional free parameter. We concluded that the two spectra exhibit the same underlying power law continuum, and therefore used the linked power law model to extrapolate the fit across the broad band (0.3−10 keV). Both spectra exhibit a strong soft excess (Figure A.1, middle left), though due to reduced data quality in the corrected spectrum it appears at a much lower significance level by comparison, albeit still extremely significant (Figure A.1, bottom left). In the high-energy band ($3 - 10$ keV) both spectra exhibit a relativistically broadened Fe Kα line, stretching from $\sim 3-7$ keV, and a deep absorption feature at ~ 7 keV (Figure A.1, middle right), though again the reduced spectral quality of the corrected spectrum reduces the significance of both features (Figure A.1, bottom right). Quantitatively, when applying a narrow ($\sigma = 10$ eV) Gaussian absorption feature to fit the high-energy absorption feature in the uncorrected spectrum we find that $\Delta C = -80.9$ for 2 additional free parameters (energy and normalisation of the line), while in the corrected spectrum we find $\Delta C = -8.5$.

These results show that while correcting for pile-up is certainly a desirable step in obtaining the most accurate representation of the intrinsic AGN source spectrum, for the goals of our work presented in Chapter 4 it is not feasible to simultaneously correct for pile-up and measure possible UFOs in the spectrum at the desired significance level owing to the degraded spectral quality imposed by the pile-up correction technique used. Thus, we are satisfied that the uncorrected spectra fit throughout Chapter 4 are not unrepresentative of the intrinsic AGN spectrum.

Appendix B

A Monte Carlo example

To better illustrate the mechanics of the Monte Carlo procedure, and subsequent analysis of its results, we highlight some of the key components that were not included in the presented material of Chapter 4 in order to avoid clutter.

Figure B.1 displays the ratio residuals of the X-ray spectrum of PG 1211+143, as in the top panel of Figure 4.1. Alongside the data, however, are now additionally plotted the 90, 95, and 99% confidence intervals of the ratio residuals of the best-fit spectral model applied to the $N = 1000$ Monte Carlo synthetic spectra. This added layer of information displays the range covered by the respective confidence interval of the synthetic data residuals, providing a 'by-eye' comparison to the data affording a preliminary evaluation of the significance of spectral features. Clearly the detected UFO at $\sim$ 7.6 keV is highly significant, as the residuals can be seen to exceed the 99% range of the $N = 1000$ synthetic spectra.

Figure B.2 displays the obtained distribution of fit improvements, here ΔC, after applying the line-search procedure to the $N = 1000$ Monte Carlo synthetic spectra as described in Section 4.4.2. The distribution of fit improvements falls off sharply moving from small improvements (i.e. $\Delta C \leq 1$) toward larger improvements. The discrete Monte Carlo significance (S) bins into which the data deviations are placed are determined based on the 90^{th},

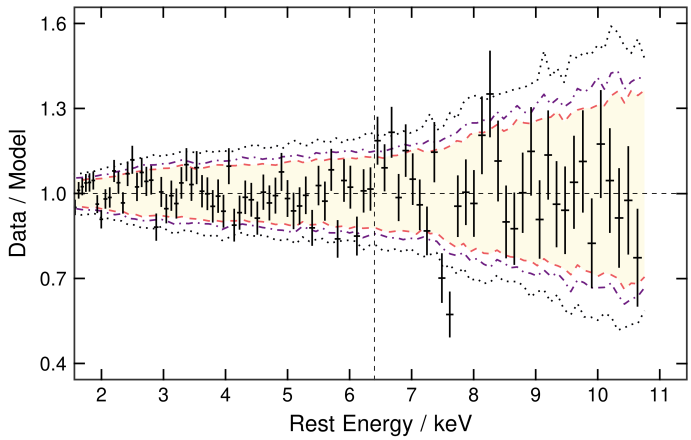

Figure B.1: Observed (black points) ratio residuals to the best-fit spectral model of PG 1211+143. The 90 (orange dashed), 95 (purple dot-dashed), and 99% (black dotted) confidence intervals are based on the ratio residuals of the best-fit model applied to the $N = 1000$ Monte Carlo synthetic spectra, with confidence levels $< 90\%$ are represented by the yellow shaded region. The black dashed vertical line denotes the Fe Kα emission line energy at 6.4 keV.

95^{th}, 99^{th} percentiles of the plotted distribution.

Finally, Figure B.3 displays the ratio residual significance contours based on the residuals from Figure B.1 and the distribution of fit improvements in Figure B.2 using the method described above (and in Section 4.4.2). In addition, here we plot the (binned by 0.1 keV) absorption lines from our "comb" based on the data in Table 4.3, with the blueshift applied given the best-fit outflow velocity as determined using the method described in Section 4.4.3.1.

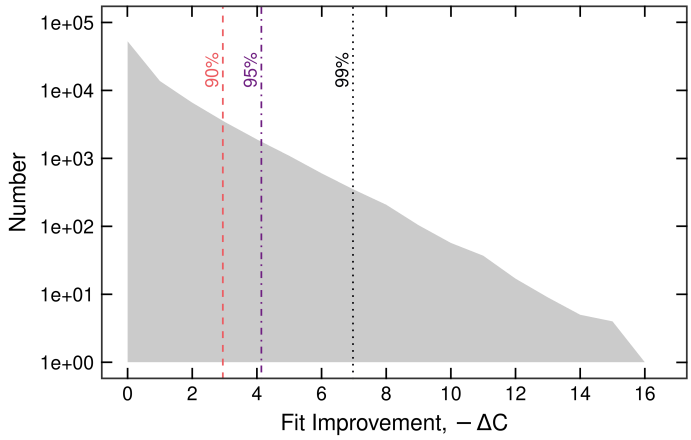

Figure B.2: The distribution of fit improvements (grey shaded region) based on the application of the line-search method to the $N = 1000$ Monte Carlo synthetic spectra of PG 1211+143 (note that the y-axis is log-scaled). The 90^{th} (orange dashed), 95^{th} (purple dot-dashed), and 99^{th} (black dotted) percentiles of the distribution are shown as vertical lines, which are used to produce the significance contour plots. Note that the negative of the fit improvement value is displayed here for visual purposes only, in order to have the curve decrease with increasing x-axis value.

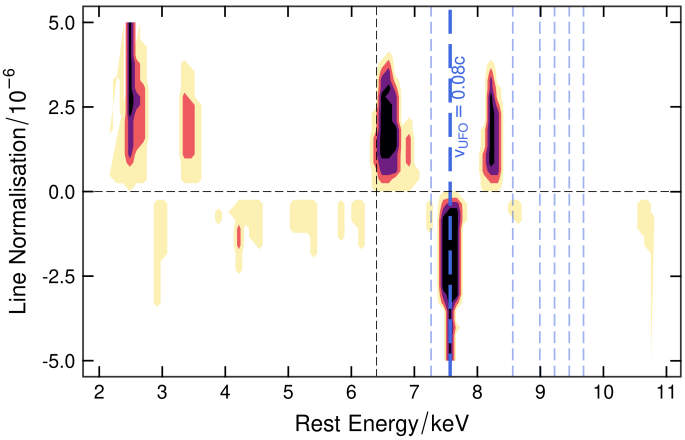

Figure B.3: Monte Carlo significance contours for the observation of PG 1211+143, as in Figure 4.1. Colour coding represents the same information as in that figure. Blue dashed vertical lines represent the absorption lines in the (binned) "comb". Heavier lines indicate the lines in the "comb" that are significantly detected for the labelled UFO velocity ($v_{\text{UFO}} = 0.08c$), with thinner lines not contributing the preliminary velocity determination. Here, one line (Fe XXVI Lyα) contributes entirely to the preliminary velocity determination of the UFO.

Appendix C

Individual source notes

1H 0419−577: With only 11.9 ks of exposure time this was the lowest quality spectrum analysed in this work, and as such our final model over-fits the data (i.e. $C/dof < 1$). Several of the reflection model parameters were fixed to their initial values as allowing them to be free to vary resulted in either an unconstrained value or insignificant fit improvement. Allowing the two UFOs to have $\log \xi_{\rm UFO}$, $N_{\rm H,UFO}$, and $v_{\rm turb}$ free to vary independently provided no statistical improvement to the fit. WA parameters were initialized based on Pal et al. (2018).

1H 0707−495: One of only two sources in the sample for which a double RELXILLD model was required in order to properly fit the data. The base model was applied in the same manner as all other sources, however, a second RELXILLD component was added, linking all parameters between the two RELXILLD components with the exception of the reflection fraction and ionisation parameter. Two high-$v_{\rm UFO}$ components were necessary to fit the exceptionally broad feature in the spectra, with a third low-$v_{\rm UFO}$ also necessary, as described in the main text. We note that despite nearly three years having elapsed between the two analysed observations, the UFO properties are essentially unchanged, indicating a long-lived wind.

Ark 120: The inclusion of an additional Fe emission line beyond the base continuum model provided an exceptionally large fit improvement here. Inserting a ZGAUSS component with $E_{\rm rest} = 6.47 \pm 0.04$ keV, $\sigma = 236^{+57}_{-64}$ eV, and $N = 5.0^{+0.9}_{-0.8} \times 10^{-5}$ provided a fit improvement of $\Delta C/N_{\rm fp} = -181/3$. Excluding this feature produces highly significant ($S \geq 95$ per cent) absorption-like features throughout the $7 - 10$ keV band, however, these are mostly eliminated via the inclusion of the described broad Fe emission line. Examination of the velocity determination curve finds $v_{\rm UFO}$ to be consistent with zero, therefore we do not consider this source to display strong UFO evidence.

IC 4329A: Four ionised absorbers (XABS) and significant neutral host-galaxy absorption (ZTBABS) are reported by Steenbrugge et al. (2005); their results were used to initialize the absorption components here. Applying these components to our EPIC pn spectrum found that adding a fourth ionised absorber provided a negligible improvement to the fit quality, and thus it was not included. No significant evidence of a UFO was found despite the apparently large residuals near ~ 7.5 keV.

IRAS 13224−3809: The second source in the sample for which a double RELXILLD model was required in order to properly fit the data. The base model was applied in the same manner as for 1H 0707−495. While only the high-$v_{\rm UFO}$ component was strongly required as per the velocity determination curves, similarly to 1H 0707−495, the inclusion of a low-vUFO component provided a substantial improvement to the fit quality.

IRAS 13349+2438: This AGN produced the lowest black hole spin measurement of the entire sample, with $a = 0.6^{+0.2}_{-0.1}$. Other works have also reported such measurements (e.g. Parker et al. 2020). Similarly to 1H 0707−495, we note that the UFO parameters in this

AGN remain essentially unchanged over the six years between observations, indicating a long-lived UFO. WA parameters were initialized based on Parker et al. (2018b).

MR 2251−178: We found that both observations required an additional highly-ionised WA at rest in the source frame that has not been previously reported. As $v_{\rm out}$ was found to be consistent with zero we did not consider this absorber when evaluating the mean UFO properties, including it instead as a WA component. We note that a second high-$v_{\rm UFO}$ component was only necessary for observation 0670120201. WA parameters were initialized based on Reeves et al. (2013). We included a photoionised emitter, which was suggested by Reeves et al. (2013) due to the presence of very broad (~ 10000 km s^{-1}) emission lines (they hypothesize an origin in the BLR) in the soft X-ray spectrum. Our PION component was only able to measure $v_{\rm turb} \lesssim 1350$ km s^{-1}, thus we froze $v_{\rm turb} = 100$ km s^{-1} during the fits as it provided no significant fit improvement when left free to vary.

Mrk 79: The inclusion of a UFO to account for the high-significance results of the Monte Carlo simulations provided a very low fit improvement of $\Delta C/N_{\rm fp} = -4/3$. Overall, parameter values were reasonably constrained, therefore we included these results in our analysis. The omission of Mrk 79 from the analyses performed in this work does not affect any conclusions. WA parameters were initialized based on Gallo et al. (2011). We note that while Gallo et al. (2011) found evidence of a photoionised emitter, the inclusion of such a component here provides no improvement to the fit.

Mrk 205: The short exposure of this observation hindered the constraint of many reflection model parameters, thus requiring that they remained frozen at their initial assumed values throughout the spectral fitting; only θ and $\log \xi_{\rm R}$ were required to achieve our final

best-fit model, which in fact over-fits the data (i.e. $C/dof < 1$).

Mrk 290: Another source with relatively low spectral quality, thus resulting in an over-fitting of the data (i.e. $C/dof < 1$) despite a relatively low number of free to vary parameters in the final model. WA parameters were initialized based on Zhang et al. (2011).

Mrk 509: Despite the large residuals near ~ 8 keV in observation 0306090201, no significant UFO evidence was found. The other two observations were found to be best-fit when applying a two-component UFO scenario. Significant changes in $\log \xi_{\rm UFO}$ and $N_{\rm H,UFO}$ are found between the observations, spanning nearly six years. Interestingly, a decrease in $\log \xi_{\rm UFO}$ and $N_{\rm H,UFO}$ correspond to an increase in Γ and decrease in $L_{\rm X}$, with other source parameters remaining essentially unchanged between the two observations. WA parameters were initialized based on Detmers et al. (2010), though here we found that the inclusion of their $\log \xi_{\rm WA} \sim 3$ erg cm^{-2} s^{-1} component produced no significant fit improvement, therefore we only included two WAs. Observation 0130720101 did not have any WA literature, and therefore we linked all WAs between it and the other observation, though only the high-ionisation component was found to produce a significant fit improvement.

Mrk 766: The inclusion of an additional Fe emission line with $E_{\rm rest} = 6.66^{+0.08}_{-0.07}$ keV, $\sigma = 269^{+35}_{-59}$ eV, and $N = 1.8 \pm 0.5 \times 10^{-5}$ provided a fit improvement of $\Delta C/N_{\rm fp} = -50/4$ over both observations. Unlike Ark 120, however, the inclusion of this feature made no impact on the detection of the two UFOs in the source, and therefore it was not included in the analysis to be consistent with other sources. WA and photoionised emission parameters were initialized based on Buisson et al. (2018). We note that here we found one WA component to exhibit similar properties as in Buisson et al. (2018), however, our second WA component

tended toward a much lower ionisation (i.e. their $\log \xi_{\rm WA} \sim 1.3$ erg cm s^{-1}, our $\log \xi_{\rm WA} \sim -1.4$ erg cm s^{-1}).

Mrk 841: A relatively simple spectral fit produced several moderately significant deviations across the $7-10$ keV band. The addition of a high-$v_{\rm UFO}$ component, although not highly significant according to the velocity determination curve, provided a substantial fit improvement for only a single additional free parameter. WA parameters were initialized based on Longinotti et al. (2010).

NGC 3516: The overall spectral complexity of this source suggests additional model components are necessary, as the final fit was still poor ($C/dof = 288/186$). WA parameters were initialized based on Mehdipour et al. (2010), noting that their Phase B WA component had $v_{\rm turb} = 400$ km s^{-1}. We found that allowing this parameter to be free to vary during the fits produced $\Delta C = -85$ for $v_{\rm turb} = 50$ km s^{-1}, and thus we froze the parameter at that value in the best-fit model; allowing $v_{\rm turb}$ to be free to vary for the other WA components provided no statistically significant fit improvement.

NGC 3783: The single absorption feature at ~ 7.8 keV was nicely fit by a single component. We note that this AGN possessed the most complex low-energy spectral fit of the sample, requiring four WAs to adequately fit the data. WA parameters were initialized based on Mao et al. (2019), however, five of their nine components were found to provide insignificant improvements to the fit and therefore were not included here.

NGC 4051: Both spectra were fit relatively poorly, with the best-fit model to 0157560101 producing significant remaining residuals. We note that the velocity determination curve of 0109141401 reported a high-$v_{\rm UFO}$ component with $v_{\rm UFO} \sim 0.28c$. The inclusion of this

component via the XABSUFO model, however, found $v_{\rm UFO} \sim 0.34c$, which in fact places the features of this component outside the *XMM-Newton* bandpass. We therefore decided not to include this feature in our analysis, though its exclusion makes no significant changes to the conclusions. WA parameters were initialized based on Pounds et al. (2004), wherein a photoionised emitter was also suggested. We found significant differences between our WA and photoionised emitter parameters, most notably that each observation could be fit by a single WA component rather than the two found by Pounds et al. (2004). We therefore treated our WA and photoionised emitter fits according to our 'standard' method, assuming $v_{\rm turb} = 100$ km s^{-1} and zero inflow/outflow velocity.

PDS 456: Our UFO parameters are similar to those derived by Nardini et al. (2015), although with an XABSUFO upper limit of $\log \xi_{\rm UFO} = 5$ erg cm s^{-1} we cannot probe their measured $\log \xi_{\rm UFO} \sim 6$ erg cm s^{-1}. We note the we additionally detected a second component with $v_{\rm UFO} = 0.45 \pm 0.02c$, and also find that 0721010601 does not exhibit any evidence of a UFO whatsoever in our analysis. WA parameters were initialized based on Nardini et al. (2015).

PG 1211+143: A single broad absorption feature was found that required the largest $N_{\rm H,UFO}$ of any UFO in the sample, being significantly greater than previously reported measurements. WA parameters were initialized based on Pounds (2014).

PG 1448+273: A single broad absorption feature was fit well by a single UFO. We note significant parameter differences when compared to Kosec et al. (2020), though that analysis did not implement a full reflection model, instead using a LAOR line to derive reflection parameters based on the relativistically broadened Fe Kα line. Neutral and WA

parameters were initialized based on Kosec et al. (2020).

Swift J2127.4+5654: Black hole spin was very poorly constrained when left free to vary. When spin was fixed to $a = 0.998$ with break radius fixed to $r_{\rm break} = 6\ r_g$, the inner emissivity index was very poorly constrained to $q_{\rm in} \lesssim 1.5$. We then tested fixing $a = 0$ with $r_{\rm break} = 10\ r_g$ (to account for the fact that $r_{\rm in,\ a=0} = 6\ r_g$) and found that $q_{\rm in} \gtrsim -3$. Both scenarios give equivalent statistical fits to the data with the difference between them being $\Delta C < 1$. When considering the extreme light-bending taking place in the region near the SMBH (i.e. Miniutti & Fabian 2004) represented by the RELXILLD model, we concluded that results for $a = 0.998$ were unphysical and therefore chose to fix $a = 0$. In either case, however, no strong UFO evidence was found. We included a neutral absorption component in the source frame based on the results of Marinucci et al. (2014).

Appendix D

Contour plots

Here we plot the ratio residuals (top), significance contours (middle), and velocity determination curve (bottom) for each observation analysed in this work. Colour coding is the same as that described in Figure 4.1.

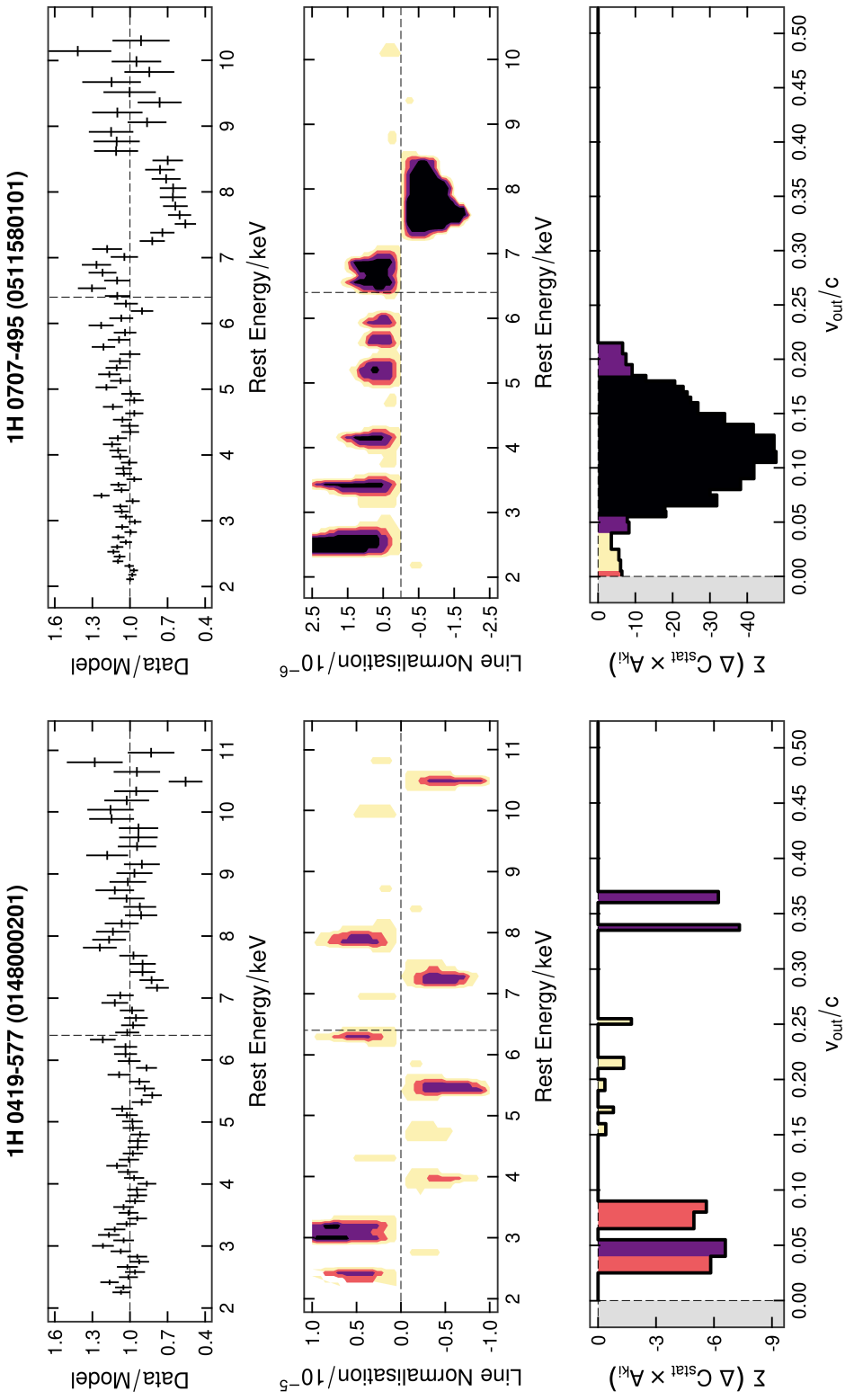
1H 0707-495 (0511580101)
1H 0419-577 (0148000201)
Data/Model
Rest Energy/keV
Line Normalisation/10⁻⁶
Line Normalisation/10⁻⁵
Σ (Δ C_stat × A_ki)
v_out/c

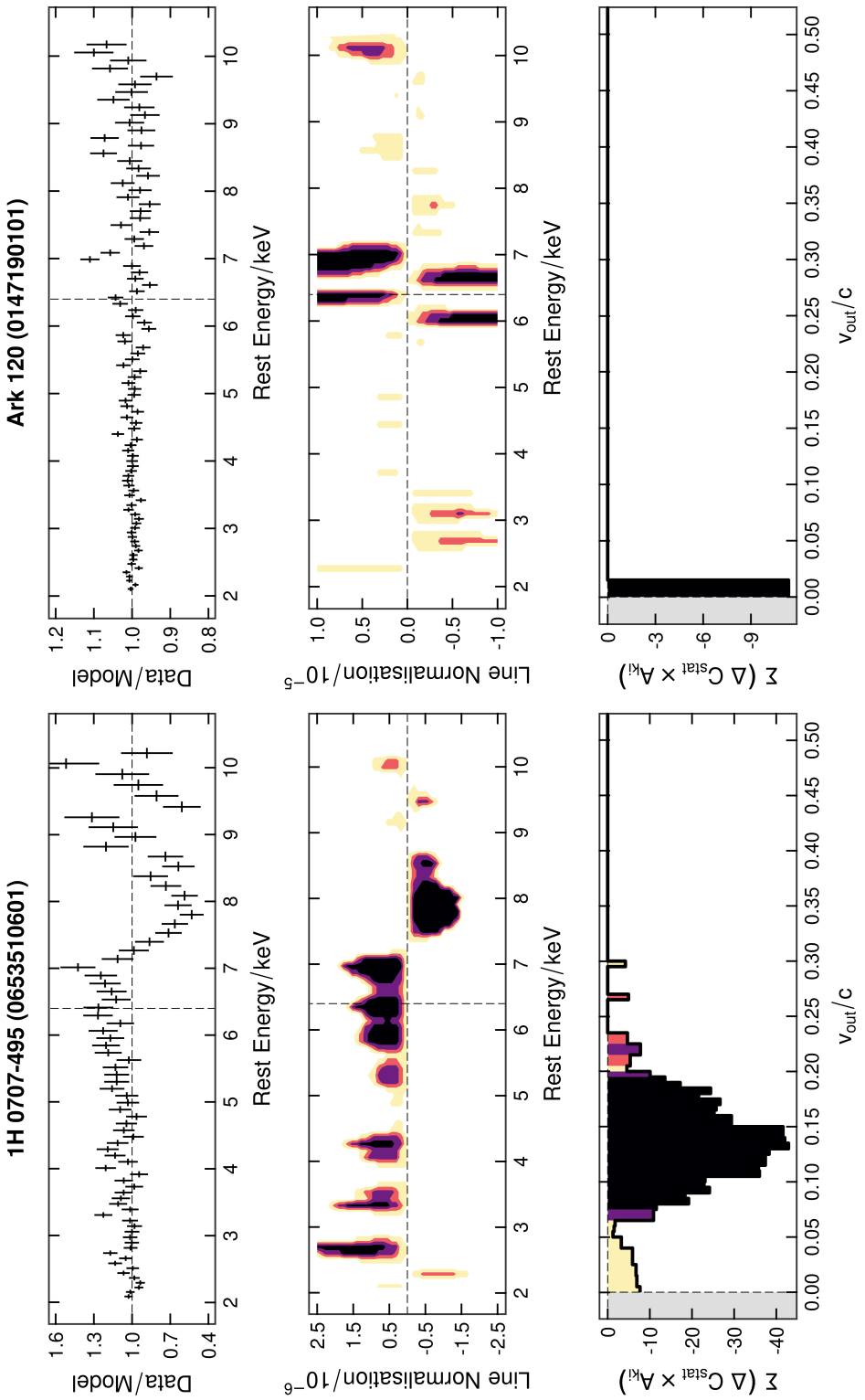
1H 0707-495 (0653510601)
Ark 120 (0147190101)
Data/Model
Rest Energy/keV
Line Normalisation/10⁻⁶
Line Normalisation/10⁻⁵
Σ (Δ C_stat × A_ki)
v_out/c

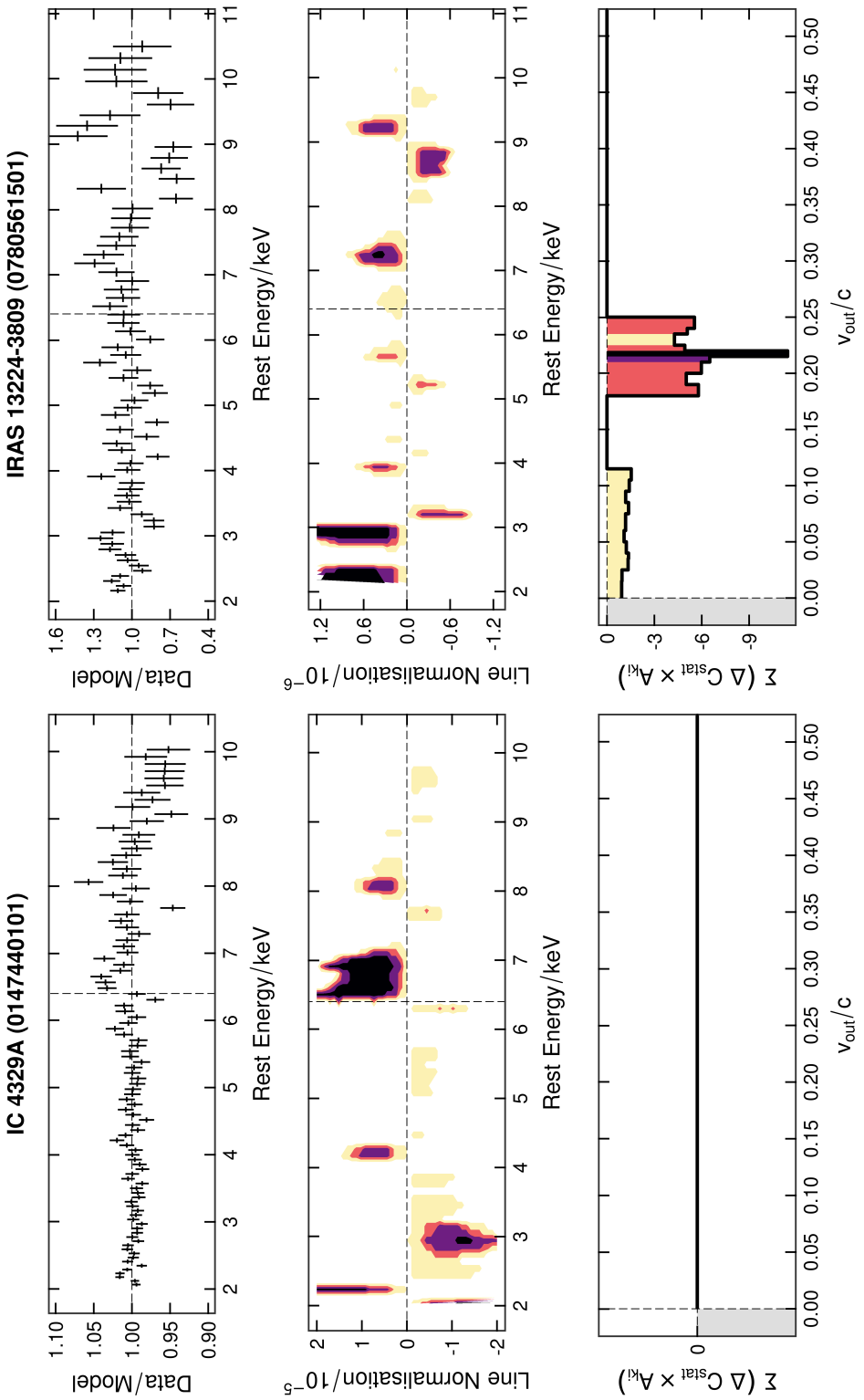
IRAS 13224-3809 (0780561501)
IC 4329A (0147440101)
Data/Model
Rest Energy/keV
Line Normalisation/10^-6
Line Normalisation/10^-5
Σ (Δ C_stat × A_ki)
v_out/c

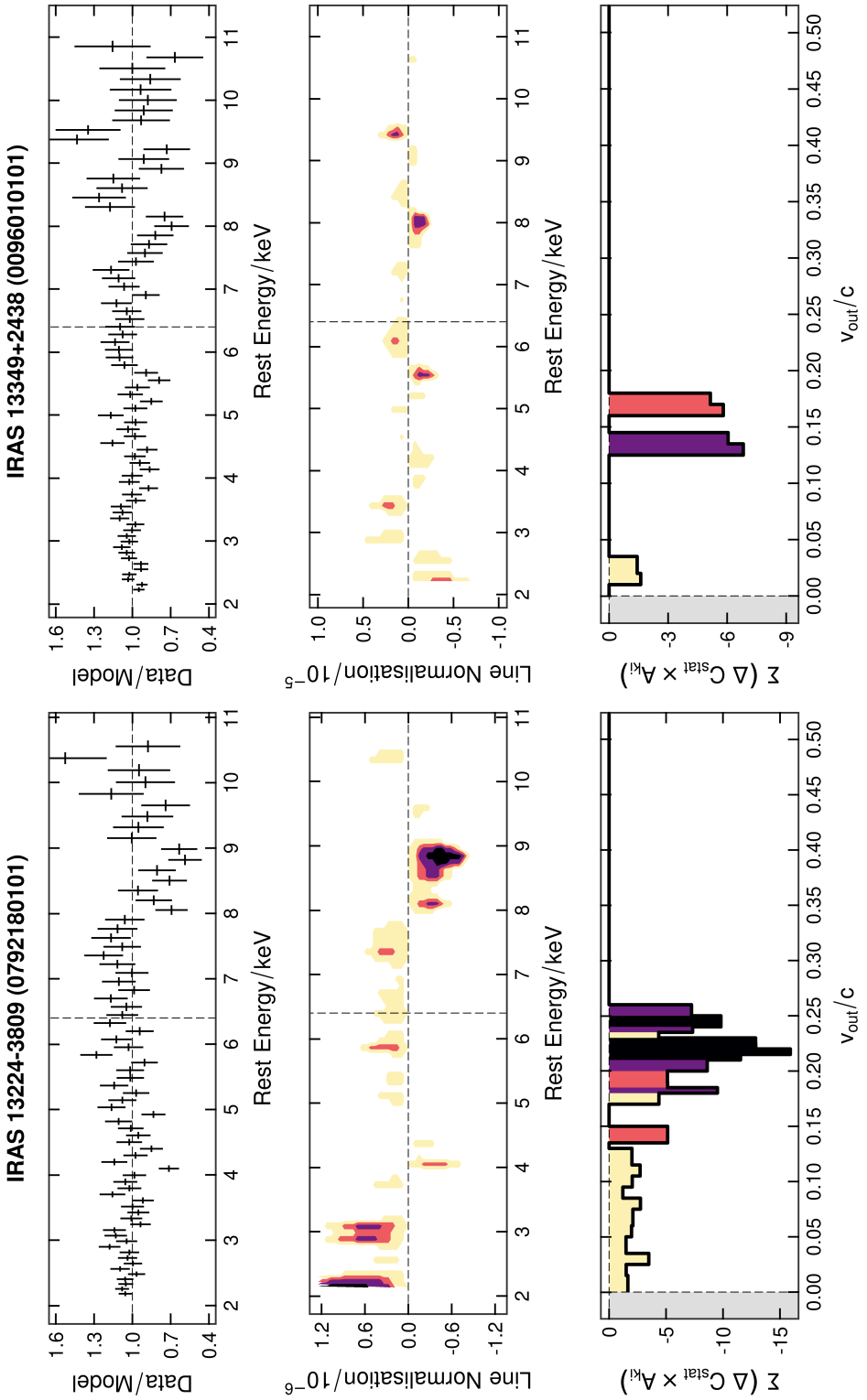
IRAS 13349+2438 (0096010101)
IRAS 13224-3809 (0792180101)
Data/Model
Rest Energy/keV
Line Normalisation/10⁻⁵
Line Normalisation/10⁻⁶
Σ (Δ C_stat × A_ki)
v_out/c

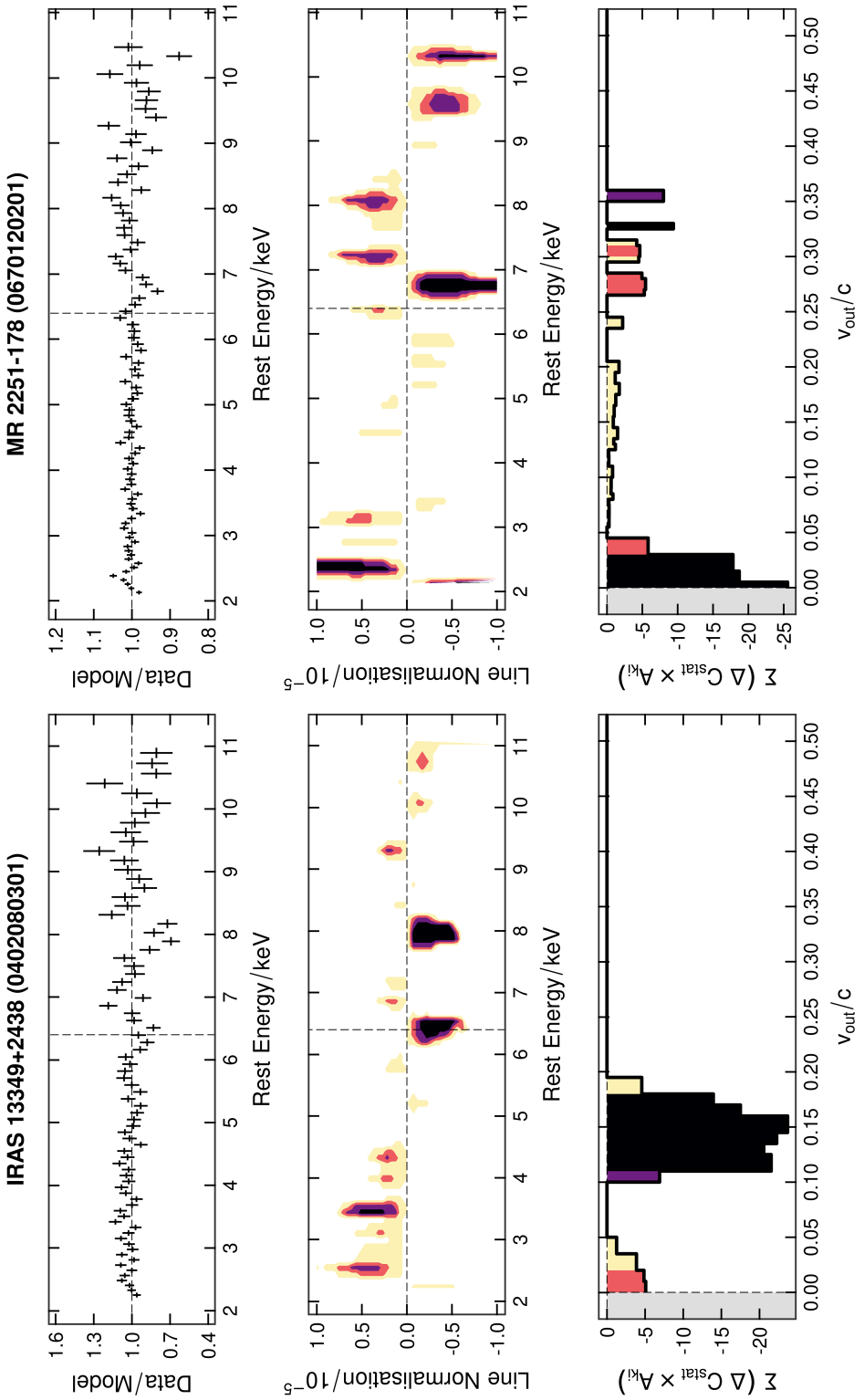
MR 2251-178 (0670120201)
IRAS 13349+2438 (0402080301)
Data/Model
Rest Energy/keV
Line Normalisation/10⁻⁵
Σ (Δ C_stat × A_ki)
v_out/c

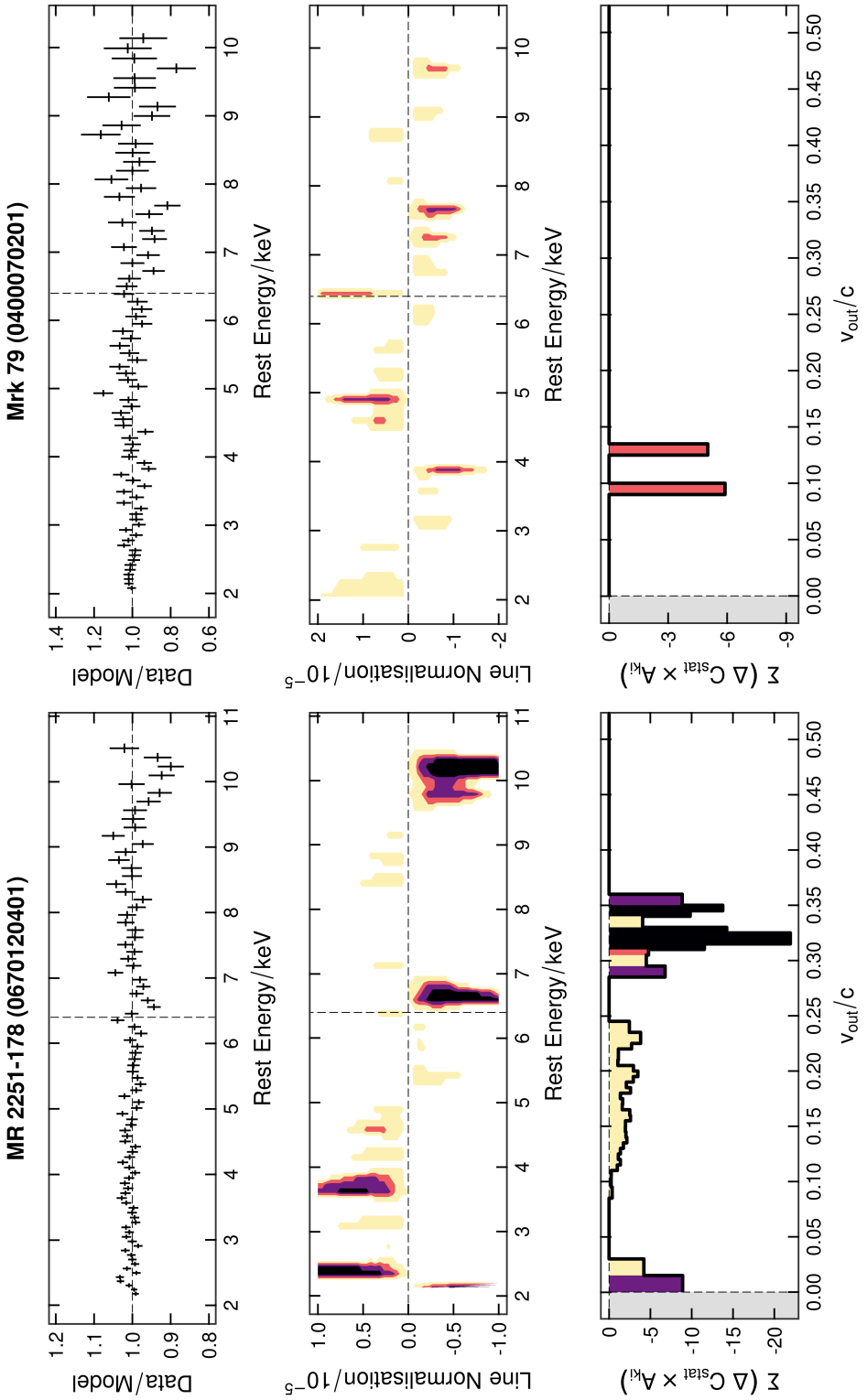
Mrk 79 (0400070201)
MR 2251-178 (0670120401)
Data/Model
Rest Energy/keV
Line Normalisation/10⁻⁵
ε (Δ C_stat × A_ki)
v_out/c

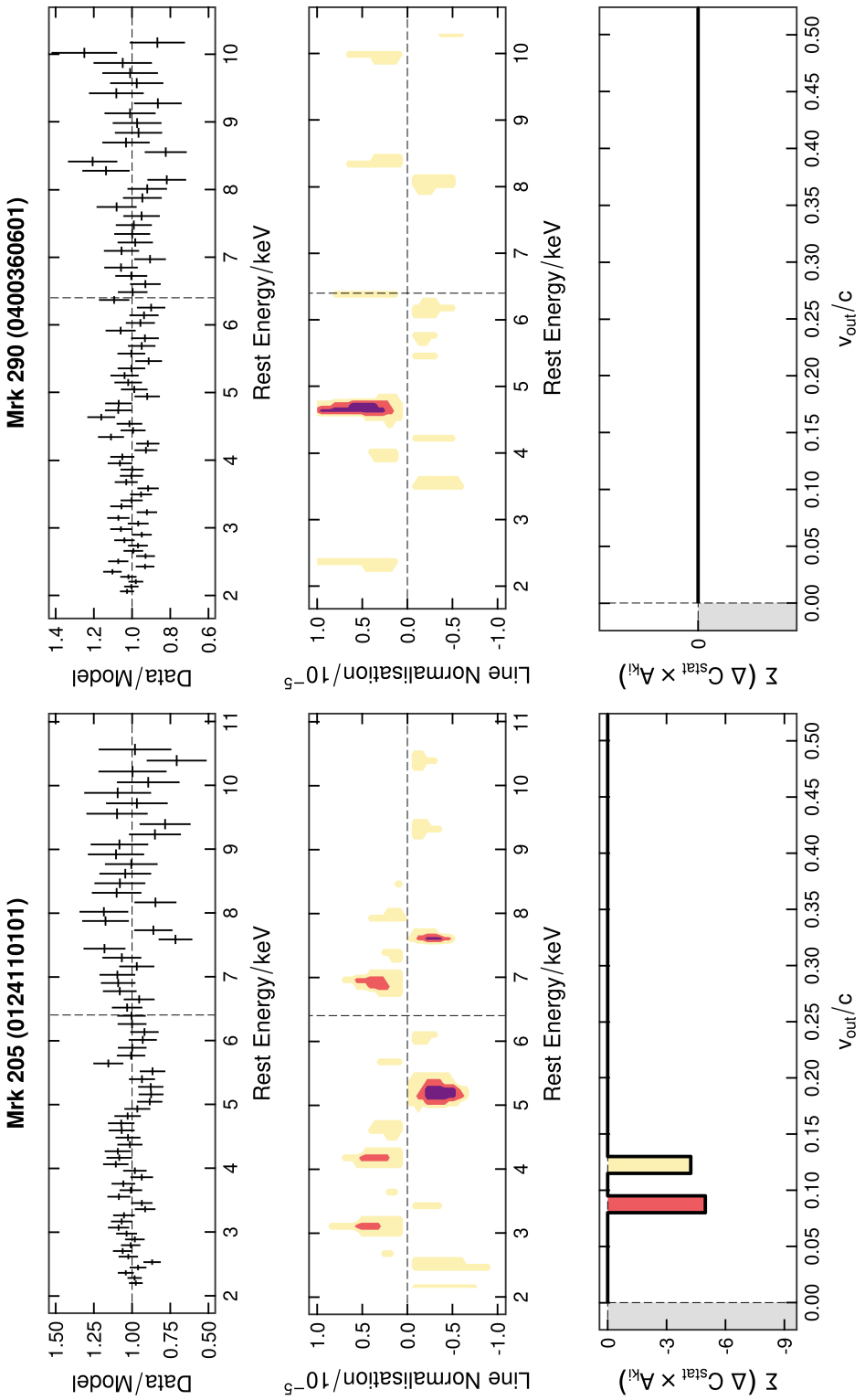
Mrk 290 (0400360601)
Mrk 205 (0124110101)
Data/Model
Rest Energy/keV
Line Normalisation/10⁻⁵
Σ (Δ Cstat × Aki)
vout/c

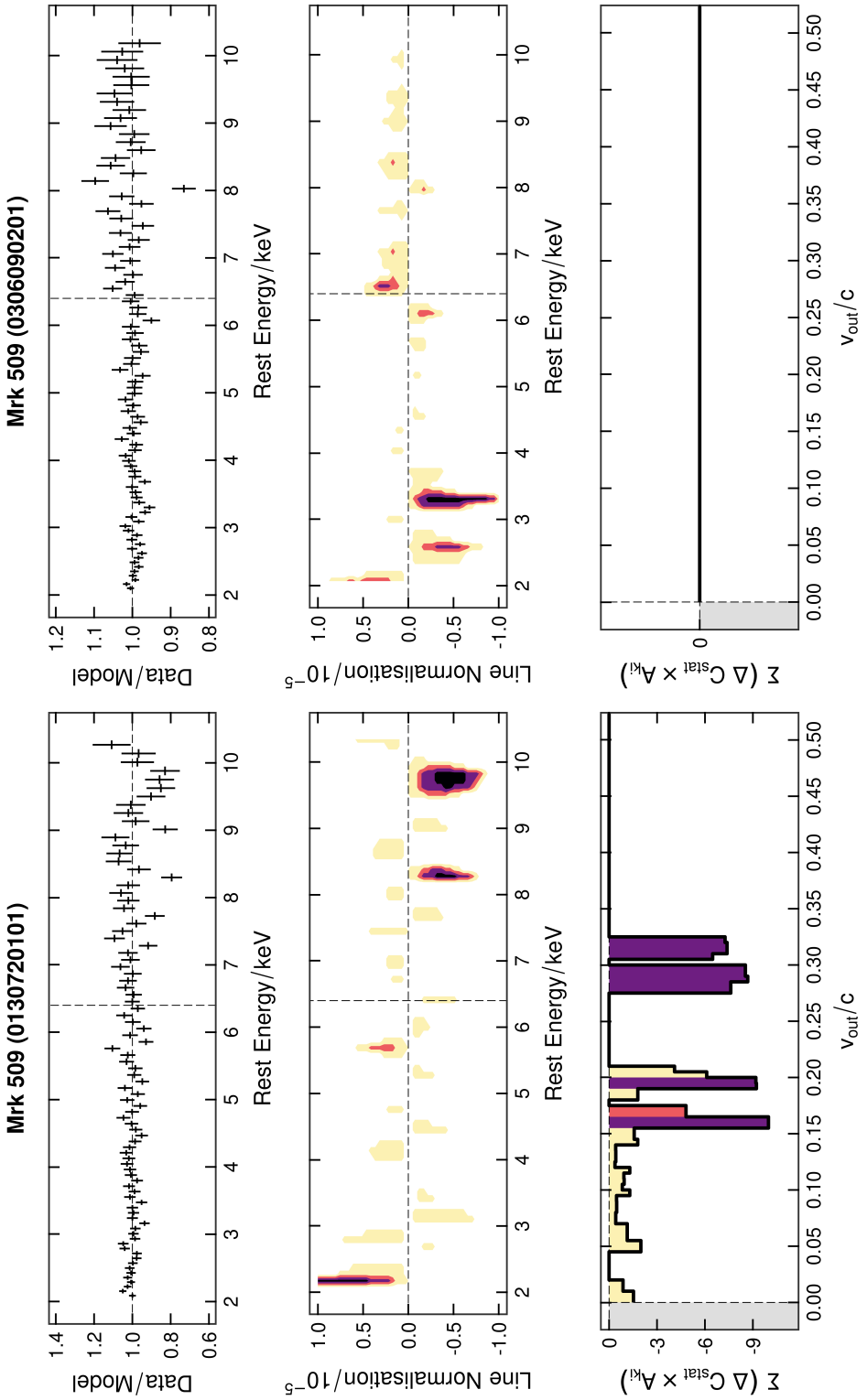
Mrk 509 (0306090201)
Mrk 509 (0130720101)
Data/Model
Rest Energy/keV
Line Normalisation/10⁻⁵
Σ (Δ C_stat × A_ki)
v_out/c

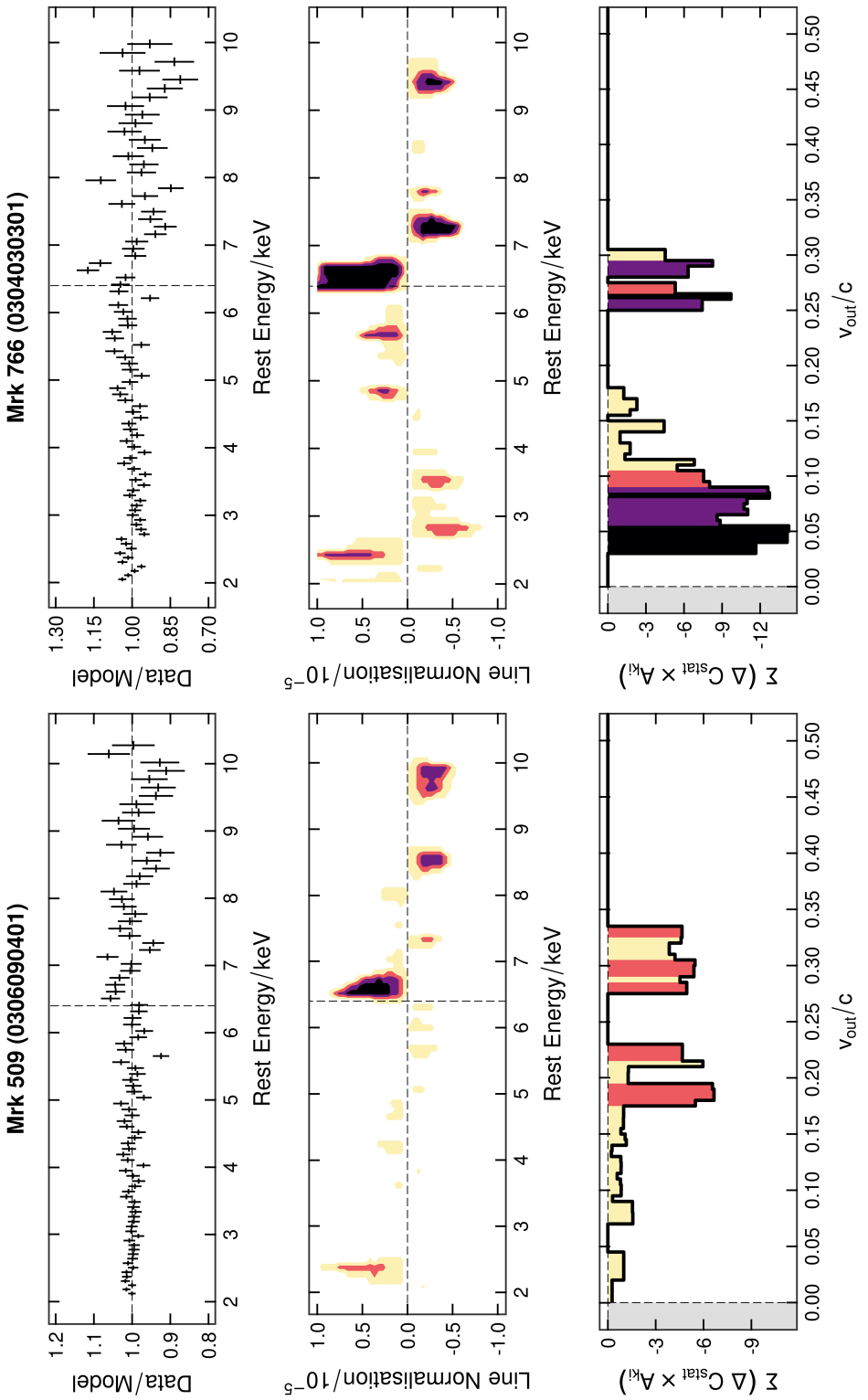
Mrk 509 (0306090401)
Mrk 766 (0304030301)
Data/Model
Rest Energy/keV
Line Normalisation/10⁻⁵
Σ (Δ C_stat × A_ki)
v_out/c

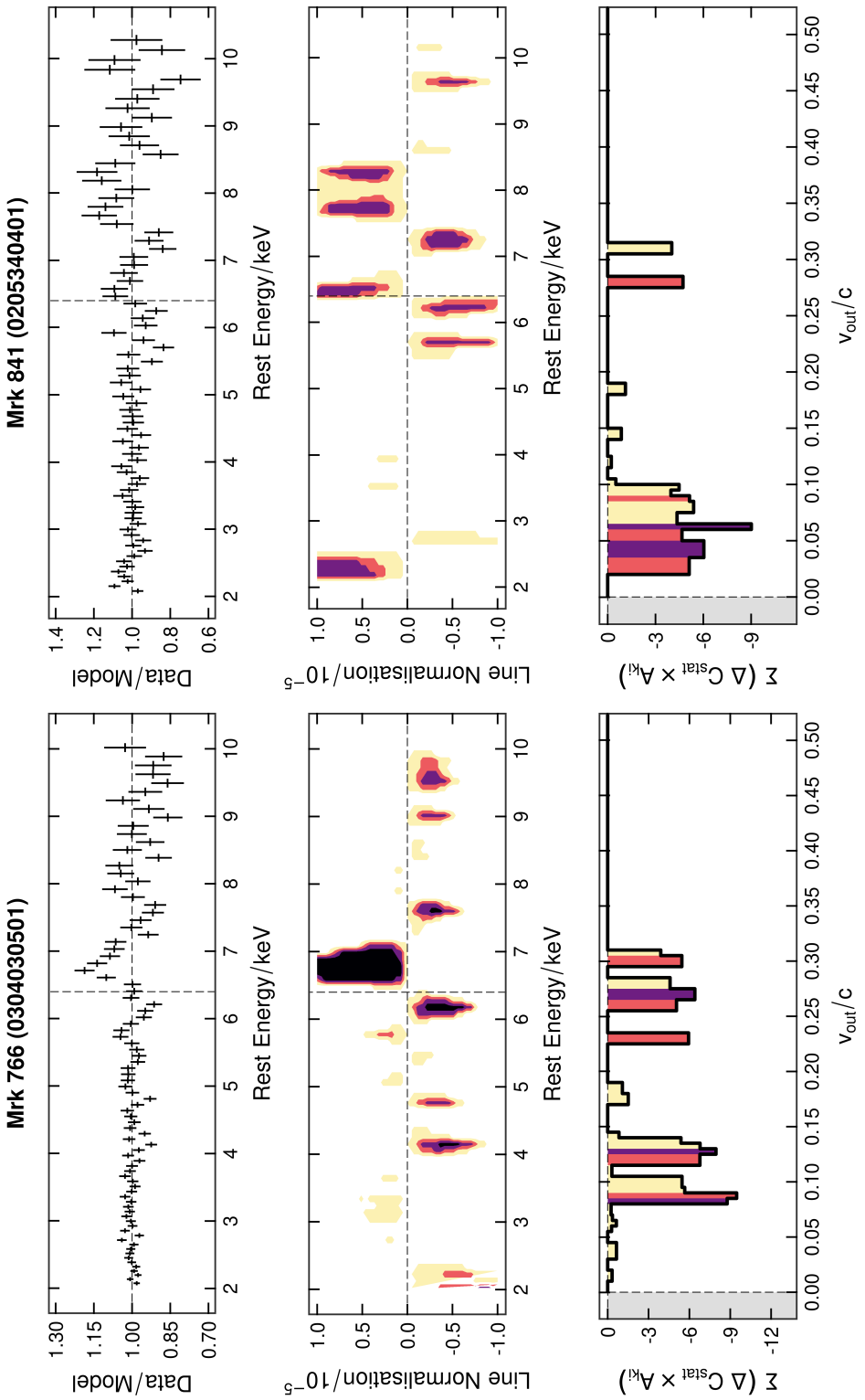
Mrk 841 (0205340401)
Mrk 766 (0304030501)
Data/Model
Rest Energy/keV
Line Normalisation/10⁻⁵
Σ (Δ C_stat × A_ki)
v_out/c

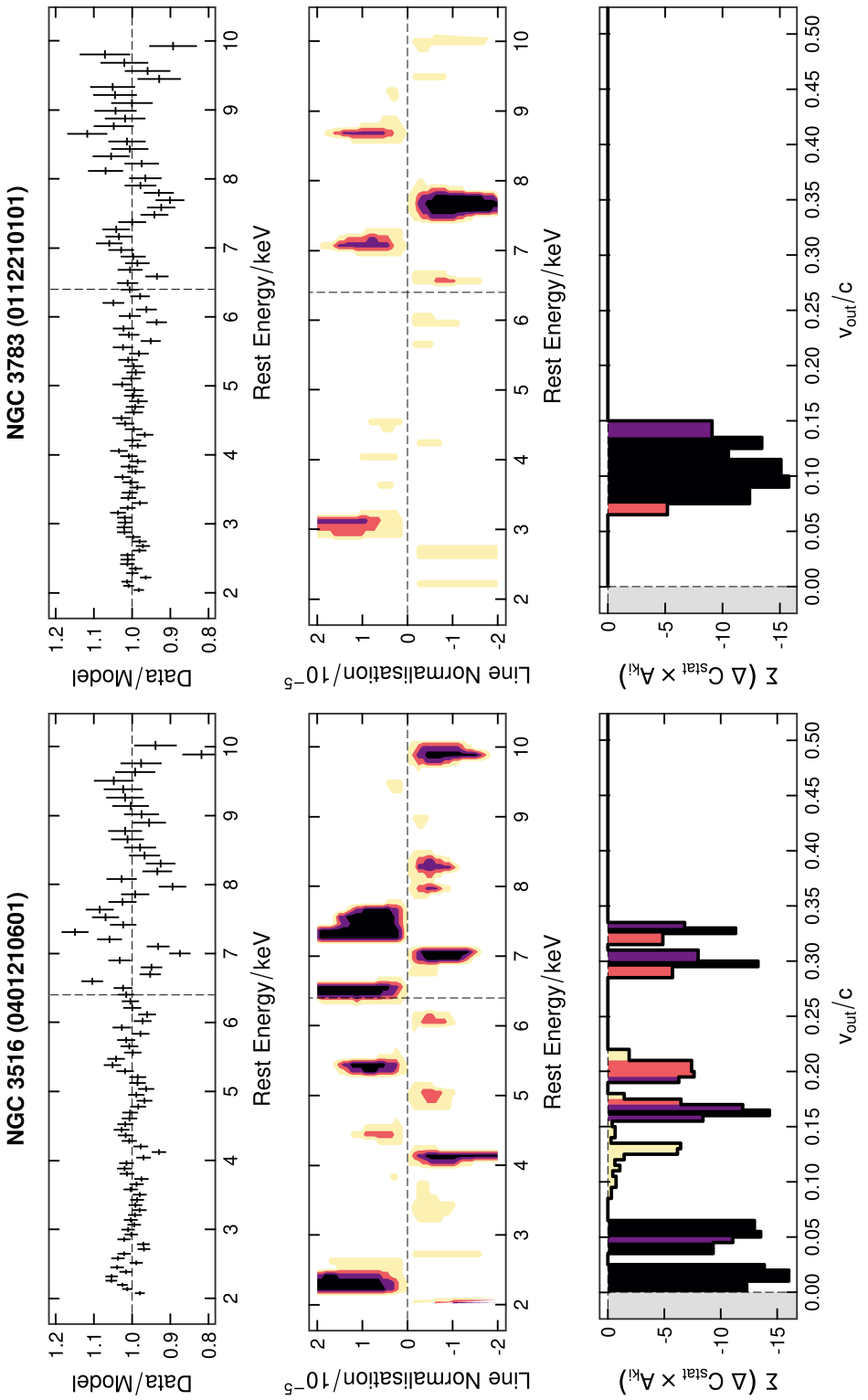
NGC 3516 (0401210601)
NGC 3783 (0112210101)
Data/Model
Rest Energy/keV
Line Normalisation/10^{-5}
Σ (Δ C$_{stat}$ × A$_{ki}$)
v$_{out}$/c

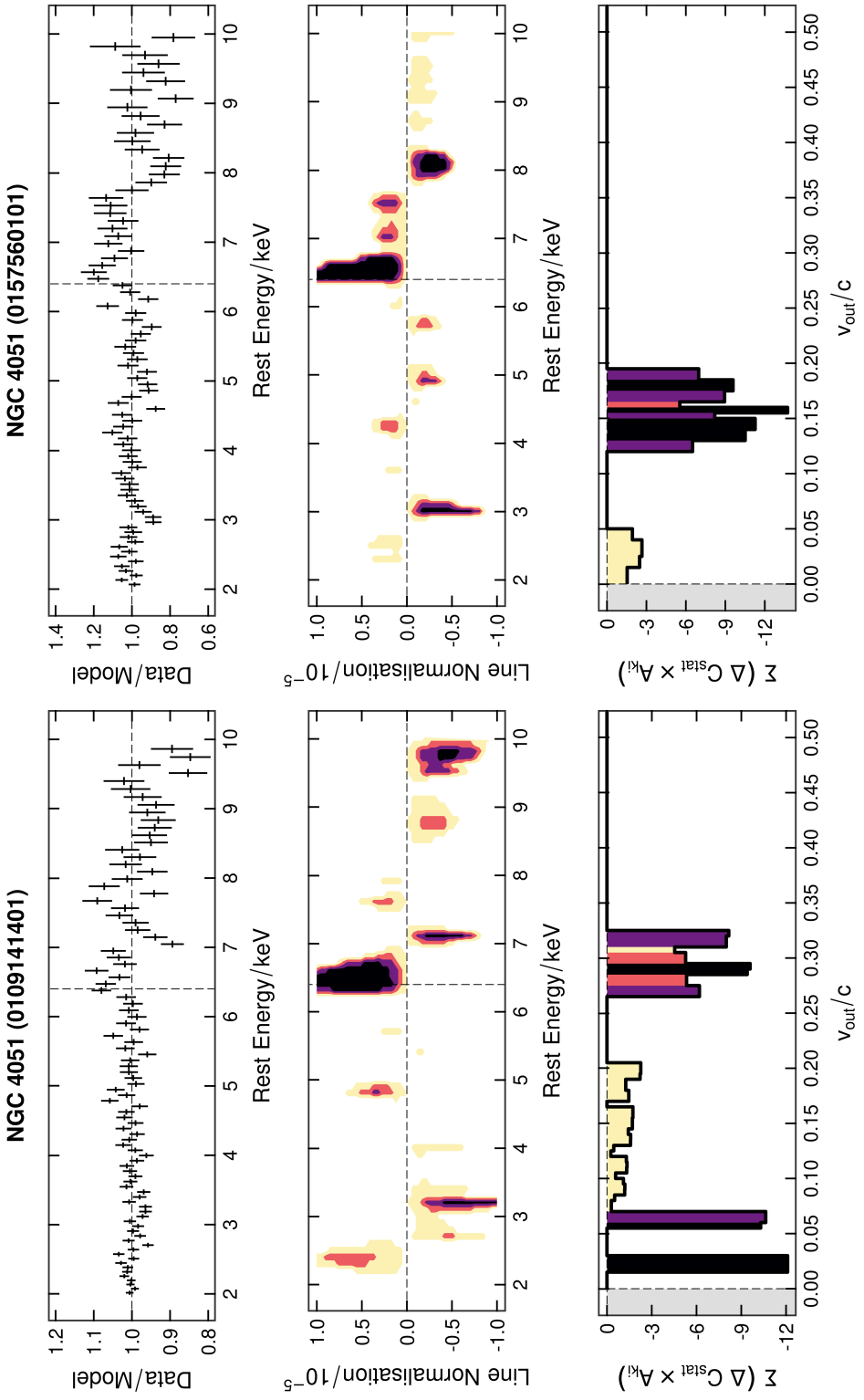
NGC 4051 (0109141401)
NGC 4051 (0157560101)
Data/Model
Rest Energy/keV
Line Normalisation/10⁻⁵
Σ (Δ Cstat × Aki)
vout/c

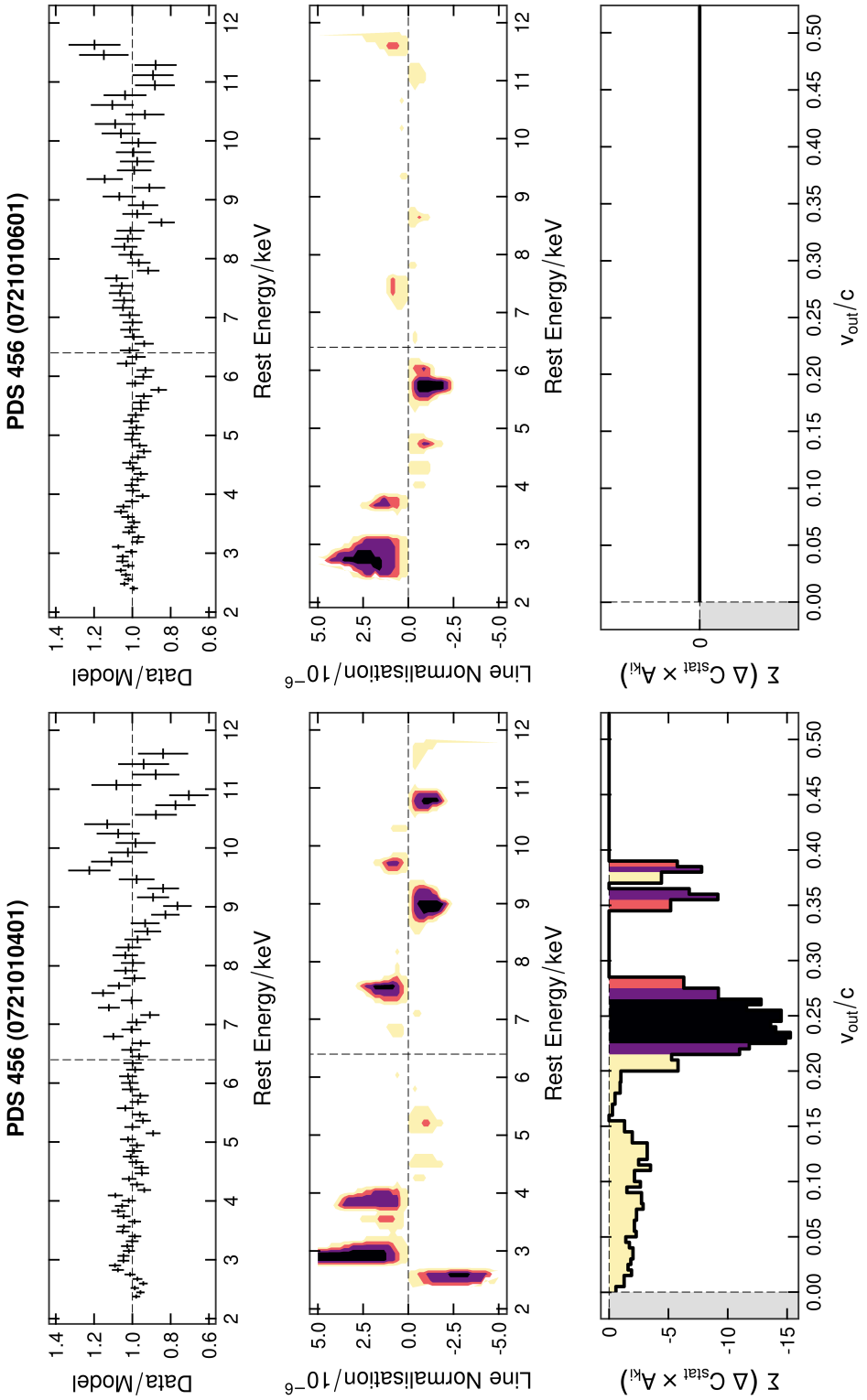
PDS 456 (0721010601)
PDS 456 (0721010401)
Data/Model
Rest Energy/keV
Line Normalisation/10^{-6}
Σ (Δ C$_{stat}$ × A$_{ki}$)
v$_{out}$/c

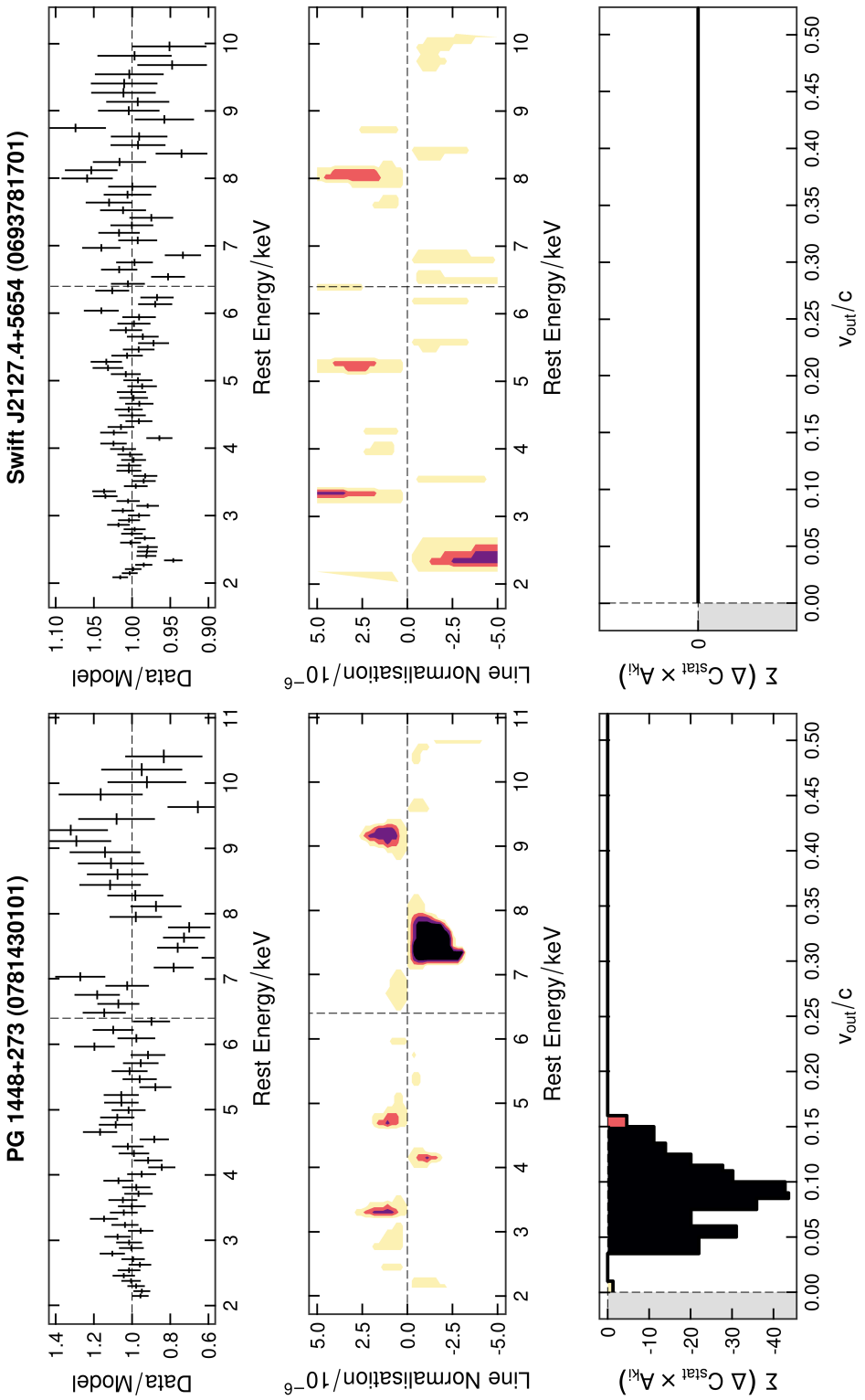
Swift J2127.4+5654 (0693781701)
PG 1448+273 (0781430101)
Data/Model
Rest Energy/keV
Line Normalisation/10^{-6}
Σ (Δ C$_{stat}$ × A$_{ki}$)
v$_{out}$/c

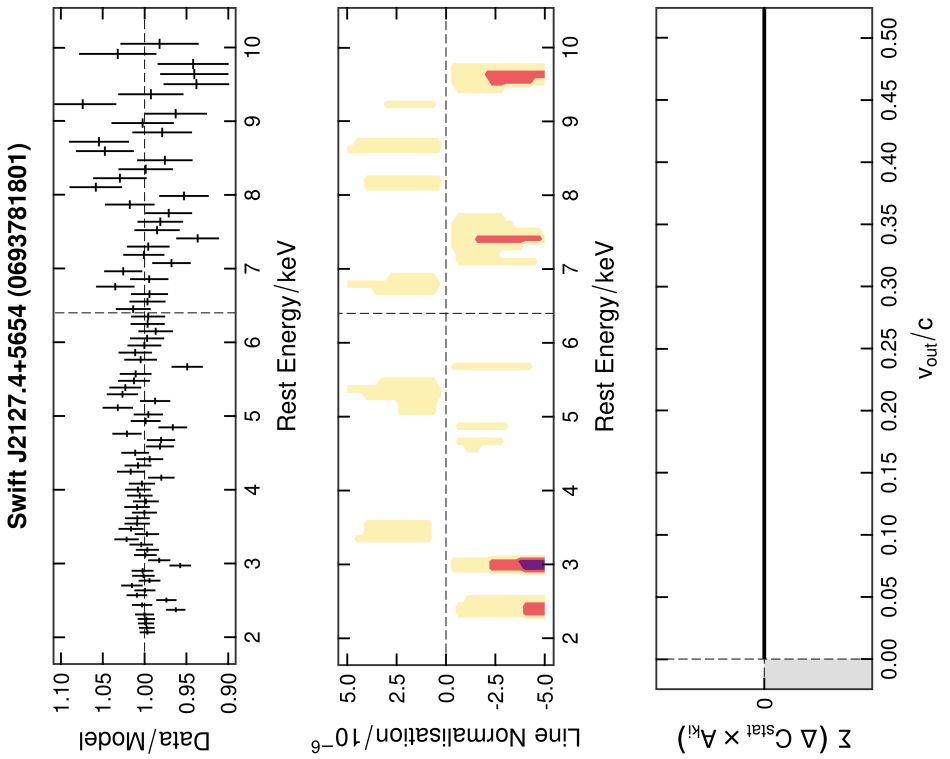
Swift J2127.4+5654 (0693781801)
Data/Model
Rest Energy/keV
Line Normalisation/10^{-6}
Rest Energy/keV
Σ (Δ C$_{stat}$ × A$_{ki}$)
v$_{out}$/c

Bibliography

Abdo, A. A., Ackermann, M., Ajello, M., et al. 2009a, ApJ , 699, 976

Abdo, A. A., Ackermann, M., Ajello, M., et al. 2009b, ApJ , 707, L142

Abramowicz, M. A., Calvani, M., & Nobili, L. 1980, ApJ , 242, 772

Abramowicz, M. A., Czerny, B., Lasota, J. P., & Szuszkiewicz, E. 1988, ApJ , 332, 646

Aller, H. D., Aller, M. F., Latimer, G. E., & Hodge, P. E. 1985, ApJS , 59, 513

Alston, W. N. 2019, MNRAS , 485, 260

Alston, W. N., Fabian, A. C., Buisson, D. J. K., et al. 2019, MNRAS , 482, 2088

Alston, W. N., Fabian, A. C., Kara, E., et al. 2020, Nature Astronomy, 2

Anderson, T. W. & Darling, D. A. 1952, Ann. Math. Statist., 23, 193

Antonucci, R. 1993, ARA&A , 31, 473

Antonucci, R. R. J. 1984, ApJ , 278, 499

Arévalo, P. & Uttley, P. 2006, MNRAS , 367, 801

Arnaud, K. A. 1996, in Astronomical Society of the Pacific Conference Series, Vol. 101, Astronomical Data Analysis Software and Systems V, ed. G. H. Jacoby & J. Barnes, 17

Arribas, S., Mediavilla, E., García-Lorenzo, B., & del Burgo, C. 1997, ApJ , 490, 227

Balbus, S. A. & Hawley, J. F. 1991, ApJ , 376, 214

Baumgartner, W. H., Tueller, J., Markwardt, C. B., et al. 2013, ApJS , 207, 19

Beckmann, V. & Shrader, C. R. 2012, Active Galactic Nuclei

Beckmann, V., Soldi, S., Ricci, C., et al. 2009, A&A , 505, 417

Bentz, M. C. & Katz, S. 2015, PASP , 127, 67

Berton, M., Congiu, E., Järvelä, E., et al. 2018, A&A , 614, A87

Berton, M., Foschini, L., Ciroi, S., et al. 2016, A&A , 591, A88

Berton, M., Foschini, L., Ciroi, S., et al. 2015, A&A , 578, A28

Bezanson, R., van Dokkum, P. G., Tal, T., et al. 2009, ApJ , 697, 1290

Bhatta, G., Mohorian, M., & Bilinsky, I. 2018, A&A , 619, A93

Blandford, R. D. & Königl, A. 1979, ApJ , 232, 34

Blandford, R. D. & Payne, D. G. 1982, MNRAS , 199, 883

Blandford, R. D. & Znajek, R. L. 1977, MNRAS , 179, 433

Blustin, A. J., Page, M. J., Fuerst, S. V., Branduardi-Raymont, G., & Ashton, C. E. 2005, A&A , 431, 111

Boehringer, H., Voges, W., Fabian, A. C., Edge, A. C., & Neumann, D. M. 1993, MNRAS , 264, L25

Boller, T., Brandt, W. N., & Fink, H. 1996, A&A , 305, 53

Bonning, E., Urry, C. M., Bailyn, C., et al. 2012, ApJ , 756, 13

Bonson, K. & Gallo, L. C. 2016, MNRAS , 458, 1927

Bonson, K., Gallo, L. C., & Vasudevan, R. 2015, MNRAS , 450, 857

Boroson, T. A. & Green, R. F. 1992, ApJS , 80, 109

Brandt, W. N., Mathur, S., & Elvis, M. 1997, MNRAS , 285, L25

Brightman, M., Silverman, J. D., Mainieri, V., et al. 2013, MNRAS , 433, 2485

Brunthaler, A., Falcke, H., Bower, G. C., et al. 2005, A&A , 435, 497

Brunthaler, A., Falcke, H., Bower, G. C., et al. 2003, PASA , 20, 126

Brunthaler, A., Falcke, H., Bower, G. C., et al. 2000, A&A , 357, L45

Buisson, D. J. K., Parker, M. L., Kara, E., et al. 2018, MNRAS , 480, 3689

Burrows, D. N., Hill, J. E., Nousek, J. A., et al. 2005, Space Sci. Rev. , 120, 165

Cano-Díaz, M., Maiolino, R., Marconi, A., et al. 2012, A&A , 537, L8

Cardelli, J. A., Clayton, G. C., & Mathis, J. S. 1989, ApJ , 345, 245

Carniani, S., Marconi, A., Maiolino, R., et al. 2016, A&A , 591, A28

Cash, W. 1979, The Astrophysical Journal, 228, 939

Castor, J. I., Abbott, D. C., & Klein, R. I. 1975, ApJ , 195, 157

Chartas, G. & Canas, M. H. 2018, ApJ , 867, 103

Chen, L., Cao, X., & Bai, J. M. 2012, ApJ , 748, 119

Chiaberge, M., Gilli, R., Lotz, J. M., & Norman, C. 2015, ApJ , 806, 147

Clements, S. D., Smith, A. G., Aller, H. D., & Aller, M. F. 1995, AJ , 110, 529

Condon, J. J. 1992, ARA&A , 30, 575

Congiu, E., Berton, M., Giroletti, M., et al. 2017, A&A , 603, A32

Congiu, E., Kharb, P., Tarchi, A., et al. 2020, MNRAS , 499, 3149

Contopoulos, J. & Lovelace, R. V. E. 1994, ApJ , 429, 139

Cresci, G., Mainieri, V., Brusa, M., et al. 2015, ApJ , 799, 82

Croton, D. J., Springel, V., White, S. D. M., et al. 2006, MNRAS , 365, 11

Crummy, J., Fabian, A. C., Gallo, L., & Ross, R. R. 2006, MNRAS , 365, 1067

Cunningham, C. T. 1975, ApJ , 202, 788

Dadina, M. 2008, A&A , 485, 417

D'Ammando, F. 2019, Galaxies, 7, 87

D'Ammando, F. 2020, MNRAS , 496, 2213

D'Ammando, F., Orienti, M., Finke, J., et al. 2012, MNRAS , 426, 317

D'Ammando, F., Orienti, M., Larsson, J., & Giroletti, M. 2015, MNRAS , 452, 520

Dauser, T., Svoboda, J., Schartel, N., et al. 2012, MNRAS , 422, 1914

De Marco, B., Adhikari, T. P., Ponti, G., et al. 2020, A&A , 634, A65

De Marco, B., Ponti, G., Cappi, M., et al. 2013, MNRAS , 431, 2441

den Herder, J. W., Brinkman, A. C., Kahn, S. M., et al. 2001, A&A , 365, L7

Detmers, R. G., Kaastra, J. S., Costantini, E., et al. 2010, A&A , 516, A61

Doi, A., Asada, K., Fujisawa, K., et al. 2013, ApJ , 765, 69

Doi, A., Asada, K., & Nagai, H. 2011, ApJ , 738, 126

Done, C., Davis, S. W., Jin, C., Blaes, O., & Ward, M. 2012, MNRAS , 420, 1848

Droste, J. 1917, Koninklijke Nederlandse Akademie van Wetenschappen Proceedings Series B Physical Sciences, 19, 197

Duras, F., Bongiorno, A., Ricci, F., et al. 2020, A&A , 636, A73

Edelson, R., Turner, T. J., Pounds, K., et al. 2002, ApJ , 568, 610

Einstein, A. 1939, Annals of Mathematics, 40, 922

Elitzur, M. 2006, New Astronomy Reviews , 50, 728

Espey, B. 1997, in Astronomical Society of the Pacific Conference Series, Vol. 113, IAU Colloq. 159: Emission Lines in Active Galaxies: New Methods and Techniques, ed. B. M. Peterson, F.-Z. Cheng, & A. S. Wilson, 175

Evans, P. A., Beardmore, A. P., Page, K. L., et al. 2009, MNRAS , 397, 1177

Event Horizon Telescope Collaboration, Akiyama, K., Alberdi, A., et al. 2019, ApJ , 875, L1

Fabian, A. C. 1994, ARA&A , 32, 277

Fabian, A. C. 1999, MNRAS , 308, L39

Fabian, A. C. 2012, ARA&A , 50, 455

Fabian, A. C., Kara, E., Walton, D. J., et al. 2013, MNRAS , 429, 2917

Fabian, A. C., Rees, M. J., Stella, L., & White, N. E. 1989, MNRAS , 238, 729

Fabian, A. C., Reynolds, C. S., Jiang, J., et al. 2020, MNRAS , 493, 2518

Fabian, A. C., Sanders, J. S., Allen, S. W., et al. 2003, MNRAS , 344, L43

Fabian, A. C., Sanders, J. S., Ettori, S., et al. 2000, MNRAS , 318, L65

Fabian, A. C., Sanders, J. S., Taylor, G. B., et al. 2006, MNRAS , 366, 417

Fabian, A. C., Vaughan, S., Nandra, K., et al. 2002, MNRAS , 335, L1

Fabian, A. C., Zoghbi, A., Ross, R. R., et al. 2009, Nature , 459, 540

Falcke, H., Bower, G. C., Lobanov, A. P., et al. 1999, ApJ , 514, L17

Falcke, H., Körding, E., & Markoff, S. 2004, A&A , 414, 895

Fanaroff, B. L. & Riley, J. M. 1974, MNRAS , 167, 31P

Ferrarese, L. & Merritt, D. 2000, ApJ , 539, L9

Fiore, F., Feruglio, C., Shankar, F., et al. 2017, A&A , 601, A143

Foschini, L. 2011, Research in Astronomy and Astrophysics, 11, 1266

Foschini, L., Berton, M., Caccianiga, A., et al. 2015, A&A , 575, A13

Fossati, G., Maraschi, L., Celotti, A., Comastri, A., & Ghisellini, G. 1998, MNRAS , 299, 433

Fukumura, K., Kazanas, D., Contopoulos, I., & Behar, E. 2010a, ApJ , 715, 636

Fukumura, K., Kazanas, D., Contopoulos, I., & Behar, E. 2010b, ApJ , 723, L228

Fukumura, K., Tombesi, F., Kazanas, D., et al. 2014, ApJ , 780, 120

Fukumura, K., Tombesi, F., Kazanas, D., et al. 2015, ApJ , 805, 17

Galeev, A. A., Rosner, R., & Vaiana, G. S. 1979, ApJ , 229, 318

Gallo, L. 2018, in Revisiting Narrow-Line Seyfert 1 Galaxies and their Place in the Universe, 34

Gallo, L. C. 2011, JRASC , 105, 143

Gallo, L. C., Blue, D. M., Grupe, D., Komossa, S., & Wilkins, D. R. 2018, MNRAS , 478, 2557

Gallo, L. C., Boller, T., Brandt, W. N., Fabian, A. C., & Vaughan, S. 2004, A&A , 417, 29

Gallo, L. C., Brandt, W. N., Costantini, E., & Fabian, A. C. 2007, MNRAS , 377, 1375

Gallo, L. C., Edwards, P. G., Ferrero, E., et al. 2006, MNRAS , 370, 245

Gallo, L. C. & Fabian, A. C. 2011, MNRAS , 418, L59

Gallo, L. C. & Fabian, A. C. 2013, MNRAS , 434, L66

Gallo, L. C., Fabian, A. C., Grupe, D., et al. 2013, MNRAS , 428, 1191

Gallo, L. C., Gonzalez, A. G., & Miller, J. M. 2021, ApJ , 908, L33

Gallo, L. C., Miniutti, G., Miller, J. M., et al. 2011, MNRAS , 411, 607

Gallo, L. C., Wilkins, D. R., Bonson, K., et al. 2015, MNRAS , 446, 633

García, J., Dauser, T., Lohfink, A., et al. 2014, ApJ , 782, 76

García, J. & Kallman, T. R. 2010, ApJ , 718, 695

García, J. A., Fabian, A. C., Kallman, T. R., et al. 2016, MNRAS , 462, 751

Gebhardt, K., Bender, R., Bower, G., et al. 2000, ApJ , 539, L13

George, I. M., Turner, T. J., Netzer, H., et al. 1998, ApJS , 114, 73

Gierliński, M. & Done, C. 2004, MNRAS , 349, L7

Giroletti, M., Panessa, F., Longinotti, A. L., et al. 2017, A&A , 600, A87

Gofford, J., Reeves, J. N., McLaughlin, D. E., et al. 2015, MNRAS , 451, 4169

Gofford, J., Reeves, J. N., Tombesi, F., et al. 2013, MNRAS , 430, 60

Gonzalez, A. G., Wilkins, D. R., & Gallo, L. C. 2017, MNRAS , 472, 1932

González-Martín, O. & Vaughan, S. 2012, A&A , 544, A80

Goodrich, R. W. 1989, ApJ , 342, 224

Gorenstein, P., Fabricant, D., Topka, K., Harnden, F. R., J., & Tucker, W. H. 1978, ApJ , 224, 718

Grier, C. J., Peterson, B. M., Pogge, R. W., et al. 2012, ApJ , 755, 60

Haardt, F. & Maraschi, L. 1991, ApJ , 380, L51

Hardcastle, M. J. & Croston, J. H. 2020, New Astronomy Reviews , 88, 101539

Harrison, F. A., Craig, W. W., Christensen, F. E., et al. 2013, ApJ , 770, 103

Helmken, H., Delvaille, J. P., Epstein, A., et al. 1978, ApJ , 221, L43

Hitomi Collaboration, Aharonian, F., Akamatsu, H., et al. 2016, Nature , 535, 117

Hitomi Collaboration, Aharonian, F., Akamatsu, H., et al. 2018, PASJ , 70, 12

Humphrey, P. J., Liu, W., & Buote, D. A. 2009, ApJ , 693, 822

Hutchings, J. B. & Campbell, B. 1983, Nature , 303, 584

Igo, Z., Parker, M. L., Matzeu, G. A., et al. 2020, MNRAS , 493, 1088

Ishibashi, W. & Fabian, A. C. 2012, MNRAS , 427, 2998

Jansen, F., Lumb, D., Altieri, B., et al. 2001, A&A , 365, L1

Jiang, J., Fabian, A. C., Dauser, T., et al. 2019, MNRAS , 489, 3436

Jiang, J., Parker, M. L., Fabian, A. C., et al. 2018, MNRAS , 477, 3711

Kaastra, J. S. 2017, A&A , 605, A51

Kaastra, J. S. & Bleeker, J. A. M. 2016, A&A , 587, A151

Kaastra, J. S. & de Korte, P. A. J. 1988, A&A , 198, 16

Kaastra, J. S., Kriss, G. A., Cappi, M., et al. 2014, Science, 345, 64

Kaastra, J. S., Mewe, R., & Nieuwenhuijzen, H. 1996, in UV and X-ray Spectroscopy of Astrophysical and Laboratory Plasmas, 411–414

Kalberla, P. M. W., Burton, W. B., Hartmann, D., et al. 2005, A&A , 440, 775

Kallman, T. & Bautista, M. 2001, ApJS , 133, 221

Kallman, T. R. 1995, ApJ , 455, 603

Kara, E., Alston, W. N., Fabian, A. C., et al. 2016, MNRAS , 462, 511

Kara, E., Fabian, A. C., Cackett, E. M., et al. 2013, MNRAS , 428, 2795

Kataoka, J., Reeves, J. N., Iwasawa, K., et al. 2007, PASJ , 59, 279

Keel, B. 2002, Optical spectrum of NGC 4151 and NGC 4941., `http://pages.astronomy.ua.edu/keel/agn/`, accessed: 2021-06-10

Kellermann, K. I. & Pauliny-Toth, I. I. K. 1966, Nature , 212, 781

Kellermann, K. I., Sramek, R., Schmidt, M., Shaffer, D. B., & Green, R. 1989, AJ , 98, 1195

King, A. 2005, ApJ , 635, L121

King, A. & Pounds, K. 2015, ARA&A , 53, 115

King, A. L., Lohfink, A., & Kara, E. 2017, ApJ , 835, 226

Kirhakos, S., Bahcall, J. N., Schneider, D. P., & Kristian, J. 1999, ApJ , 520, 67

Komossa, S. & Bade, N. 1998, A&A , 331, L49

Komossa, S., Grupe, D., Schartel, N., et al. 2017, in IAU Symposium, Vol. 324, New Frontiers in Black Hole Astrophysics, ed. A. Gomboc, 168–171

Komossa, S., Voges, W., Xu, D., et al. 2006, AJ , 132, 531

Körding, E., Falcke, H., & Corbel, S. 2006, A&A , 456, 439

Kosec, P., Zoghbi, A., Walton, D. J., et al. 2020, MNRAS , 495, 4769

Kotov, O., Churazov, E., & Gilfanov, M. 2001, MNRAS , 327, 799

Kramida, A., Ralchenko, Y., Reader, J., & NIST ASD Team. 2020, NIST Atomic Spectral Database (version 5.8) [Online], https://physics.nist.gov/asd

Lähteenmäki, A., Järvelä, E., Hovatta, T., et al. 2017, A&A , 603, A100

Lähteenmäki, A., Järvelä, E., Ramakrishnan, V., et al. 2018, A&A , 614, L1

LaMassa, S. M., Cales, S., Moran, E. C., et al. 2015, ApJ , 800, 144

Laor, A. 1991, ApJ , 376, 90

Laor, A. 2000, ApJ , 543, L111

Leighly, K. M. 1999a, ApJS , 125, 297

Leighly, K. M. 1999b, ApJS , 125, 317

Leighly, K. M. 2000, New Astronomy Reviews , 44, 395

Leighly, K. M., Kay, L. E., Wills, B. J., Wills, D., & Grupe, D. 1997, ApJ , 489, L137

Li, H. Z., Xie, G. Z., Dai, H., et al. 2010, New Astronomy , 15, 254

Lightman, A. P. & White, T. R. 1988, ApJ , 335, 57

Liska, M., Hesp, C., Tchekhovskoy, A., et al. 2017, ArXiv e-prints

Lloyd, C. 1984, MNRAS , 209, 697

Lohfink, A. M., Reynolds, C. S., Jorstad, S. G., et al. 2013, ApJ , 772, 83

Longinotti, A. L., Costantini, E., Petrucci, P. O., et al. 2010, A&A , 510, A92

Longinotti, A. L., Krongold, Y., Guainazzi, M., et al. 2015, ApJ , 813, L39

Lynden-Bell, D. & Rees, M. J. 1971, MNRAS , 152, 461

Lyubarskii, Y. E. 1997, MNRAS , 292, 679

Malizia, A., Bassani, L., Bird, A. J., et al. 2008, MNRAS , 389, 1360

Mallick, L., Dewangan, G. C., Gandhi, P., Misra, R., & Kembhavi, A. K. 2016, MNRAS , 460, 1705

Mao, J., Mehdipour, M., Kaastra, J. S., et al. 2019, A&A , 621, A99

Marinucci, A., Matt, G., Kara, E., et al. 2014, MNRAS , 440, 2347

Markowitz, A., Edelson, R., & Vaughan, S. 2003, ApJ , 598, 935

Markowitz, A., Reeves, J. N., & Braito, V. 2006, ApJ , 646, 783

Mason, K. O., Breeveld, A., Much, R., et al. 2001, A&A , 365, L36

McHardy, I. M., Koerding, E., Knigge, C., Uttley, P., & Fender, R. P. 2006, Nature , 444, 730

McKernan, B., Yaqoob, T., & Reynolds, C. S. 2007, MNRAS , 379, 1359

McNamara, B. R., Nulsen, P. E. J., Wise, M. W., et al. 2005, Nature , 433, 45

Mehdipour, M., Branduardi-Raymont, G., & Page, M. J. 2010, A&A , 514, A100

Mehdipour, M., Kaastra, J. S., & Kallman, T. 2016, A&A , 596, A65

Merloni, A. & Fabian, A. C. 2001, MNRAS , 328, 958

Merloni, A., Heinz, S., & di Matteo, T. 2003, MNRAS , 345, 1057

Mihos, C. 2018, Optical spectrum of 3C 273, courtesy of Bill Keel, University of Alabama., `http://burro.astr.cwru.edu/Academics/Astr222/Galaxies/Active/obsAGN.html`, accessed: 2021-06-10

Miller, J. M., Kaastra, J. S., Miller, M. C., et al. 2015, Nature , 526, 542

Miller, J. S. & Goodrich, R. W. 1990, ApJ , 355, 456

Miniutti, G. & Fabian, A. C. 2004, MNRAS , 349, 1435

Mitsuda, K., Bautz, M., Inoue, H., et al. 2007, PASJ , 59, S1

Murray, N., Chiang, J., Grossman, S. A., & Voit, G. M. 1995, ApJ , 451, 498

Nandra, K., Barret, D., Barcons, X., et al. 2013, arXiv e-prints, arXiv:1306.2307

Nandra, K., O'Neill, P. M., George, I. M., & Reeves, J. N. 2007, MNRAS , 382, 194

Nandra, K. & Pounds, K. A. 1994, MNRAS , 268, 405

Nardini, E., Reeves, J. N., Gofford, J., et al. 2015, Science, 347, 860

Nikołajuk, M., Czerny, B., & Gurynowicz, P. 2009, MNRAS , 394, 2141

Nomoto, K., Maeda, K., Mazzali, P. A., et al. 2004, Hypernovae and Other Black-Hole-Forming Supernovae, ed. C. L. Fryer, Vol. 302, 277–325

Nowak, M. A., Hanke, M., Trowbridge, S. N., et al. 2011, ApJ , 728, 13

Oke, J. B. 1963, Nature , 197, 1040

Orosz, J. A., McClintock, J. E., Aufdenberg, J. P., et al. 2011, ApJ , 742, 84

Osterbrock, D. E. 1977, ApJ , 215, 733

Osterbrock, D. E. & Pogge, R. W. 1985, ApJ , 297, 166

Pal, M., Dewangan, G. C., Kembhavi, A. K., Misra, R., & Naik, S. 2018, MNRAS , 473, 3584

Parker, M. L., Buisson, D. J. K., Jiang, J., et al. 2018a, MNRAS , 479, L45

Parker, M. L., Longinotti, A. L., Schartel, N., et al. 2019, MNRAS , 490, 683

Parker, M. L., Matzeu, G. A., Alston, W. N., et al. 2020, MNRAS , 498, L140

Parker, M. L., Matzeu, G. A., Guainazzi, M., et al. 2018b, MNRAS , 480, 2365

Peterson, B. M. 2006, The Broad-Line Region in Active Galactic Nuclei, ed. D. Alloin, Vol. 693, 77

Peterson, B. M., Ferrarese, L., Gilbert, K. M., et al. 2004, ApJ , 613, 682

Peterson, B. M., McHardy, I. M., & Wilkes, B. J. 2000, New Astronomy Reviews , 44, 491

Petrucci, P. O., Merloni, A., Fabian, A., Haardt, F., & Gallo, E. 2001, MNRAS , 328, 501

Petrucci, P. O., Ursini, F., De Rosa, A., et al. 2018, A&A , 611, A59

Pinto, C., Alston, W., Parker, M. L., et al. 2018, MNRAS , 476, 1021

Ponti, G., Papadakis, I., Bianchi, S., et al. 2012, A&A , 542, A83

Porquet, D., Reeves, J. N., O'Brien, P., & Brinkmann, W. 2004, A&A , 422, 85

Pounds, K. A. 2014, MNRAS , 437, 3221

Pounds, K. A., Reeves, J. N., King, A. R., & Page, K. L. 2004, MNRAS , 350, 10

Proga, D., Stone, J. M., & Kallman, T. R. 2000, ApJ , 543, 686

Ramos Almeida, C., Bessiere, P. S., Tadhunter, C. N., et al. 2012, MNRAS , 419, 687

Ramos Almeida, C. & Ricci, C. 2017, Nature Astronomy, 1, 679

Reeves, J. N., Porquet, D., Braito, V., et al. 2013, ApJ , 776, 99

Reynolds, C. S. 1997, MNRAS , 286, 513

Reynolds, C. S. 2014, Space Sci. Rev. , 183, 277

Ricci, C., Trakhtenbrot, B., Koss, M. J., et al. 2017, ApJS , 233, 17

Ricci, C. 2013, Typical structure of an AGN., `https://www.isdc.unige.ch/~ricci/Website/Active_Galactic_Nuclei.html`, accessed: 2021-06-10

Richards, G. T., Lacy, M., Storrie-Lombardi, L. J., et al. 2006, ApJS , 166, 470

Ross, R. R. & Fabian, A. C. 2005, MNRAS , 358, 211

Salpeter, E. E. 1964, ApJ , 140, 796

Salvi, N. J., Page, M. J., Stevens, J. A., et al. 2002, MNRAS , 335, 177

Sambruna, R. M., Maraschi, L., & Urry, C. M. 1996, ApJ , 463, 444

Sanfrutos, M., Longinotti, A. L., Krongold, Y., Guainazzi, M., & Panessa, F. 2018, The Astrophysical Journal, 868, 111

Santoro, F., Oonk, J. B. R., Morganti, R., Oosterloo, T. A., & Tadhunter, C. 2016, A&A , 590, A37

Schmidt, M. 1963, Nature , 197, 1040

Schwarzschild, K. 1916, Abh. Konigl. Preuss. Akad. Wissenschaften Jahre 1906,92, Berlin,1907, 1916, 189

Seyfert, C. K. 1943, ApJ , 97, 28

Shakura, N. I. & Sunyaev, R. A. 1973, A&A , 500, 33

Shapiro, I. I. & Weinreb, S. 1966, ApJ , 143, 598

Silk, J. 2005, MNRAS , 364, 1337

Silk, J. 2013, ApJ , 772, 112

Silk, J. & Rees, M. J. 1998, A&A , 331, L1

Singh, K., Meintjes, P., Ramamonjisoa, F., & Tolamatti, A. 2019, New Astronomy , 73, 101278

Snellen, I. A. G., Mack, K. H., Schilizzi, R. T., & Tschager, W. 2004, MNRAS , 348, 227

Steenbrugge, K. C., Kaastra, J. S., de Vries, C. P., & Edelson, R. 2003, A&A , 402, 477

Steenbrugge, K. C., Kaastra, J. S., Sako, M., et al. 2005, A&A , 432, 453

Storchi-Bergmann, T., Lopes, R. D. S., McGregor, P. J., et al. 2010, MNRAS , 402, 819

Strüder, L., Briel, U., Dennerl, K., et al. 2001, A&A , 365, L18

Surace, J. A., Sanders, D. B., & Evans, A. S. 2001, AJ , 122, 2791

Tananbaum, H., Avni, Y., Branduardi, G., et al. 1979, ApJ , 234, L9

Taylor, C. & Reynolds, C. S. 2018, ApJ , 855, 120

Taylor, G. L., Dunlop, J. S., Hughes, D. H., & Robson, E. I. 1996, MNRAS , 283, 930

Taylor, R. D., Uttley, P., & McHardy, I. M. 2003, MNRAS , 342, L31

Titarchuk, L. 1994, ApJ , 434, 570

Tombesi, F., Cappi, M., Reeves, J. N., & Braito, V. 2012, MNRAS , 422, L1

Tombesi, F., Cappi, M., Reeves, J. N., et al. 2011, ApJ , 742, 44

Tombesi, F., Cappi, M., Reeves, J. N., et al. 2010, A&A , 521, A57

Turner, T. J., George, I. M., & Mushotzky, R. F. 1993, ApJ , 412, 72

Turner, T. J. & Pounds, K. A. 1989, MNRAS , 240, 833

Unger, S. W., Lawrence, A., Wilson, A. S., Elvis, M., & Wright, A. E. 1987, MNRAS , 228, 521

Urry, C. M. & Padovani, P. 1995, PASP , 107, 803

Uttley, P., Cackett, E. M., Fabian, A. C., Kara, E., & Wilkins, D. R. 2014, Astronomy and Astrophysics Review, 22, 72

Uttley, P., McHardy, I. M., & Vaughan, S. 2005, MNRAS , 359, 345

Vagnetti, F., Antonucci, M., & Trevese, D. 2013, A&A , 550, A71

Vaughan, S. 2010, MNRAS , 402, 307

Vaughan, S., Edelson, R., Warwick, R. S., & Uttley, P. 2003, MNRAS , 345, 1271

Veilleux, S., Kim, D.-C., Rupke, D. S. N., et al. 2009, ApJ , 701, 587

Veilleux, S., Tully, R. B., & Bland-Hawthorn, J. 1993, AJ , 105, 1318

Vestergaard, M. & Peterson, B. M. 2006, ApJ , 641, 689

Vestergaard, M., Wilkes, B. J., & Barthel, P. D. 2000, ApJ , 538, L103

Waddell, S. G. H. & Gallo, L. C. 2020, MNRAS , 498, 5207

Wagner, A. Y., Umemura, M., & Bicknell, G. V. 2013, ApJ , 763, L18

Wang, J., Fabbiano, G., Karovska, M., et al. 2009, ApJ , 704, 1195

Wang, T., Brinkmann, W., & Bergeron, J. 1996, A&A , 309, 81

Wilkins, D. R. & Fabian, A. C. 2011, MNRAS , 414, 1269

Wilkins, D. R. & Fabian, A. C. 2012, MNRAS , 424, 1284

Wilkins, D. R. & Gallo, L. C. 2015a, MNRAS , 449, 129

Wilkins, D. R. & Gallo, L. C. 2015b, MNRAS , 448, 703

Wilkins, D. R., Gallo, L. C., Silva, C. V., et al. 2017, MNRAS , 471, 4436

Wilkins, D. R., Kara, E., Fabian, A. C., & Gallo, L. C. 2014, MNRAS , 443, 2746

Willingale, R., Starling, R. L. C., Beardmore, A. P., Tanvir, N. R., & O'Brien, P. T. 2013, MNRAS , 431, 394

Wilms, J., Allen, A., & McCray, R. 2000, ApJ , 542, 914

Wilson, A. S. & Colbert, E. J. M. 1995, ApJ , 438, 62

XRISM Science Team. 2020, arXiv e-prints, arXiv:2003.04962

Zel'dovich, Y. B. 1964, Soviet Physics Doklady, 9, 195

Zhang, S. N., Ji, L., Marshall, H. L., et al. 2011, MNRAS , 410, 2274

Zhang, Z., Gupta, A. C., Gaur, H., et al. 2019, ApJ , 884, 125

Zoghbi, A., Fabian, A. C., Uttley, P., et al. 2010, MNRAS , 401, 2419